Technische Universität Ilmenau

DISSERTATION

New Advances in Susceptibility Weighted MRI to Determine Physiological Parameters

ausgeführt zum Zwecke der Erlangung des akademischen Grades
eines Doktors der Naturwissenschaften (Dr. rer. nat.)

vorgelegt der Fakultät für Mathematik und Naturwissenschaften
der Technischen Universität Ilmenau

von Dipl. Ing. Jan Sedlacik

1.Gutachter: Prof. Dr. rer. nat. habil. Phillip Maaß
2.Gutachter: Prof. Dr. rer. nat. med. habil. Jürgen R. Reichenbach
3.Gutachter: Univ. Doz. Dipl. Ing. Dr. techn. Markus Barth

Tag der Einreichung: 22. Oktober 2007
Tag der wissenschaftlichen Aussprache: 19. November 2007

urn:nbn:de:gbv:ilm1-2007000258

List of Abbreviations

α	Flip Angle
ADC	Analog Digital Converter
$\vec{B}_0$	main magnetic field
BF	Blood Flow
BG	Background
BW	Bandwidth
γ	gyromagnetic ratio
CBF	Cerebral Blood Flow
CBV	Cerebral Blood Volume
$CMRO_2$	Cerebral Metabolic Rate for Oxygen
CPAP	Continuous Positive Airway Pressure system
CPMG	Carr-Purcell-Meiboom-Gill sequence
DWI	Diffusion Weighted Imaging
$\varnothing$	Diameter
EPI	Echo Planar Imaging
FOV	Field Of View
FID	Free Induction Decay
FLASH	Fast Low Angle Shot
FT	Fourier Transform
Gd-DTPA	paramagnetic contrast agent (Gadolinium Diethylenetriamine Pentaacetic Acid)
GESFIDE	Gradient Echo Sampling of FID and Echo
GESSE	Gradient Echo Sampled Spin Echo
Hb	deoxyhemoglobin
HbO_2	oxyhemoglobin
Hct	Hematocrit
θ	angle which characterizes the orientation between $\vec{B}_0$ and the long axis of a cylinder, capillary or vein
λ	volume fraction of a compartment within a voxel
IDEA	Integrated Integrated Development Environment for Applications
IDL	Interactive Data Language
IRSE	Inversion Recovery Spin Echo sequence
MESWI	Multi-Echo Susceptibility Weighted Imaging

mIP	minimal Intensity Projection
MR	Magnetic Resonance
MRI	Magnetic Resonance Imaging
MRO_2	Metabolic Rate for Oxygen
MSE	root Mean Square Error
NIRS	Near Infrared Spectroscopy
NMR	Nuclear Magnetic Resonance
OEF	Oxygenation Extraction Fraction
PET	Positron Emission Tomography
pO2	Oxygen partial pressure
PP	Polypropylene
R_1	spin-lattice/longitudinal relaxation rate
R_2	spin-spin/transverse relaxation rate
RF	Radio Frequency
ROI	Region Of Interest
SAR	Synthetic Aperture Radar
SNR	Signal to Noise Ratio
SQUID	Superconducting Quantum Interference Device
sPSF	sampling Point Spread Function
SWI	Susceptibility Weighted Imaging
T_1	spin-lattice/longitudinal relaxation time
T_2	spin-spin/transverse relaxation time
T_2^*	relaxation time of spin-spin relaxation and reversible signal dephasing in static magnetic field inhomogeneities
T_2'	relaxation time of reversible signal dephasing in static inhomogeneities
T_E	echo time
T_R	repetition time
Y	blood oxygenation level
χ	magnetic susceptibility
ω	angular frequency
$\Delta\chi$	difference in magnetic susceptibility between two materials
ΔB	local magnetic field inhomogeneities, e.g. caused by a magnetized cylinder

Zusammenfassung der Dissertation

Die suszeptibilitätsgewichtete Bildgebung ist eine neue Methode der Magnetresonanztomographie, die sowohl die Magnituden- als auch die Phaseninformation einer räumlich hochaufgelösten, flusskompensierten 3D T_2^*-gewichteten Gradientenechosequenz verbindet. Die suszeptibilitätsgewichtete Bildgebung wurde bereits zur Untersuchung von zerebralen Tumoren, vaskulären Veränderungen, Traumata, zur Diagnostik des Schlaganfalls und von Mikrohämorrhagien sowie als Methode zur funktionellen Bildgebung eingesetzt. Die dieser Methode zugrundeliegende Abhängigkeit des Messsignals von der Verteilung und Stärke der magnetischen Suszeptibilitätsunterschiede wurde in der vorliegenden Arbeit näher untersucht. Ziel war es, die Möglichkeit einer Quantifizierung der Suszeptibilitätsunterschiede zu erforschen, da der ermittelte Suszeptibilitätsunterschied Rückschlüsse auf den Grad der Blutoxygenierung in venösen Gefäßen bzw. dem von Blutkapillaren durchzogenen Hirngewebe erlaubt. Die genaue Kenntnis der Blutoxygenierung ist beispielsweise für die Tumordiagnostik von enormer Bedeutung, da hier die Prognose der Erkrankung durch Strahlen- und Chemotherapie direkt mit der Sauerstoffversorgung des Tumors korreliert. Gut versorgtes Tumorgewebe ist anfälliger für Strahlung bzw. Chemotherapeutika als minderversorgtes Gewebe, welches schlechter auf die Therapie anspricht. In der Diagnostik von Schlaganfällen ist die Sauerstoffversorgung ebenfalls ein wichtiger Indikator für die Überlebensfähigkeit des betroffenen Gewebes. Eine nicht-invasive schnittbildgebende Bestimmung der Blutoxygenierung birgt daher ein enormes Potential zur besseren Charakterisierung von Pathologien.

Die Magnetresonanztomographie bietet die Möglichkeit der Bestimmung des Blutoxygenierungsgrades kleiner venöser Gefäße und damit lokaler Hirnareale mit Hilfe einer Multiecho-Gradientenecho-Sequenz. Mit dieser Sequenz kann der Signalzerfall in einem Voxel, welches von einer einzelnen Vene bzw. von Blutkapillaren durchzogen ist, bestimmt werden. Der Signalzerfall ist charakteristisch für die von der Vene oder den Kapillaren erzeugten Feldinhomogenitäten, so dass sich Aussagen über den Blutoxygenierungsgrad und Blutvolumenanteil treffen lassen. Bei Betrachtung einzelner Venen ist es notwendig, dass sich die gefäßumgebende Feldinhomogenität innerhalb des zu messenden Voxels befindet. Damit können Gefäße, die nur einen Bruchteil des Voxelvolumens einnehmen, untersucht werden.

Als theoretisches Modell für einzelne venöse Gefäße diente in der vorliegenden Arbeit ein unendlich langer, homogen magnetisierter Zylinder. Die Feldverteilung inner- und außerhalb des Zylinders kann anhand von, aus der Magnetostatik bekannten, Formeln analytisch berechnet werden, wobei die Orientierung der Zylinderachse zum Magnetfeld eine wichtige Rolle spielt. Bei einer parallelen Ausrichtung zum Hauptmagnetfeld wird keine Feldinhomogenität in der Umgebung des Zylinders induziert. Mit zunehmender Verkippung nimmt die Ausprägung der extravaskulären Feldverzerrung zu und ist bei senkrechter Orientierung maximal. Das stets homogene Magnetfeld im Zylinderinneren wird ebenfalls durch die Orientierung des Zylinders beeinflusst. Seine Differenz zum

Hauptmagnetfeld ist jedoch, im Gegensatz zur extravaskulären Feldverzerrung, maximal bei einer parallelen und minimal bei einer senkrechten Ausrichtung. Zusätzlich ist die Stärke des von dem Zylinder induzierten inneren und äußeren Feldes noch proportional zu dessen Suszeptibilitätsunterschied zur Umgebung. Der Zeitverlauf des MR-Signals zeigt charakteristische Modulationen, die in ihrer Ausprägung sehr empfindlich von den Feldinhomogenitäten und deren Änderungen abhängen. Die Form des Voxels spielt dabei eine entscheidende Rolle, da sie bestimmt, wie die extravaskuläre Inhomogenität das Voxelsignal beeinflusst. Das Signalverhalten in einem einzelnen Voxel wurde in der vorliegenden Arbeit unter Berücksichtigung verschiedener Orientierungen, Gefäßgrößen, Suszeptibilitäten und Voxelformen numerisch simuliert.

Durch Fitten der simulierten Signalverläufe an gemessene Phantom- und Probandendaten konnte gezeigt werden, dass es mit der hier vorgestellten Methode möglich ist, den venösen Blutoxygenierungsgrad zu quantifizieren. Weiterhin konnte eine durch gezielte Modulation des zerebralen Blutflusses hervorgerufene Änderung der Blutoxygenierung *in vivo* nachgewiesen werden.

Die Erweiterung des Modells eines einzelnen, unendlich langen Zylinders auf ein Netzwerk von randomisiert angeordneten und orientierten Zylindern diente als Grundlage zur theoretischen Beschreibung der Blutkapillaren, die das Hirngewebe durchziehen und mit Sauerstoff versorgen. In Phantomexperimenten konnte verifiziert werden, dass die gemessenen Signalverläufe die aus dem theoretischen Modell erhaltenen Verläufe wiedergeben. Dagegen zeigte sich bei einer Probandenmessung, dass es nicht möglich ist einzig anhand des gemessenen Signalverlaufs valide Werte für die Blutoxygenierung und den Blutvolumenanteil eindeutig zu bestimmen. Beide Größen sind freie Parameter für den Fitalgorithmus, da weder die Oxygenierung noch der Volumenanteil a priori bekannt sind. Die hohe Korrelation zwischen beiden Parametern bewirkt, dass mehrere Paare von Oxygenierungs- und Volumenwerten passende Signalkurven liefern. Eine unabhängige Quantifizierung oder Abschätzung des venösen Blutvolumens kann hier helfen eindeutige Oxygenierungswerte zu erhalten.

Im Rahmen der vorliegenden Dissertation konnte das Signalverhalten von suszeptibilitätssensitiven Messungen in der Magnetresonanztomographie genauer untersucht und eine Methode zur nicht-invasiven Bestimmung der venösen Blutoxygenierung an einzelnen Gefäßen entwickelt werden. Die Erweiterung der Methode auf das Blutkapillarnetzwerk wurde in Phantommessungen verifiziert. Erste *in vivo* Anwendungen verdeutlichen, dass für eine genaue Quantifizierung der Blutoxygenierung weitere Parameter, die das Signalverhalten beeinflussen, unabhängig bestimmt werden müssen. Inwieweit sich dadurch die Quantifizierung der Blutoxygenierung im Kapillarnetzwerk besser und genauer bewerkstelligen lässt, ist in weiteren Studien zu untersuchen. Es ist dennoch möglich, die Methode am einzelnen Blutgefäß zur besseren Charakterisierung von Pathologien sowie physiologischen Änderungen, z.B. bei der funktionellen Magnetresonanztomographie, einzusetzen.

Summary of Thesis

Susceptibility weighted imaging is a novel magnetic resonance imaging technique. It combines the MR signal's magnitude and phase to enhance contrast between structures with different magnetic susceptibilities such as venous vessels. Susceptibility weighted imaging has already been applied to investigate cerebral tumors, vascular malformations, trauma, stroke, microhemorrhages and hemodynamic changes during neuronal activation. The aim of the work presented in this thesis was to gain a deeper understanding of the fundamental relations between the measured signal and magnetic susceptibility in order to quantify the blood oxygenation of venous cerebral vessels or brain tissue by exploiting susceptibility differences. An important aspect of this work were new insights that can be drawn from a quantification of susceptibility differences on the blood oxygenation of venous vessels or brain tissue. Knowledge of the blood oxygenation is of high importance, for instance, in tumor diagnostics. Blood oxygenation of tumor tissue is a reliable marker of the tumor's sensitivity to chemotherapy and radiotherapy and, thus, of the patient's prognosis. Tumor tissue with a good blood supply shows a higher sensitivity to such therapies than less perfused tumor tissue. Furthermore, stroke diagnosis could benefit from a better characterization of tissue at risk and its viability by quantitative blood oxygenation levels. Thus, a non-invasive blood oxygenation imaging method would be very beneficial for a better characterization of pathologies and therapy monitoring.

Magnetic resonance imaging allows to determine the blood oxygenation level of small venous vessels or the blood capillary network by evaluating the signal formation acquired with multi-echo gradient-echo sequences. The evolution of a signal over time of a voxel traversed by a vein or embedded in a capillary network exhibits a characteristic decay or modulation from which the blood oxygenation and blood volume fraction can be derived. For single vessels it is necessary to take the surrounding field inhomogeneity generated by the vessel into account. This enables the investigation of veins, which are even smaller than the size of a voxel – on other words veins that occupy only a fraction of the voxel's volume.

The model of an infinitely long homogeneously magnetized cylinder was used to simulate the signal formation of a single vessel. The field distribution of such a magnetized cylinder can be calculated using magnetostatics. The cylinder's orientation is of importance and scales the local field. In case of a cylinder orientation parallel to the main magnetic field, no extravascular field inhomogeneity is induced. On the other hand, the surrounding field inhomogeneity is maximized in case of a perpendicular orientation. The field inside the cylinder is always homogeneous but its difference to the main magnetic field is maximal for the parallel and minimal for perpendicular cylinder orientation. The difference in magnetic susceptibility between the cylinder and its surroundings additionally determines the magnitude of the inner and outer field. The simulated signal-time curves show characteristic oscillations which are sensitive to the local field of the cylinder and change as the local field changes. Therefore, also the shape

of the voxel is important, because it determines how the extravascular field distribution contributes to the voxel signal. For this work the signal was simulated numerically for various cylinder orientations, diameters, susceptibility differences and voxel geometries.

It has been demonstrated that the signal obtained from systematic phantom measurements correctly matched predictions obtained with the numerical signal simulation. By fitting the simulated signal to *in vivo* measurements of cerebral venous vessels, vessel size and venous blood oxygenation were determined quantitatively. Furthermore, it was possible to detect and quantify a physiologically induced change in cerebral venous blood oxygenation.

The extension of this single cylinder to a network was used as the basis of a theoretical model to simulate the signal of the blood capillaries in normal brain matter. The network model is formed by randomly oriented and positioned infinitely long cylinders. The signal simulation was validated with phantom experiments. The network's parameters were reproduced by fitting the simulated signal to the measured signal. It was also demonstrated that the two parameters describing the network, the blood volume fraction and blood oxygenation level, are correlated to each other. This means that a separation of both parameters is not possible without additional information. This finding was of special importance in the initial *in vivo* measurements conducted in the presented work. For which an independent determination of the blood volume may help to further validate the quantified blood oxygenation level.

In the presented work a non-invasive method was developed to quantify cerebral blood oxygenation levels in single veins. This was possible by investigating the signal evolution of susceptibility sensitive magnetic resonance imaging. The extension to the capillary network was validated in phantom measurements. The initial result of the measurements of a network's signal *in vivo* reveals, that for obtaining a valid blood oxygenation level, the volume fraction has to be further determined by an independent measurement. This uncertainty is caused by a correlation between these two parameters. Methods to improve an independent determination of these parameters, have to be explored in further studies. Nevertheless, is has been demonstrated that the quantification of the blood oxygenation level in single venous vessels is possible and can be applied in clinical diagnosis for better characterization of cerebral pathologies or in physiological investigations, like in functional magnetic resonance imaging.

Contents

"Es gibt keine Naturkraft, welche so modulationsfähig ist wie die Electrizität, denn es ist ein leichtes, sie in alle Formen der Energie umzugestalten; bald verwenden wir sie als Kraft, bald als Wärme, bald als Licht, bald als Magnetismus, bald als chemisch wirkenden Strom"

Professor Georg Schmidt, director of the Thüringisches Technikum Ilmenau on its opening ceremony Nov 03, 1894

Introduction

Blood oxygenation levels of cerebral tissue provide important information on the physiological and pathological state of the brain. This information can be exploited to better characterize the oxygenation status of tumor tissues or tissue at risk in case of ischemic events. For example, a low tumor oxygenation status (hypoxia) is known to be a poor prognostic factor for the therapeutic outcome in solid tumors (Vaupel and Mayer, 2007). Several endeavors have been made to enhance the tumor's sensitivity to chemotherapeutics and/or radiation therapy by increasing the tumor oxygenation during the treatment (Thomas, 2002; Kaanders et al., 2004; Harrison and Blackwell, 2004). Evidence is also rising that tumor hypoxia may contribute to mutagenesis (Kondo et al., 2001).

A non-invasive technique which produces cross sections of the blood oxygenation level in cerebral tissue would be extremely powerful in characterizing differences of pathologies and for treatment monitoring.

Several invasive and non-invasive methods are available for the quantification of cerebral blood oxygenation. Jugular bulb oximetry is an invasive way to monitor cerebral blood oxygenation by inserting a catheter directly into the vessel. Magnetic resonance susceptometry is a non-invasive method (Fernández-Seara et al., 2006), but allows only to extract a global value from a large draining vein. Near infrared spectroscopy (NIRS) also measures the blood oxygenation non-invasively, however, only superficial cortical regions are accessible to this method (Ferrari et al., 2004). With positron emission tomography (PET) cerebral blood oxygenation, cerebral blood flow (CBF), cerebral blood volume (CBV) and cerebral metabolic rate of oxygen ($CMRO_2$) can be determined.

However, the technique is quite expensive, not ubiquitously available, and requires radioactive ^{15}O as a marker (Ito et al., 2004).

In contrast to all these methods, magnetic resonance imaging (MRI) has the potential to measure non-invasively spatially resolved oxygenation levels of the blood capillary network embedded in a tissue matrix. The signal in gradient echo MRI is subject to a decay characterized by the time constant T_2^*, which stems from the signal decay of irreversible spin-spin interactions (T_2-decay) and the decay associated with static field inhomogeneities (T_2'- decay). This signal decay depends on the vascular network which, in turn, can be characterized by the volume fraction, occupied by the network within the voxel, and the amount of oxygen in blood. The theory of the signal's behavior in presence of a vascular network was first described by Yablonskiy and Haacke (1994) and recently applied in healthy human subjects (He and Yablonskiy, 2007). However, an independent verification has not been carried out yet.

The purpose of the work presented here was to verify this influence on the MR-signal by modeling and investigating the influence of a single blood vessel on the MR signal in both, phantom experiments and numerical simulations. Furthermore, an extension of the single vessel model to the blood capillary network as proposed by Yablonskiy and Haacke (1994) by considering mutual avoiding cylinders (Kiselev, 2004) was investigated and verified in a phantom study and an initial *in vivo* measurement. Conclusions were also drawn for future studies in which the findings of the presented work could be further validated and improved.

"I have not yet lost a feeling of wonder, and of delight, that this delicate motion should reside in all the things around us, revealing itself only to him who looks for it. I remember, in the winter of our first experiments, just seven years ago, looking on snow with new eyes. There the snow lay around my doorstep - great heaps of protons quietly precessing in the earth's magnetic field. To see the world for a moment as something rich and strange is the private reward of many a discovery."

Edward Mills Purcell, Nobel lecture (11th December, 1952), won the Nobel prize in 1952 for his detection of nuclear magnetic resonance.

2 Basic Principles

2.1. Nuclear Magnetic Resonance

Nuclear Magnetic Resonance (NMR) was first described by Purcell et al. (1946) and Bloch (1946). For their discovery both received the Nobel Prize in Physics 1952. This section will give a brief introduction to the physical phenomena necessary for understanding Magnetic Resonance Imaging (MRI). The classical descriptions of these phenomena are only valid for a large amount of decoupled or weakly coupled spins with a spin quantum number of $I = \frac{1}{2}$, which is the case in H^1-MRI. For further reading the standard works of Abragam (1994) or Slichter (1992) are recommended.

2.1.1. Nuclear Spin and Magnetic Moment

Unpaired elementary particles (fermions) like neutrons, protons and electrons possess a spin with the spin quantum number of $I = \frac{1}{2}$. In nuclei, protons and neutrons pair up separately by canceling their spins and orbital motions. Nuclei with an even number of neutrons and protons, e.g. ^{16}O and ^{12}C, have a total spin of zero and therefore no magnetic moment. They can not be imaged in MRI. However, nuclei with an odd number of protons, neutrons or both, possess a spin larger than zero. The angular momentum $\vec{J}$ is related to the magnetic moment $\vec{\mu}$ by

$$\vec{\mu} = \gamma \vec{J}. \tag{2.1}$$

The gyromagnetic ratio γ is the proportional constant of this relationship and characteristic for each nucleus (Tab. 2.1).

Table 2.1: *List of selected nuclei with their spins and associated magnetic moments. The latter is given in units of $\mu_N = \frac{e\hbar}{2m_p}$ with the elementary charge e and the mass of a proton m_p. The gyromagnetic ratio $\gamma = \frac{\gamma}{2\pi}$ in units of $MHz \cdot T^{-1}$ and the relative body abundance in units of 1 M = 1 molar = 1 mole/liter. A negative sign for the moment and gyromagnetic ratio refers to the fact that the magnetic moment is anti-parallel to the angular momentum vector. Table adapted from Haacke et al. (1999).*

Nuclei	Total spin	Magnetic moment / μ_N	γ / MHz·T^{-1}	Abundance in human body
hydrogen ^{1}H	1/2	2.793	42.58	88 M
sodium ^{23}Na	3/2	2.216	11.27	80 mM
phosphorus ^{31}P	1/2	1.131	17.25	75 mM
oxygen ^{17}O	5/2	-1.893	-5.77	16 mM
fluorine ^{19}F	1/2	2.627	40.08	4 μM

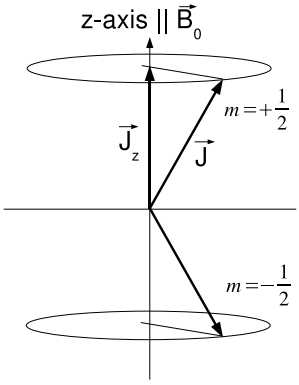

Figure 2.1: *The two different orientations of a spin with $I = \frac{1}{2}$ in an external magnetic field.*

The magnitude of the angular momentum of the nucleus, $|\vec{J}|$, is quantized in steps of $\hbar$ ($\hbar = h/2\pi = 1.0545 \cdot 10^{-34}$ Js):

$$|\vec{J}| = \sqrt{I(I+1)}\hbar \quad \text{with} \quad I = 0, \frac{1}{2}, 1, \frac{3}{2}, \ldots . \tag{2.2}$$

Thus, the z component of the angular momentum is quantized as well, when an external magnetic field is originated along the z-axis (Fig. 2.1):

$$J_z = m_I \hbar \quad \text{with} \quad m_I = -I, -I+1, ..., I-1, I. \tag{2.3}$$

This quantization is due to the discrete energy states in quantum mechanics. Therefore the orientation of the angular momentum with respect to the external magnetic field is also discretized as well as the magnetic moment and it is given by

$$\mu_z = \gamma J_z = \gamma m_I \hbar. \tag{2.4}$$

The energy of a dipole $\vec{\mu}$ in a magnetic field[1] $\vec{B}_0$ is given classically by

$$E = -\vec{\mu} \cdot \vec{B}_0. \tag{2.5}$$

The different orientations of the spin with respect to the external magnetic field correspond to the discrete energy eigenvalues:

$$E_m = -\gamma B_0 m_I \hbar, \tag{2.6}$$

with m_I being one of the $2I + 1$ possible values of μ_z. For a nucleus with $I = \frac{1}{2}$, two orientations, parallel: $m = \frac{1}{2}$ and anti-parallel: $m = -\frac{1}{2}$, are possible and with it two different energy levels. The gap between these two levels is proportional to the magnitude of B_0 (Fig. 2.2), whereas a transition between these two levels is accompanied by emission and absorption of a photon. The photon energy of $\hbar\omega_0$ is absorbed by a transition from the lower (parallel orientation) to the higher (anti-parallel orientation) energy level. The transition from the higher to the lower level goes along with a photon emission. According to Eq. 2.6 the energy difference is

$$\Delta E = E_{m=-\frac{1}{2}} - E_{m=+\frac{1}{2}} = \gamma B_0 \hbar. \tag{2.7}$$

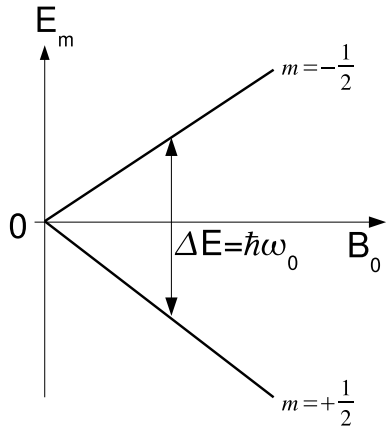

Figure 2.2: *Energy gap between the two different orientations of a spin with $I = \frac{1}{2}$ versus the strength of the external magnetic field.*

The photon energy is equal to the energy difference (Eq. 2.7). The angular frequency of the gyromagnetic precession given by

$$\vec{\omega}_0 = -\gamma \vec{B}_0. \tag{2.8}$$

This angular frequency is called the Larmor frequency and denotes the resonance frequency of a nucleus.

[1] $\vec{B}$ is the magnetic flux, density field or the magnetic induction field, but most people in MRI call it the magnetic field, as we will do it.

2.1.2. Macroscopic Magnetization

In MRI the typical size of the measured volume is on the order of $1\,\mathrm{mm}^3$ and the measured objects mainly consist of water. In a volume of $1\,\mathrm{mm}^3$ of water about 0.111 mmol of hydrogen nuclei "are crowded" together. Multiplication with the Avogadro constant ($N_A = 6.0221415 \cdot 10^{23}\,\mathrm{mol}^{-1}$) gives the number of $6.69 \cdot 10^{19}$ protons, which is high enough to allow a macroscopic description of basic NMR processes as it will be accomplished in the following sections of this work.

The two energy states of the parallel and anti-parallel spin orientation will be populated in thermal equilibrium according to the Boltzmann statistics:

$$\frac{n_{-1/2}}{n_{1/2}} = \exp\left(-\frac{\Delta E}{k_B T}\right) = \exp\left(-\frac{\gamma\hbar B_0}{k_B T}\right), \tag{2.9}$$

where $n_{1/2}$ and $n_{-1/2}$ are the populations of the parallel and anti-parallel spin alignment, respectively. The thermal energy, with the Boltzmann constant $k_B = 1.3807 \cdot 10^{-23}\,\mathrm{J \cdot K^{-1}}$ and the temperature T, is at body temperature much larger than the magnetic energy associated with typical clinical MRI magnetic fields of e.g., $B_0 = 1.5$ or 3 T. Inserting these values in Eq. 2.9 yields a population ratio of 1.00001, which means that just 10 ppm more spins are oriented parallel than anti-parallel to the external magnetic field. However, due to the huge amount of protons, e.g. in $1\,\mathrm{mm}^3$ water, the overplus of spins in the parallel orientation is $\Delta n = 6.54 \cdot 10^{14}$. This means that in thermal equilibrium there is a slight polarization of the spin angular momentum vector along the direction of the external magnetic field (Fig. 2.3). With $N = n_{1/2} + n_{-1/2}$ and $\Delta n = n_{1/2} - n_{-1/2}$ Eq. 2.9 can be converted to

$$\Delta n = N \cdot \tanh\left(\frac{\gamma\hbar B_0}{2k_B T}\right) \approx N\frac{\gamma\hbar B_0}{2k_B T} \tag{2.10}$$

and the macroscopic magnetization in thermal equilibrium can then be calculated with

$$\vec{M}_0 = \vec{\mu} \cdot \Delta n \approx \vec{\mu} N \frac{\gamma\hbar B_0}{2k_B T}. \tag{2.11}$$

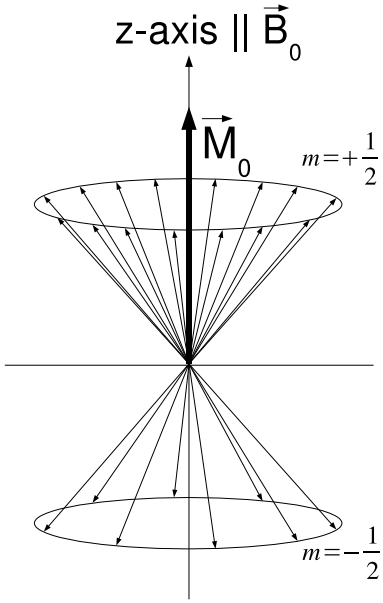

Figure 2.3: *Formation of the proton spins in an external magnetic field parallel to the z-axis. In the thermal equilibrium a slightly higher amount of spins are aligned parallel to $\vec{B}_0$ orientation and form the macroscopic magnetization $\vec{M}_0$. Figure adapted from G. Brix: Physikalische Grundlagen, In: Reiser and Semmler (1992).*

2.1.3. Motion of Magnetic Moments in an External Field

Due to the related angular momentum with the magnetic moment of single spins (Eq. 2.1), also the macroscopic net magnetization vector $\vec{M}$ of ensembles of spins is related to an angular momentum $\vec{J}$ and is given by

$$\vec{M} = \gamma \vec{J}. \tag{2.12}$$

An external magnetic field causes a torque on the magnetization vector, which is given by

$$\vec{T} = \vec{M} \times \vec{B}_0. \tag{2.13}$$

The torque $\vec{T}$ acts perpendicular to the plane of the vectors $\vec{M}$ and $\vec{B}_0$ (Fig. 2.4) and changes the system's total angular momentum, according to

$$\vec{T} = \frac{d\vec{J}}{dt} = \vec{M} \times \vec{B}_0. \tag{2.14}$$

Applying Eq. 2.12 yields

$$\frac{d\vec{M}}{dt} = \vec{M} \times \gamma \vec{B}_0. \tag{2.15}$$

With Eq. 2.8 for the Larmor frequency the change of the magnetic moment can be written as

$$\frac{d\vec{M}}{dt} = \vec{\omega}_0 \times \vec{M}. \tag{2.16}$$

The mechanical analogon to this kind of precession is the gyroscopic precession of a spinning top tilted out of a parallel alignment with the direction of a constant gravitational field.

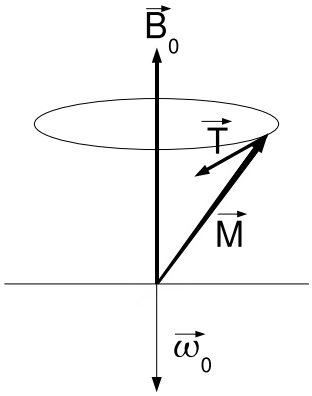

Figure 2.4: *Torque on a magnetization vector in an external magnetic field. The resulting gyromagnetic precession of $\vec{M}$ is depicted by $\vec{\omega}_0$.*

2.1.4. Radio Frequency Fields

The resonance phenomenon results from the application of an oscillating magnetic field $\vec{B}_1$ oriented transversely to the main magnetic field $\vec{B}_0$ and oscillating with the angular frequency $\vec{\omega}_0$. The circularly polarized component of the transverse field will then be in the same sense as the spin precession, namely

$$\vec{B}_1(t) = \begin{pmatrix} B_1 \cos \omega_0 t \\ B_1 \sin \omega_0 t \\ 0 \end{pmatrix}. \tag{2.17}$$

Including Eq. 2.17 in Eq. 2.15 the equation of motion of the magnetization vector can be written as

$$\frac{d\vec{M}}{dt} = \vec{M} \times \gamma \vec{B} \quad \text{with} \quad \vec{B}(t) = \begin{pmatrix} B_1 \cos \omega_0 t \\ B_1 \sin \omega_0 t \\ B_0 \end{pmatrix}. \tag{2.18}$$

The simultaneous precession about the B_0 and B_1 field will result in some complicated motion of the magnetization vector. Therefore, a rotating frame of reference (x', y', z') is introduced, which rotates around the z-axis (z=z') with the rotating frequency $\vec{\omega}_0$. In this rotating coordinate system the precession about B_0 is compensated and only the precession about the B_1 field, which will be aligned to the x'-axis, is observed (Fig. 2.5). Eq. 2.18 changes then to

$$\frac{d\vec{M}'}{dt} = \vec{M}' \times \gamma \vec{B}' \quad \text{with} \quad \vec{B}'(t) = \begin{pmatrix} B_1 \\ 0 \\ 0 \end{pmatrix}. \tag{2.19}$$

This precession motion about the B_1 field tips the magnetization vector by an angle α, called flip angle, out of the z-direction with

$$\alpha = \omega_1 t = \gamma B_1 \Delta t. \tag{2.20}$$

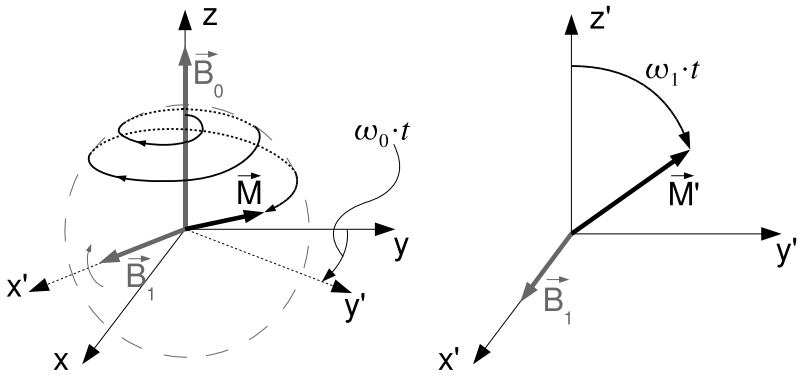

Figure 2.5: Left: *The motion of the magnetization vector due to the $\vec{B}_0$ and $\vec{B}_1$ fields in the stationary frame of reference. The rotating frame is turning with the same frequency as $\vec{B}_1$, so that the precession of $\vec{M}$ about the $\vec{B}_0$ field is compensated and the $\vec{B}_1$ field always be aligned to the x'-axis.* **Right:** *The motion of the magnetization in the rotating coordinate system can be easily described by precession about the $\vec{B}_1$ field.*

Thus, the degree of the flip angle can be arbitrarily adjusted just by the magnitude of B_1 and the duration Δt during which the B_1 field is applied. In common spin echo experiments the magnetization is mostly flipped about multiples of 90°, e.g. an excitation pulse with $\alpha = 90° = \pi/2$, refocusing or inversion pulse of $\alpha = 180° = \pi$.

2.1.5. Relaxation Phenomena

2.1.5.1. Spin-Lattice Relaxation

After the longitudinal magnetization M_L has been flipped by a B_1-field into the x'y'-plane, it starts to return back to the thermal equilibrium. In the equilibrium it will be aligned to the z-axis as prior to the B_1 excitation. Because the spin system exchanges the excess energy with the surrounding (i.e. the lattice) during this process, the latter is referred to as spin-lattice relaxation. This process can be described phenomenologically by a first order linear differential equation

$$\frac{dM_L}{dt} = -\frac{M_L - M_0}{T_1}. \tag{2.21}$$

The change of the longitudinal magnetization $\frac{\mathrm{d}M_L}{\mathrm{d}t}$ depends on the difference to the equilibrium magnetization $M_L - M_0$ and the relaxation constant $R_1 = \frac{1}{T_1}$. Solving Eq. 2.21 leads to

$$M_L(t) = M_0 \left(1 - e^{-\frac{t}{T_1}}\right) + M_{L(t=0)} \cdot e^{-\frac{t}{T_1}}, \tag{2.22}$$

where $M_{L(t=0)}$ is the longitudinal magnetization immediately after the excitation pulse. The time constant T_1 is the longitudinal or spin-lattice relaxation time. Some typical

T_1-relaxation times of human tissues are given in Tab. 2.2 and the relaxation process is shown schematically in Fig. 2.6.

Table 2.2: *Approximate values of relaxation times (T_1 and T_2) for protons in human tissues at $B_0 = 1.5\,\mathrm{T}$. Table adapted from Haacke et al. (1999).*

Tissue	T_1/ms	T_2/ms
fat	250	60
muscle	900	50
white matter	600	80
gray matter	950	100
arterial blood	1200	200
venous blood	1200	100
cerebrospinal fluid	4500	2200

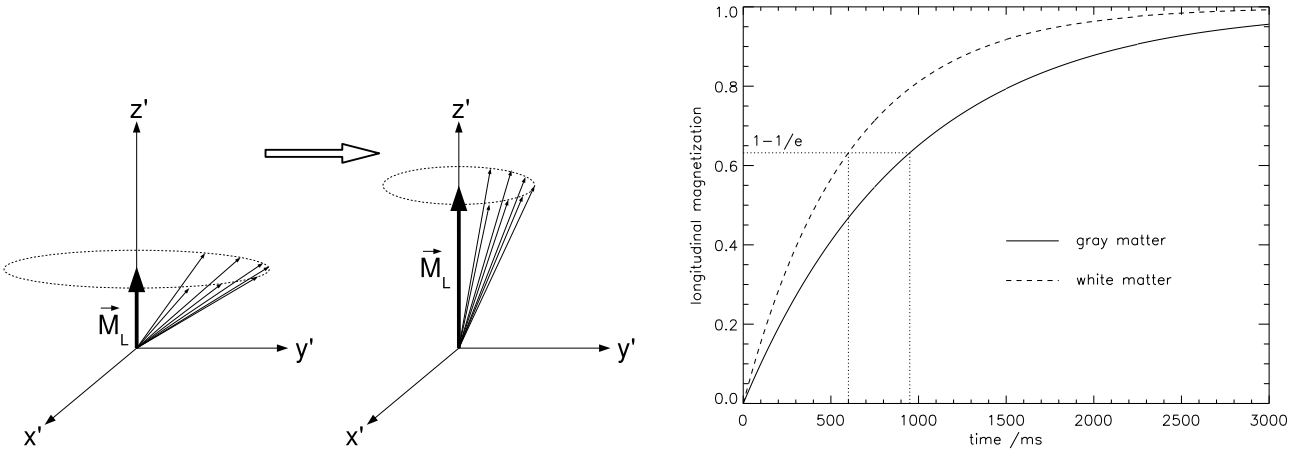

Figure 2.6: *Schematic view of the longitudinal relaxation. After excitation, the magnetization returns to its equilibrium state (Adapted from Lurie et al. (2001)). The increase of M_L for gray and white matter is shown in the left panel, where $M_L = 1$ denotes the equilibrium magnetization M_0.*

2.1.5.2. Spin-Spin Relaxation

A second relaxation process occurs due to dephasing of the transverse magnetization. This dephasing is a result of the Brownian motion of the water molecules and their interaction among each other. It is referred to as the spin-spin relaxation. This motion and interaction of the molecules cause a quickly varying local magnetic field which leads to a wider distribution of the resonance frequency around ω_0. Due to this resonance frequency distribution the phase coherence of the transverse magnetization is lost with

time and leads to a loss of net magnetization in the x'y'-plane (Fig. 2.7). This loss can be described phenomenologically by

$$\frac{dM_T}{dt} = -\frac{M_T}{T_2}, \tag{2.23}$$

where the change of the magnetization $\frac{dM_T}{dt}$ only depends on the transverse relaxation constant $R_2 = \frac{1}{T_2}$. Solving this first order linear differential equation leads to

$$M_T(t) = M_{T(t=0)} \cdot e^{-\frac{t}{T_2}}, \tag{2.24}$$

where the time constant T_2 is the transverse or spin-spin relaxation time and $M_{T(t=0)}$ denotes the transverse magnetization immediately after excitation. Some typical T_2-relaxation times of human tissues are given in Tab. 2.2.

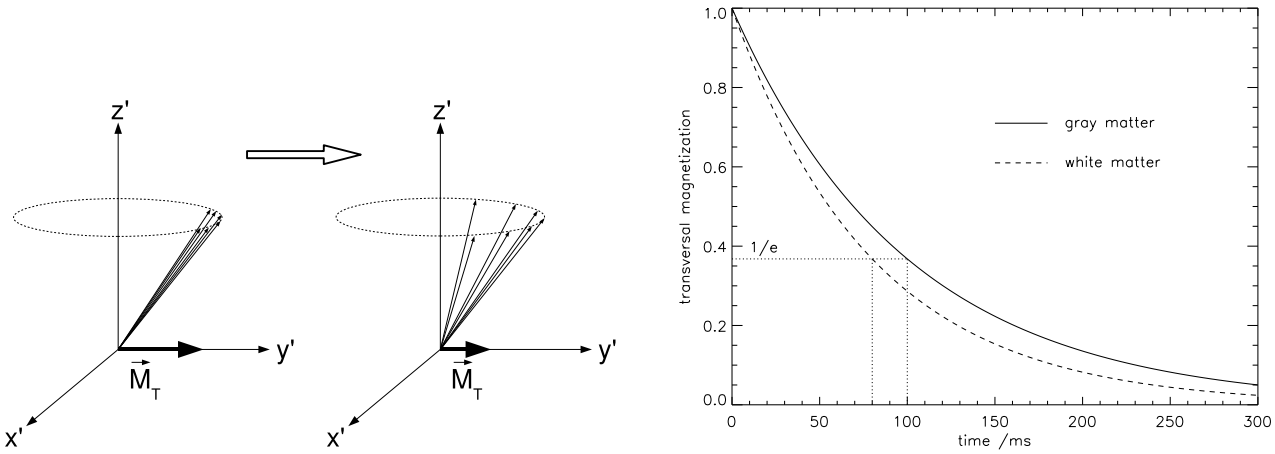

Figure 2.7: *Schematic view of the transverse relaxation. After excitation, the magnetization begins to dephase and the residual transverse magnetization drops (Adapted from Lurie et al. (2001)). The decrease of M_T for gray and white matter is shown in the left panel.*

While during the spin-lattice relaxation the equilibrium magnetization is reached due to energy exchange with the lattice, the spin-spin relaxation is a pure entropy effect and is not connected to energy exchange. Both relaxations occur independently of each other, but after the magnetization has returned to its equilibrium state no transverse magnetization exists anymore. Therefore, the T_2-relaxation time is always smaller than the T_1 time ($T_2 < T_1$). These differences in the relaxation times of different tissue types are responsible for the great the variety of possible image contrasts in MRI.

2.1.5.3. Spin Dephasing in Static Field Inhomogeneities

An additional signal loss of transverse magnetization is caused by spin dephasing in static field inhomogeneities which is characterized, together with the spin-spin interaction, by the time constant T_2^*. The loss of transverse magnetization is then described

by

$$M_T(t) = M_{T(t=0)} \cdot e^{-\frac{t}{T_2^*}}, \tag{2.25}$$

where T_2^* is given by

$$\frac{1}{T_2^*} = \frac{1}{T_2'} + \frac{1}{T_2}. \tag{2.26}$$

T_2' denotes the signal decay associated with static field inhomogeneities. This monoexponential signal decay is only valid for a Lorentzian distribution of resonance frequencies, which is, for instance, produced by randomly distributed magnetic dipoles, such as small ferromagnetic grains embedded in a medium with a different magnetic susceptibility (Brown, 1961). Other geometries such as vascular networks or single blood vessels lead to non-monoexponential signal decays and will be discussed later in this work (see Sec. 2.3.5.3 and Sec. 2.3.6).

2.1.6. Bloch Equations

Including the relaxation effects (Eq. 2.22, Eq. 2.24) in Eq. 2.18 yields a phenomenologically description of the time-dependent behavior of all magnetization, the so called Bloch equations:

$$\begin{aligned}
\frac{dM_x}{dt} &= \gamma\left(\vec{M} \times \vec{B}\right)_x - \frac{M_x}{T_2} \\
\frac{dM_y}{dt} &= \gamma\left(\vec{M} \times \vec{B}\right)_y - \frac{M_y}{T_2} \\
\frac{dM_z}{dt} &= \gamma\left(\vec{M} \times \vec{B}\right)_z - \frac{M_z - M_0}{T_1}.
\end{aligned} \tag{2.27}$$

The M_z magnetization in these equations is equivalent to the longitudinal magnetization ($M_z = M_L$), where the the transverse magnetization M_T is expressed by $M_x = \cos\gamma B_0 t \cdot M_T$ and $M_y = \sin\gamma B_0 t \cdot M_T$. It is obvious that the transverse magnetization can also be expressed in a complex manner:

$$M_T = M_x + iM_y = M_T \cdot e^{i\gamma B_0 \cdot t}. \tag{2.28}$$

Eqns. 2.27 can be written for M_L and M_T and by assuming a homogeneous main magnetic field after spin excitation ($\vec{B} = (0, 0, B_0)^T$) as follows

$$\frac{dM_T}{dt} = -i\gamma B_0 M_T - \frac{M_T}{T_2} \tag{2.29}$$

$$\frac{dM_L}{dt} = -\frac{(M_L - M_0)}{T_1}. \tag{2.30}$$

2.1.7. NMR-Signal Detection

The transverse magnetization in NMR experiments is detected by using coils. The precessing magnetization vector acts like a tiny generator and induces a voltage in the receiving coil. The induced voltage amplitude is typically in the range of μV and proportional to the detected magnitude of the transverse magnetization. Longitudinal magnetization will induce no signal, which allows to write the signal as a solution of Eq. 2.29:

$$S(\vec{r},t) \propto M_T(\vec{r},t=0) \cdot e^{-i\gamma B_0 t} \cdot e^{-\frac{t}{T_2}}. \tag{2.31}$$

The magnitude of the magnetization and therefore of the received signal depends on the spin density which can further fluctuate spatially. Thus, the signal is a function of the position vector $\vec{r}$. However, in MRI the signal is received from the whole measuring volume not from single points which makes an integration over the volume necessary:

$$S(t) = S_0 \cdot \int_V M_T(\vec{r},t=0)\mathrm{d}\vec{r} \cdot e^{-i\gamma B_0 t} \cdot e^{-\frac{t}{T_2}}, \tag{2.32}$$

where S_0 denotes the proportional factor between the magnetization and the signal.

2.2. Magnetic Resonance Imaging

To obtain NMR-images it is necessary to know the localization of the NMR-signal in the measured volume. The beginning of MRI was set by Mansfield and Grannell (1973) and Lauterbur (1973), who used linear field gradients to obtain spatially different resonance frequencies. Lauterbur's method, which he called *Zeugmatography*, produced the first MR-images in a feasible measurement time. Lauterbur and Mansfield received the Nobel Prize in Medicine 2003. Today, a plethora of different imaging methods exists. In the following section the most common techniques of spatial signal encoding and imaging methods are outlined. For further reading the books of Callaghan (1995), Haacke et al. (1999), Vlaardingerbroek and den Boer (2003) and Bernstein et al. (2004) are suggested.

2.2.1. Slice Selection

In MRI the received signal originates from all spins excited in the imaging object. Therefore, if the object is larger than the imaging volume, only the spins within the imaging volume will be excited. This is achieved by simultaneously applying a linear field gradient, e.g., in z-direction[2] (G_z) and a radio frequency (RF) pulse with a certain

[2]The z-direction is chosen for convenience, actual the slice can be selected in any direction.

bandwidth (Garroway et al., 1974) (Fig. 2.8, B). Due to the slice selection gradient, the resonance frequency of the protons differs along the z-axis with

$$\omega(z) = \gamma B(z) = \gamma(B_0 + zG_z) = \omega_0 + \gamma G_z z. \tag{2.33}$$

Thus, the slice thickness $\Delta z = |z_1 - z_2|$ can be defined as

$$\Delta z = \frac{|\omega(z_1) - \omega(z_2)|}{\gamma G_z} = \frac{\Delta\omega_{RF}}{\gamma G_z}. \tag{2.34}$$

To obtain a slice profile with square edges, the bandwidth $\Delta\omega_{RF}$ of the RF-pulse has to match the corresponding resonance frequencies correctly. For small flip angles the slice profile in the frequency domain corresponds to the Fourier Transform (FT) of the RF-pulse envelope. A sinc-shaped envelope will result in frequency bandwidth with a square profile and therefore in a square slice profile (Fig. 2.8, **A**).

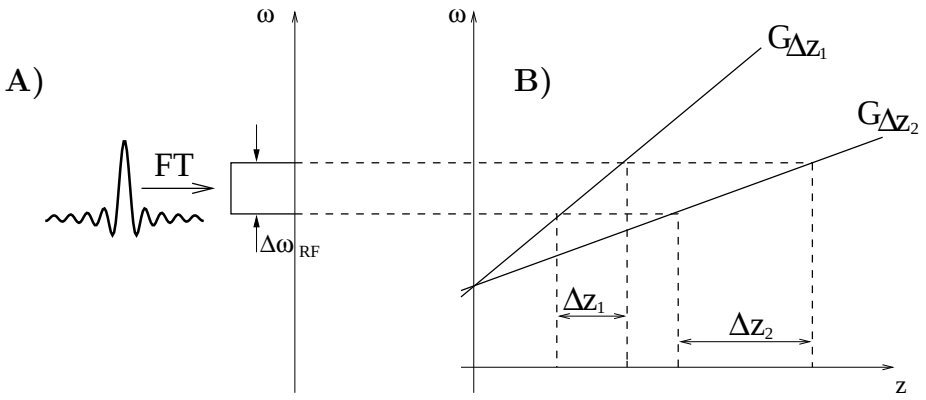

Figure 2.8: *A sinc-shaped RF-pulse envelope results in a square frequency bandwidth $\Delta\omega_{RF}$* **(A)**. **B:** *Different slice selection gradient strengths ($G_{\Delta Z1} > G_{\Delta Z2}$) lead to different slice thicknesses ($\Delta z_1 < \Delta z_2$) (Adapted from Liang and Lauterbur (2000)).*

2.2.2. Frequency Encoding

After exciting the spins within the slice the received signal has to be spatially encoded in the two remaining directions in space. In one direction, e.g., the x-direction[3], the signal is encoded during signal readout by applying a constant linear field gradient, like it was first proposed by Mansfield and Grannell (1973) and Lauterbur (1973). The precession frequency of the excited spins depends now on the location along the x-direction (Fig. 2.9):

$$\omega(x) = \omega_0 + \gamma G_x x. \tag{2.35}$$

[3]Since the slice selection gradient was denoted G_z the frequency and phase encoding gradients are denoted G_x and G_y, respectively.

The received encoded signal $S(t_x)$ during the readout time t_x contains different frequencies, which allow the positioning of the signal origin along the x-axis (lower part of Fig. 2.9). The received signal is expressed as

$$S(t_x) = S(t) \int_x e^{-i\gamma G_x x t_x} \mathrm{d}x, \tag{2.36}$$

where $S(t)$ is given by Eq. 2.32. Assuming $T_2 >> t_x$ the transverse relaxation can be neglected during signal encoding and readout. Furthermore, the time line of t and t_x coincide, but for better understanding of the later presented concept of the k-space the additional time variable t_x is introduced.

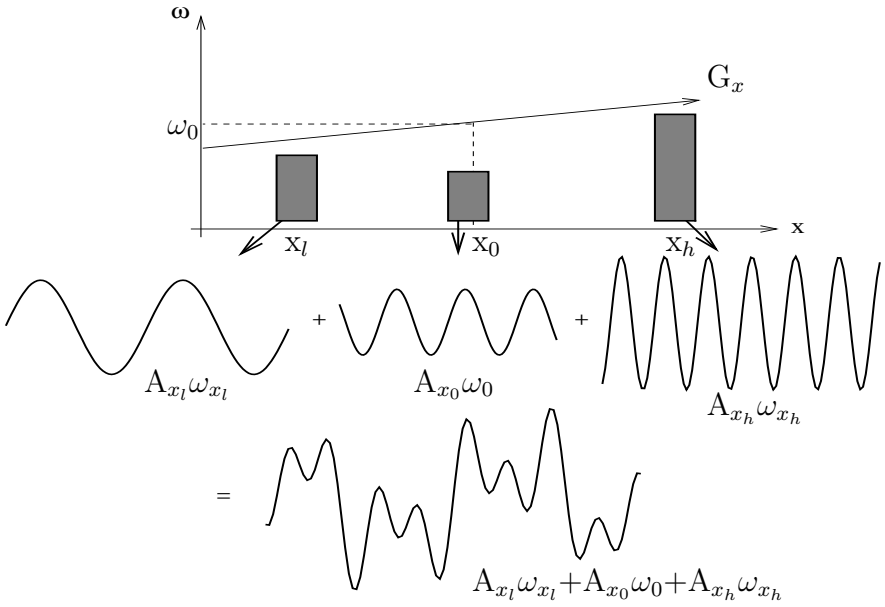

Figure 2.9: *Effect of a frequency encoding gradient G_x. The rectangles represent homogeneous samples at three different locations along the x-axis (x_l-lowest , x_0-center and x_h-highest position). The amplitude (A) of the signal is proportional to the amount of protons in the samples (indicated by the area of the rectangles), its frequency depends on the location along the x-direction (Adapted from Lurie et al. (2001)).*

Bandwidth (BW) The bandwidth of the received signal depends on the strength of the applied readout gradient. The difference between the lowest and highest frequency is defined as:

$$\Delta\omega = \omega(x_h) - \omega(x_l) = \gamma G_x \cdot (x_h - x_l). \tag{2.37}$$

2.2.3. Phase Encoding

To achieve a signal encoding in the remaining y-direction a second gradient, the phase encoding gradient (G_y), has to be switched on for a certain period of time (t_y). Such a

method of the 2D Fourier NMR imaging was first introduced by Kumar et al. (1975). During the time t_y, where G_y is switched on, the magnetization along the y-axis is precessing with different frequencies and accumulates a phase difference, which corresponds to their location in y-direction. After t_y, the phase encoding gradient is turned off and the precession frequency is the same as before, but the phase difference $\phi(y)$ remains and is given by

$$\phi(y) = \phi_0 + \gamma G_y y t_y. \tag{2.38}$$

The signal can not be spatially resolved by simply one phase encoding step, because the superimposed signal will contain no different frequencies in y-direction. To overcome this, the phase encoding has to be repeated many times by changing G_y in small steps, which also changes the phase and amplitude of the superimposed signal.

The signal, encoded in both directions ($S(t_x, G_y)$), can then be written as

$$S(t_x, G_y) = S(t) \int_x \int_y e^{-i\gamma(G_x x t_x + G_y y t_y)} \mathrm{d}x\mathrm{d}y. \tag{2.39}$$

It is also possible to apply an additional phase encoding in the z-direction as it is done with 3D-imaging (Johnson et al., 1983). There, a thick slice of the object is excited, which can further be subdivided in very thin partitions by phase encoding. This allows a much higher spatial resolution in the z-direction compared to 2D-imaging, where no sufficient signal can be received due to the low amount of excited spins of thin slices.

2.2.4. k -Space

The terms $\gamma G_x t_x$ and $\gamma G_y t_y$ (Eq. 2.39), which denote the signal encoding in the different directions, can be understood as wave numbers of a Fourier transform with

$$\begin{aligned} k_x &= \frac{\gamma}{2\pi} G_x t_x \\ k_y &= \frac{\gamma}{2\pi} G_y t_y. \end{aligned} \tag{2.40}$$

The sampled signal in Eq. 2.39 can now be written as

$$S(k_x, k_y) = S(t) \int_x \int_y e^{-i2\pi(x k_x + y k_y)} \mathrm{d}x\mathrm{d}y. \tag{2.41}$$

This allows the description of the spatial signal encoding as a sampling of k_x and k_y in the Fourier space, for which the term k-space has been established in MRI. To obtain the desired image, the k-space has to be Fourier transformed. The notation of the k-space gives a powerful description of signal encoding and image generation even for imaging sequences with complex signal encoding schemes (Ljunggren, 1983; Twieg, 1983). The switching of gradients and RF-pulses of MRI-sequences is described using

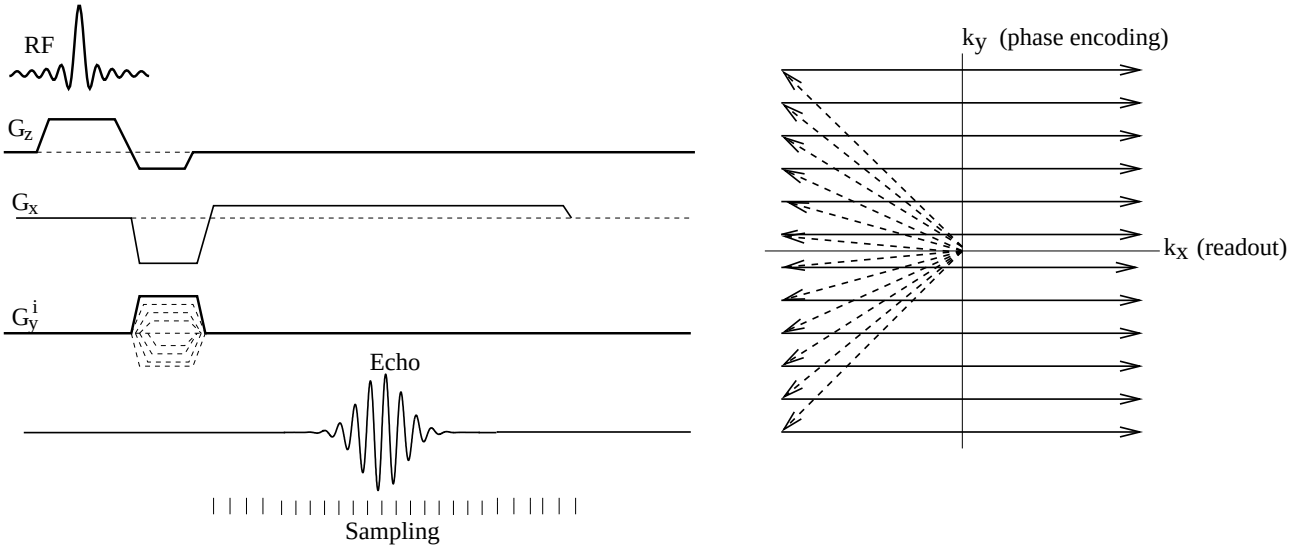

Figure 2.10: *Pulse diagram of a "spin warp" sequence (Edelstein et al., 1980) (left) and its corresponding trajectory in k-space (right). The displayed sequence scheme has to be repeated for each phase encoding step G_y^i, which shifts the k_x lines (solid arrows) along k_y (dashed arrows). Figure adapted from Rauscher (2005).*

so-called pulse diagrams (Fig. 2.10, left), which allows a direct derivation of the k-space trajectory (Fig. 2.10, right).

In practice it is not possible to cover the whole k-space continuously and infinitely, but only a subset of discrete points. This has several implications for the imaging process which are discussed in the following sections. For a deeper understanding of Fourier transforms and convolutions, the standard books of Jennison (1961), Brigham (1974) and Bracewell (1986) provide help.

2.2.4.1. Discrete Sampling of k-Space

In Cartesian k-space sampling, the signal is digitized while a constant frequency encoding gradient is switched on. Here the sampling time (Δt_x) denotes the distance between two k_x points, Δk_x. The discrete sampling in phase encoding direction is effected, as mentioned above, by changing the phase encoding gradient in small steps (ΔG_y) which defines the distance between two k_y points, Δk_y.

$$\begin{aligned} \Delta k_x &= \frac{\gamma}{2\pi} G_x \Delta t_x \\ \Delta k_y &= \frac{\gamma}{2\pi} \Delta G_y t_y. \end{aligned} \tag{2.42}$$

The digitized signal (S') can be written mathematically as a multiplication of the continuous signal with a train of equally spaced delta (δ) functions (i.e., a Dirac comb

function):

$$S'(k_x, k_y) = S(k_x, k_y) \cdot \Delta k_x \sum_{n=-\infty}^{\infty} \delta(k_x - n\Delta k_x) \cdot \Delta k_y \sum_{m=-\infty}^{\infty} \delta(k_y - m\Delta k_y), \qquad (2.43)$$

where $S(k_x, k_y)$ follows according to Eq. 2.41.

The Fourier transform of a comb function with period Δk results again in a comb function, with period $\frac{1}{\Delta k}$:

$$\Delta k \sum_{p=-\infty}^{\infty} \delta(k - p\Delta k) \overset{FT}{\longleftrightarrow} \sum_{q=-\infty}^{\infty} \delta\left(r - \frac{q}{\Delta k}\right). \qquad (2.44)$$

Fourier transforming the sampled k-space leads to a convolution of the continuous image space $\rho(x, y)$ with the Fourier transform of the comb function:

$$\rho'(x, y) = \rho(x, y) \otimes \sum_{v=-\infty}^{\infty} \delta\left(x - \frac{v}{\Delta k_x}\right) \otimes \sum_{w=-\infty}^{\infty} \delta\left(y - \frac{w}{\Delta k_y}\right). \qquad (2.45)$$

This convolution ($\otimes$) can be understood as a reoccurring image space at each position ($\frac{1}{\Delta k}$) of a δ-function. To avoid an image overlapping, $\frac{1}{\Delta k}$ has to be chosen larger than the field of view (FOV), where the sampling criterion is given by

$$\Delta k \leq \frac{1}{\mathrm{FOV}}. \qquad (2.46)$$

Inserting Eq. 2.42 in Eq. 2.46 and using $\mathrm{FOV}_x = N_x \Delta x$ and $\mathrm{FOV}_y = N_y \Delta y$, for the size of the measuring volume, yields the sampling criteria

$$\begin{aligned} \Delta t_x &\leq \frac{2\pi}{\gamma G_x N_x \Delta x} \\ \Delta G_y &\leq \frac{2\pi}{\gamma t_y N_y \Delta y}. \end{aligned} \qquad (2.47)$$

These are requirements for the imaging sequence to avoid image overlapping and they are equivalent to the Nyquist sampling theorem, which claims that the sampling rate of a digitized signal has to be more than twice the maximal signal frequency (Roberts, 1965).

The image pixel size (Δx, Δy), i.e. the resolution, is determined by the maximum magnitude of the k-space vector, where Δx and Δy can be calculated accordingly:

$$\begin{aligned} \Delta x &= \frac{2\pi}{\gamma G_x \Delta t_x N_x} \\ \Delta y &= \frac{2\pi}{\gamma \Delta G_y t_y N_y}. \end{aligned} \qquad (2.48)$$

The image resolution can simply be increased by enlarging the readout gradient G_x or the sampling time Δt_x. If the number of samples N_x is kept constant, this will reduce the FOV_x. The same happens for the y-direction (FOV_y) if the duration t_y or the step width ΔG_y of the dephasing gradient are increased, while the number of samples N_y is kept constant. To avoid an image overlapping here, the numbers of samples ($N_{x,y}$) have to be increased accordingly with image resolution.

2.2.4.2. Sampling Point Spread Function

In consequence of the finite sampling window of the k-space the equally spaced δ-functions are not progressing from $-\infty$ to ∞. Therefore, the previously assumed periodic comb function and its Fourier transform (Eq. 2.44) do not correctly describe the image sampling. Rather, the comb function in the k-space has to be multiplied by a unit step function $U(k, k_{min}, k_{max})$, given by

$$U(k, k_{min}, k_{max}) = \begin{cases} 1 & \forall \quad k_{min} < k < k_{max} \\ 0 & \forall \quad \text{else} \end{cases} . \tag{2.49}$$

For a symmetrically sampled k-space the modulus of the minimum and maximum k-space vector are equal and k_{min} can be written as $k_{min} = -k_{max}$. The Fourier transform of $U(k, k_{max})$ results then in a sinc-function:

$$U(k, k_{max}) \overset{FT}{\longleftrightarrow} \frac{\sin(\pi k_{max} r)}{\pi r} = \frac{\sin(\pi \frac{r}{\Delta r})}{\pi r}. \tag{2.50}$$

After the Fourier transform of the k-space the comb function is convolved with the sinc function resulting in equally spaced sincs, which are again convolved with the continuous image space:

$$\rho'(x,y) = \rho(x,y) \otimes \sum_{v=-\infty}^{\infty} \delta\left(x - \frac{n}{\Delta k_x}\right) \otimes \sum_{w=-\infty}^{\infty} \delta\left(y - \frac{m}{\Delta k_y}\right) \otimes \frac{\sin(\pi k_{x,max} x)}{\pi x} \otimes \frac{\sin(\pi k_{y,max} y)}{\pi y}. \tag{2.51}$$

This means that each point of the measuring volume is imaged as its convolution with the sinc function. The "sampling point spread function" (sPSF) can now be achieved by substituting $\rho(x, y)$ in Eq. 2.51 with a δ-function (Johnson and Hutchison, 1985):

$$P(x,y) = \frac{\sin(\pi \frac{x}{\Delta x})}{\pi x} \cdot \frac{\sin(\pi \frac{y}{\Delta y})}{\pi y}. \tag{2.52}$$

This ideal sPSF for Cartesian k-space sampling is only valid for $T_2 \to \infty$ where the transverse relaxation during k-space sampling can be neglected and the sPSF can be written as a two dimensional sinc function (Haacke, 1987). This consideration can be applied vice versa for a single point in the image whose signal is originated by a sinc shaped signal distribution in the measuring volume.

2.2.5. Imaging Methods

In heterogeneous biological tissue not only the spin density (Tab. 2.3) but also the relaxation behavior differ spatially (Tab. 2.2). MRI offers a large variety of image contrasts due to different methods of k-space sampling and sequence timings of gradients and RF-pulses.

Table 2.3: *Water content of various human tissues. Table adapted from Mansfield (1988)*

Tissue	Water (%)	Tissue	Water (%)
Liver	71.1	Skeletal muscle	79.2
Kidney	81.0	Bone	12.2
Brain, white matter	84.3	Heart	80.0
Brain, grey matter	70.6	Blood	93.0
Cerebrospinal fluid	97.5		

2.2.5.1. Spin Echo Sequence

In the beginning of MRI and MRS (Magnetic Resonance Spectroscopy), the applied main magnetic field was limited in its spatial homogeneity, and the transverse magnetization of the imaged volume dephased quickly. Additional field inhomogeneities induced by heterogeneous probes, such as biological tissues, contribute also to this dephasing and cause a quick loss of the measurable signal. Hahn (1950) proposed the spin echo technique to overcome this problem. After the magnetization is flipped in the xy-plane (90°-pulse), it dephases quickly and the detectable signal drops with the T_2^* decay time. Then, after a certain time ($T_E/2$), a refocusing pulse with α=180° flips the transverse magnetization within the xy-plane which causes a rephasing of the magnetization. After the same time which elapsed between the excitation and the refocusing pulse, the magnetization is recovered and the spin echo occurs at T_E. The signal measured at T_E is still limited by the spin-spin relaxation but the effects of static field inhomogeneities (resulting in T_2') are compensated (Fig. 2.11).

For spin echo imaging, spatial encoding field gradients have to be switched before the spin echo occurs (Fig. 2.12). A disadvantage of the spin echo method remains. The repetition time for the next phase encoding step has to be in the order of hundreds of milliseconds to allow sufficient time for longitudinal magnetization recovery. Otherwise, the signal rapidly decreases after few excitations, because not enough magnetization is relaxed which can be excited the next time. The need of long T_R times causes long imaging times and makes 3D measurements not feasible due to the additional phase encoding direction, especially in living subjects.

2.2.5.2. Gradient Echo Sequence

With ongoing development of MRI hardware, in particular with a homogeneous main magnetic field over a large FOV, it was possible to abdicate the refocusing pulse of the spin echo method. The signal echo is then recalled only by the imaging gradients (Fig. 2.13). Due to the missing 180°-pulse the echo time T_E can be much smaller.

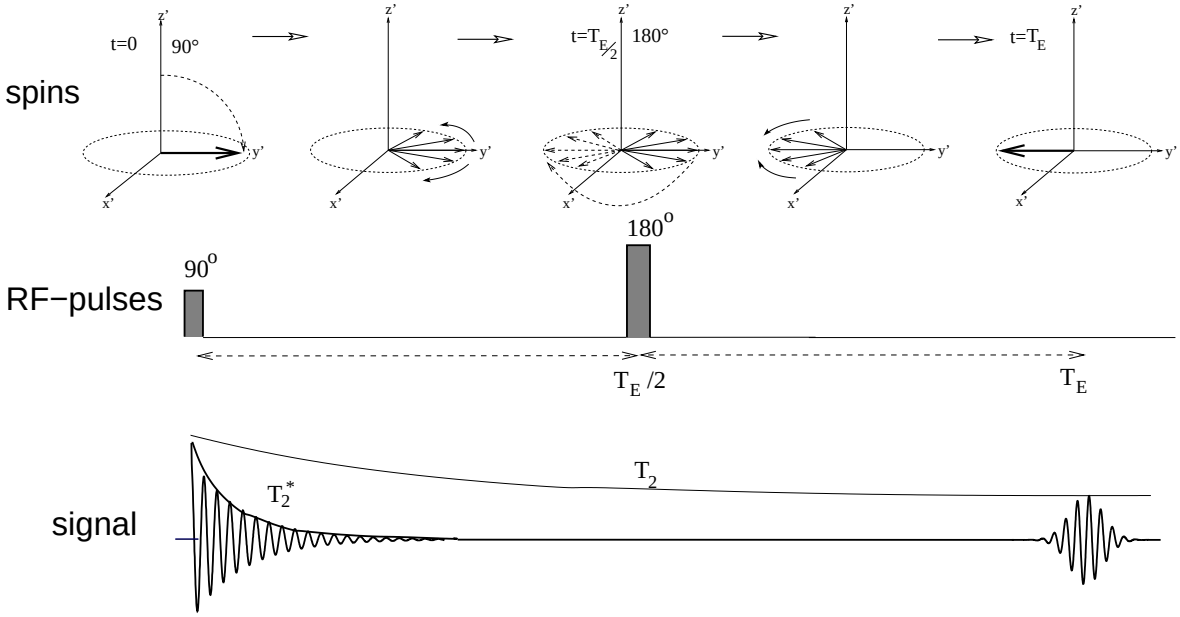

Figure 2.11: *Scheme of the spin echo method. Due to the refocusing pulse (180°) at $T_E/2$ the dephased magnetization M_T is rephasing at T_E. The envelope of the T_2^* decay denotes the signal loss due to spin dephasing in static field inhomogeneities. The envelope of the T_2 decay denotes the signal loss due to spin-spin relaxation. Figure adapted from Rauscher (2005).*

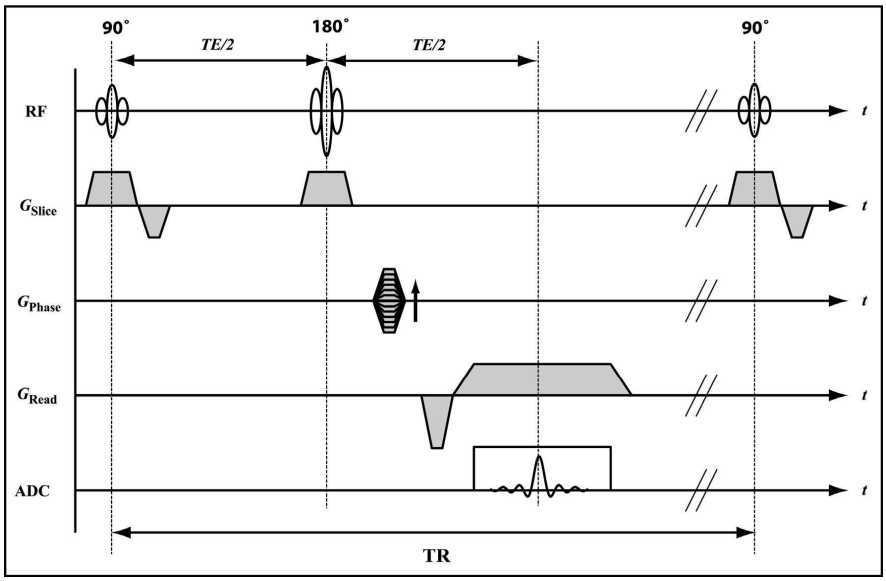

Figure 2.12: *Spin Echo sequence scheme. After excitation (90°-pulse) a refocusing pulse (180°) appears at half echo time ($T_E/2$). Both are switched slice selectively (G_{slice}). The signal echo occurs at $T_E/2$ after the 180°-pulse and is spatially encoded in phase (G_{phase}) and frequency direction (G_{read}). The signal is sampled during the analog digital converter (ADC) is switched on. The repetition time (T_R) denotes the time between two excitations of the slice, for which the next phase encoding step is carried out. Figure adopted from Schröder (2005).*

Furthermore, it is possible to flip the longitudinal magnetization a few degrees (for example 15°) in the xy-plane. As an advantage the repetition time and therefore the imaging time can be shortened dramatically, which makes also 3D imaging practically feasible. This method was proposed by Haase et al. (1985) and is known as Fast Low Angle Shot (FLASH).

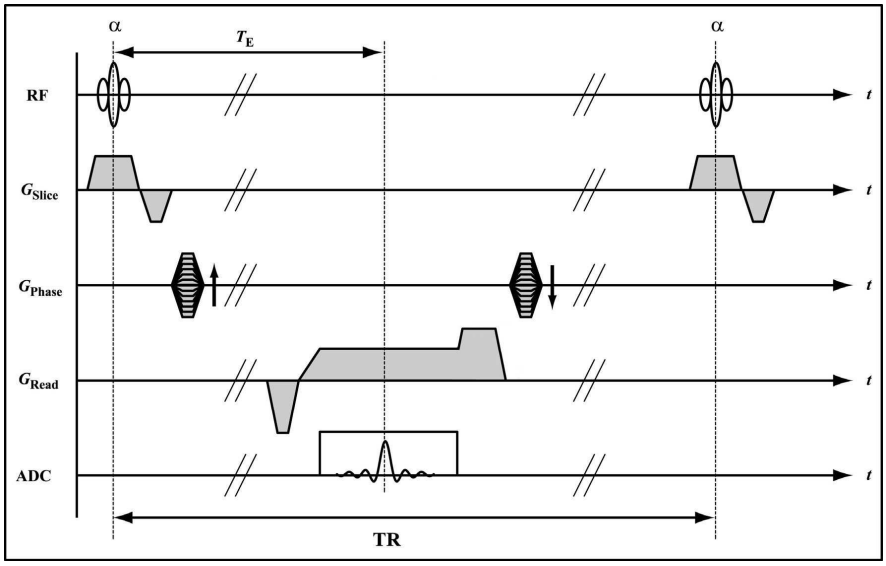

Figure 2.13: *Gradient echo sequence scheme. The slice selective (G_{slice}) excitation is carried out with a flip angle α. The signal is then phase encoded (G_{phase}) and generated after short dephasing (negative G_{read}) only by the read out gradient (G_{read}) and occurs at T_E. Figure adapted from Schröder (2005).*

To avoid the detection of previously excited spins in the following echoes, the residual transverse magnetization can be destroyed by an additional spoiling gradient. To avoid an uncontrolled signal dephasing, the phase encoding direction is reversed and the spoiling is applied in just one direction, usually in readout direction, after the echo readout is finished (Epstein et al., 1996).

The excited signal magnitude of a spoiled gradient echo sequence in the steady state depends on the flip angle, the repetition time and the spin-lattice relaxation time

$$S_0 = \frac{1 - e^{-T_R/T_1}}{1 - \cos\alpha \cdot e^{-T_R/T_1}} \cdot \sin\alpha. \tag{2.53}$$

The value of the flip angle, which maximizes Eq. 2.53, depends on the given repetition T_R and T_1-relaxation time of the investigated probe. It can be calculated as follows

$$\cos\alpha_{ernst} = e^{-\frac{T_R}{T_1}} \tag{2.54}$$

and is known as “Ernst angle” (Ernst and Anderson, 1966).

2.2.5.3. Echo Planar Imaging

Spin echo and gradient echo sequences acquire with each spin excitation just one phase encoding step and the k-space is scanned line by line. In contrast, Mansfield (1977); Mansfield and Pykett (1978) proposed an imaging technique which allows the sampling of the whole k-space with only one excitation pulse (Fig. 2.14). However, the requirements on the gradient system are extremely high, so that this imaging technique was first feasible in the last decade of the 20^{th} century. Data acquisition of one slice is finished after 50 to 100 ms which is of the same order as T_2^*. In fact, T_2^* is constraining the trajectory in k-space as it limits the number of samples which can be acquired during this period of time. Therefore, image resolution is relatively low and the voxel size is even today typically $3 \times 3 \times 3\,\mathrm{mm}^3$. Echo planar imaging is also very sensitive to static field inhomogeneities which leads to strong signal loss, geometric image distortion and ghosting. In contrast to these disadvantages it is possible to detect signal changes induced by changes of the oxygenation state of the venous blood during neuronal activation. Together with its ability to acquire the same slice after each T_R it enables the mapping of active areas in the brain (Kwong et al., 1992).

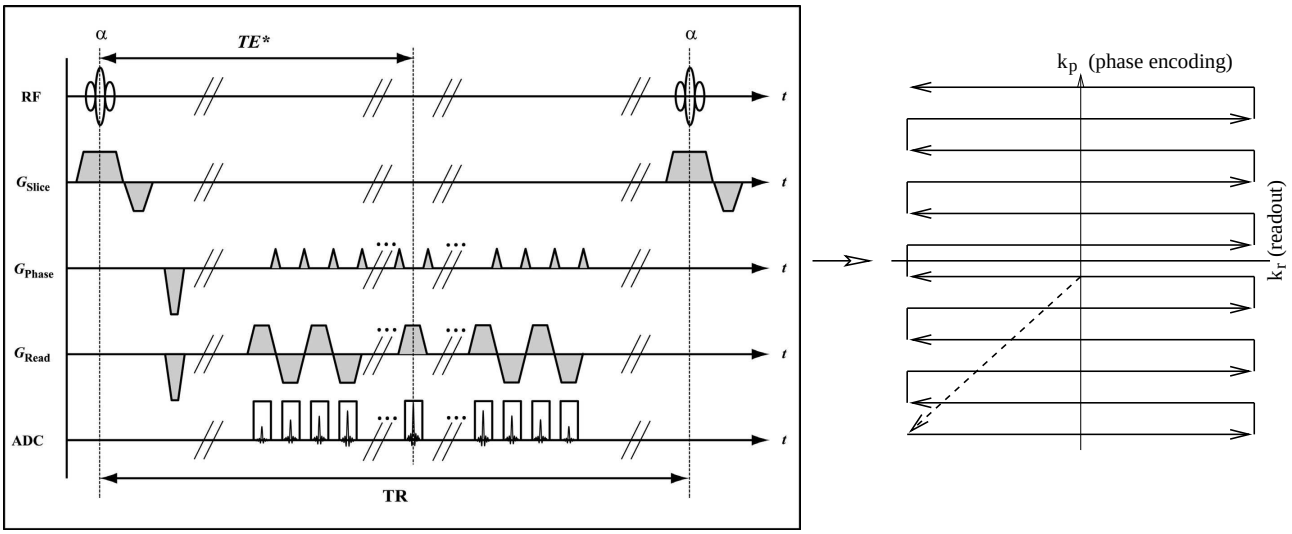

Figure 2.14: *Echo planar imaging (EPI) sequence scheme (left) and its k-space trajectory (right). After the imaging slice is excited (α-pulse) the negative lobes of G_{read} and G_{phase} move the k-space vector to its starting position in the lower left corner of k-space (dashed arrow). The short G_{phase}-blips cause the k-space vector to step from line to line and during the alternating G_{read} each line of the k-space is read out with alternating direction (solid arrows). The effective echo time (T_E^*) is defined when the k-space center line is sampled. After the repetition time (T_R) the slice will be again completely sampled which allows MR-imaging with high temporal resolution. Figure adapted from Schröder (2005) and Rauscher (2005).*

2.3. Magnetic Heterogeneous Tissues

The two relevant kinds of magnetism for organic matter and biological tissues are diamagnetism and paramagnetism. Materials which show an attenuation of an external magnetic field are called diamagnetic. In biological tissues diamagnetic materials such as water and fat are predominant.

Materials which show an amplification of an external magnetic field, but no intrinsic field are called paramagnetic. Iron with its two different oxidation states Fe^{2+} and Fe^{3+} is a very important paramagnetic element in biological tissue, especially in blood. It changes its electron configuration, and thus magnetic property, depending on its state. Unpaired electrons in the outer orbitals of the iron ions align to the external magnetic field and amplify it within the sample. Due to the weak interaction between the iron ions no intrinsic magnetic field is formed. An important role in MRI diagnosis play also paramagnetic contrast agents, e.g. Gd-DTPA (gadolinium diethylenetriamine pentaacetic acid), where the molecular contrast agent induces proton relaxation changes in its surroundings due to its large magnetic moment (Reichenbach et al., 1997c; Weinmann et al., 1984). Some biological substances such as ferritin and hemosiderin also include Fe^{3+} ions. They serve as iron storage or hemoglobin degradation product and show an iron content of about 20 to 40%. Due to the dense packing of iron ions ferritin and hemosiderin show superparamagnetic properties (Schenck, 1996). Superparamagnetic particles are characterized by a much higher amplification of an external magnetic field as compared to paramagnetism. However, no intrinsic field is exhibited by superparamagnetic particles.

2.3.1. Magnetic Susceptibility

Material brought into a magnetic field responds with a magnetic polarization which is either caused by magnetic moments produced by the external field or moments already existing and aligning by the external field. On a macroscopic level this is described by the magnetization $\vec{M}$. The magnetic flux density[4] in matter becomes

$$\vec{B} = \vec{B}_0 + \mu_0 \vec{M} = (1 + \chi) \cdot \vec{B}_0, \tag{2.55}$$

with $\mu_0 = 4\pi \cdot 10^{-7} \frac{\mathrm{Vs}}{\mathrm{Am}}$ the magnetic permeability of vacuum. The dimensionless constant χ is called magnetic susceptibility. Substances with $\chi < 0$ are diamagnetic, substances with $\chi > 0$ are paramagnetic (Fig. 2.15). The lowest value of $\chi = -1$ denotes the magnetic property of superconductors, where the magnetic field lines are completely displaced to the outside of the superconductor.

[4] In this section we use the correct notation of flux density for B.

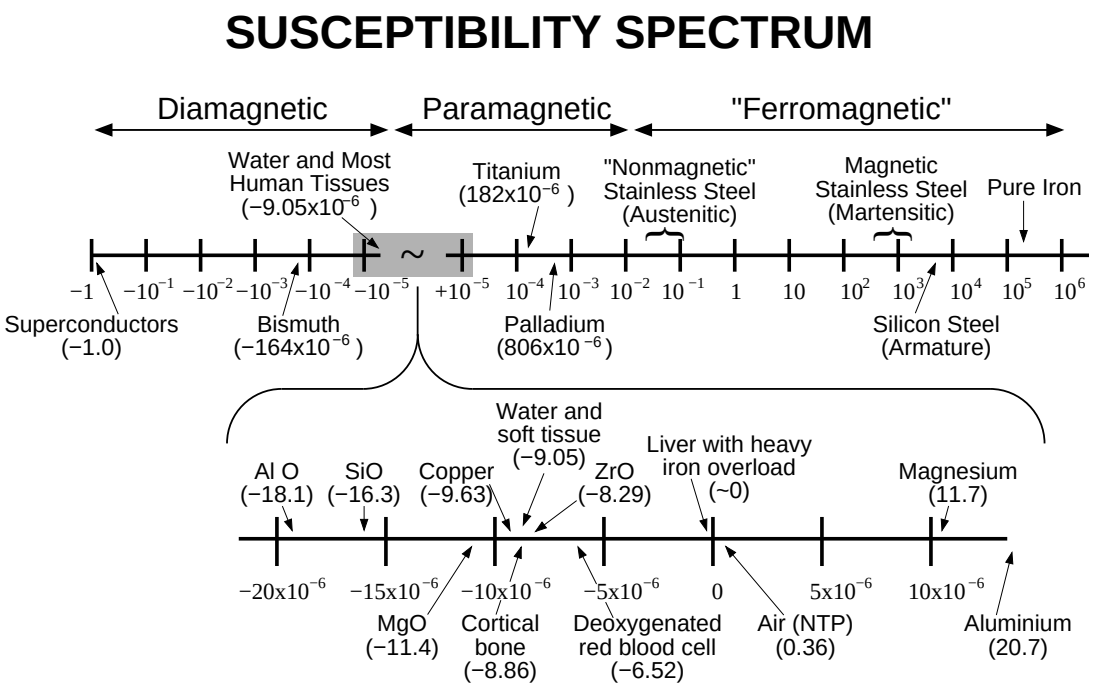

Figure 2.15: *Susceptibility spectrum. The upper diagram uses a logarithmic scale to indicate the full range of observed magnetic susceptibility values: it extends from χ = -1.0 for superconductors to $\chi = 10^6$ for soft ferromagnetic materials. The bottom diagram uses a linear scale (in ppm) to indicate the properties of some materials with $|\chi| < 20$ ppm. The susceptibility of most human tissues is in the range of -7.0 to -11.0 ppm. (Figure adapted from Schenck (1996))*

2.3.1.1. Macroscopic Magnetic Field

The magnetic flux given in Eq. 2.55 is only valid for spatially infinite samples. For finite samples the demagnetization field $\vec{B}_{dm}$ has to be considered which is caused by magnetization currents along the surface of the object. $\vec{B}_{dm}$ is given as

$$\vec{B}_{dm} = -\mu_0 \cdot N \cdot \vec{M}, \tag{2.56}$$

where the demagnetization factor N is a shape dependent number between zero and one. For generalized ellipsoids of revolution the factor N was calculated analytically (Osborn, 1945). Values of N and the resulting macroscopic magnetic flux density $\vec{B}_m$ are given in Tab. 2.4 for special cases of the ellipsoid.

2.3.1.2. Local Magnetic Field

For continuous matter the macroscopic magnetic flux density $\vec{B}_m$ can be well determined inside and outside of a macroscopic uniform object following Eq 2.55 and Eq 2.56. However, in NMR experiments, microscopic nuclear magnetic dipoles are measured. On a microscopic scale the medium can not assumed to be continuous. In fact, the local

Table 2.4: *Demagnetization factors and macroscopic magnetic flux for special ellipsoids.*

	sphere	long cylinder		thin disk	
		$\parallel$ to $\vec{B}_0$	$\perp$ to $\vec{B}_0$	$\parallel$ to $\vec{B}_0$	$\perp$ to $\vec{B}_0$
N	1/3	0	1/2	1	0
$\vec{B}_m$	$\vec{B}_0 + \frac{2}{3}\mu_0\vec{M}$	$\vec{B}_0 + \mu_0\vec{M}$	$\vec{B}_0 + \frac{1}{2}\mu_0\vec{M}$	$\vec{B}_0$	$\vec{B}_0 + \mu_0\vec{M}$

magnetic field is modified due to the fields produced by all the discrete microscopic dipoles in the surroundings of the nucleus. The construct of a hypothetical sphere surrounding each spin, the so-called "Sphere of Lorentz", helps to obtain the local magnetic flux $\vec{B}_{loc}$ (Springer, 1994; Levitt, 1996).

The Sphere of Lorentz was first applied in NMR by Dickinson (1951). It is an imaginary sphere drawn around a spin large enough for all external microscopic dipoles to be assumed as a continuum. Within the sphere, the investigated spin is imagined to sit in a vacuum surrounded by individual dipoles whose net electromagnetic effect vanishes for an isotropic spin distribution. The effect of introducing a spherical cavity into a uniform continuous medium results, according to the macroscopic flux density of a spherical object without the external $\vec{B}_0$ and with negative polarity, in the following equation:

$$\vec{B}_L = -\frac{2}{3}\mu_0\vec{M}. \tag{2.57}$$

The local magnetic flux can then be calculated by

$$\vec{B}_{loc} = \vec{B}_m + \vec{B}_L \tag{2.58}$$

and results, e.g. for a spherical object, in $\vec{B}_{loc} = \vec{B}_0 + \frac{2}{3}\mu_0\vec{M} - \frac{2}{3}\mu_0\vec{M} = \vec{B}_0$. This means spins inside a magnetized spherical object will experience the same magnetic field as outside the object. The local magnetic fields of some special ellipsoids are given in Tab. 2.5 and the effect of the Lorentzian Sphere is graphically depicted in Fig. 2.16.

Table 2.5: *The resulting local magnetic flux of spins inside special ellipsoids.*

	sphere	long cylinder axis		thin disk axis	
		$\parallel$ to $\vec{B}_0$	$\perp$ to $\vec{B}_0$	$\parallel$ to $\vec{B}_0$	$\perp$ to $\vec{B}_0$
$\vec{B}_{loc}$	$\vec{B}_0$	$\vec{B}_0 + \frac{1}{3}\mu_0\vec{M}$	$\vec{B}_0 - \frac{1}{6}\mu_0\vec{M}$	$\vec{B}_0 - \frac{2}{3}\mu_0\vec{M}$	$\vec{B}_0 + \frac{1}{3}\mu_0\vec{M}$

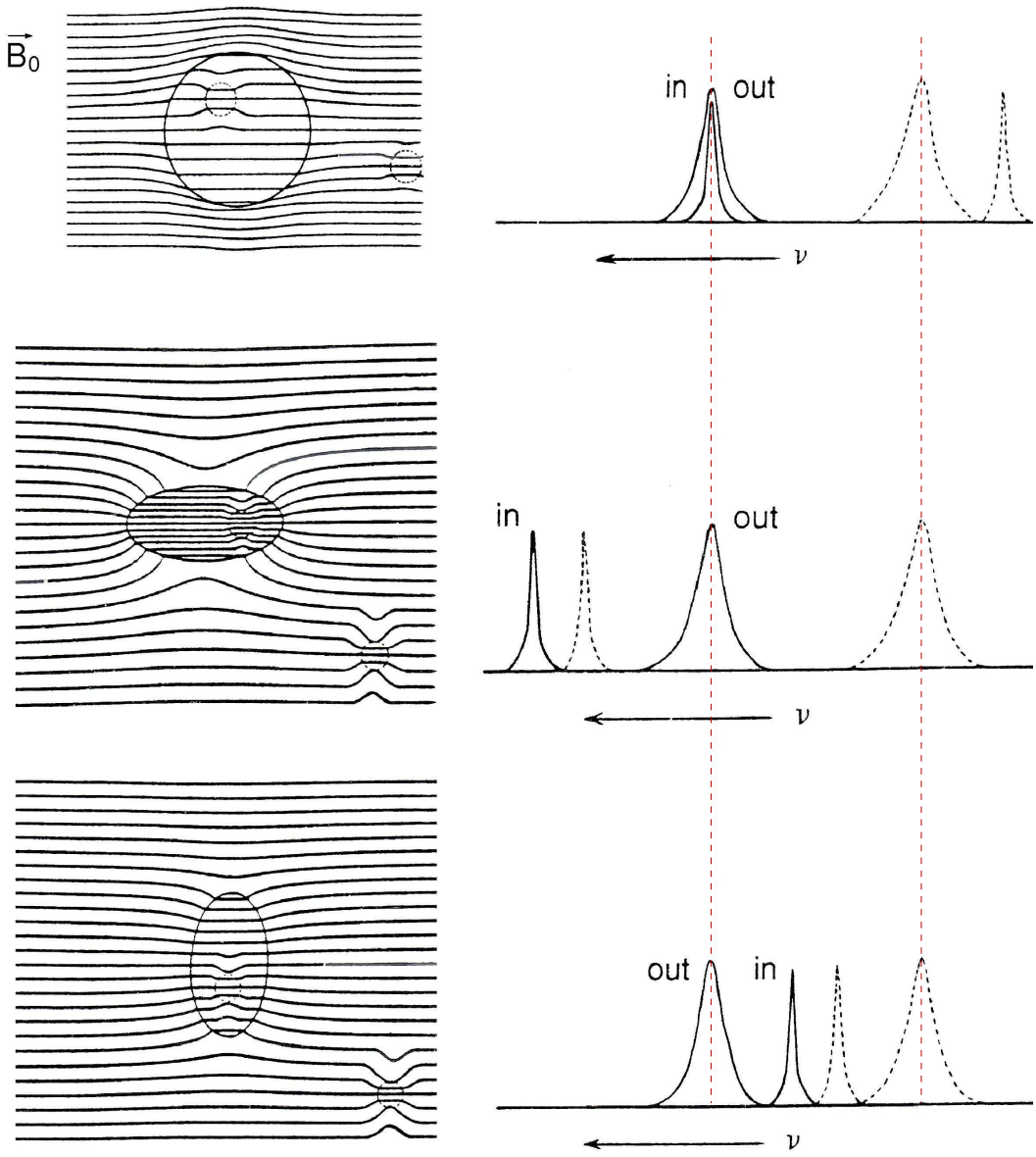

Figure 2.16: *Illustration of the effect of the Sphere of Lorentz. In the top left panel, a spherical compartment containing a diamagnetic medium is suspended in a less diamagnetic medium. In the bottom two panels on the left a prolate ellipsoidal compartment filled with a diamagnetic medium is suspended in a more diamagnetic medium, with the same magnetic susceptibility as that in the top panel. In the middle panel the ellipsoid is oriented parallel to the external magnetic field while in the bottom panel it is perpendicular to it. The imaginary Spheres of Lorentz are pictured as dashed circles. The right panels picture the resonance frequencies (ν) of spins inside and outside the compartments. The dashed peaks represent the situation if one neglects the effect modelled by the Sphere of Lorentz (Figure adapted from Springer (1994))*

2.3.2. Physiologic Properties of Blood

The circulation of blood is essential for humans. It connects all organs which extract necessary substances, such as oxygen, nutrients and hormonal messengers. Thus, blood serves as a transport and communication medium. It mainly consists of water where electrolytes, water soluble nutrients, vitamins and gases are in solution. Proteins circulate in the aqueous solution and are also in some extend attached to water insoluble substances and different cell populations. The main cell components are: Erythrocytes (red blood cells), Leukocytes (white blood cells) and Thrombocytes (blood platelets). The hematocrit (Hct) denotes the volume fraction of these cells of the total blood volume. 99% of the hematocrit are red blood cells. The normal range of the hematocrit for women is 0.37-0.47 and for men 0.40-0.54 (Klinke, 2005).

The red blood cells serve as oxygen (O_2) and carbon dioxide (CO_2) transporters. For the oxygen transport the O_2 molecule is reversibly bound to the Fe^{2+} ion in the hemoglobin. The Fe^{2+} ion is not changing its oxidation status during this process. Thus, the bounding process is called oxygenation, not oxidation. Hemoglobin consists of four polypeptid subunits, each hosting a heme molecule with a twofold oxidized iron ion in its center (Fig. 2.17).

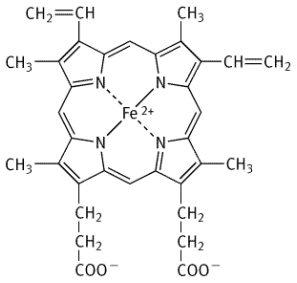

Figure 2.17: *Heme molecule with a twofold oxidized iron atom in its center which is necessary for the reversible oxygen adsorption. (Figure adapted from Elliott and Elliott (2005))*

The iron is localized inside a porphyrin molecule and forms a coordination compound, a so-called metal complex. Hemoglobin with bound O_2 is called oxyhemoglobin (HbO_2), hemoglobin without bound O_2 deoxyhemoglobin (Hb). The O_2 saturation of hemoglobin, also called blood oxygenation level (Y), is defined as the ratio between the HbO_2 and the total hemoglobin (HbO_2+Hb) concentration:

$$Y = \frac{\mathrm{HbO_2}}{\mathrm{Hb} + \mathrm{HbO_2}}. \tag{2.59}$$

The hemoglobin oxygen saturation is a function of the O_2 partial pressure (pO_2). It was found empirically by Rossi-Bernardi et al. (1975); Winslow et al. (1977) and can be calculated using the following equation by Stryer (1994)

$$Y = \frac{(\mathrm{pO_2})^{2.8}}{(\mathrm{pO_2})^{2.8} + (\mathrm{p_{0.5}})^{2.8}}. \tag{2.60}$$

$P_{0.5}$ is the partial pressure at half oxygen saturation and is equal to 3.6 kPa under normal physiological conditions. The S-shape of the oxygenation saturation curve can

be explained by the cooperative interaction between the subunits (Fig. 2.18). If the heme of one subunit bonds an O_2 molecule, the affinity of the residual subunits with deoxygenized heme will rise. Thus, the saturation of arterial blood is nearly 100% even at breathing normal air.

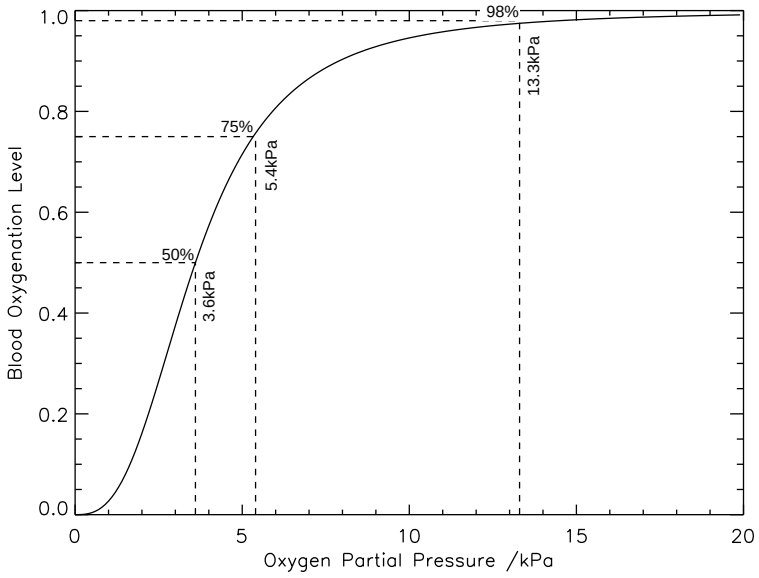

Figure 2.18: *Oxygenation saturation curve of hemoglobin. The curve is given for a healthy adult under normal condition: pH = 7.4, temperature = 37°C, carbon dioxide partial pressure = 5.3 kPa. The emphasized values represent normal values for arterial blood (Y = 0.98), global mixed venous blood (Y = 0.75) directly before entering the lung and the half oxygenation saturation value (Y = 0.50).*

2.3.3. Tissue Oxygen Consumption

The oxygen consumption can be quantified by the metabolic rate for oxygen (MRO_2) and is defined as the ratio between the absolute O_2 consumption in mole per time and the tissue mass in gram

$$\mathrm{MRO_2} = \frac{\mathrm{O_2\text{-consumption}}}{\text{tissue mass}} \qquad \left[\frac{mol/s}{g}\right]. \tag{2.61}$$

While the MRO_2 quantifies the absolute O_2 consumption, the so-called oxygen extraction fraction (OEF) denotes the ratio between the O_2 consumption by the tissue and the O_2 delivery by the arterial blood. It quantifies the oxygen utilization of the tisue and is defined as

$$\mathrm{OEF} = \frac{\mathrm{O_2\text{-consumption}}}{\mathrm{O_2\text{-delivery}}}. \tag{2.62}$$

Since oxygen exchange takes place in blood capillaries the OEF can be calculated directly by the difference of the oxyhemoglobin content of arterial and venous blood.

$$\mathrm{OEF} = \frac{\mathrm{HbO}_{2,\,arterial} - \mathrm{HbO}_{2,\,venous}}{\mathrm{HbO}_{2,\,arterial}} = 1 - \frac{\mathrm{HbO}_{2,\,venous}}{\mathrm{HbO}_{2,\,arterial}} = 1 - \frac{Y_{venous}}{Y_{arterial}}. \tag{2.63}$$

Due to the nearly 100% O_2 saturation in arterial blood the OEF can be approximated with

$$\mathrm{OEF} \approx 1 - Y_{venous}. \tag{2.64}$$

The oxygen extraction fraction varies over different organs and depends on the actual state of stress. In the myocardial and skeletal muscle the OEF is about 0.4 to 0.6 in the resting state and can rise to nearly 0.9 at extreme physical stress (Schmidt and Thews, 1987). Hagendorff et al. (1994) investigated the OEF in normal rat brain by invasive measurements using oxygen microelectrodes. They found OEF values of about 0.4 ± 0.07.

The oxygen extraction fraction (OEF) and consumption (MRO_2) are correlated by the absolute oxygen delivery, which can be calculated from the blood flow (BF) and the oxyhemoglobin concentration of the arterial blood

$$\mathrm{MRO}_2 = \mathrm{OEF} \cdot \mathrm{BF} \cdot \mathrm{HbO}_{2,\,arterial}. \tag{2.65}$$

During physical strain the absolute O_2 consumption can then be increased by raising the oxygen extraction fraction, tissue perfusion or both. For example, the oxygen demand of the myocardium can rise up to 4 time the resting state value which is mainly compensated by a 4-fold increase of blood perfusion (Schmidt and Thews, 1987).

2.3.4. Oxygenation Dependent Magnetic Property of Blood

Pauling and Coryell (1936) investigated the magnetic properties for oxyyhemoglobin (HbO_2) and deoxyhemoglobin (Hb) and reported the absence of unpaired electrons for HbO_2. The magnetic susceptibility of deoxyhemoglobin itself was found to correspond to an effective magnetic moment of 5.46 Bohr magnetons ($\mu_b = \frac{e}{2m_e}\hbar = 9,274 \cdot 10^{-24}\,\mathrm{Am}^2$) per heme calculated for independent hemes.

Iron with a twofold oxidation status (Fe^{2+}) has six electrons in the 3d orbitals which are filled up with two paired electrons and four unpaired. Due to the ligand field in the heme molecule the energy level of the 3d z^2 and x^2-y^2 orbital split off from the xy, yz and xz energy level. The energy gap between the two orbital groups rises during heme oxygenation due to the stronger ligand field induced by the adsorption of the O_2 molecule. Thus, the two electrons of the z^2 and x^2-y^2 orbitals are paired up in the yz and xz orbital which corresponds in this case to the lowest energy state (Fig. 2.19).

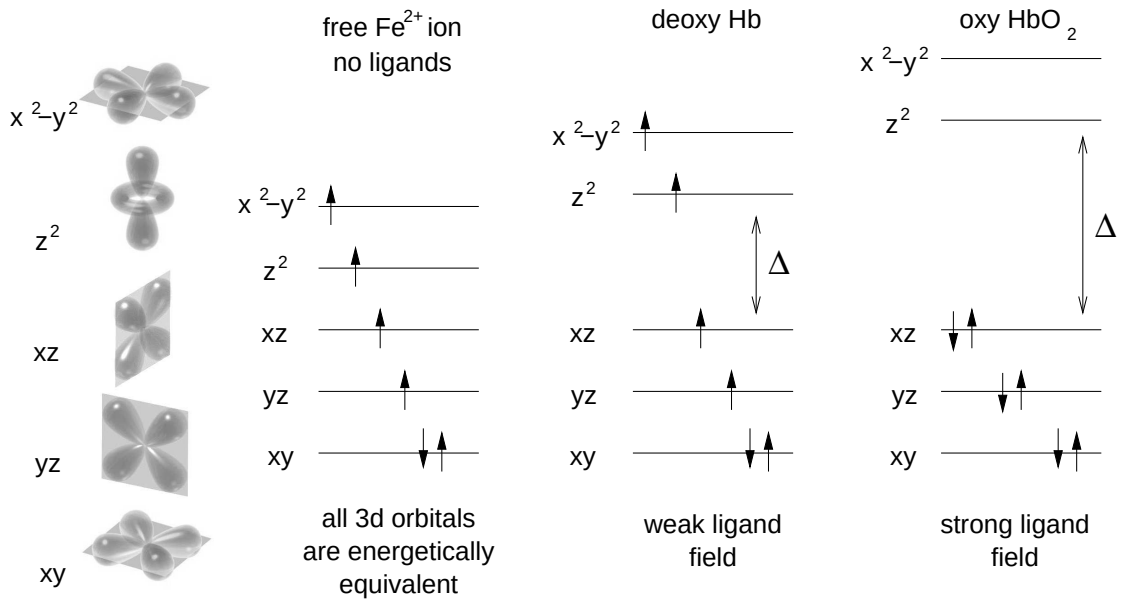

Figure 2.19: *3d orbitals of the Fe^{2+} ion (left). The energy states of the orbitals are equal for the free Fe^{2+} without any influencing ligands (middle left). The ligands in the heme molecule influence the orbital energy, thus the z^2 and x^2-y^2 orbital energy is split off by a Δ-energy gap (middle right). Oxygenated heme shows a much higher energy gap Δ, thus the z^2 and x^2-y^2 electrons has to pair up with the yz and xz electrons (right). (Figure adapted from Bunn and Forget (1986))*

The total magnetic susceptibility of blood is proportional to the magnetic susceptibility of the red blood cells (χ_{rbc}) and of the blood plasma (χ_{plasma}) as well as the hematocrit (Hct):

$$\chi_{blood} = \mathrm{Hct} \cdot \chi_{rbc} + (1 - \mathrm{Hct}) \cdot \chi_{plasma}. \tag{2.66}$$

The value of χ_{rbc} depends linearly on the amount of oxygenated and deoxygenated hemoglobin and Eq. 2.66 can be written as (Spees et al., 2001)

$$\chi_{blood} = \mathrm{Hct} \cdot (Y \cdot \chi_{rbc,\,ox} + (1 - Y) \cdot \chi_{rbc,\,deox}) + (1 - \mathrm{Hct}) \cdot \chi_{plasma}, \tag{2.67}$$

where $\chi_{rbc,\,ox}$ and $\chi_{rbc,\,deox}$ denote the magnetic susceptibility of completely oxy- and deoxygenated red blood cells.

Further investigations on magnetic properties of blood and its components found that the susceptibility of blood plasma, due to its low protein content, is similar to that of water ($\chi_{plasma} = \chi_{H_2O\,at\,37°C} = -9.05\,\mathrm{ppm}$) (Schenck, 1996). Fully oxygenated hemoglobin HbO_2 was found to be more diamagnetic than water ($\chi_{HbO_2} = 4\pi \cdot (-0.791) = -9.94\,\mathrm{ppm}$) (Philo et al., 1984; Cerdonio et al., 1985). The hemoglobin concentration within red blood cells is about 333 g/l (Schmidt and Thews, 1987) which changes the susceptibility of red blood cells $\chi_{rbc,\,ox}$ to about $4\pi \cdot (-0.738) = -9.27\,\mathrm{ppm}$. This value is in a good agreement with measurements of Spees et al. (2001) and Weisskoff and Kiihne (1992). Due to the small difference in the magnetic susceptibility of blood

plasma and oxygenated red blood cells ($\chi_{plasma} \approx \chi_{rbc,\,ox}$) they can be assumed to be equal. Expressing the difference between fully oxygenated and deoxygenated red blood cells as $\Delta\chi_{do} = \chi_{rbc,\,deox} - \chi_{rbc,\,ox}$, Eq. 2.67 can now be simplified to

$$\chi_{blood} = \chi_{rbc,\,ox} + \mathrm{Hct} \cdot (1 - Y) \cdot \Delta\chi_{do}. \tag{2.68}$$

Since blood vessels are embedded in soft tissue, the susceptibility difference $\Delta\chi$ between the parenchyma and the blood is of interest. Assuming that the magnetic susceptibilities of soft tissue and oxygenated red blood cells are also nearly equal, $\Delta\chi$ follows directly from Eq. 2.68

$$\Delta\chi = \mathrm{Hct} \cdot (1 - Y) \cdot \Delta\chi_{do} = \mathrm{Hct} \cdot \mathrm{OEF} \cdot \Delta\chi_{do} \tag{2.69}$$

Actually, different values of $\Delta\chi_{do}$ are given in literature Thulborn et al. (1982) specified a value of $\Delta\chi_{do} = 4\pi \cdot 0.2 = 2.51\,\mathrm{ppm}$, whereas Weisskoff and Kiihne (1992) obtained $\Delta\chi_{do} = 4\pi \cdot 0.18 = 2.26\,\mathrm{ppm}$. In a more recent study $\Delta\chi_{do} = 4\pi \cdot 0.27 = 3.39\,\mathrm{ppm}$ was determined (Spees et al., 2001). All three studies measured whole blood samples inside NMR spectrometers or MRI devices. In the work of Spees et al. (2001) additional SQUID magnetometer measurements were presented. A different method was used by Plyavin' and Blum (1983). They investigated the migration of red blood cells in a magnetic field gradient and calculated the cell susceptibility from the measured migration velocity. A magnetic susceptibility of $\chi_{rbc,\,ox} = -9.19\,\mathrm{ppm}$ and $\chi_{rbc,\,deox} = -6.7\,\mathrm{ppm}$ was found for oxy- and deoxygenated red blood cells, resulting in a $\Delta\chi_{do}$ of 2.49 ppm. These results of red blood cell magnetophoresis were confirmed by a more recent study of Zborowski et al. (2003).

2.3.5. Model of a Single Cylindric Vessel

2.3.5.1. Field Distribution of an Infinitely Long Cylinder

The model of an infinitely long, homogeneous magnetic cylinder is a good starting point to describe straight single venous vessels (Fig. 2.20). The magnetic field induced by the cylinder consist of a homogeneous D and inhomogeneous part I and can be written as (Springer, 1994)

$$\vec{B}_{cyl} = \{1 + D + I\} \cdot \vec{B}_0 \tag{2.70}$$

The field is split into the internal ($\vec{B}_{int}$) and external ($\vec{B}_{ext}$) field of the cylinder. The external magnetic field is defined as

$$\begin{aligned} \vec{B}_{ext} &= \left\{ \quad 1 \quad + \quad D_e \quad + \qquad\qquad I_e \qquad\qquad \right\} \cdot \vec{B}_0 \\ &= \left\{ \quad 1 \quad + \quad \tfrac{\chi_e}{3} \quad + \quad \tfrac{\Delta\chi}{2} \cdot \sin^2\theta \cdot a^2 \cdot \tfrac{\cos 2\Phi}{r^2} \quad \right\} \cdot \vec{B}_0 \qquad \forall r > a, \end{aligned} \tag{2.71}$$

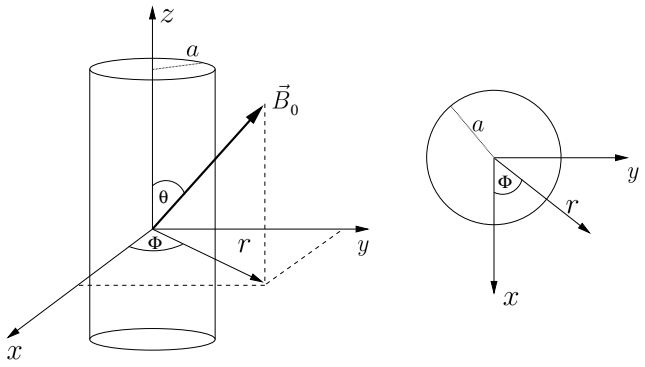

Figure 2.20: *Cylinder in an external magnetic field (Figure adapted from Deistung (2005))*

The homogeneous part outside of the cylinder is $D_e = \chi_e/3$, whereas the inhomogeneous external field I_e depends on the difference between the cylinder and surrounding magnetic susceptibility ($\Delta\chi = \chi_e - \chi_i$), the vessel orientation (θ) as well as the cylinder diameter (a). The spin position is given in polar coordinates $\frac{\cos 2\Phi}{r^2}$ (see Fig. 2.20). The inhomogeneous term is zero for the parallel cylinder orientation with respect to the external field ($\theta = 0°$) and increases to a maximum for the perpendicular cylinder orientation ($\theta = 90°$) (Fig. 2.21). The internal magnetic field of the cylinder is homogeneous for all orientations, thus $I_i = 0$. However, the homogeneous part (D_i) depends on θ and $\Delta\chi$ which produces the internal magnetic field of the cylinder with

$$\begin{aligned} \vec{B}_{int} &= \left\{ \quad 1 \quad + \qquad\qquad D_i \qquad\qquad + \quad I_i \quad \right\} \cdot \vec{B}_0 \\ &= \left\{ \quad 1 \quad + \quad \tfrac{\chi_e}{3} + \tfrac{\Delta\chi}{6} \cdot (3\cos^2\theta - 1) \quad + \quad 0 \quad \right\} \cdot \vec{B}_0 \qquad \forall r < a. \end{aligned} \tag{2.72}$$

The homogeneous term D_i changes from $\chi_e/3 + \Delta\chi/3$ for $\theta = 0°$ to $\chi_e/3 - \Delta\chi/6$ for the perpendicular orientation. For $\theta = \arccos\sqrt{1/3} = 54.74°$ the term $(3\cos^2\theta - 1)$ in D_i is zero and the homogeneous parts of the external and internal magnetic fields will be equal ($D_i = D_e$). This special angle is called "magic angle" and plays an important role in NMR spectroscopy where cylindrical sample holders are tilted by 54.74° (Badurek, 1998).

2.3.5.2. Partial Volume Effect

MRI of heterogeneous biological probes causes voxels to contain different tissue types such as tissues with water or fat, single veins or the blood capillary network as well as free water of the cerebrospinal fluid. For instance, the signal of a homogeneous voxel containing a single venous vessel is the addition of the intra- and extravascular signal. The fraction of both signals depends on the volume fraction λ of the intravascular compartment. A scheme of a partial volume effect is displayed in Fig. 2.22, the total voxel signal is written as

$$\vec{S}_{vox} = \lambda \cdot \vec{S}_{int} + (1 - \lambda) \cdot \vec{S}_{ext}. \tag{2.73}$$

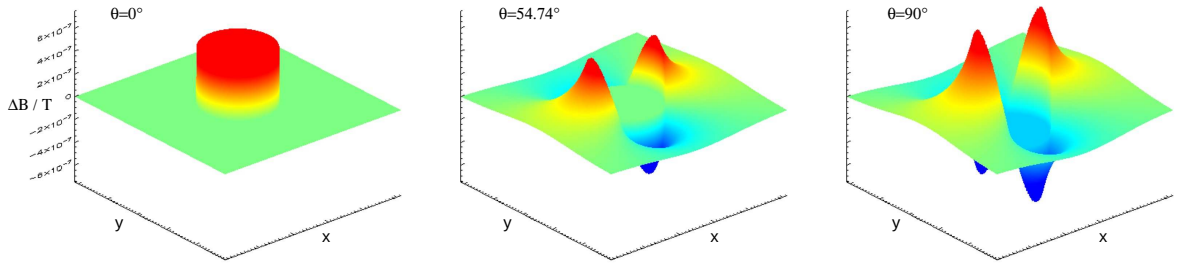

Figure 2.21: *Magnetic field distribution of a single magnetic cylinder for different orientations with respect to the external field $\vec{B}_0$. The $\vec{B}_0$ field was tilted in the x-z plane in such a way that for $\theta = 0°$ $\vec{B}_0$ is parallel to the z axis and for $\theta = 90°$ parallel to the x axis. The susceptibility difference between the cylinder and the surroundings was set to $\Delta\chi = 1\,ppm$, whereas the magnetic difference ΔB denotes the induced field changes respectively to the main magnetic field with $\vec{B}_0 = 1.5\,T$. Note that for a cylinder orientation of $\theta = 54.74°$ the internal field is equal to the homogeneous part of the outer field ($D_i = D_e$).*

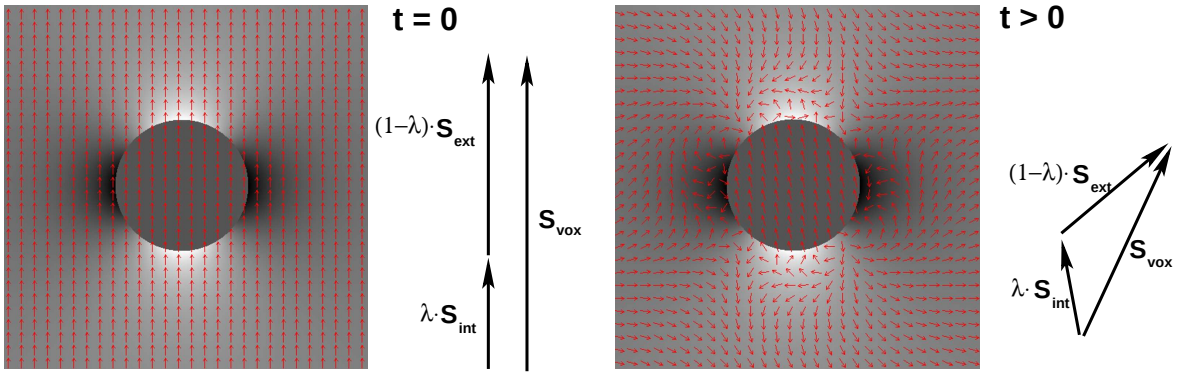

Figure 2.22: *Visualization of the voxel signal generation in the presence of a cylindric vessel oriented perpendicular to the main magnetic field. All spins (tiny arrows within the voxel) contribute to the total signal (S_{vox}) with their own phase and magnitude. At $t = 0$ all spins have the same phase. Later ($t > 0$), the spins dephase which results in signal loss and different phasing of the external ($(1-\lambda)\cdot S_{ext}$) and internal signal ($\lambda \cdot S_{int}$) contribution. The volume fraction of the cylinder on the total voxel is denoted by λ.*

2.3.5.3. Analytical Solution of MR-Signal Decay in the Presence of a Magnetized Cylinder

The signal vectors in Eq. 2.73 can be expressed as complex numbers which yields

$$S_{vox}(t) = \lambda \cdot S_{int,0} \cdot e^{-i\cdot\gamma\Delta B\cdot t} \cdot e^{-t/T_{2,\,int}} + (1-\lambda) \cdot S_{ext,0} \cdot e^{-t/T_{2,\,ext}} \cdot \eta, \qquad (2.74)$$

where $S_{ext/int,0}$ denotes the signal directly after excitation ($t = 0$). The frequency shift $\gamma\Delta B$ is determined by the difference between the homogeneous terms of the intra- and

extravascular field with

$$\Delta B = D_i - D_e = \frac{\Delta\chi}{6}(3cos^2\theta - 1) \cdot B_0. \tag{2.75}$$

The transverse signal decay time constants of the irreversible spin-spin interaction are $T_{2,\,ext/int}$. The additional extravascular signal loss η, due to spin dephasing caused by the static field inhomogeneity around the vessel, has been calculated analytically by Yablonskiy and Haacke (1994) as

$$\eta = 1 - f_{cyl}\,(\delta\omega_\theta \cdot t) \cdot \frac{\lambda}{1-\lambda} + f_{cyl}\,(\lambda \cdot \delta\omega_\theta \cdot t) \cdot \frac{\lambda}{1-\lambda}, \tag{2.76}$$

where $\delta\omega_\theta$ denotes the characteristic frequency shift induced by the cylinder and is given by

$$\delta\omega_\theta = \gamma \cdot \frac{\Delta\chi}{2} \cdot B_0 \cdot \sin^2\theta. \tag{2.77}$$

The function f_{cyl} is given by

$$f_{cyl}(x) = \int_0^1 \frac{1 - J_0(xu)}{u^2}\,\mathrm{d}u, \tag{2.78}$$

where J_0 is the Bessel function of order 0. This analytical signal equation (Eq. 2.74), however, is only valid if the cylinder is embedded coaxially in a cylindrical voxel and by neglecting diffusion effects.

For parallel vessel orientation ($\theta = 0°$) $\delta\omega_\theta$ is zero and η is 1 for all echo times, because no field inhomogeneity exists and therefore no extravascular static spin dephasing occurs. The beat frequency of the constructive and destructive signal interference is determined by $\gamma\Delta B = \Delta\chi/3 \cdot \gamma B_0$ (obtained from Eq. 2.75, with $\theta = 0$), which defines directly the frequency shift between the inner and the outer compartment. The amplitude of the signal beat depends on the volume fraction λ, the magnitude of the two signal components $S_{ext/int,\,0}$ as well as on $T_{2,\,ext/int}$ (Fig. 2.23, left).

For the vessel orientated at the "magic angle" with respect to the external magnetic field the frequency shift $\gamma\Delta B$ is zero (Eq. 2.75) and only the external field inhomogeneity denoted by η as well as $S_{ext/int,\,0}$ and $T_{2,\,ext/int}$ determine the voxel signal (Fig. 2.23, middle).

For a perpendicular vessel orientation ($\theta = 90°$) $\delta\omega_\theta$ is maximal and so is the influence of η on the external signal contribution. The voxel signal decay is then characterized by a rapid signal loss due to spin dephasing, but also by local signal minima and maxima, whose position and magnitude depend mainly on η as a result of the high symmetry of the field inhomogeneity. The frequency shift between the internal and external signal with $\gamma\Delta B = -\Delta\chi/6 \cdot \gamma B_0$ (Eq. 2.75) has only little influence on the signal formation (Fig. 2.23, right).

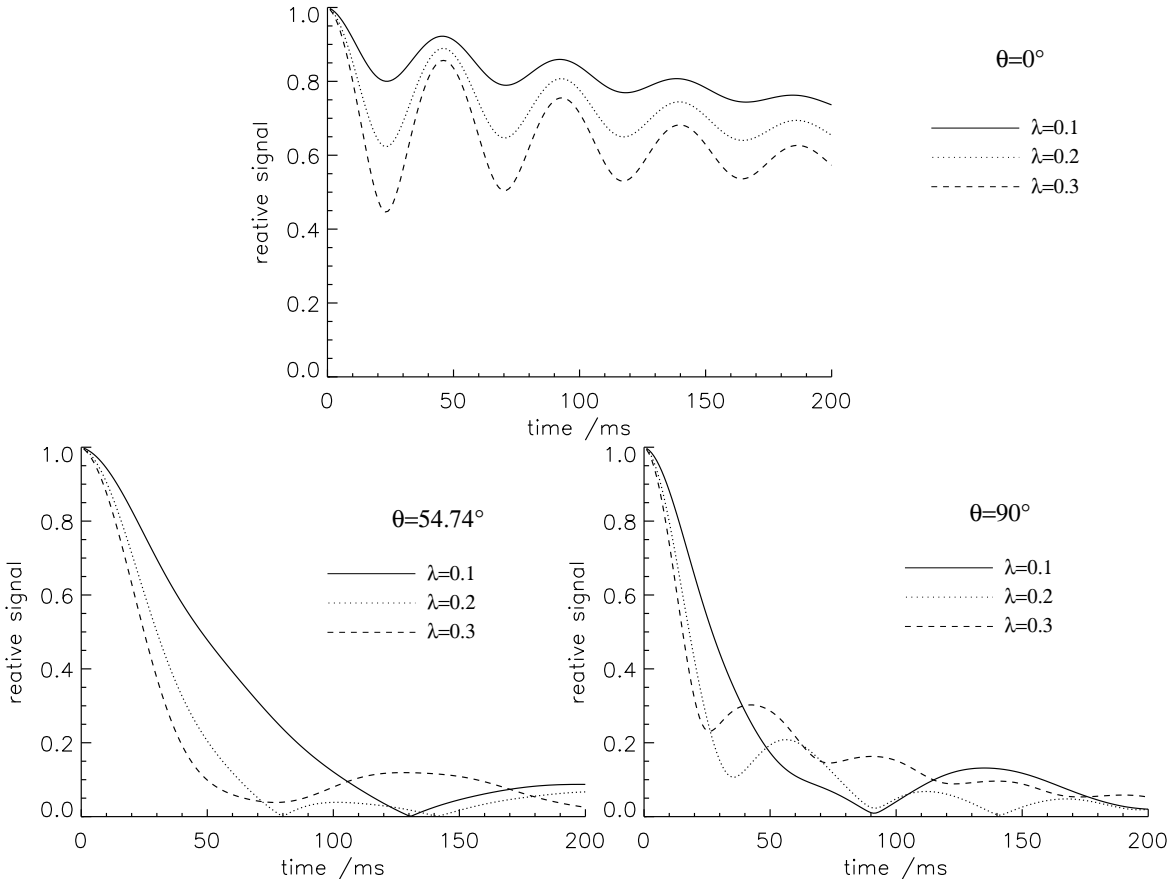

Figure 2.23: *Voxel signal decay relative to S_{vox}(t=0) for the parallel (top), "magic angle" (left) and perpendicular (right) cylinder orientation. Simulation parameters were: $B_0 = 1.5\,T$, $\Delta\chi = 1\,ppm$, $S_{ext,0} = S_{int,0}$, $T_{2,ext} = 1000\,ms$, $T_{2,int} = 100\,ms$.*

2.3.5.4. Static Dephasing Regime

If spin motion, e.g. due to self diffusion, is neglected during the NMR experiment, the spins can be assumed to remain in fixed positions and the field inhomogeneity they experience is time-invariant. The criterion for the application of the static dephasing regime is given by

$$\delta\omega_\theta^{-1} << \frac{R_0^2}{D}, \tag{2.79}$$

where $\delta\omega_\theta^{-1}$ is the characteristic signal decay time induced by the field inhomogeneity and R_0 the characteristic length of the inhomogeneity. In the case of the single cylinder this length is set equal to the cylinder radius ($R_0 \equiv a$). The self diffusion constant D of water is about $D_{H_2O} = 2.07 \cdot 10^{-3}\,\mathrm{mm^2/s}$ at a room temperature of 21°C (Price et al., 1999; Güllmar et al., 2005).

A cylinder oriented perpendicular ($\theta = 90°$) to the main magnetic field ($\vec{B}_0 = 1.5\,\mathrm{T}$) with $\Delta\chi = 1\,\mathrm{ppm}$ causes a $\delta\omega_\theta$ (Eq. 2.77) of $200\,s^{-1}$ and therefore a characteristic signal decay time $\delta\omega_\theta^{-1}$ of 5 ms. Using water with the diffusion coefficient at room

temperature the characteristic size of the inhomogeneity is $\sqrt{\delta\omega_\theta^{-1} \cdot D_{H_2O}} = 3.2\,\mu$m. To safely assume the static dephasing regime, the cylinder radius has to be much larger than R_0 which is the case if the radius is on the order of hundreds of microns.

The self diffusion coefficient of human brain tissue is smaller than that of free water due to the presence of cell walls and membranes. Thus, the static dephasing regime can be assumed for *in vivo* measurements since the investigated venous vessel radius is on the order of hundreds of microns, too. The self diffusion of water was determined by Le Bihan et al. (1995) to be about $80 \cdot 10^{-5}\,\mathrm{mm}^2/\mathrm{s}$ for gray and $64 - 107 \cdot 10^{-5}\,\mathrm{mm}^2/\mathrm{s}$ for white brain matter parallel and perpendicular to nerve fibers. The diffusion in biological tissues, especial white matter, is not isotropic but rather anisotropic with higher diffusion along fibers and lower across them (Basser et al., 1995).

2.3.6. Model of Cylinder Network

The network formed by blood vessels and capillaries in the human brain ranges from 120-240 μm for the intracortical supplying arteries and 80-120 μm for draining veins (Fig. 2.24, left). The capillary network which connects the arterial and venous branches is supplied by vessels with a size between 30-40 μm. The capillaries form an equally spatially distributed vessel network (Fig. 2.24, right). Their diameters are distributed from 20 down to 4 μm. The blood capillary density differs between gray and white matter resulting in a different cerebral blood volume (CBV) which was determined by Yamaguchi et al. (1986) using $C^{15}O$-PET (positron emission tomography). They found 4.3 ml blood/100 g in cortical gray and 2.1 ml blood/100 g in white matter. Newman et al. (2003) reproduced these findings using a dynamic T_2^*-weighted MRI method with a paramagnetic contrast agent. Comparing different MRI studies, which measured slightly different values for the blood volume, all studies showed a consistent blood volume ratio between gray and white matter of about 2:1.

Moskalenko (1980) fractionated cerebral blood vessels into five groups: two for arteries with average radii of 0.5 and 0.06 mm, capillaries with r=0.003 mm and two groups of veins with r=0.1 and 0.5 mm. He quantified the average number of vessels, their length and the corresponding fractions on the total CBV of each vessel group (10%, 17%, 29%, 19%, 25%) in dogs weighting 9-12 kg. Assuming deoxygenated blood only in venous vessels and capillaries, the venous blood volume is the sum of the last three vessel groups measured by Moskalenko (1980). Thus, the total blood volume is reduced by the factor 0.7. This value is the deoxygenated blood volume λ which is used in later MR signal calculations.

Because only the deoxygenated blood of the blood vessel network induces a frequency shift and its volume fraction on brain tissue is rather low, the intravascular signal contribution is neglected for the following considerations.

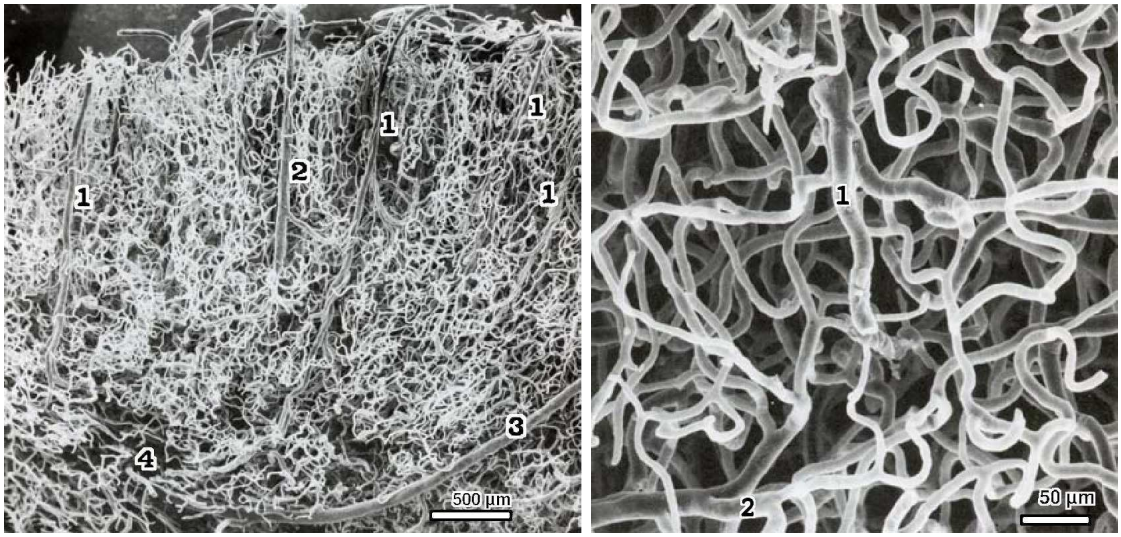

Figure 2.24: *Network of cortical blood vessels in the human brain. Intravascular resign injection (Mercox) and scanning electron microscopy. 1) artery of gray matter, 2) vein of gray matter, 3) artery of white matter, 4) smaller vessels of the white matter. (Figures adapted from (Duvernoy et al., 1981))*

To obtain an analytical solution of the MR signal, the model of the single cylinder is extended by averaging over randomly spatially distributed and oriented cylinders. Such a cylinder network model is only valid for low blood volumes ($\lambda < 5\%$), because the pure statistical positioning of the cylinders allows an unrealistic overlapping or coinciding of cylinders. In the static dephasing regime the vessel radius is not influencing the network signal, it depends only on the blood volume fraction λ and the susceptibility difference between blood and its surrounding tissue $\Delta\chi$. Furthermore, the following calculation accomplished by Yablonskiy and Haacke (1994) neglects the intravascular signal contribution, which is a further limitation of the model, but sufficient for a low blood volume.

The frequency shift induced by the capillary network is given by

$$\delta\bar{\omega} = \gamma \cdot \frac{\Delta\chi}{3} \cdot B_0. \tag{2.80}$$

The extravascular network signal is calculated by

$$S_{ext}(t) = (1-\lambda) \cdot S_{ext,\,0} \cdot e^{-\lambda \cdot f_{net}(\delta\bar{\omega}\cdot t)} \cdot e^{-t/T_{2,\,ext}}, \tag{2.81}$$

with

$$f_{net}(x) = \frac{1}{3} \cdot \int_0^1 (2+u) \cdot \sqrt{1-u} \cdot \frac{1 - J_0(3/2 \cdot xu)}{u^2}\,\mathrm{d}u. \tag{2.82}$$

The signal in Eq. 2.81 exhibits an asymptotic behavior were the short and long term

asymptotes are given as

$$S_{ext,\,short}(t) = S_{ext,\,0} \cdot e^{-0.3\cdot\lambda\cdot(\delta\bar{\omega}\cdot t)^2} \cdot e^{-t/T_{2,\,ext}} \qquad \forall\, |\delta\bar{\omega}\cdot t| \leq 1.5 \tag{2.83}$$

$$S_{ext,\,long}(t) = S_{ext,\,0} \cdot e^{-\lambda\cdot\delta\bar{\omega}\cdot(t-1/\delta\bar{\omega})} \cdot e^{-t/T_{2,\,ext}} \qquad \forall\, |\delta\bar{\omega}\cdot t| \geq 1.5\,. \tag{2.84}$$

The characteristic time where the short term asymptotic behavior changes to the long term behavior is calculated by

$$t_c = \frac{1.5}{\delta\bar{\omega}}. \tag{2.85}$$

2.3.6.1. Diffusion

Considering the discussion of the static dephasing regime (Sec. 2.3.5.4) the size of the blood capillaries is too small to neglect the effect of diffusion, even in brain tissue where diffusion is restricted due to cell walls. Kiselev and Posse (1998) developed an analytical signal dephasing model which accounts for the effect of diffusion in the microvascular network. They also included an analytical description of the previously neglected intravascular signal contribution (Kiselev and Posse, 1999). Due to the homogeneous field distribution inside the vessels and the assumption of impermeable vessel walls the intravascular signal contribution is not affected by diffusion in the microvascular network. However, due to the vessel surrounding field inhomogeneity the extravascular signal contribution is affected and the signal decay depends on the diffusion effect (Fig. 2.25). Unfortunately, the effect of diffusion on the network signal scales not only with the diffusion coefficient but also inversely proportional with the vessel diameter. Thus, the underlying vessel size distribution and diffusion coefficient have to be known for a valid theoretical calculation of the MR signal.

As shown in Fig. 2.25, the signal formation with the consideration of diffusion strongly differs from the zero diffusion signal after the refocusing pulse. In the diffusion case, the maximal signal magnitude is not reached at the spin echo position. It is rather lowered and shifted to a shorter echo time. This effect is caused by the partly irreversible signal dephasing which occurs in the microvascular network due to spin diffusion. However, the signal affected by diffusion shows only a slight difference to the zero diffusion signal before the refocusing pulse. This will also be observed for the signal after the refocusing pulse if a much shorter spin echo time is used. Thus, the effect of diffusion on the network signal can be minimized using short spin echo times.

A very recent study of He and Yablonskiy (2007) developed a more realistic tissue model for quantitative venous blood volume and oxygenation extraction fraction mapping by including a signal fraction of interstitial water and a intravascular signal fraction of the blood. The latter model with the intravascular blood signal was developed by Sukstanskii and Yablonskiy (2001). However, the authors assumed a negligible deviation from the static dephasing regime at a high field strength ($B_0 = 3\,\mathrm{T}$) and at a short spin echo

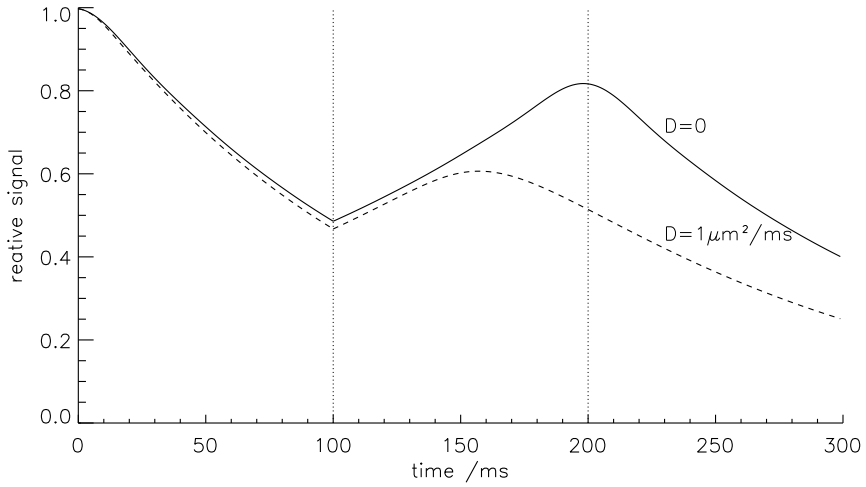

Figure 2.25: *Signal time course S(t)/S(t=0) with a refocusing pulse applied at $t = 100\,ms$ resulting in a spin echo at $t = 200\,ms$ and assuming an irreversible signal decay with $T_2 = 1000\,ms$. The microvascular network is simulated by monosized vessels with a radius of $10\,\mu m$, volume fraction of $\lambda = 5\%$ and $\Delta\chi = 1\,ppm$. The signal contribution of the innervascular compartment was set to zero. The solid line shows the signal decay for the static dephasing regime (diffusion coefficient $D = 0$, upper line) and the dashed line with considering diffusion in the microvascular network ($D = 1\,\mu m^2/ms$, lower line).*

time ($T_{SE} = 33\,\text{ms}$) which were used in their work. They also obtained physiologically reasonable results for the total cerebral venous blood oxygenation of $Y \approx 0.6$.

2.3.6.2. Mutual Avoiding Cylinders

Pawlik et al. (1981) investigated the capillary topography in the cerebral cortex of cats and obtained a homogeneous spatial distribution of blood capillaries. The capillaries form a network showing equal intercapillary distances (median $24.2\,\mu m$) with significant interregional differences, e.g. white and gray matter. The cortical blood supplying vessel network in human brain shows also a highly organized vessel network (Fig. 2.26). The previously described signal computation, based on statistical independent cylinder positions (Sec. 2.3.6), did not consider correlated cylinder positions of mutual avoiding cylinders.

A cylinder network model which regards such mutual avoiding cylinders was developed for special diffusion measurements in MRI by Kiselev (2004). He showed that the measured signal will deviate from the pure statistical model with increasing volume fraction or susceptibility difference between the capillaries and the surrounding tissue. Kiselev (2004) introduced a correction parameter z which characterizes the correlation in mutual positions of the blood vessels. If this parameter is, e.g., $z = 1$, the cylinders will still be randomly positioned, an overlapping of cylinders will be excluded. For lower

z values an almost regular pattern is formed by the vessels. For $z > 1$, a partial vessel overlap is allowed. In the limit of $z \to \infty$, the vessel positions become statistically independent as assumed in the previous network model of Yablonskiy and Haacke (1994). Actually, no theoretical values of the z parameter exist for biological tissue. However, this parameter should be rather low to restrict vessel overlapping and to form a highly organized vessel network. Kiselev (2004) proposed values of $z = 1.4 - 2\lambda$ for brain tissue in comparison with experimental data from Does et al. (1999).

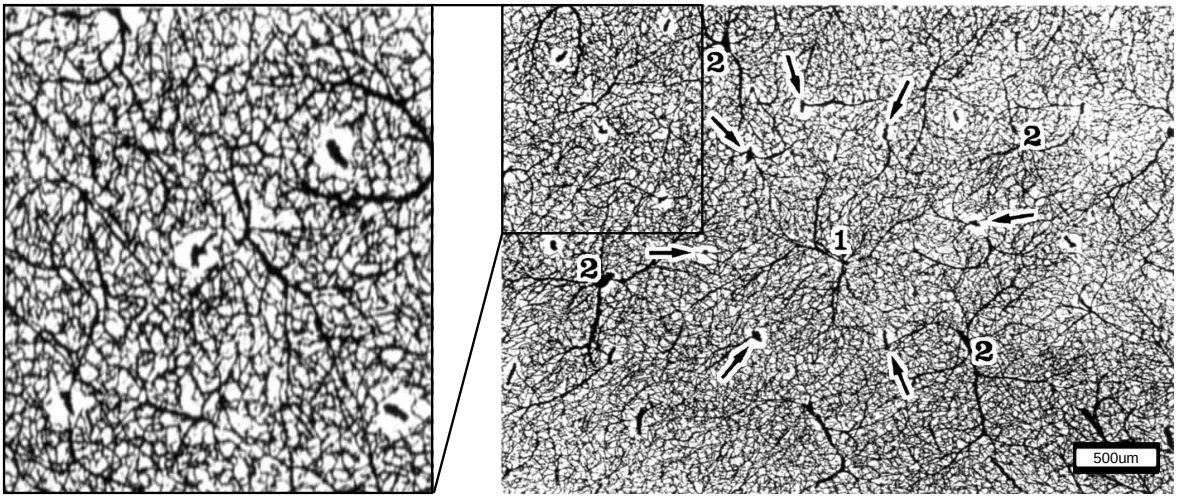

Figure 2.26: *Intracortical network: section of the cortex tangential to the cortical surface. Intravascular india ink injection. 1) possible vascular unit centered by an intracortical vein which is surrounded by a ring of several intracortical arteries (arrows) 2) neighbouring vascular units. (Figure adapted from (Duvernoy, 1999)).*

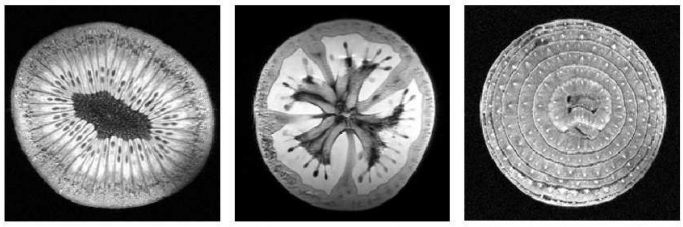

MR images of a kiwi, a tomato and an onion.

MRI @ Paul Scherrer Institute, CH-5232 Villigen PSI, Switzerland

III

Materials and Methods

3.1. Susceptibility Weighted Imaging - SWI

Magnetic heterogeneity of tissues is not only caused by the venous vascular system but also by different tissue iron concentrations, calcifications or the presence of hemosiderin. These heterogeneities are the origin of contrast in susceptibility weighted imaging. The method of SWI was first applied in cerebral venographic imaging with high spatial resolution by Reichenbach et al. (1997b) and was later called SWI by Haacke et al. (2004). Meanwhile, the method has been successfully applied in imaging venous vessels (Reichenbach and Haacke, 2001), arteriovenous malformations (Essig et al., 1999; Lee et al., 1999), multiple sclerosis (Tan et al., 2000), stroke (Hermier and Nighoghossian, 2004; Wycliffe et al., 2004) and hemorrhagic lesions (Tong et al., 2004; Shen et al., 2007). Further applications include diagnosis of Sturge Weber syndrome (Mentzel et al., 2005), characterization of paramagnetic and diamagnetic cerebral lesions (Deistung et al., 2006), delineation of cerebral tumors (Barth et al., 2003; Noebauer-Huhmann et al., 2006) and combination of the method with gaseous agents (Rauscher et al., 2005a, c).

3.1.1. Acquisition of SWI data

Structures with a different magnetic susceptibility than their surroundings produce changes in the magnetic field. If these structures are small with dimensions on the order of or even smaller than the voxel size, they lead to intravoxel spin dephasing

and signal loss in gradient echo sequences. If the structures are larger, the induced field inhomogeneity extends to and varies over more voxels. In such a situations the magnetic field can then be considered to be nearly constant within each voxel and no additional spin dephasing occurs. However, an offset in the resonance frequency will be induced that can be detected in the phase of the acquired signal. Consequently, contrast between areas with different magnetic susceptibilities can be improved by combining magnitude and phase information.

For the visualization of venous vessels in the sub-millimeter range a T_2^*-weighted sequence with high spatial resolution is necessary. Since the effect utilized to imaging the veins is not based on flow, i.e. moving spins, but rather on magnetic susceptibility differences, a fully velocity compensated 3D acquisition scheme is employed (Laub and Kaiser, 1988; Frank et al., 1992). Typical sequence parameters and options are described below.

Acquisition Matrix: The acquisition matrix should be rather large to obtain small voxels. In these voxels small susceptibility perturbations, such as venous vessels of diameters down to 100 μm, can still induce sufficient signal loss due to its surrounding field inhomogeneity to be detected by SWI. Furthermore, background gradients or macroscopic field inhomogeneities, which are caused by tissue bone or tissue air boundaries, do not appreciably dephase the spins inside such small voxels or cause serious image artifacts. Typical acquisition matrices are 512 (readout) $\times$ 256 (phase y) $\times$ 36 to 64 (phase z) leading to voxel sizes of about 0.5 $\times$ 0.67 $\times$ 1.5 to 2 mm^3 depending on the adjusted FOV.

Bandwidth: The readout bandwidth (BW) should be chosen low to ensure a sufficiently high signal-to-noise ratio (SNR). Typical values are 50 to 100 Hz/pixel.

Echo Time: Since the susceptibility effect scales with the echo time long echo times are needed to obtain a good contrast. Generally, echo times of about 40 ms and 20 ms are used at 1.5 T and 3 T, respectively (Reichenbach et al., 2000).

Repetition Time: The repetition time T_R is mainly limited by T_E and ranges typically from 55 to 67 ms at 1.5 T. Longer T_R leads to unacceptable long acquisition times. Shorter T_R times, which are possible at higher field strengths due to the shorter T_E, are not necessarily preferable. According to Ernst and Anderson (1966) the optimum flip angle has to be lowered with shorter T_R (Eq. 2.54) which reduces the signal intensity and thus the SNR.

Flip Angle: The flip angle is adjusted to the optimum flip angle (Ernst angle) which depends on T_R and the T_1 relaxation time of the investigated sample. Typical flip angles range from 15 to 25° in SWI. With the prolongation of T_1 at higher field strengths, the Ernst angle becomes even smaller. Using flip angles slightly larger than the Ernst angle produces more pronounced T_1-weighting, which allows a better differentiation between gray and white matter.

Velocity Compensation: Moving spins in blood vessels (arteries as well as veins) accumulate a phase which depends on the moving velocity. In consequence to the necessarily long echo times used with SWI, moving spins which are not rephased, e.g. in a non-compensated sequence, cause signal loss and miss-registration artifacts of the vessels. Only in 3D sequences, with two phase encoding directions, a full velocity compensation is possible which enables the compensation of moving spins in oblique vessels (Frank et al., 1992). However, with a first order flow compensation, i.e. velocity compensation, only non-accelerated linear motion can be compensated. Accelerated spins are not compensated.

Parallel Imaging: Long echo and thus repetition times are necessary to obtain sufficient susceptibility weighted contrast. This can lead to acquisition times of 10 min or longer for high resolution 3D SWI scans. The parallel acquisition of the MR signal, with multiple coils arranged in a certain manner around the measuring object, offers the possibility to save scan time by k-space undersampling. Recent works of Sedlacik et al. (2005) and Lupo et al. (2007) tested image quality and venous visibility in SWI by applying the generalized autocalibrating partially parallel acquisition algorithm (Griswold et al., 2002). It was found that this parallel imaging technique works properly for an accelerating factor of 2 with about 12 to 16 auto calibration lines.

3.1.2. Reconstruction of SWI data

The signal received in MRI is a complex quantity and represents not only the magnitude of the magnetization vector but also its phase. During the acquisition process the Larmor frequency $\omega_0 = -\gamma B_0$ is demodulated from the received signal and the phase of spins exposed exactly to B_0 would experience no frequency offset and no phase shift. Differences in the main magnetic field ΔB cause offsets to the Larmor frequency $\Delta\omega$ which remain in the demodulated signal. Thus, phase shifts will be detected in the obtained MR image (Fig. 3.1). The phase shift is defined by:

$$\Delta\phi = -\Delta\omega \cdot T_E = -\gamma \Delta B \cdot T_E, \tag{3.1}$$

where the echo time T_E denotes the time point where gradient recalled signal echo occurs.

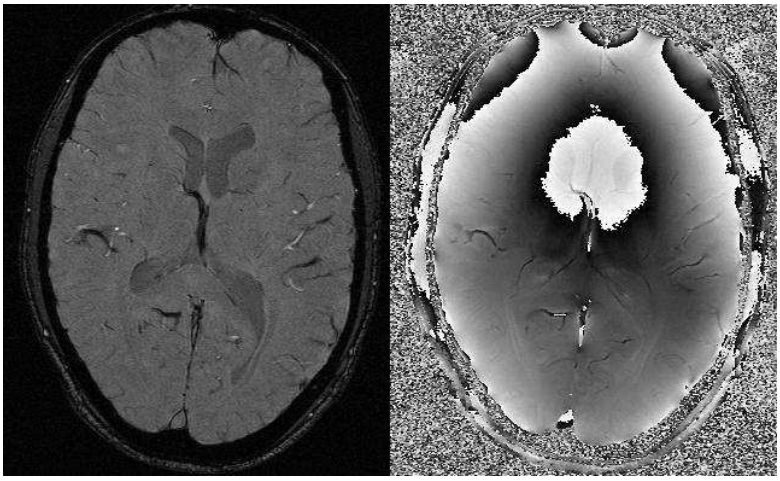

Figure 3.1: *Magnitude (left) and phase (right) of center slice of transverse measured 3D slab. Sequence parameters were:* $B_0 = 1.5\,T$, $T_E/T_R/\alpha = 40\,ms/57\,ms/20°$, *acquisition matrix* $= 512 \times 256 \times 38$, $FOV = 256 \times 192 \times 78\,mm^3$, *bandwidth* $= 78\,Hz/pixel$.

The phase changes globally due to macroscopic field gradients caused by air tissue boundaries, e.g. the sinuses or nasal cavity. On the other hand, local phase changes are also visible, e.g., in veins. The phase, which is defined only between 0 and 2π, can, however, exceed the upper or lower limit which causes the phase to wrap. These phase wraps, which are easy visible in the frontal and central region in the phase image (Fig. 3.1), can compromise the demonstration and evaluation of phase images.

To be able to utilize the phase information, the phase has to be unwrapped and filtered. One method is demodulation with a homodyne reference (Noll et al., 1991), which produces high pass filtered MR phase images almost free of phase wraps. The homodyne demodulation reference is obtained from the MR data itself by low pass filtering (Fig. 3.2, left). The original complex data is then divided by the low pass filtered complex data which results in a phase subtraction. Due to this demodulation the phase is high pass filtered and wraps are effectively eliminated (Fig. 3.2, middle). One drawback of this method is the simultaneous high pass filtering of the phase. During this process all information of phase changes below a certain spatial frequency are lost.

An alternative way works via a region growing directly on the real values of the phase image. One implementation was first described by Xu and Cumming (1999) to unwrap synthetic aperture radar (SAR) interferograms with a difficult step topography. Rauscher et al. (2003) adapted this region growing phase unwrapping algorithm for medical MR imaging, especially for SWI, which was subsequently improved by Witoszynskyj et al. (2007). The right image in Fig. 3.2 shows such an unwrapped phase image which also represents the field map according to Eq. 3.1. (Rauscher et al., 2006).

To further utilize these unwrapped phase images for SWI, they has to be high pass filtered, e.g., by subtraction with the likewise unwrapped low pass filtered phase image. The result is a phase image comparable with the homodyne filtered phase image (Fig. 3.2, center). In a work of Rauscher et al. (2005b) it was demonstrated that phase images reconstructed with these methods already show excellent image contrasts and

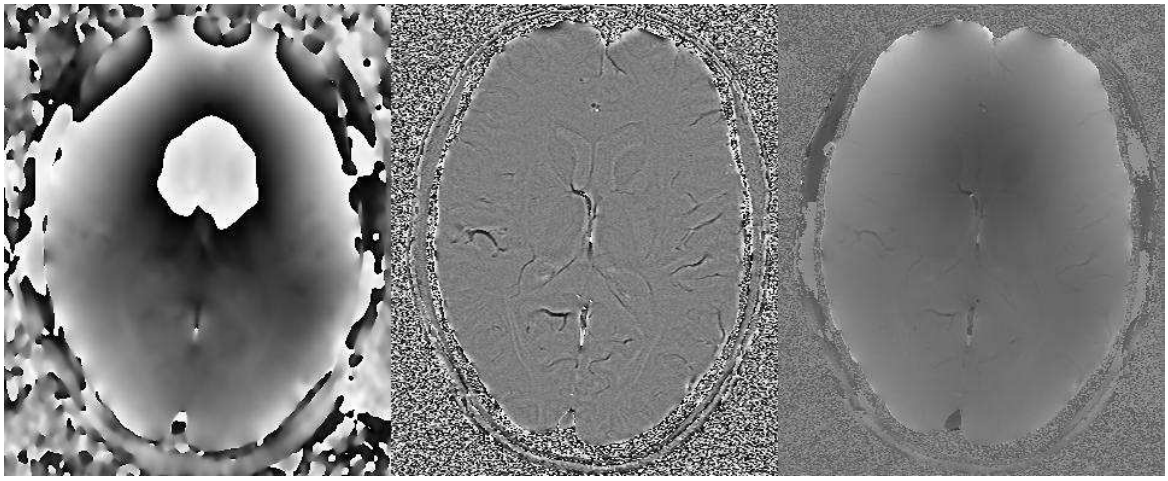

Figure 3.2: Left: *Phase of the low pass filtered complex image from Fig. 3.1.* **Middle:** *Homodyne filtered phase image obtained by complex division of the original and low pass filtered image.* **Right:** *Unwrapped phase image obtained by a region growing algorithm.*

revealed anatomic structures that were not visible on the corresponding magnitude images.

In SWI the magnitude and phase information is combined by a phase mask which is generated from the unwrapped and filtered phase data. For a transverse image orientation a negative phase mask is used. It weights phase values from -π to 0 linear from 0 to 1. All phase values larger than 0 are weighted with 1 and all values smaller than -π are set to 0 (Fig. 3.3, A). Due to the symmetrical field inhomogeneity around the vessel the phase has to be weighted with a positive or triangular phase mask for lateral image orientations to enhance the venous contrast (Fig. 3.3, B, C) (Reichenbach and Haacke, 2001). Recently Santiesteban et al. (2007) demonstrated that a sigmoid-type phase mask produces good results in both types of image orientation (Fig. 3.3, D).

Finally, the SWI data is computed by multiplication of the phase mask with the image magnitude. The phase mask can be multiplied several times to enhance the SWI contrast. Haacke et al. (2004) demonstrated that 4 multiplications result in an optimum contrast-to-noise ratio for small structures, like venous vessels.

To further visualize the SWI data, minimal intensity projections (mIPs) over several partitions of the 3D slab are computed. A vein which traverse the slab in an oblique orientation is imaged as a single dark spot in each slice which shifts from one slice to another. The mIP connects all these spots as a dark line in a final projection image. As it can be seen in the left and center image of Fig. 3.4, the mIP works quite well over thin slabs of SWI data. To compute the mIP over the whole measured slab, it is advantageous to process the SWI data with a median filter and subtract the filtered data from the original data. This eliminates all larger structures as the dark background as well as the ventricles. This method of median filtering prior to the mIP was first suggested

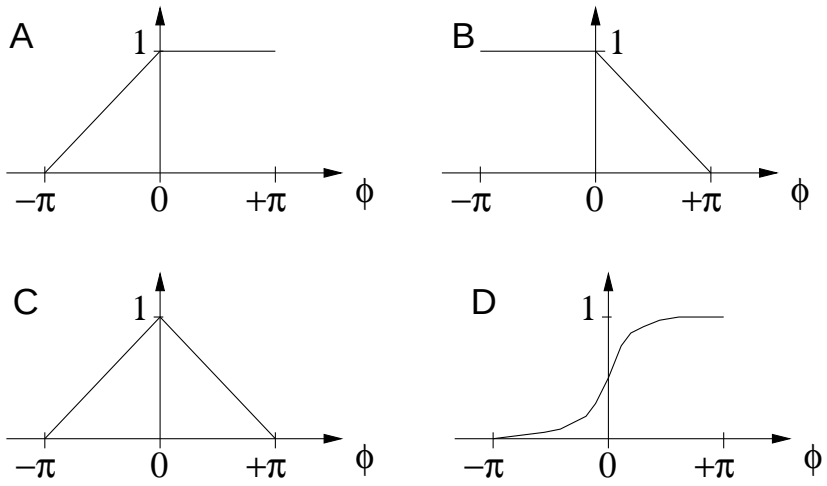

Figure 3.3: *A: negative phase mask as used regularly in transverse image orientation. B: positive and C: triangular phase mask which is used in lateral image orientations. D: sigmoid phase mask which yields good results in both image orientations.*

by Alexander et al. (2000) and applied to cerebral black blood MR angiographies. Kholmovski and Parker (2006) demonstrated the same procedure on SWI data with impressive results (Fig. 3.4, right).

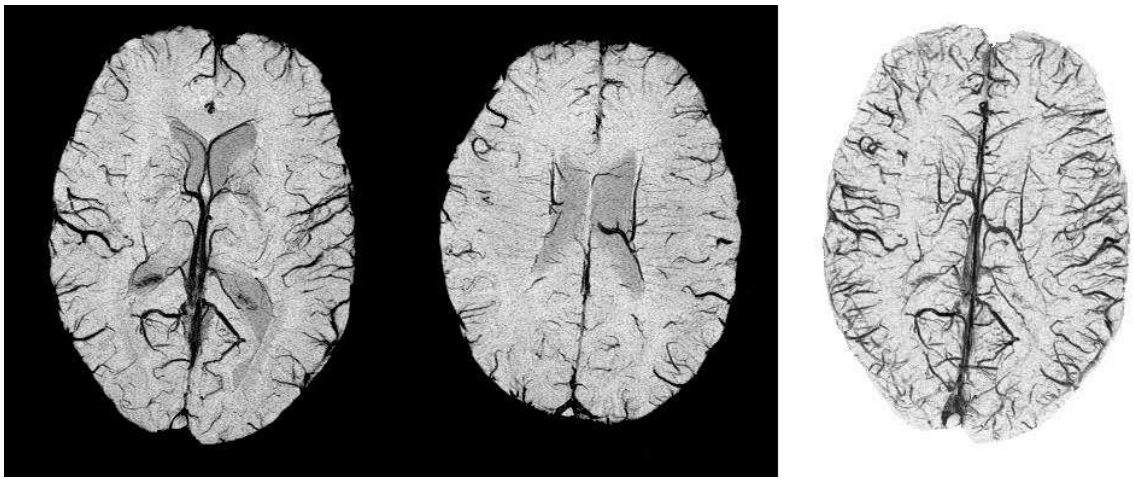

Figure 3.4: Left: *minimal value projection (mIP) over a 10 mm thick slab of SWI data.* **Middle:** *mIP over a 10 mm thick superior located slab.* **Right:** *mIP over a 50 mm thick slab of median filtered SWI data where lower and higher located venous vessels can be displayed in one image. Of note is the absence of the black background and the ventricles in the median filtered mIP.*

3.2. MR Sequences

The following section introduces the MR sequences applied in this work. They were implemented using a proprietary development software environment provided by the MR device manufacturer.

3.2.1. MR Scanners

All measurements where carried out on two MR scanners with different magnetic field strengths (B_0 = 1.5 and 3 T, Fig. 3.5). Both systems share the same sequence developing environment named IDEA (Integrated Integrated Development Environment for Applications).

Figure 3.5: Left: *Siemens MAGNETOM Sonata with 1.5 T main magnetic field.* **Right:** *Siemens Tim Trio with 3 T main magnetic field.*

3.2.2. Single Echo SWI

The SWI sequence is characterized by high spatial resolution, velocity compensation in all directions and a narrow bandwidth (see Sec. 3.1.1). As can be seen in Fig. 3.6, the velocity compensation is achieved by a gradient pair with opposite directions. These gradient pulse pairs are visible directly prior to the analog digital converter (ADC) event of the readout (x-gradient) and directly after the RF-pulse of the slab selection (z-gradient axis). The pulse pairs of the phase encoding (y-, z-gradient) are varying from each k-space line to another. The first gradient intensity steps from negative to positive, whereas the following gradient steps from positive to negative. The narrow bandwidth of the sampled signal is realized by a low but long readout gradient. The readout takes a relatively long time (in size of 10 ms) due to the high spatial resolution and low bandwidth. Residual transverse magnetization is eliminated by a spoiling gradient after the signal readout. The spoiling is carried out in just one direction, whereas

the stationary spins are rephased in both phase encoding directions (stepping y- and z-gradients after the ADC event). This procedure ensures equal signal dephasing of every k-space line which prevents possible image artifacts caused by stimulated echos. The repetition time is usually set to the shortest possible value directly after the spoiling and refocussing gradients; the flip angle to the corresponding Ernst angle of gray matter.

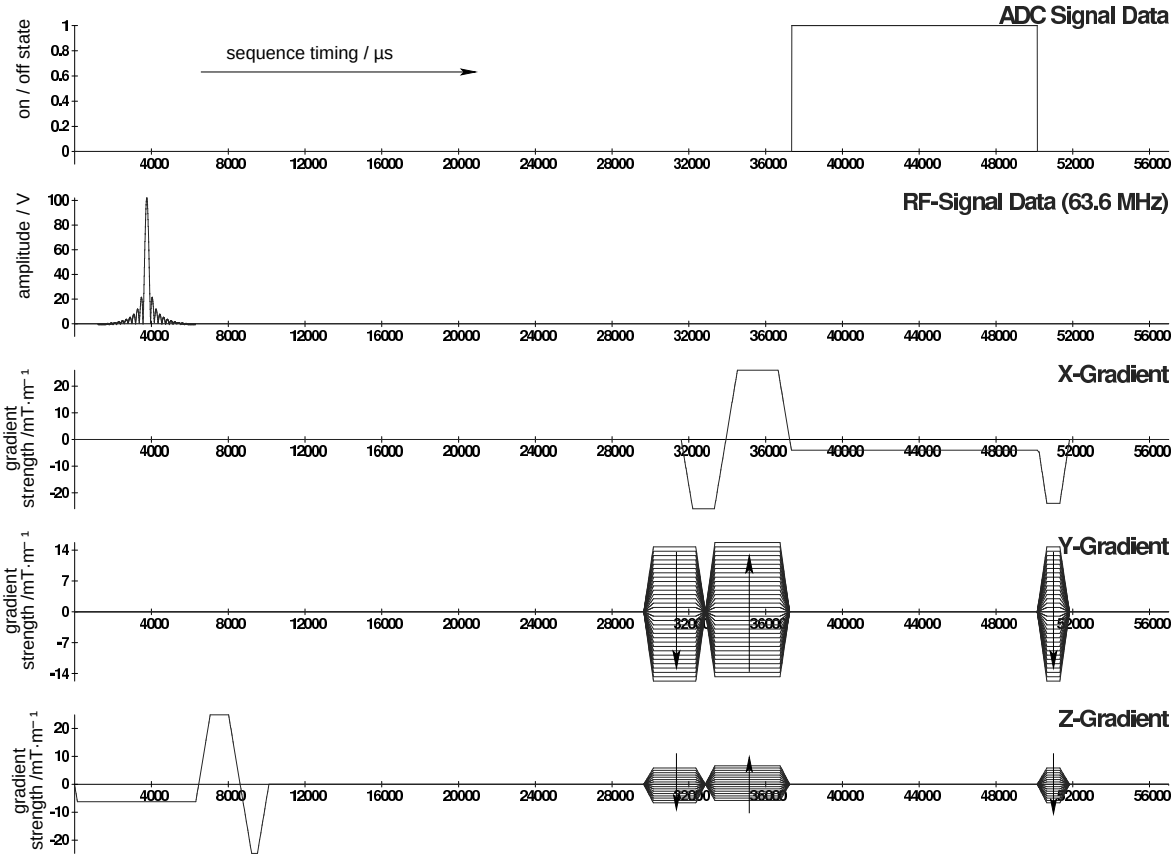

Figure 3.6: *Scheme of a fully velocity compensated SWI sequence with T_E = 40 ms, which is the optimum echo time for detecting venous vessels at 1.5 T (Reichenbach and Haacke, 2001). The repetition time was set to 57 ms with a flip angle of 20° which is close to the Ernst angle for gray matter at this particular T_R. Due to the high spatial resolution and narrow bandwidth (FOV/matrix = 256 mm/512 pixel and BW = 80 Hz/pixel) the readout gradient strength is low and the readout duration long. Note that the time line starts here at the beginning of the sequence, but the echo and repetition times are given relative to the center of the RF pulse.*

3.2.3. Multi Echo SWI

The multi echo SWI sequence is characterized by a monopolar readout train where the signal sampling is always performed during the same polarity of the readout gradients.

To achieve such a monopolar readout, the spins have to be rephased with short, high gradients between the readouts. A symmetrical position of this rephasing gradient pulse between the readouts ensures velocity compensation for each readout, if the echo of the first readout was compensated. Therefore, the rephasing and readout gradients act like the gradient pair necessary for velocity compensation (Bradley, 1988). The multi echo SWI sequence is also compensated for moving spins in slab selection direction. For velocity compensation in the phase encoding direction, the echo time T_E has to be considered. For an echo readout train with multiple echo times it is not feasible to compensate every single echo in the phase encoding direction. Thus, it was resigned to compensate for moving spins in the phase encoding directions. The implemented sequence has a fixed bandwidth of 390 Hz/pixel with aquire up to 32 echos. The shortest possible echo time spacing depends on the image resolution, i.e. selected FOV and matrix. Besides these limitations the echo spacing as well as the numbers of echos can be chosen freely. The shortest possible repetition time depends on the length of the readout train. An exemplary sequence scheme is shown in Fig. 3.7.

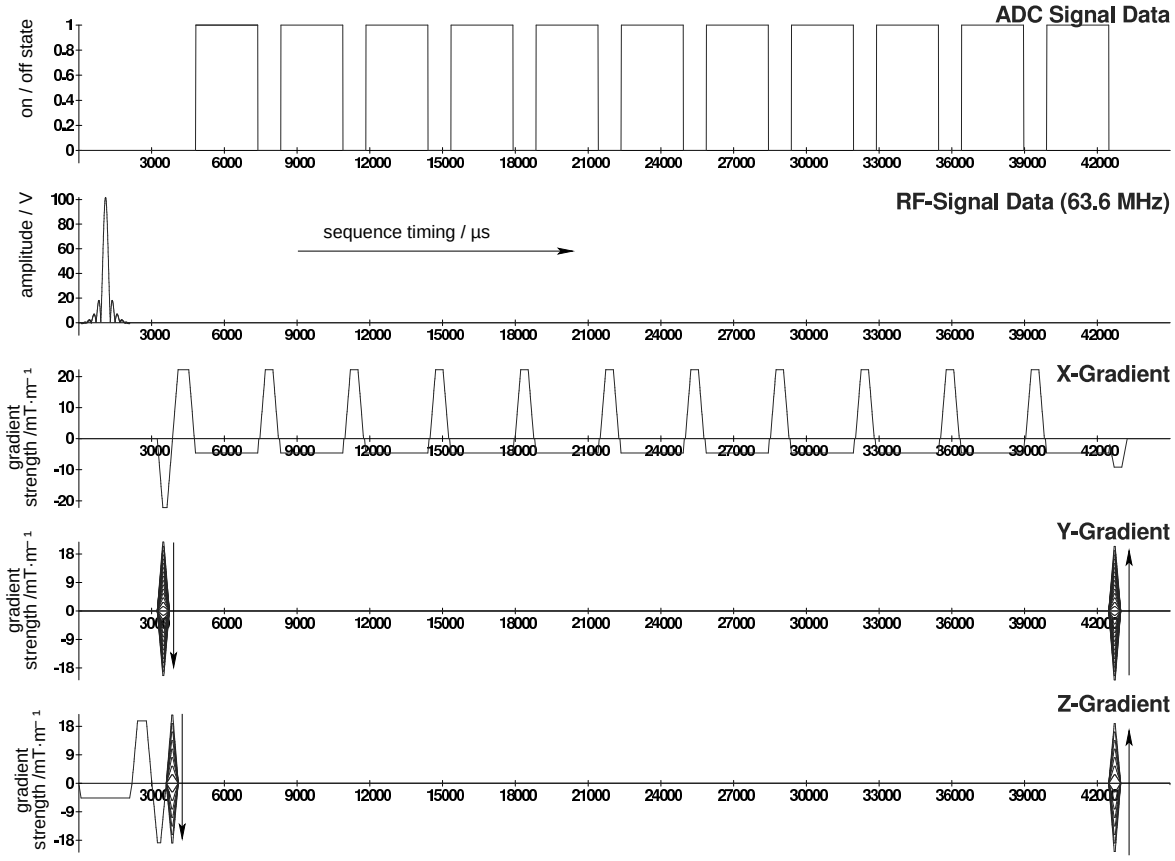

Figure 3.7: *Exemplary scheme of the implemented multi echo SWI sequence with 11 readouts at echo times ranging from $T_E = 5$ to 40 ms with an echo spacing of $\Delta T_E = 3.5$ ms. The repetition time was 45 ms, the flip angle 20° and the FOV 256 mm with a matrix of 128 pixel.*

3.2.4. Gradient Echo Sampled Spin Echo (GESSE)

A 2D-sequence which allows the sampling of the signal formation around a spin echo as proposed by Yablonskiy (1998), was also implemented on both MR systems. This sequence was designed to sample the signal only after the 180°-refocusing RF-pulse, which is characteristic for the so-called GESSE sequence. With some sequence modifications it is also possible to sample the signal decay directly after the excitation RF-pulse and around the spin echo after the 180°-refocusing RF-pulse. This sequence type is known in the literature under the acronym GESFIDE (gradient-echo sampling of FID and echo) (Ma and Wehrli, 1996). The sequence used here, acquires up to 32 echos after the 180°-refocusing RF-pulse with a monopolar readout train and adjustable bandwidth. The minimum possible echo spacing depends on the selected FOV, matrix and bandwidth. However, the number and timing of the gradient echos can be adjusted freely. The spin echo can be chosen independently of the gradient echo timing. This allows, for example, to have the spin echo between two gradient echos. An exemplary sequence scheme is shown in Fig. 3.8.

This sequence was not flow compensated, but it worked properly in phantoms without moving spins and also *in vivo* for the investigation of the blood capillary network, where the extravascular field inhomogeneities of the capillaries are induced in stationary brain tissue. The loss of signal inside the capillaries which is caused by moving spins of the blood is acceptable, because the network signal theory used in the present work neglects the intravascular signal contribution anyway.

An advantage of the GESSE approach is the possibility to isolate the irreversible signal decay from the reversible decay caused by static field inhomogeneities. Spins which are dephased due to static field inhomogeneities are rephased after the refocussing pulse and dephase again after the spin echo. Contrary to this, the irreversible spin-spin interaction is always present and dephases the spins before, during and after the spin echo. This makes it possible to determine both signal dephasing processes independently by an almost symmetrically sampled spin echo. Following these considerations the signal around a spin echo can be expressed as

$$S(t) = S_0 \cdot e^{-|t-T_{SE}|/T_2'} \cdot e^{-(t-T_{SE})/T_2} \tag{3.2}$$

where T_{SE} is the time of the spin echo. The term $(t-T_{SE})$ is the time with respect to T_{SE} and is negative before and positive after the spin echo. Therefore, the term $e^{-|t-T_{SE}|/T_2'}$ will be smaller than 1 at both sides of the echo, whereas the term $e^{-(t-T_{SE})/T_2}$ will give values larger than 1 before and smaller than 1 after the spin echo. Fitting Eq. 3.2 to the measured signal around the spin echo makes it possible to separately determine T_2 and T_2' and not conjuncted in a single T_2^* time (Eq. 2.26).

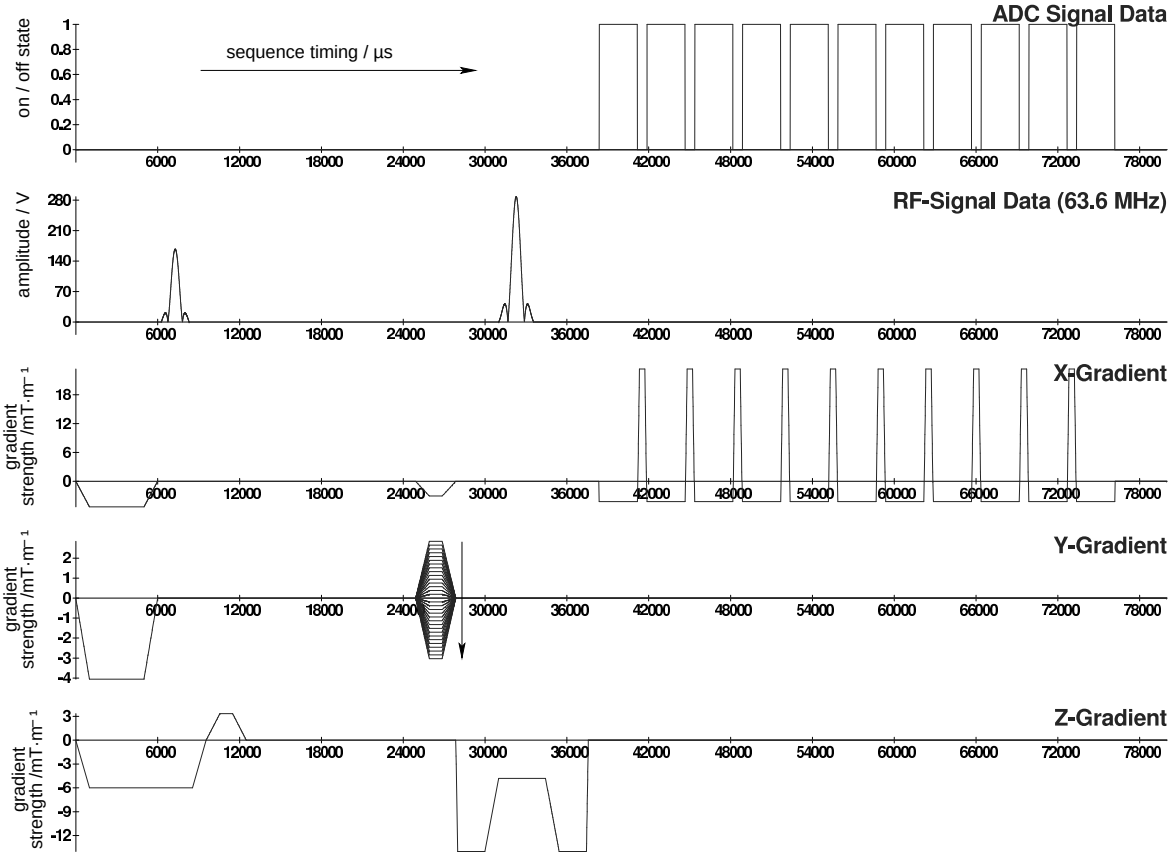

Figure 3.8: *Exemplary scheme of the implemented gradient echo sampled spin echo sequence (GESSE). The spin echo occurs here at $T_{SE} = 50$ ms which coincide with the sixth gradient echo. The gradient echo times range from $T_E = 32.5$ to 67.5 ms with an echo spacing of $\Delta T_E = 3.5$ ms. A FOV/matrix of 256 mm/128 pixel and a bandwidth of 390 Hz/pt was used. The flip angle was 90° and T_R 2000 ms.*

3.3. Single Capillaries and Veins

3.3.1. Numerical Simulation of a Single Cylinder

Since the analytical solution of a single cylinder is only valid for a cylindrical vessel inside and coaxial with a cylindrical voxel (Yablonskiy and Haacke, 1994; Ziener et al., 2005), a numerical simulation was performed to investigate the signal behavior for arbitrary voxel geometries as well as for glass tubes with a finite wall thickness (Fig. 3.9). Due to the two-dimensional nature of the cylinder model, simulations were performed on a 2D grid with a matrix size of about $2^{10} \times 2^{10}$ points. This array contained the field distribution inside and around the capillary as shown in Fig. 3.10 a.

To calculate the field distribution of this three-compartment model, the previously described single cylinder (Sec. 2.3.5.1) was extended by the capillary wall and it could be calculated accordingly to Bhagwandien et al. (1992). The external field of the single

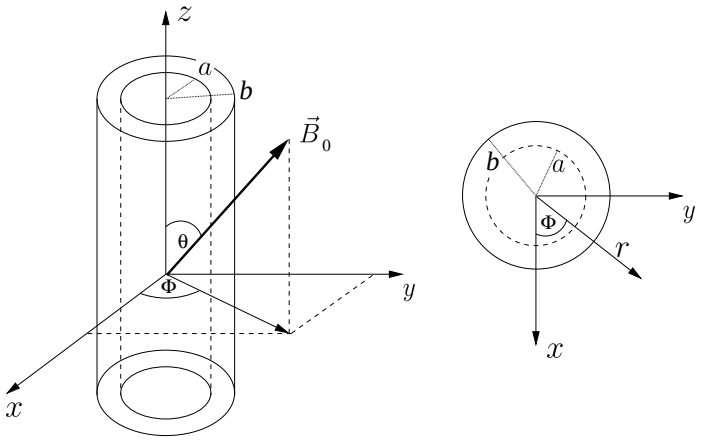

Figure 3.9: *Capillary with a finite capillary wall in an external magnetic field.*

cylinder (Eq. 2.71) turns for the cylinder model with a finite cylinder wall to:

$$\vec{B}_{ext} = \left\{ 1 + \frac{\chi_{ext}}{3} + \frac{1}{2}\sin^2\theta \cdot \frac{\cos 2\Phi}{r^2} \left[(\chi_{glass} - \chi_{int}) \cdot a^2 + (\chi_{ext} - \chi_{glass}) \cdot b^2 \right] \right\} \cdot \vec{B}_0 \quad \forall\, r > b \tag{3.3}$$

The parameters a and b denote the inner and outer radius of the capillary, respectively, and χ_{glass} is the magnetic susceptibility of the wall material. The internal magnetic field $\vec{B}_{int}$ is not affected by the capillary wall and is still calculated as in Eq. 2.72:

$$\vec{B}_{int} = \left\{ 1 + \frac{\chi_{ext}}{3} + \frac{\chi_{ext} - \chi_{int}}{6} \cdot (3\cos^2\theta - 1) \right\} \cdot \vec{B}_0 \quad \forall r < a. \tag{3.4}$$

The magnetic field $\vec{B}_{glass}$ between the inner and outer compartment of the capillary can be calculated as

$$\vec{B}_{glass} = \left\{ 1 + \frac{\chi_{ext}}{3} + \frac{\chi_{ext} - \chi_{glass}}{6} \cdot (3cos^2\theta - 1) + \frac{\chi_{glass} - \chi_{int}}{2} \cdot \sin^2\theta \cdot a^2 \frac{\cos 2\Phi}{r^2} \right\} \cdot \vec{B}_0$$

$$\forall\, a < r < b\,. \tag{3.5}$$

Since the glass material does not produce any measurable signal in conventional MRI, the field distribution in this compartment was neglected.

In consequence of the finite and discrete sampling in MR imaging, the sampling point spread function (sPSF) (Sec. 2.2.4.2) has to be taken into account for signal simulation. Due to the sPSF, the signal from spins located beyond the voxel boundary contributes to the signal of the voxel in the image. To test the influence of different voxel geometries, they were investigated by multiplying the simulation array with a weighting function according to the desired voxel shape, as shown in Fig. 3.10 b-d.

For a given echo time T_E each matrix point represents the complex signal of a very small spin packet with its own local phase which is determined by the local field strength. Its magnitude is determined by the spin density and T_2 decay. The complex values of each

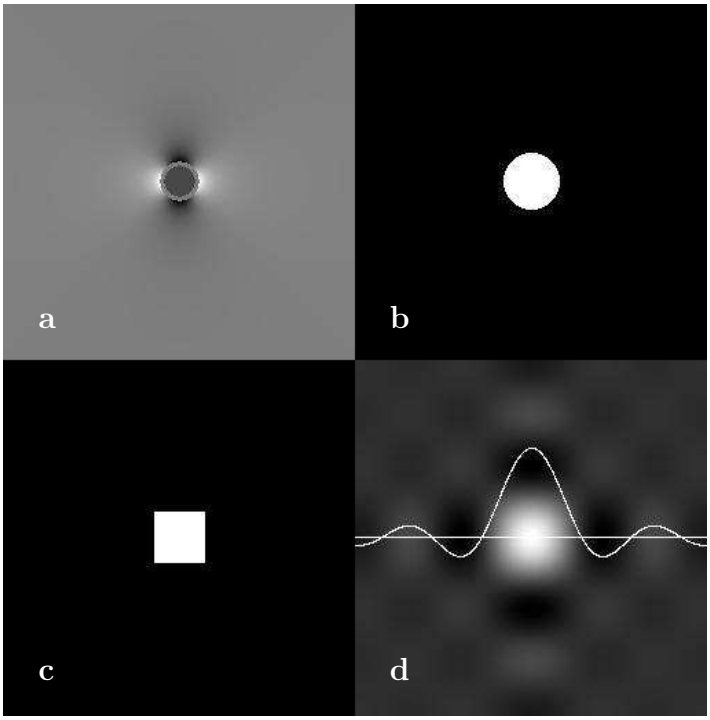

Figure 3.10: a: *Simulated field distribution of the glass tube filled with paramagnetic aqueous solution.* **b**: *Weighting function to simulate a cylindrical voxel shape with* $\lambda = 0.3$ *and* **c**: *a square voxel with the same volume fraction. Black in* **b** *and* **c** *denotes the weighting value zero.* **d**: *Weighting function of the square voxel with consideration of the sampling point spread function (sPSF), again with the same volume fraction. A horizontal profile of the sPSF is plotted along the center line of the array (straight white line). This line also represents the zero-line of the plotted sPSF profile. Note, that the nearest neighborhood of the voxel adds negative fractions to the voxel signal. The influence of the sPSF is taken into account for an area of* 7×7 *times the original square voxel size.*

matrix element were added for a given echo time T_E. Due to the complex nature of the signal, constructive and destructive interference between the spin packets occur as a function of echo time, leading to a signal behavior that reflects the physical properties of the vessel-voxel combination.

The signal of the voxel containing the magnetized cylinder can be expressed mathematically as:

$$S(t) = \int_{\vec{r}} W(\vec{r}) \cdot S_0(\vec{r}) \cdot e^{-i \cdot \gamma \Delta B(\vec{r}) \cdot t} e^{-t/T_2(\vec{r})} \mathrm{d}\vec{r}, \tag{3.6}$$

where the weighting function $W(\vec{r})$ describes the different voxel shapes which are displayed in Fig. 3.10 b-d. The field distribution of the magnetized cylinder $\Delta B(\vec{r})$ is shown in Fig. 3.10 a. The basic signal fraction $S_0(\vec{r})$ of each point in the measured volume depends on its local spin density as well as the T_1 relaxation time and the

repetition time T_R of the MR measurement.

For comparing the results of the numerical simulation with the analytical solution of the single cylinder (Eq. 2.74) as proposed by Yablonskiy and Haacke (1994) the thickness of the capillary wall was set to zero. To compare the simulation with measured signals of the single capillary phantom used in this work, wall thickness of the cylinder was set to the thickness of the used glass tube. This allows a sufficient consideration of the influenced surrounding field inhomogeneity by the glass material. However, the signal contribution of the glass itself was set to zero, because, as already mentioned, it gives no measurable signal in MRI.

To plot the local signal fractions as a function of their resonance frequency shift ($\Delta\omega = \gamma\Delta B$) the Fourier transform of the signal given in Eq. 3.6 was calculated under the assumptions of vanishing transverse relaxation ($R_2(\vec{r}) = 0$), infinitely thin capillary wall and $S_0(\vec{r}) = 1$:

$$S(\Delta\omega) = \mathsf{FT}\Big\{S(t)\Big\} = \mathsf{FT}\Bigg\{\int_{\vec{r}} W(\vec{r}) \cdot e^{-i\cdot\gamma\Delta B(\vec{r})\cdot t}\mathrm{d}\vec{r}\Bigg\}. \tag{3.7}$$

The real part of $S(\Delta\omega)$ corresponds to the absorption spectra shown in Results (Fig. 4.1 b and c), where the negative signal fractions in the spectra of sPSF voxel near the Larmor frequency originate from the first negative lobes of the sPSF near the magnetized cylinder.

3.3.2. Data Reconstruction and Evaluation

3.3.2.1. Subvoxel Shift

The analytical solution as well as the numerical simulation of the signal decay used in this work assume that the cylinder is located in the center of the voxel. To ensure that this was the case, subvoxel shifts were applied by phase gradients in the measured k-space using the Fourier shift theorem (Barrett and Myers, 2004) for all phantom and *in vivo* measurements. The step size of these shifts was about 5% of the voxel width and the steps were repeated until the symmetry of phase and magnitude in the neighboring voxels indicated that the vessel was located at the center of the investigated voxel (Fig. 3.11).

The influence on the signal of a single voxel with a magnetized cylinder in off-center position was simulated for $\lambda = 0.3$, $\Delta\chi = 1\,\mathrm{ppm}$, $S_{0,\,ext} = 1$, $T_{2,\,ext} = 1000\,\mathrm{ms}$, $S_{0,\,int} = 1.8$ and $T_{2,\,int} = 70\,\mathrm{ms}$. The cylinder was shifted successively from the center to off-center in steps of 5% voxel width (Results shown in Fig. 4.8).

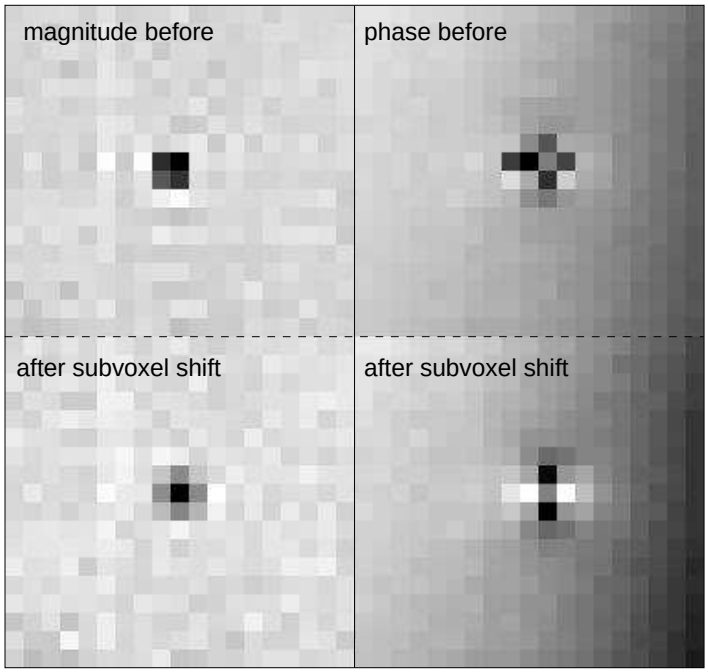

Figure 3.11: *Magnitude and phase images of the capillary phantom before and after adding phase gradients in k-space to obtain intravoxel shifts which map the capillary in the voxel center.*

3.3.2.2. Fitting Routine

The signal magnitude of the voxel containing the capillary was plotted as a function of echo time T_E. The numerical simulation (Eq. 2.81) of the signal behavior for the sPSF voxel was fitted to the measured curves for the single vessel experiments by employing the IDL fitting routine *CURVEFIT*. It uses a gradient-expansion algorithm to compute a non-linear least squares fit to the user-supplied functions, i.e. the numerical single cylinder simulation. If the partial derivatives of this user-function can not be calculated analytically, they are approximated numerically by the *CURVEFIT* routine. Iterations of the fitting routine were performed until the root mean square error (MSE) is minimized, or until a maximum number of iterations has been performed.

Signal noise was estimated for each T_E by the standard deviation of a region of interest (ROI) in a homogeneous area near the evaluated voxels. This noise estimation procedure is valid since a Gaussian signal distribution can be assumed for signal to noise ratios (SNR) greater than two (Gudbjartsson and Patz, 1995). The SNR in these homogeneous regions was always larger than 2 for all measurements, also at late echo times.

All simulations, image reconstruction and post processing were computed using self-written software with IDL (Interactive Data Language, ITT visual systems, Boulder, CO, U.S.A.).

3.3.3. Single Capillary Phantom

A glass capillary (length: 50 mm, outer diameter = 1 mm, inner diameter = 0.79 mm) was mounted on a pivotable holder inside a hemispherical glass bowl. The bowl was

filled with three liters of standard physiological NaCl solution. The glass consisted of 69 % SiO_2, 17 % Na_2O, 7 % CaO and 7 % other ingredients which were not further specified (*www.hilgenberg-gmbh.de*, glass *no. 140*).

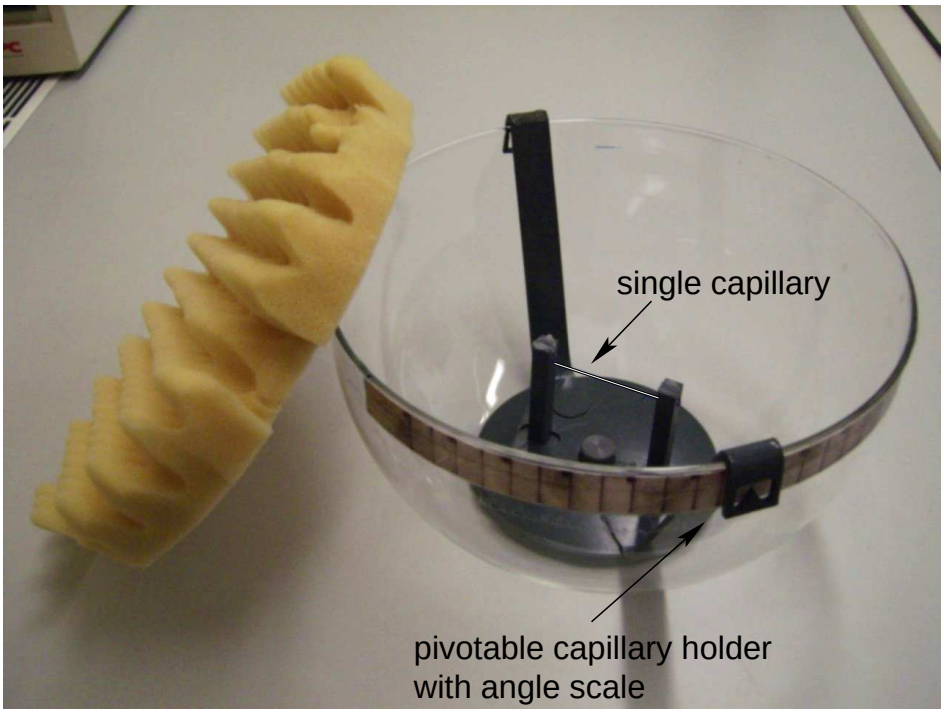

Figure 3.12: *Capillary phantom construction where the single capillary was mounted on a pivotable sample holder. The bowl was filled with aqueous solution and covered with foamed material to slow down the water movement which is induced during phantom positioning inside the scanner.*

The differences in magnetic susceptibility between the glass material and the outer solution were minimized by adding Gd-DTPA (gadolinium diethylenetriamine pentaacetic acid) to the outer solution. The field distribution caused by the glass material only was observed using high resolution phase imaging (Rauscher et al., 2005b). With 1.6 mM Gd-DTPA concentration in the surrounding aqueous solution the local field inhomogeneities induced by the glass vanished. Since the molar susceptibility of Gd-DTPA, $\chi_{M,Gd-DTPA} = 4\pi \cdot (0.027 \pm 0.001)\,\frac{\text{ppm}}{\text{mM}}$ (Weisskoff and Kiihne, 1992), and the susceptibility of water, $\chi_{H_2O} = -4\pi \cdot 0.72\,\text{ppm}$ (Gupta, 1986) are known, a magnetic susceptibility of -8.5 ppm was estimated for the glass material.

The 1.6 mM Gd-DTPA concentration for the outer solution was also used for the subsequent phantom experiments. As this concentration results in a relative short T_1 relaxation time of about 136 ms at 1.5 T (Reichenbach et al., 1997a), additional experiments were performed using a Gd-DTPA concentration of 0.2 mM with T_1 of about 1 sec.

Different levels of Y were mimicked by adjusting the susceptibility difference between the intra- and extracapillary compartment. For the experiments with 1.6 mM Gd-DTPA

concentration of the outer solution the inner compartment contained 3 and 4 mM Gd-DTPA yielding susceptibility differences of 0.48 ppm and 0.82 ppm, respectively. For the experiments with a concentration of 0.2 mM Gd-DTPA in the outer solution, 2 and 3 mM Gd-DTPA concentrations were used in the inner solution, resulting in susceptibility differences of $\Delta\chi = 0.61$ ppm and $\Delta\chi = 0.95$ ppm, respectively.

The phantom experiments were performed at room temperature for three different volume fractions ($\lambda = 0.1, 0.2, 0.3$) and three different orientations between the main magnetic field and the capillary axis: $\theta = 0\,^\circ$ (parallel), $55\,^\circ$ (magic angle) and $90\,^\circ$ (perpendicular). These measurements were carried out at $B_0 = 1.5$ T and at 3 T. For $B_0 = 1.5$ T both Gd-DTPA concentrations of the surrounding solution (0.2 mM and 1.6 mM) were measured, whereas at $B_0 = 3$ T only the 0.2 mM Gd-DTPA solution was used. Overall, 54 different phantom measurements were conducted.

3.3.4. Parameters of Phantom and In Vivo Measurements

The multi echo SWI sequence as introduced in Sec. 3.2.3 was used on the 1.5 T MR system (Magnetom Sonata, Siemens, Erlangen, Germany) with the following imaging parameters: $T_R = 110$ ms, $T_E = 5 - 100$ ms, $\Delta T_E = 5$ ms, bandwidth $= 390\,\frac{\text{Hz}}{\text{pixel}}$ and 4 averages. The dimension of the acquisition matrix was 128 and the field of view (FOV) was 283 mm for $\lambda = 0.1$, 200 mm for $\lambda = 0.2$ and 164 mm for $\lambda = 0.3$. The 3D slab was always oriented perpendicular to the capillary and partitioned into 16 slices each of 3 mm thickness.

On the 3 T system, phantom measurements were carried out only for the 0.2 mM Gd-DTPA concentration of the surrounding solution. No *in vivo* measurements were performed at 3 T. The multi echo SWI sequence was measured twice with an echo time distance of $\Delta T_E = 4$ ms. The second measurement was applied with a shifted echo train of 2 ms. Thus, an inter echo time distance of 2 ms was achieved.

Data from three healthy male volunteers (mean age: 25 y) were acquired on the 1.5 T MR system during normoxia. The venous vascular architecture was visualized using the single echo SWI sequence as introduced in Sec. 3.2.2. The measuring parameters were $T_R = 57$ ms, flip angle 20°, $T_E = 40$ ms and bandwidth $= 80\,\frac{\text{Hz}}{\text{pixel}}$. The dimension of the acquisition matrix was $512 \times 256 \times 40$ and the field of view (FOV) $256 \times 192 \times 80\,\text{mm}^3$. The image data was interpolated by zero filling during image reconstruction to voxel sizes of $0.5 \times 0.5 \times 1\,\text{mm}^3$. Finally, the SWI data was computed as described in Sec. 3.1.2 applying a homodyne phase filter and negative phase mask. For the multi-echo acquisition, the same echo and repetition times were used as in the phantom measurements. The imaging slab was always oriented perpendicular to the investigated veins, e.g. transverse for parallel and coronal for blood vessels oriented perpendicular to $\vec{B}_0$, with a matrix size of 128 and a square FOV of 192 mm. Immediately after the

measurement, a blood sample was drawn from each individual and the hematocrit was determined in the local clinical laboratory.

Changes in blood oxygenation induced by carbogen (5 %CO_2, 95 %O_2) breathing were investigated. Since carbogen increases the cerebral blood flow (CBF) (Watson et al., 2000), it also leads to increased venous blood oxygenation (Rauscher et al., 2005a). Data from a healthy 23 year old female volunteer were acquired using the multi echo SWI sequence with echo times ranging from 4 ms to 172 ms and an echo distance of 7 ms. Air was applied first followed by carbogen using a continuous positive airway pressure system (CPAP - CF 800, Dräger Medical, Lübeck, Germany) with a gas flow rate of about 25 L/min. During the measurement the arterial oxygen saturation, the pulse rate, the inspired and expired oxygen concentration as well as the breathing rate were monitored. The venous architecture was visualized with SWI. One parallel and one perpendicular cerebral venous vessel were chosen for investigation at each breathing condition.

Further *in vivo* experiments were carried out while the CBF and, thus, the venous blood oxygenation were changed due to the ingestion of caffeine. Caffeine acts as an adenosine antagonist and inhibits the A_{2A} receptors (Ongini and Fredholm, 1996). The consequence of this inhibition is a vasoconstriction of cerebral vessels (Nehlig et al., 1992; Meno et al., 2005) and therefore a decrease in CBF (Cameron et al., 1990; Field et al., 2003; Lunt et al., 2004). The decreased CBF causes a lower venous blood oxygenation which was quantified using the multi echo SWI technique.

Caffeine is a widely used neuronal stimulant which is naturally available and mainly consumed in the form of coffee and tea. Caffeine absorption from the gastrointestinal tract is rapid and reaches nearly 100% in humans in about 45 min after ingestion (Fredholm et al., 1999). Therefore, the volunteer, a 26 year old female, was measured first under a native condition as described for the carbogen experiment. Afterwards, 200 mg caffeine, dissolved in 0.1 L water, was ingested orally (Coffeinum N 0,2 g; Merck dura GmbH, Darmstadt, Germany) containing 200 mg caffeine. After 45 min the measurements of the same veins were repeated.

All subjects had given written informed consent prior to the study and the protocols had been approved by the local ethics committee.

For each measurement in this study, macroscopic inhomogeneities were minimized by careful local shimming of a region around the voxel of interest. This region was much larger than the voxel size, but smaller as the phantom or the subject's head.

The influence of macroscopic field gradients was investigated by a single capillary phantom measurement where a linear field gradient was applied by changing the shim currents of one shim coil. The signal influenced by such a background field gradient was observed for the single voxel with the capillary as well as for a bigger voxel (Fig. 4.9).

3.4. Capillary Network

3.4.1. Statistical Averaging of Cylinders

The equations and calculations presented in Sec. 2.3.6 are based on statistical averaging over the effects of the cylinders which further explicated in the following considerations. The following equations for statistical averaged cylinders were derived with reference to Yablonskiy and Haacke (1994); Kiselev and Posse (1998). Each cylinder creates a frequency offset $\omega(r, \Phi, \theta)$ due to its external field

$$\omega(r, \Phi, \theta) = \delta\omega_\theta \cdot a^2 \frac{\cos(2\Phi)}{r^2} \quad \forall r > a \tag{3.8}$$

with $\delta\omega_\theta$ given in Eq. 2.77. The signal calculation of the capillary network is based on a model of N uniformly distributed and isotropically oriented cylinders. The total signal S_{ext} can be expressed by multiplying the averaged effect of each single cylinder $\langle\Psi_n\rangle$ to the extravascular signal:

$$S_{ext} = (1 - \lambda) \cdot S_{ext,0} \cdot e^{-t/T_{2,ext}} \cdot \prod_{n=1}^{N} \langle\Psi_n\rangle. \tag{3.9}$$

Here the index n runs over all cylinders N. The average effect of each single cylinder on the extravascular signal $\langle\Psi_n\rangle$ is calculated by integration over the cylinder orientation θ with an isotropic distribution function of $(\sin\theta)/2$. The cylinder position is calculated by the integration over Φ and r with an uniform distribution function of $1/(A - \pi a^2)$. A is the cross-sectional area of the measurement volume perpendicular to the cylinder axis and πa^2 is the circular area of the cylinder. The region $r < a$ is excluded for the calculation of the extravascular signal.

$$\langle\Psi_n\rangle = \int_0^\pi \mathrm{d}\theta \frac{\sin\theta}{2} \int_0^{2\pi} \mathrm{d}\Phi \int_a^\infty \mathrm{d}r \frac{r}{A} \cdot e^{-i\cdot\omega(r,\Phi,\theta)\cdot t}. \tag{3.10}$$

Eq. 3.10 can be transformed to

$$\langle\Psi_n\rangle = 1 - \frac{\pi a^2}{A} \int_0^\pi \mathrm{d}\theta \frac{\sin\theta}{2} \int_0^{2\pi} \mathrm{d}\Phi \int_a^\infty \mathrm{d}r \frac{r}{\pi a^2} \cdot \left(1 - e^{-i\cdot\omega(r,\Phi,\theta)\cdot t}\right) \tag{3.11}$$

by substituting $e^{-i\cdot\omega(r,\Phi,\theta)\cdot t}$ with $1 - (1 - e^{-i\cdot\omega(r,\Phi,\theta)\cdot t})$. The volume fraction of a single vessel on the whole volume $\pi a^2/A$ is very small and, therefore, Eq. 3.11 is about 1:

$$1 - \frac{\pi a^2}{A} \int_0^\pi \mathrm{d}\theta \frac{\sin\theta}{2} \int_0^{2\pi} \mathrm{d}\Phi \int_a^\infty \mathrm{d}r \frac{r}{\pi a^2} \cdot \left(1 - e^{-i\cdot\omega(r,\Phi,\theta)\cdot t}\right) \approx 1. \tag{3.12}$$

Thus, Eq. 3.12 can also be expressed as an exponential function

$$\exp\left[-\frac{\pi a^2}{A}\int_0^{\pi}\mathrm{d}\theta\frac{\sin\theta}{2}\int_0^{2\pi}\mathrm{d}\Phi\int_a^{\infty}\mathrm{d}r\frac{r}{\pi a^2}\cdot\left(1-e^{-i\cdot\omega(r,\Phi,\theta)\cdot t}\right)\right]\approx 1. \tag{3.13}$$

Substituting Eq. 3.13 in Eq. 3.9 and calculating the product results in the following signal equation

$$\ln\left[\frac{S_{ext}}{(1-\lambda)\cdot S_{ext,0}\cdot e^{-t/T_{2,ext}}}\right]=-\lambda\int_0^{\pi}\mathrm{d}\theta\frac{\sin\theta}{2}\int_0^{2\pi}\mathrm{d}\Phi\int_a^{\infty}\mathrm{d}r\frac{r}{\pi a^2}\cdot\left(1-e^{-i\cdot\omega(r,\Phi,\theta)\cdot t}\right), \tag{3.14}$$

where $\lambda = \pi a^2 N/A$ is the volume fraction occupied by all cylinders. For a proper numerical integration the substitution

$$u=\frac{a^2}{r^2} \tag{3.15}$$

with its according differential

$$\mathrm{d}r=-\frac{r^3}{2a^2}\mathrm{d}u\,. \tag{3.16}$$

changes the upper and lower limit of $r=\infty \Rightarrow x=0$ and $r=R \Rightarrow x=1$. Applying this substitution to Eq.3.14 gives

$$\ln\left[\frac{S_{ext}}{(1-\lambda)\cdot S_{ext,0}\cdot e^{-t/T_{2,ext}}}\right]=-\lambda\int_0^{\pi}\mathrm{d}\theta\frac{\sin\theta}{2}\int_0^{2\pi}\mathrm{d}\Phi\int_1^{0}\frac{r^3}{-2a^2}\mathrm{d}u\frac{r}{\pi a^2}\cdot\left(1-e^{-i\cdot\omega(r,\Phi,\theta)\cdot t}\right) \tag{3.17}$$

and back substitution of $r^4=a^4/u^2$ yields

$$\ln\left[\frac{S_{ext}}{(1-\lambda)\cdot S_{ext,0}\cdot e^{-t/T_{2,ext}}}\right]=-\lambda\int_0^{\pi}\mathrm{d}\theta\frac{\sin\theta}{2}\int_0^{2\pi}\mathrm{d}\Phi\int_0^{1}\mathrm{d}u\frac{1}{2\pi u^2}\cdot\left(1-e^{-i\cdot\omega(r,\Phi,\theta)\cdot t}\right). \tag{3.18}$$

The integrals of this signal equation were further simplified by Yablonskiy and Haacke (1994) as given in Sec. 2.3.6 Eq. 2.81 which allows a much faster numerical integration. Thus, only Eq. 2.81 was used for all capillary network signal simulations in the present work, except for the model of mutual avoiding cylinders.

3.4.1.1. Model of Mutual Avoiding Cylinders

The concept of mutual avoiding cylinders for describing the MR signal of the cerebral blood capillary network was first proposed by Kiselev (2004), who applied this theory to MR diffusion measurements. In this section the model of mutual avoiding cylinders, derived from Kiselev (2004), is developed to simulate the signal dephasing in a microvascular network without diffusion.

To describe the effect of mutual avoiding cylinders we considered randomly distributed cylinders as shown in Fig. 3.13 A for the cross-sectional view of a simple 2D case of parallel cylinders. The cross-sectional area is then subdivided in small squares with the area of ϵ as shown in Fig. 3.13 B. The stochastic vessel positioning can be achieved by random and independent occupation of these squares. The probability for a cylinder occupying a square is p. Empty squares do not have an effect on the signal formation and thus contribute only a factor of unity. Eq. 3.9 can now be written as

$$S_{ext} = (1-\lambda) \cdot S_{ext,0} \cdot e^{-t/T_{2,ext}} \cdot \prod_{m=1}^{M} \left[(1-p) + p\Psi_m\right]. \tag{3.19}$$

Here the index m is counting over all squares M, with $1-p$ being the probability of the square to be empty and p being the probability to contain a cylinder. The effect on the extravascular signal of a single cylinder m is denoted as $\Psi_m = e^{-i\cdot\omega_m\cdot t}$. The construction of occupied or empty squares eliminates the occurrence of coinciding cylinders, but still allows a possible crossing of non-parallel cylinders.

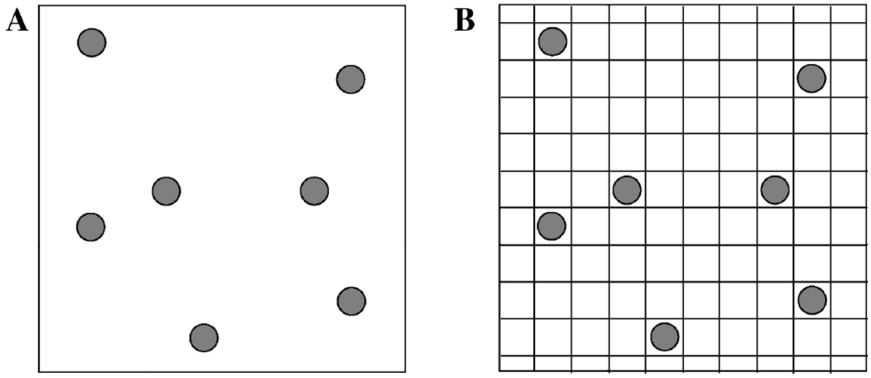

Figure 3.13: *Model of mutual avoiding cylinders for the simplified case of a parallel arrangement. The random distribution of the cylinders (circles) in* **A** *is assumed as random occupation of defined small squares with the area* ϵ *(***B***). (Figure adapted from Kiselev (2004))*

The product in Eq. 3.19 can be transformed in a sum taking the logarithm of both sides:

$$\ln\left[\frac{S_{ext}}{(1-\lambda)\cdot S_{ext,0}\cdot e^{-t/T_{2,ext}}}\right] = \sum_{m=1}^{M} \ln\left[1 - p\cdot(1-\Psi_m)\right]. \tag{3.20}$$

To take random cylinder orientations into account, the angular dimension θ has to be added. The sum has to be calculated for each orientation angle and the occupation probability p has to be reduced according to the increased number of available orientations. This results in the same signal equation as in Eq. 3.20, but the counter m will now step over all in-plane positions as well as orientations.

The sum over m can be replaced by an integration over θ and the polar coordinates Φ and r. This results in a signal equation similar to Eq. 3.14:

$$\ln\left[\frac{S_{ext}}{(1-\lambda)\cdot S_{ext,0}\cdot e^{-t/T_{2,ext}}}\right] = \int_0^{\pi} \mathrm{d}\theta \frac{\sin\theta}{2} \int_0^{2\pi} \mathrm{d}\Phi \int_a^{\infty} \mathrm{d}r \frac{r}{\epsilon} \cdot \ln\left[1 - p\cdot\left(1 - e^{-i\cdot\omega(r,\Phi,\theta)\cdot t}\right)\right], \tag{3.21}$$

The model parameters p and ϵ are related to the volume fraction with $\lambda = pz$ and $z = \pi a^2/\epsilon$. This consideration can easily be understood by the fact that the whole cross-sectional area is $A = \epsilon \cdot M$ and that the square and cylinder numbers are connected due to the probability with $N = p \cdot M$. By substituting $p = \lambda/z$ and $\epsilon = \pi a^2/z$ in Eq. 3.21 yields

$$\ln\left[\frac{S_{ext}}{(1-\lambda)\cdot S_{ext,0}\cdot e^{-t/T_{2,ext}}}\right] = z\int_0^{\pi} \mathrm{d}\theta \frac{\sin\theta}{2} \int_0^{2\pi} \mathrm{d}\Phi \int_a^{\infty} \mathrm{d}r \frac{r}{\pi a^2} \cdot \ln\left[1 - \frac{\lambda}{z}\cdot\left(1 - e^{-i\cdot\omega(r,\Phi,\theta)\cdot t}\right)\right]. \tag{3.22}$$

Applying the substitution from Eq. 3.15 and 3.16 gives

$$\ln\left[\frac{S_{ext}}{(1-\lambda)\cdot S_{ext,0}\cdot e^{-t/T_{2,ext}}}\right] = z\int_0^{\pi} \mathrm{d}\theta \frac{\sin\theta}{2} \int_0^{2\pi} \mathrm{d}\Phi \int_0^{1} \mathrm{d}u \frac{1}{2\pi u^2} \cdot \ln\left[1 - \frac{\lambda}{z}\cdot\left(1 - e^{-i\cdot\omega(r,\Phi,\theta)\cdot t}\right)\right]. \tag{3.23}$$

The integrals in Eq. 3.23 and Eq. 3.18 as well as Eq. 2.78 and Eq. 2.82 were solved in IDL by the numerical integration using the *QROMO* function. This function evaluates the integral over the open interval (A, B) using a modified Romberg's method (Press et al., 1992). The multidimensional integral was solved by nesting the *QROMO* function.

3.4.2. Construction of Capillary Network Phantom

The capillary network phantom was build by applying spherical geometries which prevent distortions of the magnetic field inside the probe. The edges, for instance, of cubed phantom geometry will cause such macroscopic field inhomogeneities which definitely compromise the quality of such phantom experiments. Different capillary diameters were investigated to prove the theory's prediction of an MR-signal which is insensitive on the vessel diameter distribution if the effect of diffusion can be neglected.

Polypropylene (PP) strings (G. KRAHMER GmbH, Buchholz, Germany) with different diameters and lengths were randomly coiled and put into separated hollow plastic spheres (Fig. 3.14). The spheres had an inner diameter of 4.8 mm and, thus, a volume

of 58 ml. The volume fraction occupied by the strings is the ration between the total volume of the strings and the volume of the sphere (Tab. 3.1). The volume of the strings was calculated by the known diameter and length of each string, but also determined by immersing the whole string network into ethanol and measuring the displaced volume.

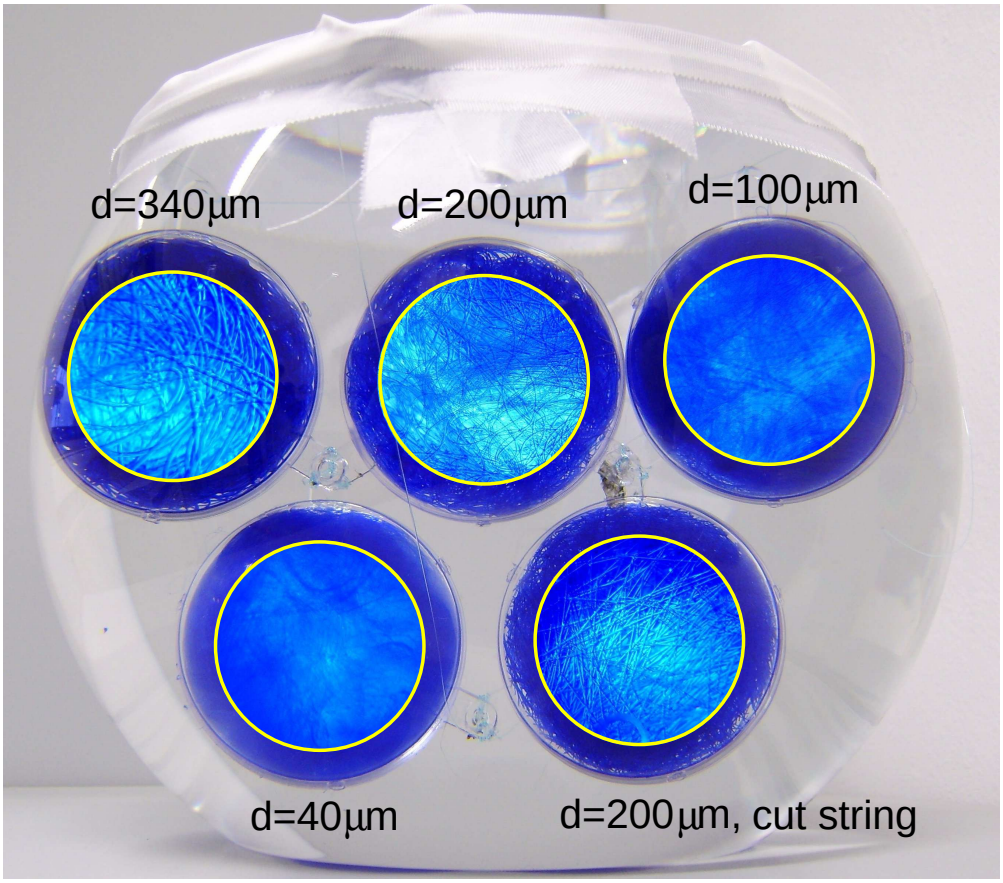

Figure 3.14: *Construction of the string network phantom. The spherical compartments contain randomly coiled polypropylene strings with different diameters. An enlarged view of the string network in each sphere is shown. The whole phantom is filled with 5 L silicone oil which totally wet the strings without leaving residual air bubbles inside the network.*

Another $\varnothing = 200\,\mu$m string was cut into pieces with 5 to 15 mm length which were put into an additional sphere (Fig. 3.14, lower right). This string compartment was used to verify whether or not the preparation of the capillary network had any influence on the measured signal.

Silicone oil was used to fill the phantom. It was chosen for its ability to fully wet the hydrophobic surface of the strings without leaving residual air bubbles. Furthermore, the oil is characterized by a very low diffusion coefficient of $8.17 \cdot 10^{-6}\,\mathrm{mm^2/s}$, which was measured using diffusion weighted imaging (DWI) (Güllmar et al., 2002; Le Bihan et al., 1986). In contrast to this, water has a 260-fold higher diffusion coefficient with

		calculated		measured	
$\varnothing/\mu$m	l/m	vol./ml	λ/%	vol./ml	λ/%
340	50	4.5	7.8	4.4 ± 0.08	7.6 ± 0.14
200	100	3.1	5.4	3.1 ± 0.07	5.3 ± 0.12
100	500	3.9	6.8	4.2 ± 0.06	7.2 ± 0.10
40	2000	2.5	4.3	2.6 ± 0.19	4.5 ± 0.33

Table 3.1: *String parameters: diameter, length, volume and volume fraction inside the spheres. The volume fraction was determined by using calculated but also measured volumes of the strings.*

$2140 \cdot 10^{-6}\,\mathrm{mm}^2/\mathrm{s}$ (Becker et al., 1994). Due to the low self diffusion of the oil a static spin dephasing regime can be assumed for the phantom measurements, even for the smallest string with $40\,\mu$m diameter. The spin-spin relaxation time T_2 of the oil was measured with a Carr-Purcell-Meiboom-Gill (CPMG) sequence (Pell et al., 2006; Meiboom and Gill, 1958) and found to be about $T_{(2,\,CPMG)} \approx 420\,\mathrm{ms}$. The spin-lattice relaxation time was measured with an inversion recovery spin echo sequence (IRSE) (Kingsley et al., 1998; Vold et al., 1968) by varying the inversion time and found to be about $T_1 \approx 1035\,\mathrm{ms}$.

To be able to verify the measured signals of the capillary network phantom, single strings with diameters 100, 200 and $340\,\mu$m were investigated (Fig. 3.15). The susceptibility difference between the used extravascular oil and string material was determined using the numerical simulation of the single cylinder model.

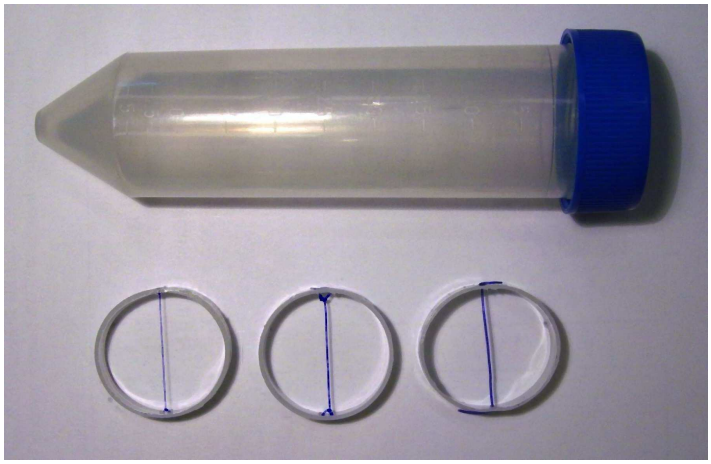

Figure 3.15: *Single strings $l = 25\,\mathrm{mm}$ with $\varnothing = 100$, 200 and $340\,\mu$m (from left to right). The strings were immersed with the sample holder into the silicone oil filled sample tube.*

3.4.3. Measuring Parameters of Capillary Network Phantom

All capillary phantom measurements were carried out on the 3 T MRI scanner. First, the capillary phantom was measured using the high resolution single echo SWI sequence to check the homogeneity of the capillary network. Measuring parameters were

$T_R = 36\,\text{ms}$, flip angle 15°, $T_E = 20\,\text{ms}$, bandwidth $= 40\,\frac{\text{Hz}}{\text{pixel}}$. The dimension of the acquisition matrix was $512 \times 320 \times 128$ and the field of view (FOV) $256 \times 160 \times 64\,\text{mm}^3$ resulting in $0.5 \times 0.5 \times 0.5\,\text{mm}^3$ voxels.

To determine the signal behavior as a function of time, the capillary network phantom as well as the single strings were measured by using the gradient echo sampled spin echo (GESSE) sequence. The imaging parameters for the single string experiments were: 2 mm slice thickness with a perpendicular orientation of the slice to the string axis, $T_R = 2000\,\text{ms}$, $T_E = 20 - 168\,\text{ms}$, $\Delta T_E = 8\,\text{ms}$, bandwidth $= 200\,\frac{\text{Hz}}{\text{pixel}}$ and 2 averages. The measurement was carried out twice. The second sequence was run with a 4 ms shifted readout echo train which reduced the inter echo time distance to 4 ms. The spin echo occurred always at $T_{SE} = 20\,\text{ms}$. The acquisition matrix and the field of view were adjusted to achieve in-plane voxel sizes of 0.30, 0.35 and $0.50\,\text{mm}^2$ for string diameters of 100, 200 and $340\,\mu\text{m}$, respectively. This resulted in volume fractions of 8.9, 25.4 and 36.3% for the corresponding strings.

The capillary network phantom was imaged with a single slice of 3 mm thickness which was acquired in axial orientation to obtain a cross-section of all five spherical compartments. The imaging parameters were: $T_R = 3000\,\text{ms}$, $T_E = 77 - 205\,\text{ms}$, $\Delta T_E = 4\,\text{ms}$, bandwidth $= 370\,\frac{\text{Hz}}{\text{pixel}}$, 2 averages. The sequence was carried out ten times. The sequences were run with a 0.4 ms shifted readout echo train which reduced the inter echo time distance to 0.4 ms. The spin echo occurred always at $T_{SE} = 140\,\text{ms}$. The acquisition matrix and field of view were adjusted to obtain in-plane voxel sizes of 0.96, 1.91, 4.45 and $6.31\,\text{mm}^2$ for the string diameters of 40, 100, 200 and $340\,\mu\text{m}$, respectively (Fig. 3.16). These different voxel sizes ensured that about 100 strings were inside of a single voxel of the corresponding string diameter. Due to this high amount of strings the statistical approach may justified and also comparable between the different strings. The ROIs of each string compartment were drawn with sufficient distance to the walls of the spheres to prevent signal compromising field inhomogeneities caused by residual air trapped in the connection seam between the two hemispheres.

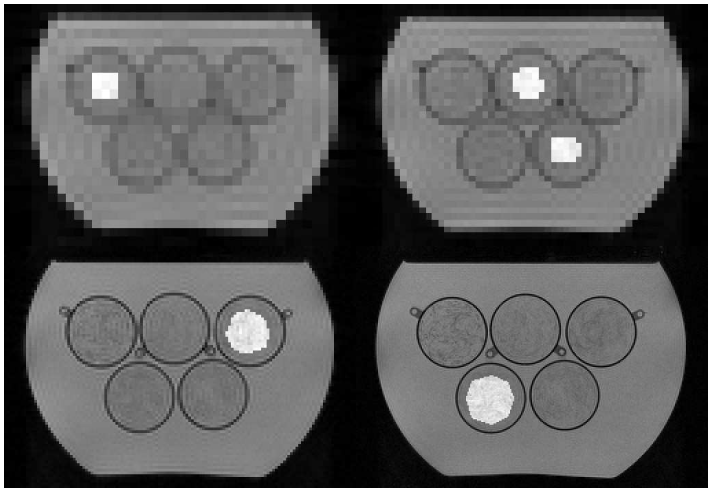

Figure 3.16: *Magnitude images of the GESSE sequence at the spin echo. The image resolution was adapted to the string diameter. About 100 strings were located in one voxel of the corresponding string diameter. The ROIs drawn in each string compartment are highlighted.*

Macroscopic field inhomogeneities were minimized by proper shimming of the imaged volume inside the phantom. The shimming volume was also chosen to be several times larger than the imaging slice. This ensured that macroscopic field gradients were also well minimized through the slice profile.

3.4.4. In Vivo Measurement

An initial measurement for the assessment of the blood capillary network *in vivo* was carried out on the 3 T MR system. The GESSE sequence was used with the following measuring parameters: $T_R = 1500\,\text{ms}$, $T_E = 40 - 98\,\text{ms}$, $\Delta T_E = 4\,\text{ms}$, bandwidth $= 370\,\frac{\text{Hz}}{\text{pixel}}$, 2 averages. The sequence was measured twice with a shifted gradient echo train of 2 ms. This resulted in an effective inter echo distance of 2 ms. The spin echo occurred always at $T_{SE} = 68\,\text{ms}$. The acquisition matrix was 128×96 with a FOV of $256 \times 192\,\text{mm}^2$ and slice thickness of 3 mm. ROIs were drawn in white and gray matter by carefully excluding inhomogeneities such as larger vessels or cerebrospinal fluid between the gyri of the cortex (Fig. 3.17).

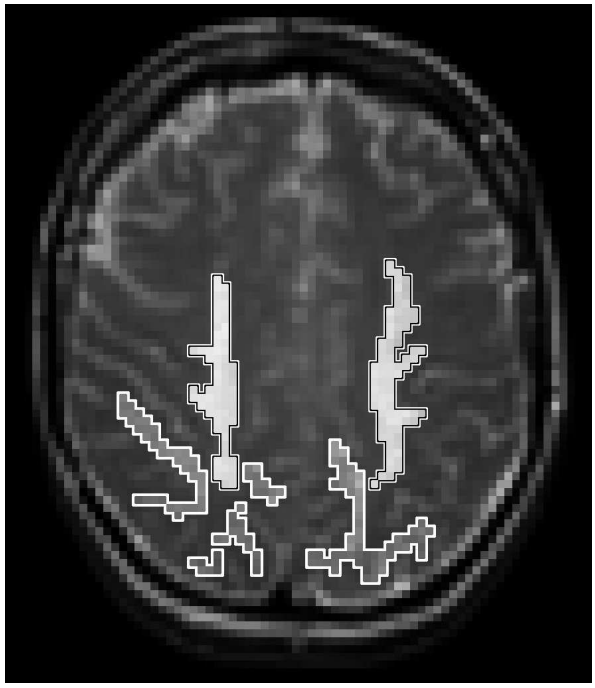

Figure 3.17: *Magnitude image of the GESSE sequence at the spin echo. The ROIs drawn in white and gray matter are highlighted.*

The influence of macroscopic field gradients was minimized by proper shimming the imaging volume in the volunteer's brain, where the shimming volume was also chosen several times larger than the imaging slice. The cranial slice location and the occipital ROI definition further minimize the influence of the nasal cavity of the sinuses.

To eliminate inflow artifacts the imaging slice was flanked by 50 mm thick saturation slabs in 5 mm distance axial to the imaged slice.

3.4.5. Data Evaluation

The signal formation of phantom and *in vivo* measurements around the spin echo of the GESSE sequence was first corrected for the irreversible T_2 decay. This was achieved by fitting Eq. 3.2 to the measured signal far enough from the spin echo. This allows to assume the long time scale asymptotic behavior of the signal (Eq. 2.84) which is mono-exponentially decaying. Thus, a separation of T_2 and T_2' according to Eq. 3.2 is possible. The previously described IDL fitting routine *CURVEFIT* (Sec. 3.3.2.2) was employed for this purpose.

The capillary network signal formation was calculated for various parameter sets of λ and Y or $\Delta\chi$ using Eq. 2.81 and compared on the basis of the root mean square error between signal simulation and measurement. The multidimensional integrals in Eq. 3.23 and Eq. 3.18 were not used to describe the measured signals, because the nested calculation of the integrals is very time consuming and not feasible for an iterative signal calculation.

"Too much iron in your blood"

Magneto in X2:X-Men United, USA 2003

IV Results

4.1. Single Capillaries and Veins

4.1.1. Simulation

Based on the theoretical consideration presented in Sec. 3.3.1 simulations were used as the first step to investigate how the voxel geometry influences signal formation in the presence of a single vessel. The analytically calculated signal-time curve which is only valid for a cylindrical voxel was plotted together with the numerically simulated signals for a cylindrical and a square voxel as well as a square voxel under consideration of the sampling point spread function (sPSF) (Fig. 4.1 a).

The signal was calculated using Eq. 3.6 by setting S_0 to 1.8 for the intra- and to 1 for the extravascular compartment. The higher inner signal fraction takes the shorter T_1 relaxation time into account caused by a paramagnetic contrast agent used for the single capillary phantom measurements in this work. The transverse relaxation time T_2 also varies for the different contrast agent concentrations. T_2 was set to 70 ms for the intra- and 1000 ms for the extravascular compartment. To obtain comparable results of the numerical simulation with the analytical solution of Yablonskiy and Haacke (1994), the thickness of the capillary wall was set infinitely small in this numerical simulation. Furthermore, the signal curves were computed for a vessel oriented perpendicular to $\vec{B}_0$ ($\theta = 90°$). As can be seen from Fig. 4.1 a only the numerical simulation for the cylindrical voxel shape produces an identical result compared to the analytical solution. The

simulated signal curves for the other voxel shapes differ distinctly from the analytical solution for echo times longer than 20 ms. The values for the volume fraction λ, the susceptibility difference $\Delta\chi$ and the angle θ were the same for all three simulations. The differences between the curves are caused by the extravascular field distribution which contributes differently to the signal formation depending on the voxel shape.

Assuming $T_2 \to \infty$, the spectra of the voxel signal as a function of frequency relative to the Larmor frequency at B_0 are shown in Fig. 4.1 b and c. For all three voxels the signal of the inner compartment produces a sharp peak at a frequency offset of about +10.5 Hz. The symmetric frequency distribution around 0 Hz is caused by the extravascular field inhomogeneity. It exhibits two separate broad peaks for the cylindrical voxel which are shifted and lowered for the square voxel. In the latter case an additional peak appears at 0 Hz (Fig. 4.1 b). This peak represents the signal contributions originating from spins located in the corners and along the diagonals of the square voxel where the local magnetic field inhomogeneity is close to zero.

Taking the sPSF into account, large positive and negative signal fractions are obtained around the center frequency of 0 Hz (Fig. 4.1 c). These are caused by the interaction between the local field inhomogeneity and the negative and positive lobes of the sPSF. For example, the two negative signal peaks at ±1 Hz stem from spins located in the first negative lobes of the sPSF near the magnetized cylinder (see Fig. 3.10 a and d).

These characteristic differences in the resonance frequency distribution of the signals are ultimately responsible for the varying signal-time behavior of the different voxel shapes, as seen in Fig. 4.1 a.

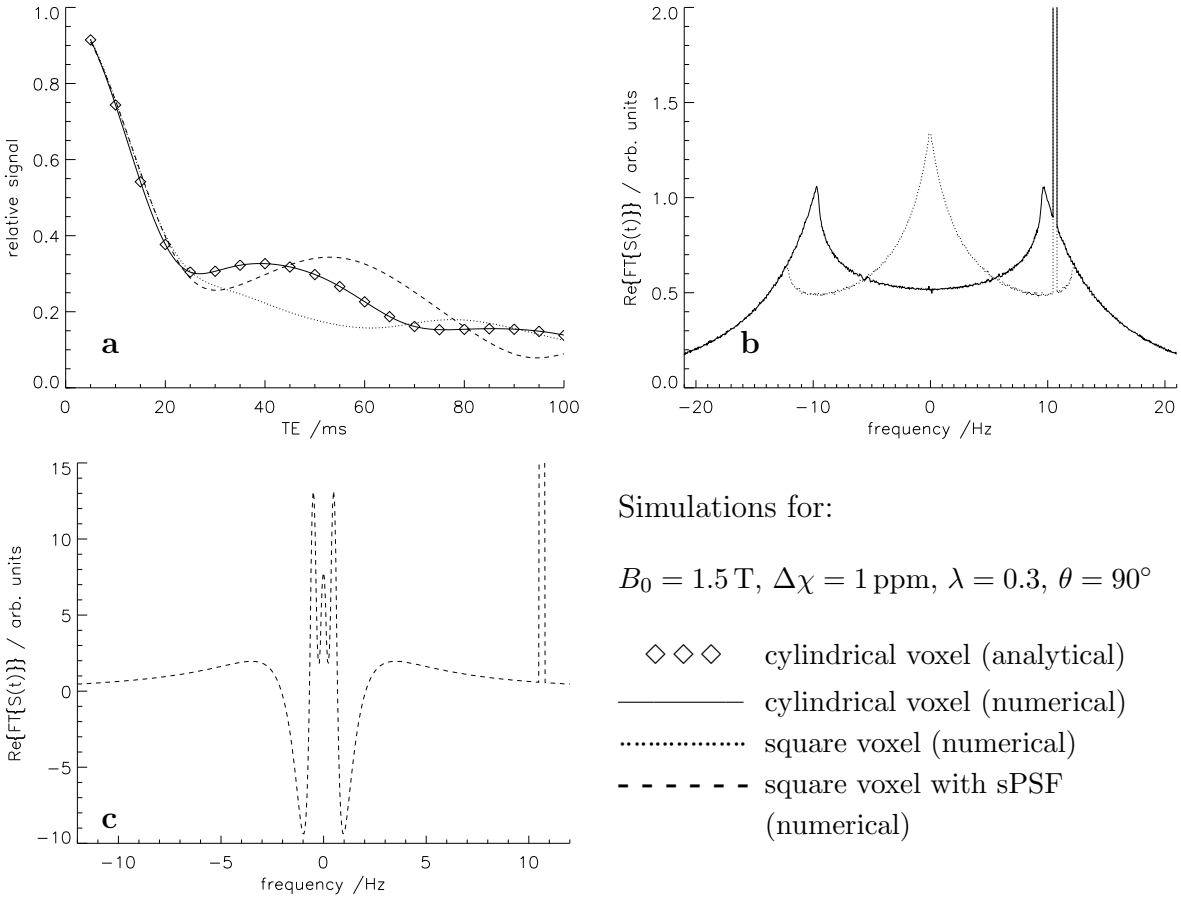

Figure 4.1: a: *Simulated signal as a function of echo time T_E for a cylinder perpendicular to the main magnetic field $B_0 = 1.5\,T$ with a susceptibility difference $\Delta\chi = 1\,ppm$, a volume fraction $\lambda = 0.3$ and different voxel geometries.* **b**: *Corresponding absorption spectra of the cylindrical and square voxel signal,* **c**: *corresponding absorption spectra with consideration of the sPSF. All spectra were generated by neglecting the irreversible transverse relaxation time ($T_2 \to \infty$). Note the different scales of the spectra which were chosen for better visualization. The maximum frequency shift (not shown in these diagrams) for all three voxel shapes was $\pm\frac{\Delta\chi}{2} \cdot \frac{\gamma}{2\pi} B_0 = \pm\ 32\,Hz$.*

4.1.2. Phantom Measurements

The phantom experiments were performed for 54 different parameter settings where the parameters were chanced accordingly: $\lambda = 0.1\text{-}0.3$, $\Delta\chi = 0.48\text{-}0.95\,\text{ppm}$, $\theta = 0\text{-}90°$ and $B_0 = 1.5\text{-}3\,\text{T}$. Fig. 4.2 shows an exemplary subsample of the conducted measurements. The results of all of these measurements are shown in the Appendix (Sec. A.1.1).

The measured signal of the voxel containing the capillary exhibited an oscillating behavior for the parallel vessel orientation (Fig. 4.2 a, b). This signal beat is caused by the two different resonance frequencies of the inner and outer compartment. The beat frequency is proportional to the susceptibility difference $\Delta\chi$ and the main magnetic field strength, whereas the beat amplitude depends only on λ. Since there are no extravascular field inhomogeneities at $\theta = 0°$ the voxel shape has no influence on the signal.

With orientations of $\theta = 55°$ and $90°$ of the capillary axis (Fig. 4.2 c, d and e, f) the signal is decaying to lower values as compared to the parallel orientation. This is caused by the additional signal dephasing due to the induced extravascular field inhomogeneity. However, the signal is also recovering at certain echo times, especially for the perpendicular vessel orientation with the higher volume fraction. In such cases, the locations and amplitudes of the signal minima and maxima depend on both, λ and $\Delta\chi$. Only the simulation of the sPSF voxel was able to fit the measured signal behavior for non-parallel ($\theta > 0°$) vessel orientations reasonably. Neglecting the sPSF will lead to inferior fits with large deviations between measured and fitted data. The mean coefficient of determination (r^2) averaged over all fits was $r^2 = 0.994$ with a lowest value of 0.936. Ten fits had lower and 44 fits had higher r^2 values than 0.994. The r^2 values for all phantom measurements are listed in Tab. A.1 in the Appendix.

It was possible to estimate the susceptibility difference from the fitted data with a mean difference of -0.8 % and standard deviation σ of about 10 % over all phantom measurements relatively to the experimentally adjusted values. Thus, the molar susceptibility of Gd-DTPA ($\chi_{M,Gd-DTPA}$) could be calculated as $4\pi \cdot (0.026 \pm 0.0025)\,\frac{\text{ppm}}{\text{mM}}$, which is in good agreement with the value known from literature with $\chi_{M,Gd-DTPA} = 4\pi \cdot (0.027 \pm 0.001)\,\frac{\text{ppm}}{\text{mM}}$ (Weisskoff and Kiihne, 1992).

The values for the volume fraction λ could also be extracted from the fits with a mean difference of -3.2 % compared to the original parameter. This result was reproducible with a standard deviation of about 12 % over all experiments. The λ and $\Delta\chi$ values, as well as their relative difference to the known values from experimental setup, are listed in Tab. A.2 and Tab. A.3 in the Appendix for all phantom measurements.

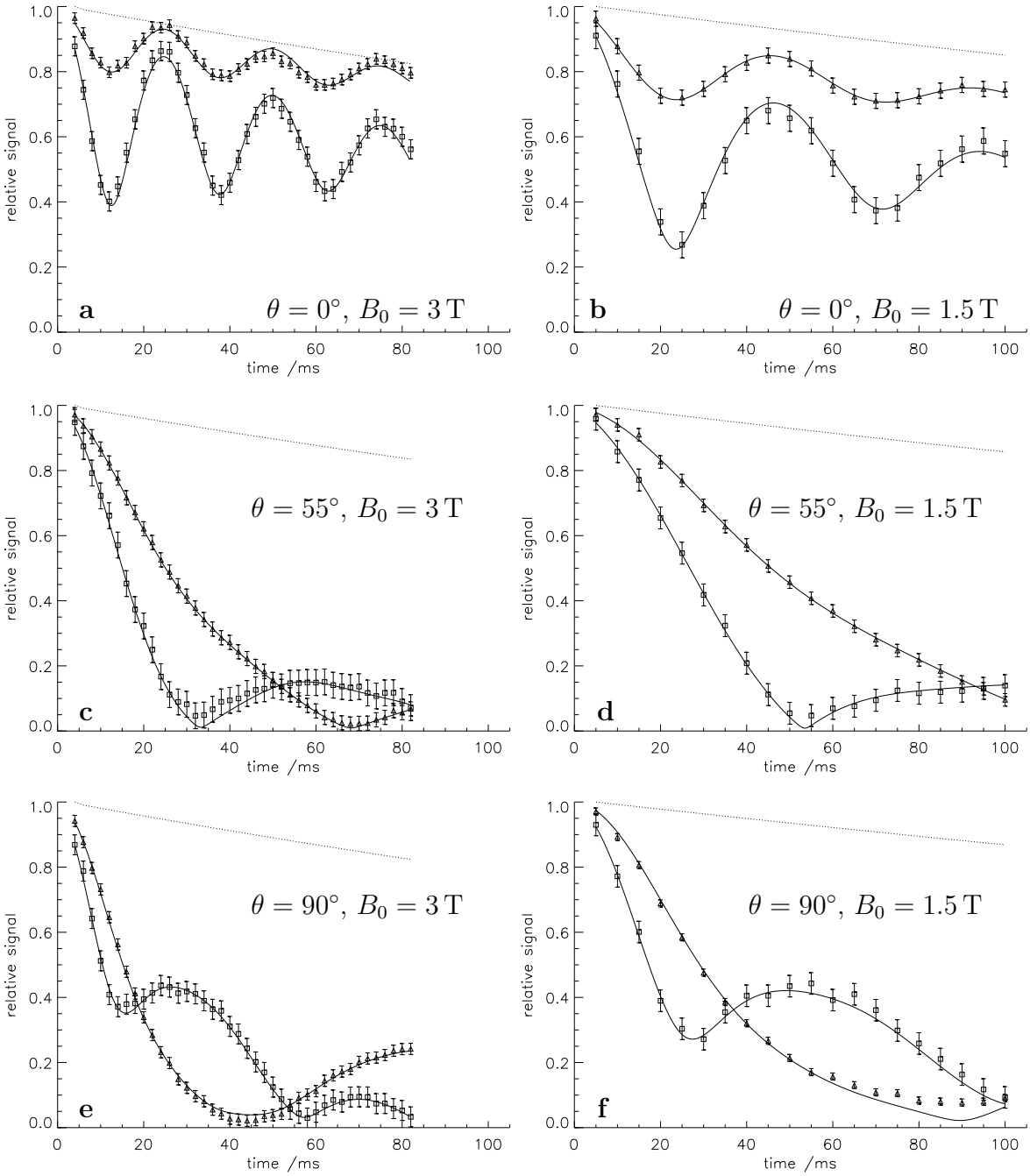

△: $\lambda = 0.1$, □: $\lambda = 0.3$, ····· signal of homogenous voxel, —— fitted signal simulation

Figure 4.2: *Phantom measurements exemplarily shown for the parallel cylinder orientation ($\theta = 0°$) (**a**, **b**), $\theta = 55°$ (**c**, **d**) and the perpendicular cylinder orientation ($\theta = 90°$) (**e**, **f**). The volume fraction was $\lambda = 0.3$ (box symbols) and $\lambda = 0.1$ (triangles). The susceptibility difference was $\Delta\chi = 0.95\,\mathrm{ppm}$. The fitting curves (solid lines) were calculated by numerical simulation taking the sampling point spread function (sPSF) into account. The dotted lines represent the signal of a homogenous ROI near the evaluated single voxel. The error bars correspond to the standard deviations of the signal determined from the homogenous ROI for each echo time. All plots of all the phantom measurements are shown in the Appendix (Sec. A.1.1).*

4.1.3. In Vivo Measurements

Values for $\Delta\chi$ were obtained by fitting the numerical simulation of the sPSF voxel to the measured signal of vessels oriented parallel or perpendicular to the main magnetic field (Fig. 4.3). The extracted $\Delta\chi$ values were converted to the blood oxygenation level Y using Eq. 2.69 with $\Delta\chi_{do} = 2.26\,\text{ppm}$ (Weisskoff and Kiihne, 1992).

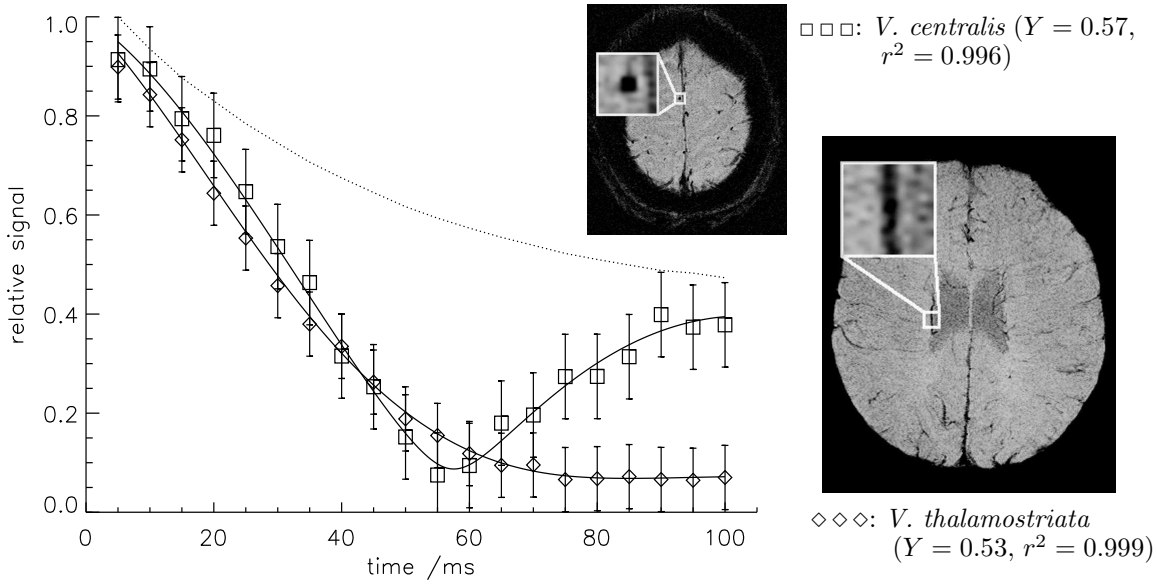

Figure 4.3: *Measured (symbols) and simulated (solid line) signal for two veins (V. centralis, $\theta = 0°$; V. thalamostriata, $\theta = 90°$) of volunteer A. The dotted line represents the signal of a homogenous ROI near the evaluated single voxel. The parallel vein displays the signal beat expected from simulations and phantom measurements, with a local minimum at $T_E \approx 55\,\text{ms}$ and a local maximum at $T_E \approx 100\,\text{ms}$. For the perpendicular vein the weak signal recovery would occur after the latest echo time of 100 ms and was not detected. The error bars denote the standard deviation which was determined in the homogenous ROI.*

Averaged over all veins and volunteers, the mean blood oxygenation level extracted from multi-echo SWI scans was found to be $\bar{Y}_{MESWI} = 0.55 \pm 0.02$ (Tab. 4.1). The fitting routine also optimized the values of the intra- and extravascular T_2 relaxation time as well as the blood volume fraction λ.

Additionally, the phase information of the SWI scan, that was performed to visualize the cerebral venous vascular system, was used to retrieve venous blood oxygenation Y_{PHSWI} using a similar method as described by Haacke et al. (1995). For this purpose the phase of a single voxel, which has to be located completely inside a venous vessel, was extracted and used to calculate the blood oxygenation level according to the field

distribution of the single cylinder model (Sec. 2.3.5.1). To eliminate any effects of macroscopic field inhomogeneities, the phase was taken from the homodyne filtered phase images. It was further regarded to exclude voxels which were not unwrapped during this filtering procedure. Due to the high in-plane resolution, the relatively large slice thickness of 2 mm and the axial orientation of the SWI scan, only the *Vv.centrales*, which were oriented parallel to $\vec{B_0}$, could be investigated. The mean Y value obtained with this method was $\bar{Y}_{PHSWI} = 0.53 \pm 0.03$.

volunteer		veins	λ (MESWI)	Y (MESWI)	Y (PHSWI)
		V. centralis 1	0.49	0.567	0.529
A		*V. centralis* 2	0.44	0.582	0.467
Hct=0.42		*V. centralis* 3	0.28	0.541	0.508
	right	*V. thalamostriata*	0.25	0.531	
		V. centralis 1	0.42	0.559	0.577
B		*V. centralis* 2	0.57	0.525	0.529
Hct=0.43		*V. centralis* 3	0.44	0.542	0.534
	left	*V. septi pellucidi*	0.21	0.578	
		V. centralis 1	0.51	0.554	0.528
C		*V. centralis* 2	0.23	0.540	0.529
Hct=0.46		*V. centralis* 3	0.18	0.537	0.532
	right	*V. thalamostriata*	0.27	0.549	
mean $\pm$ standard deviation:			$\bar{Y}_{MESWI} = 0.55 \pm 0.02$		$\bar{Y}_{PHSWI} = 0.53 \pm 0.03$

Table 4.1: *Y and λ values extracted in vivo from signal decays obtained with multi-echo gradient echo (MESWI) measurements and by high resolution phase images (PHSWI).*

4.1.3.1. Modulation of Blood Oxygenation

Carbogen

Applying carbogen (5%CO_2, 95%O_2) to a healthy volunteer forces a cerebral blood flow (CBF) increase, whereas the oxygen consumption of the brain tissue can be assumed to stay constant. This results in a decrease of the venous deoxyhemoglobin (Hb) concentration. The contrast of the veins nearly vanishes in susceptibility weighted images (Fig. 4.4) due to the blood oxygenation level depended (BOLD) effect (Ogawa et al., 1990).

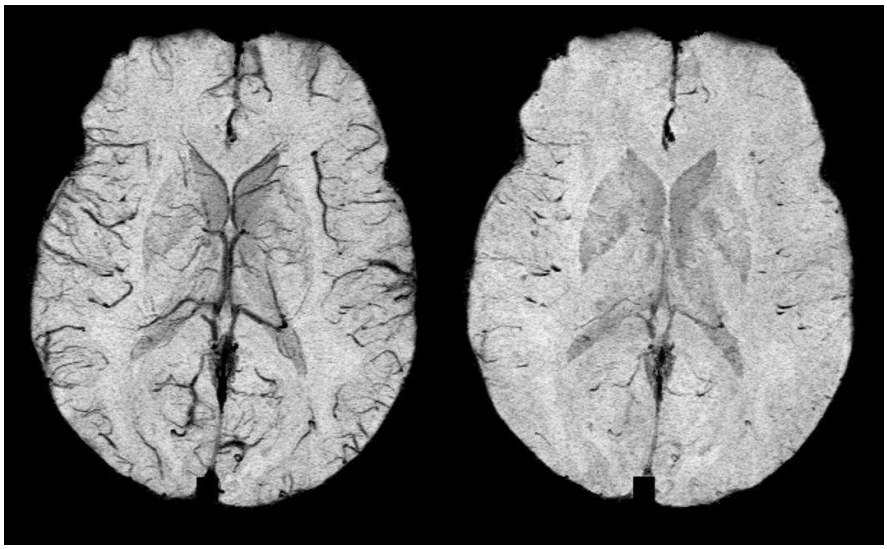

Figure 4.4: *Minimum intensity projection (mIP) over a 20 mm thick slab of 3D high resolution SWI data at 1.5 T ($T_E/T_R/\alpha$ = 40 ms/57 ms/20°, FOV = 256×192×76 mm^3, matrix = 512×256×38).* **Left:** *scan with air breathing.* **Right:** *scan during carbogen (5% CO_2, 95% O_2) breathing. Note that both SWI projections were calculated and windowed with identical parameters, but not comparable with the native and caffeine SWI scans of Fig. 4.6.*

Fitting the signal behavior of a sPSF voxel to the measured signal yielded a blood oxygenation of $Y_{air} \approx 0.5$ during air breathing and $Y_{carbogen} \approx 0.7$ during carbogen breathing (Fig. 4.5). The investigated voxels were located similar to those shown in Fig. 4.3. Most notably, in the voxel with the vessel parallel to the main magnetic field the first minimum during carbogen breathing coincides with a local maximum during air breathing. This is a direct *in vivo* demonstration of the influence of the blood oxygenation level on the MR signal which impressively changes the signal's oscillation frequency depending on Y.

In the vessel perpendicular to the main magnetic field, the signal decay was slower during carbogen as during air breathing, because the decreased extravascular field inhomogeneity leads to a decelerated spin dephasing.

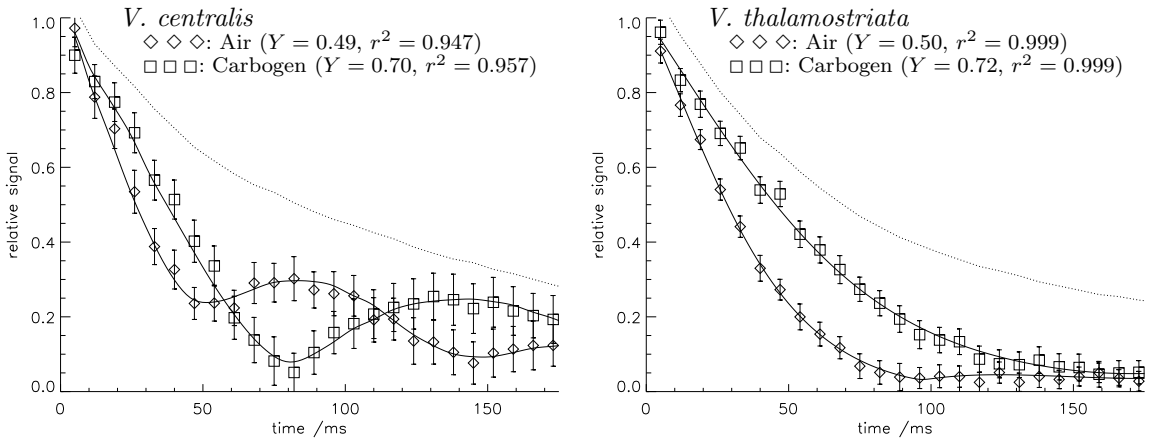

Figure 4.5: *In vivo measurements of single vessels. Signal for a parallel (V. centralis) and a perpendicular vein (V. thalamostriata) during air and carbogen breathing of a single volunteer with Hct=0.43. Note the significantly higher signal with a lower Y for echo times around 80 ms in the left graph. The dotted line represents the signal of a homogenous ROI near the evaluated single voxel. The error bars denote again the standard deviations which were determined in the homogenous ROI.*

Caffeine

Caffeine acts contrary to carbogen by decreasing the CBF. The oxygen consumption of the brain tissue can be assumed to be constant or even increased due to the analeptic effect of caffeine. These facts cause an accumulation of deoxygenated hemoglobin in the veins. The increased Hb concentration increases the venous contrast in SWI images (Fig. 4.6). The impact of caffeine on the venous contrast in SWI was first described by Haacke et al. (2003).

The changes in the signal's evolution are less pronounced compared to the carbogen stimulation, but still strong enough to induce detectable changes in the blood oxygenation. Fitting the signal curve of the sPSF voxel to the measured signal, resulted in a blood oxygenation of $Y_{native} \approx 0.55$ before and $Y_{caffeine} \approx 0.42$ 45 min after caffeine ingestion (Fig. 4.7). The first minimum and maximum of the signal oscillation of the vessel oriented parallel to $\vec{B}_0$ occurred about 15 and 30 ms earlier for the post caffeine condition as compared to the native condition. This faster signal oscillation is a result of the increased difference of the magnetic field between the intra- and extravascular compartment. In the perpendicular vessel the signal decay was slightly faster after caffeine ingestion as compared to the native condition, because the increased extravascular field inhomogeneity leads to an accelerated spin dephasing.

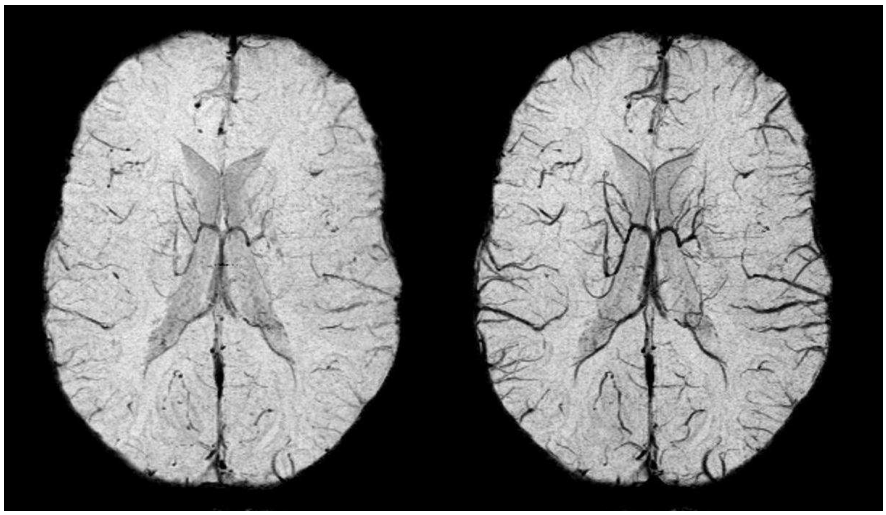

Figure 4.6: *Minimum intensity projection (mIP) over a 20 mm thick slab of 3D high resolution SWI data at 1.5 T ($T_E/T_R/\alpha$ = 40 ms/57 ms/20°, FOV = 256×192×76 mm^3, matrix = 512×256×38).* **Left:** *native scan.* **Right:** *50 min after caffeine intake. Note that the native and post caffeine SWI projections were calculated and windowed with identical parameters, but not comparable with the air and carbogen breathing SWI scans of Fig. 4.4*

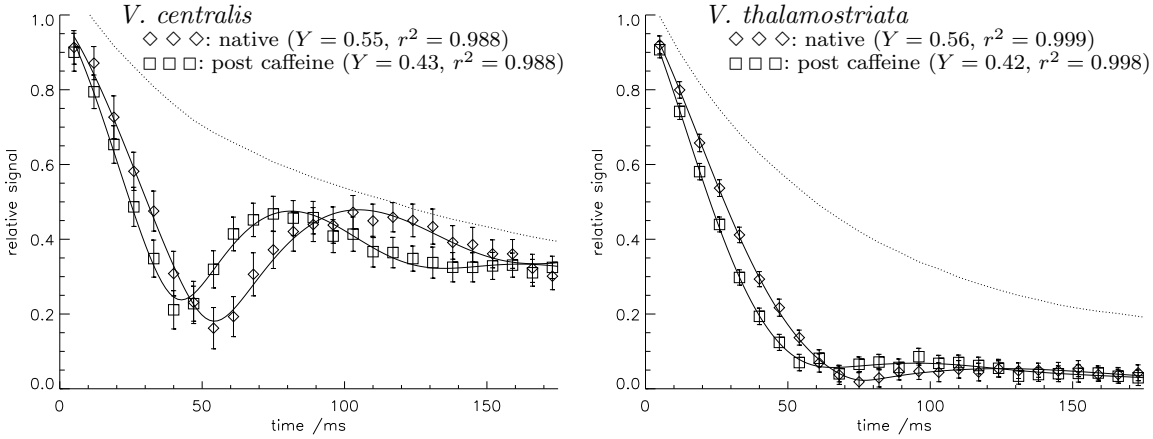

Figure 4.7: *Signal of a parallel (V. centralis) and a perpendicular vein (V. thalamostriata) of a single volunteer with Hct=0.41 before and 55 min after caffeine intake. The dotted line represents the signal of a homogenous ROI near the evaluated single voxel. The error bars denote the standard deviations which were determined in the homogenous ROI.*

4.1.4. Off-Center Subvoxel Shifts

The signal decays for different off-center positions of the capillary with respect to the voxel center were investigated by numerical simulations (Fig. 4.8). The capillary was shifted diagonally to off-center positions in 5%-steps of the x and y voxel dimension size. For each position the signal decay was calculated numerically. The numerical simulations assuming a centered position were then used to fit the off-center signal. Slightly off-centered positions, i.e. ±5%, of the vessel do not lead to strong changes in the field distribution within the voxel. For of larger shifts, the errors become more dominant as the areas with steep field topography may be shifted outside the voxel. Surprisingly, it was found that $\Delta\chi$, which depends on the blood oxygenation, was very stable, even at far off-center positions. The value of the $T_{2,\,ext}$-decay time, on the other hand, was underestimated severely. The lower signal curves in Fig. 4.8, corresponding to larger off-centered positions, were caused by additional spin dephasing due to the decreased field symmetry inside the voxel. Assuming an on-center capillary position for the numerical signal simulation, the fit algorithm can only converge with the curves by mainly decreasing $T_{2,\,ext}$. The volume fraction λ and intravascular signal fraction $S_{0,\,int}$ were also affected by off-center shifts, but to a much lesser extent than $T_{2,\,ext}$. The parameters $S_{0,\,ext}$ and $T_{2,\,int}$ were nearly independent of the vessel position.

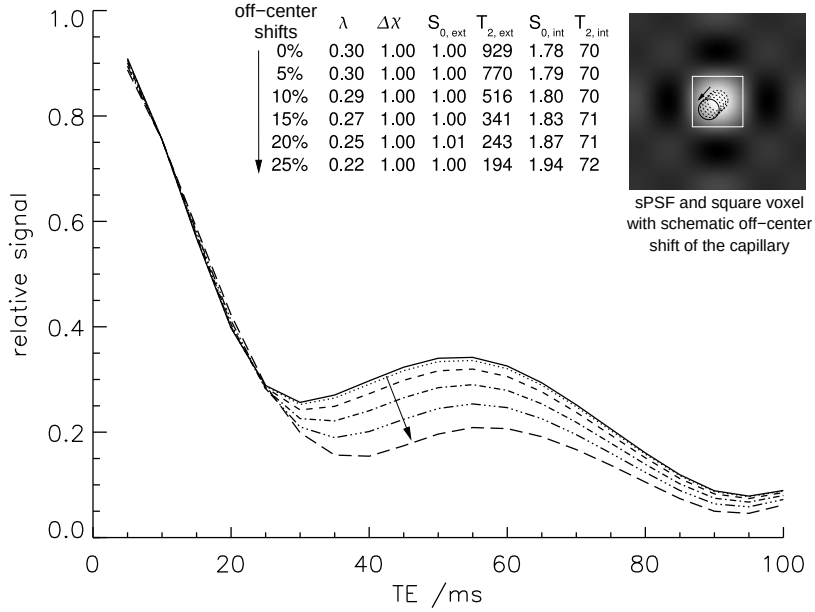

Figure 4.8: *Signal curves and fitted parameters obtained by diagonally shifting the cylindric vessel out of the center position. The true parameters of the simulations were $\lambda = 0.3$, $\Delta\chi = 1\,ppm$, $S_{0,\,ext} = 1$, $T_{2,\,ext} = 1000\,ms$, $S_{0,\,int} = 1.8$, $T_{2,\,int} = 70\,ms$. The first row denotes the extracted parameters from the fit algorithm where the capillary was in on-center position. They were very close to the true parameter set. The largest sensitivity to displacements of the capillary shows $T_{2,\,ext}$, whereas $\Delta\chi$ seems insensitive in this range of up to 25% diagonal off-center shifts.*

4.1.5. Macroscopic Field Inhomogeneities

To investigate the influence of background field gradients the signal decay of the capillary phantom was measured under different shim conditions. The voxel's signal was investigated by applying a linear field gradient parallel or perpendicular to the capillary axis. In Fig. 4.9 the voxel signal is shown for a gradient perpendicular to the cylinder axis. Starting with an optimized shim where almost no background field gradient exists, a linear macroscopic field gradient up to $15\,\mu$T/m was generated by successively changing the shim current of the corresponding shim coil. Even a poor shim had no severe effect on the signal decay of the single voxels (solid and dashed lines in Fig. 4.9). An effect was only seen for the signal of a larger region with $3 \times 3 \times 3$ voxels in the homogenous surrounding which was calculated by complex summation (dotted lines in Fig. 4.9).

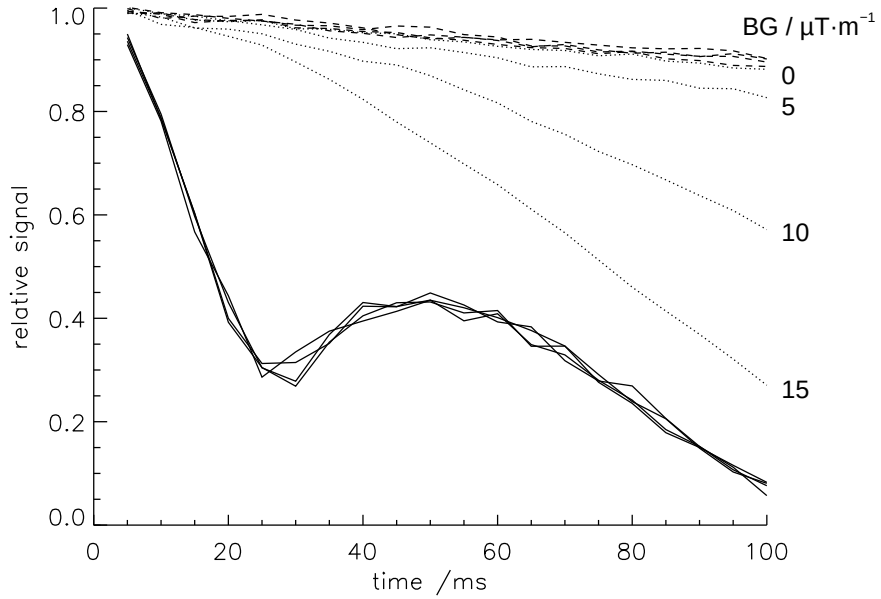

Figure 4.9: *Measured signal for a single voxel including the capillary (solid lines) and a single voxel in the homogenous surrounding (dashed lines). No influence from background linear field gradients (BG), which were produced by poor shimming, s observed. All dashed and all solid lines nearly coincide with each other. To demonstrate the situation for a large voxel, the voxel size was enlarged virtually by complex summation of 3×3×3 voxels. This leads to significantly faster signal decay (dotted lines) due to the increased volume for slowly varying field inhomogeneities. The lowest dotted line (i.e., fastest decay) corresponds to a very poor shim condition, under which no gradient echo measurement would be performed.*

4.2. Capillary Network

4.2.1. Simulation

4.2.1.1. Dependency of Volume Fraction and Blood Oxygenation

The signal decay caused by a capillary network was calculated using Eq. 2.81 with an exemplary parameter set of $\lambda = 0.05$, $Y = 0.55$ and $T_2 = 100\,\text{ms}$. The parameter set was chosen to simulate the signal expected of brain matter *in vivo*. The result is shown in Fig. 4.10 for the solid black line. The signal decays obtained by varying λ and Y (dashed lines) were added to the graph. For the blue curves the volume fraction was $\lambda = 0.025$ which caused a higher initial signal than compared to the curves with higher λ. For the green curves, λ was set to 0.05 which caused the same initial signal at $T_E = 0$ as for the solid black line. The red dashed curves were calculated with $\lambda = 0.075$ and they had the lowest signal at $T_E = 0$ compared to all other curves. The blood oxygenation was set to $Y = 0.25$, 0.5 and 0.75 and the signal was calculated for each λ and Y combination. This results in three dashed lines of equal colors for each λ, where the lowest curve of one color (λ) is that calculated with the lowest blood oxygenation level. Consequently, the highest signal curve of each color is that with $Y = 0.75$.

As visible in Fig. 4.10 the signal curves decrease slightly faster with lower blood oxygenation values. Furthermore, it is also seen that some curves nearly coincide despite different λ and Y values. This suggests that several λ and Y pairs, which generate nearly equal signal-time curves, can not be distinguished by simply evaluating the signal decay.

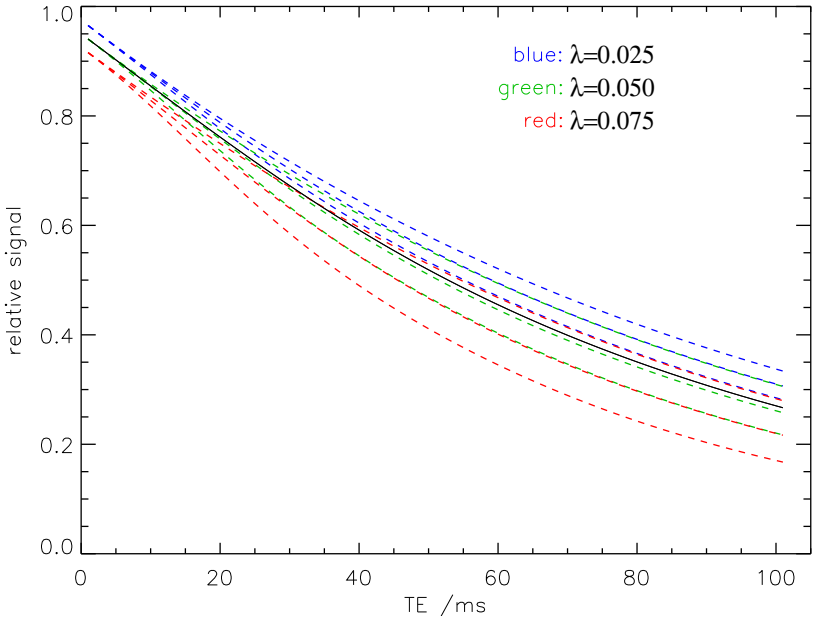

Figure 4.10: *Signal decay of a capillary network with* $\lambda = 0.05$, $Y = 0.55$ *and* $T_2 = 100\,\text{ms}$ *at 1.5 T (solid black line) flanked by signal decays calculated with different* λ *and* Y *pairs* ($\lambda = 0.025, 0.05, 0.075$ *and* $Y = 0.25, 0.5, 0.75$).

The root mean square error (MSE) between the signal curve obtained with $\lambda = 0.05$, $Y = 0.55$ and all other curves calculated by changing λ from 0 to 0.1 and Y from 0 to 1 is plotted in Fig. 4.11. The MSE shows a huge increase for high λ and low Y values. Signal curves calculated with such parameters are characterized by a rapid decay as shown in Fig. 4.10 for the lowest red dashed line ($\lambda = 0.075$ and $Y = 0.25$). The MSE rises not as high for low λ or high Y parameters. The signal curve with $\lambda = 0.025$ and $Y = 0.75$, for example, (highest blue dashed line in Fig. 4.10) is closer to the solid line than the curve with high λ and Y values as discussed above. A wide band of low values is formed in the MSE plot by corresponding λ and Y pairs which produces well fitting signal curves to the original function. Thus, the minimum MSE = 0 for the exactly matching parameter pair of $\lambda = 0.05$ and $Y = 0.55$ is not visible in the linear scaled MSE. In a logarithmic scale, the minimum MSE of zero can be recognized very well at the $\lambda = 0.05$ and $Y = 0.55$ position. A narrow valley of low MSE values which is formed by the correlating λ and Y values is also clearly visible and reaches from $\lambda = 0.023$, $Y = 0$ to $\lambda = 0.1$, $Y = 0.8$. However, this clear position of the minimum MSE is only observed in exact signal simulation. For measurements, where the signal is compromised by noise, the position of minimal MSE was not reproducible for the original parameter set. To investigate the influence of signal noise on the obtainable minimal MSE, noisy signal curves were simulated in the following section.

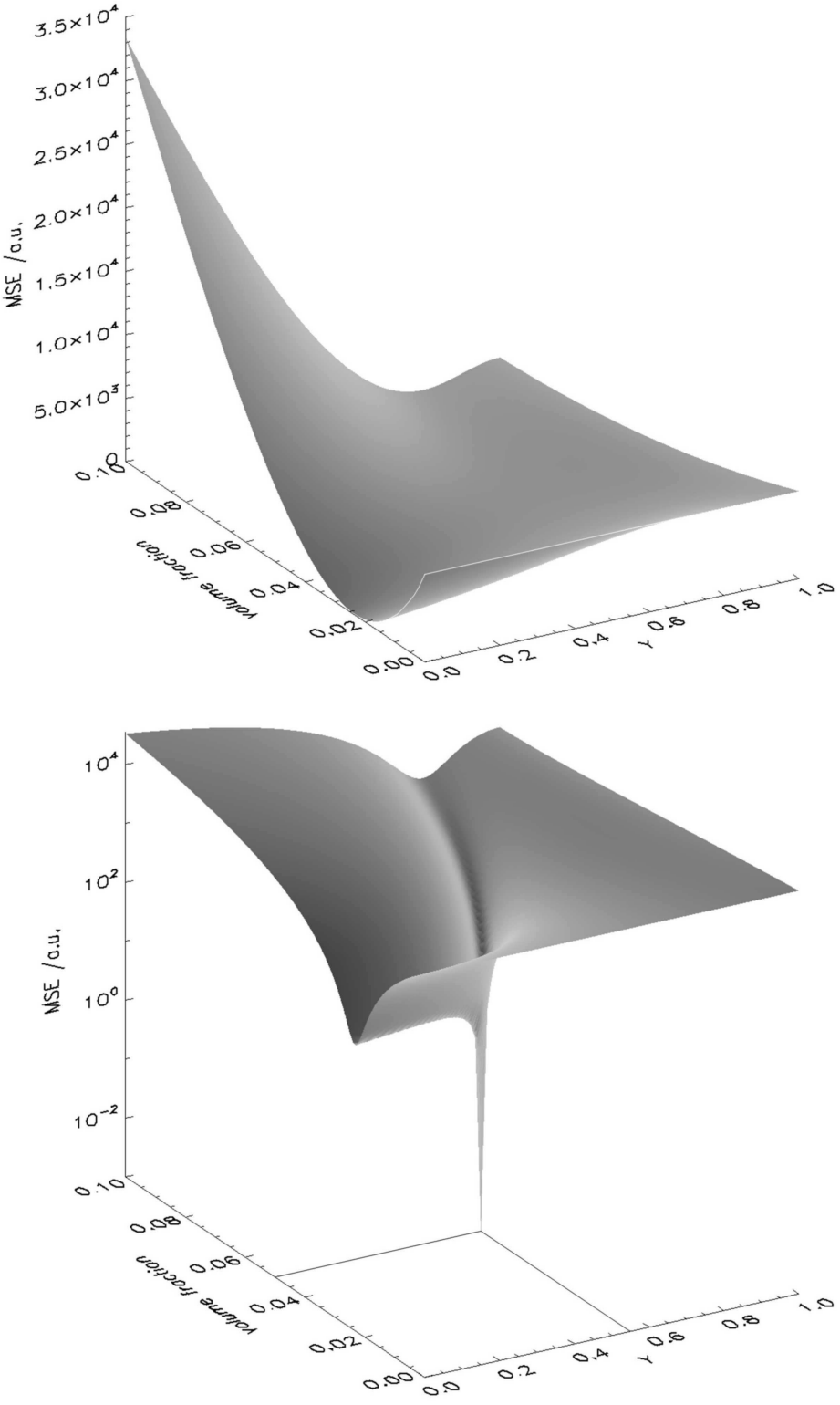

Figure 4.11: *Shaded surfaces of root mean square errors (MSE) between the signal decay of the parameter set $\lambda = 0.05$, $Y = 0.55$ and all other decays for $\lambda =$ 0-0.1 and $Y =$ 0-1. The top surface was plotted with a linear scale. The bottom surface shows a logarithmic scale for the MSE.*

4.2.1.2. Noisy Signal Decay

An estimation of the robustness of the network signal formation in terms of noisy signal decays was investigated to further verify its application for real experiments. Simulated noise with standard deviations of $\sigma = 0.01$, 0.02 and 0.04 was added to an exemplary signal decay with $\lambda = 0.05$, $Y = 0.55$ and $T_2 = 100\,\text{ms}$ (Fig. 4.12). These signal-to-noise ratios ($1/\sigma$) of 25, 50 and 100 were chosen, because they represent typical SNR values for MR images.

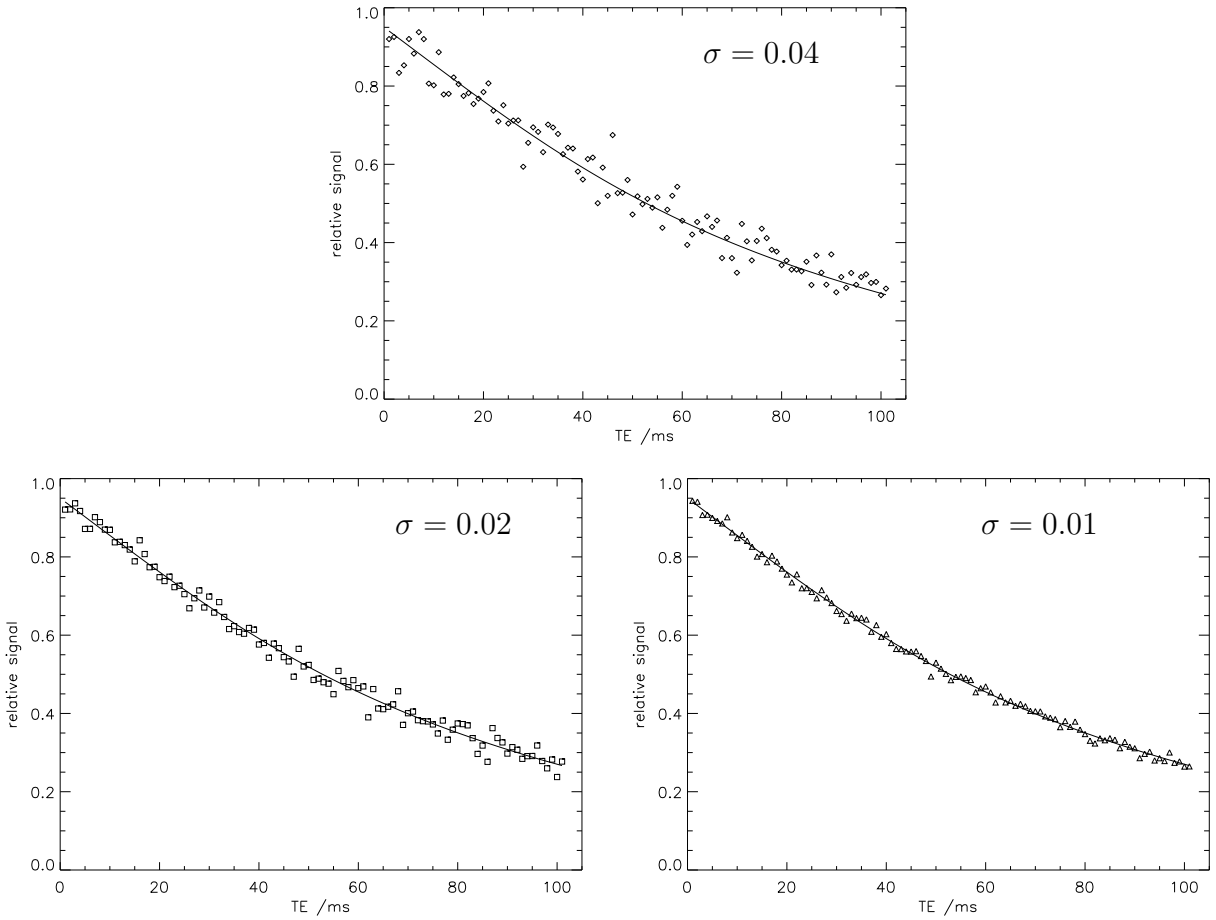

Figure 4.12: *Signal decays of a capillary network with $\lambda = 0.05$, $Y = 0.55$ and $T_2 = 100\,\text{ms}$ at 1.5 T. The solid lines show the signal without noise. The diamonds, boxes and triangles simulate a noisy signal with standard deviations of $\sigma = 0.01$, 0.02 and 0.04, respectively.*

The minimal MSEs were calculated between the theoretical signal curve without noise and 50 noisy signal decays. Fig. 4.13 visualizes the distribution of the determined minimal MSEs for all 50 noisy signals. The underlying contour plot is equivalent to the shaded surfaces as shown in Fig. 4.11 with the logarithmic scale. The original parameter pair ($\lambda = 0.05$, $Y = 0.55$) is marked by the solid straight lines. The minimal MSEs of all 50 noisy signals are marked by symbols. They spread along the valley of low MSEs

which is formed by the correlated λ and Y pairs. The distribution of the minimal MSEs is also broader for high noise and narrower for low noise. Nevertheless, they seem to vary symmetrically around the true parameter set with $\lambda = 0.05$ and $Y = 0.55$. The mean values and variations of this minimal MSE distribution show a distinct lowering of the λ and Y values as compared to the original λ, Y pair. The standard deviation increases, as already seen in the contour plots, with higher signal noise (Tab. 4.2).

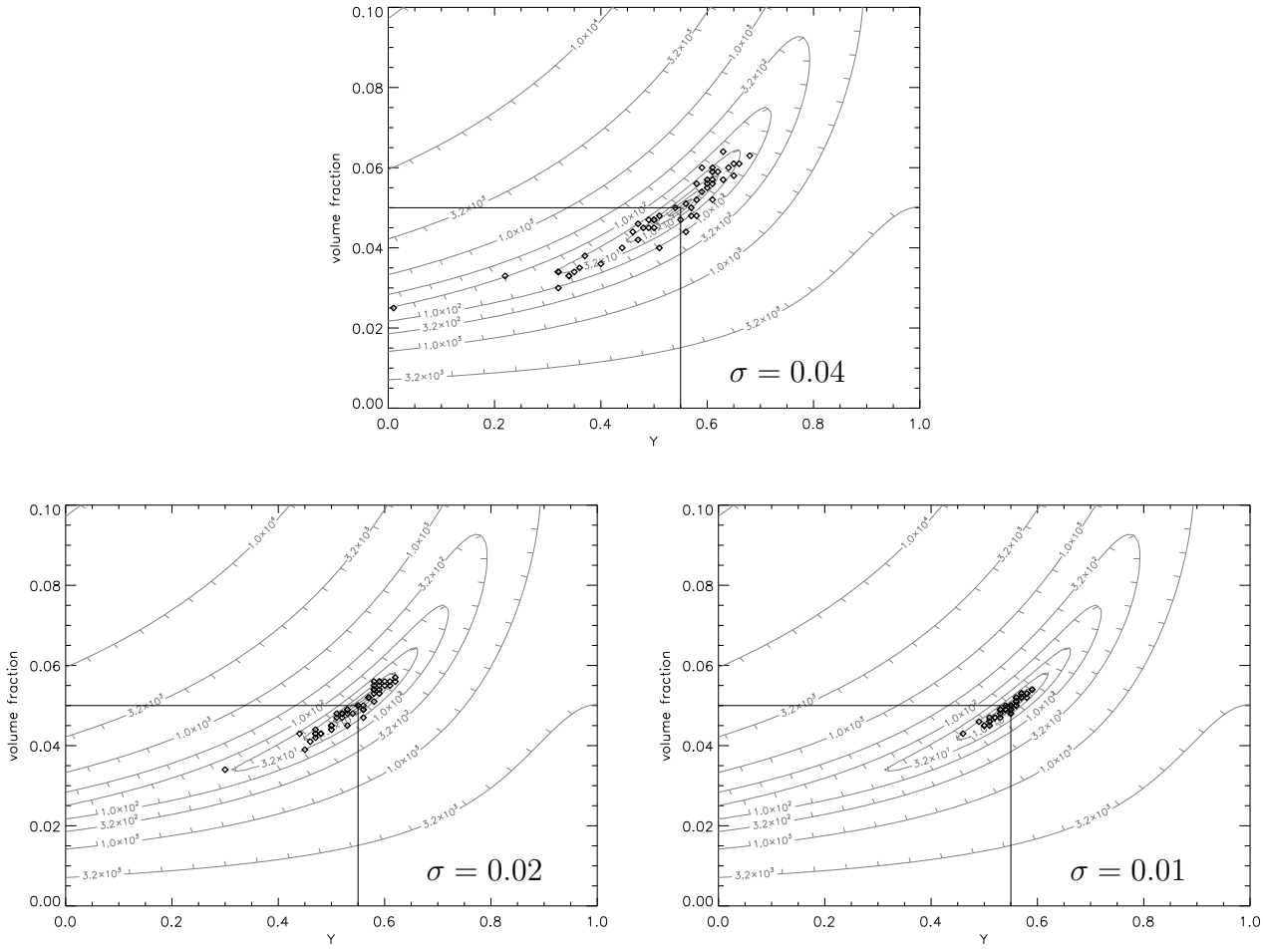

Figure 4.13: *Distributions of minimal root mean square errors (MSEs) obtained by noisy signals with $\sigma = 0.01$, 0.02 and 0.04, respectively (diamonds). The underlying contour plot corresponds to MSE plot with logarithmic scale as displayed in Fig. 4.11. The minimal MSE for the original parameter set of $\lambda = 0.05$ and $Y = 0.55$ is marked by the solid straight lines.*

noise σ	$\lambda/\%$	$Y/\%$
0.04	4.81 ± 1.0	51.1 ± 13.2
0.02	4.92 ± 0.5	53.8 ± 5.9
0.01	4.96 ± 0.3	54.5 ± 2.8

Table 4.2: *Mean values and standard variation of λ and Y parameters obtained by noisy signal decays.*

4.2.1.3. Mutually Avoiding Cylinders

Fig. 4.14 shows the simulated signal decay under the assumption of mutual avoiding cylinders. It was calculated for $B_0 = 1.5\,\mathrm{T}$ using Eq. 3.23 with parameters $\lambda = 0.05$, $Y = 0.55$, $T_2 = 100\,\mathrm{ms}$. Mutual avoiding of the cylinders was taken into account by the correlation parameter z which was set to $z \to \infty$, $z = 1$ and $z = 0.1$.

A z value of ∞ corresponds to the network model with pure statistically cylinder positioning. Thus, the signal curve for $z \to \infty$ coincides with curves calculated by Eq. 2.81 where no mutual avoiding is considered. The value of $z = 1$ describes a network of also randomly positioned cylinders, but the case of coinciding or even overlapping cylinders is excluded by $z = 1$. Such a network was generated by the string network constructed and measured in the work presented in this thesis, because the randomly coiled strings of this phantom can not overlap. As visible seen in Fig. 4.14 the curves for $z \to \infty$ (green line) and $z = 1$ (red line) nearly coincide. The correlation r^2 between both curves is nearly unity with $r^2 = 1 - 0.3 \cdot 10^{-6}$. This means that the effect of mutual avoiding does not influence the signal decay of the applied string network phantom.

To simulate the effect of mutual avoiding *in vivo*, z was set to 2λ ($z = 0.1$). This z value was chosen accordingly to the proposed z for biological tissue by Kiselev (2004). The signal curve with $z = 0.1$ shows a distinct difference to the curves with $z = 1$ or $z \to \infty$ for times later than 30 ms (Fig. 4.14, blue curve). The time point of $t = 30\,\mathrm{ms}$ is marked in Fig. 4.14 as a solid straight line.

To estimate a possible systematic deviation, which would occur by determining λ and Y without the consideration of mutual avoiding cylinders, the positions of the minimal MSEs were tested. They were calculated between the signal curves, which accounted for mutual avoiding cylinders ($z = 1$, 0.1) and the signal obtained by the pure statistical network model ($z \to \infty$). Fig. 4.15 shows the contour plot of the MSEs similar to the surface plot in Fig. 4.11 with the logarithmic scale. The minimal MSEs of the mutual avoiding signals with $z = 1$, 0.1 are labeled. The minimal MSE with the label (a) is obtained from the $z = 1$ curve, where the full time range between 0 and 100 ms was used to calculate the MSE. The minimal MSE (b), which shows a significant underestimated blood oxygenation level, is obtained by $z = 0.1$ for the full time range. If the MSE is calculated only for the time range between 0 and 30 ms, the minimal MSE for $z = 1$

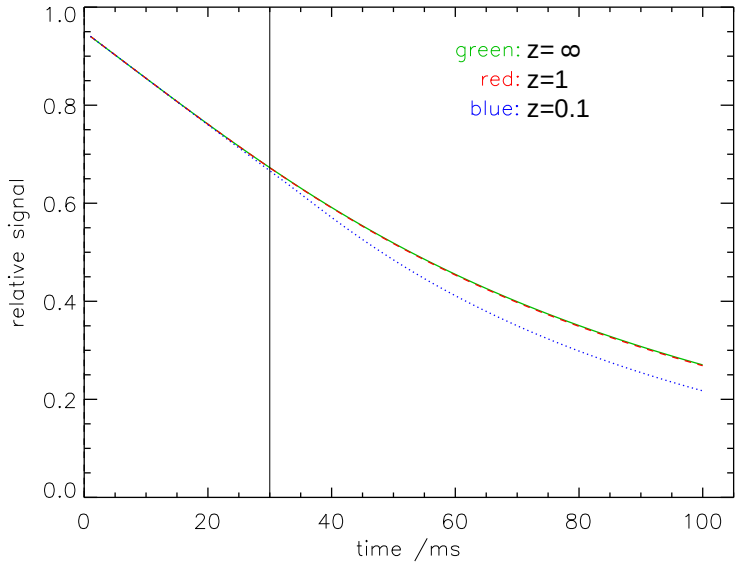

Figure 4.14: *Signal decay of a capillary network with $\lambda = 0.05$, $Y = 0.55$ and $T_2 = 100\,\text{ms}$ at 1.5 T. The red, green and blue line denote the signal decay for $z \to \infty$, $z = 1$ and $z = 0.1$, respectively.*

(c) matches the original parameter pair exactly. Also for the $z = 0.1$ signal curve the minimal MSE (d) is now much closer to the original parameter pair as compared to (b).

The results of Fig. 4.15 are summarized in Tab. 4.3, where the misestimated λ and Y parameters and their difference to the original parameter set of $\lambda = 0.05$ and $Y = 0.55$ is shown. The deviation between the original parameter set is negligible for $z = 1$. However, with $z = 0.1$ the blood oxygenation will be underestimated significantly. For a MSE calculation between the signal curves for times $\leq 30\,\text{ms}$, the relative systematic error in the blood oxygenation level estimation would be less than 10%. This suggests that the effect of mutual avoiding can also be neglected for *in vivo* measurements if the signal decay is acquired only till 30 ms after spin excitation or around the spin echo.

label	z	λ / %	Y
a	1	5.0 ± 0	$0.54 + 0.01$
b	0.1	$4.3 + 0.7$	$0.21 + 0.34$
c	1	5.0 ± 0	0.55 ± 0
d	0.1	$4.9 + 0.1$	$0.50 + 0.05$

Table 4.3: *Estimated λ and Y parameter pairs from signal decays influenced by the effect of mutual avoiding cylinders with theirs difference to the original parameter pair $\lambda = 0.05$ and $Y = 0.55$. The parameters for a and b were obtained from the signal decays with $t \leq 100\,\text{ms}$ and for c and d with $t \leq 30\,\text{ms}$. Please see Fig. 4.15 for the corresponding MSE contour plot.*

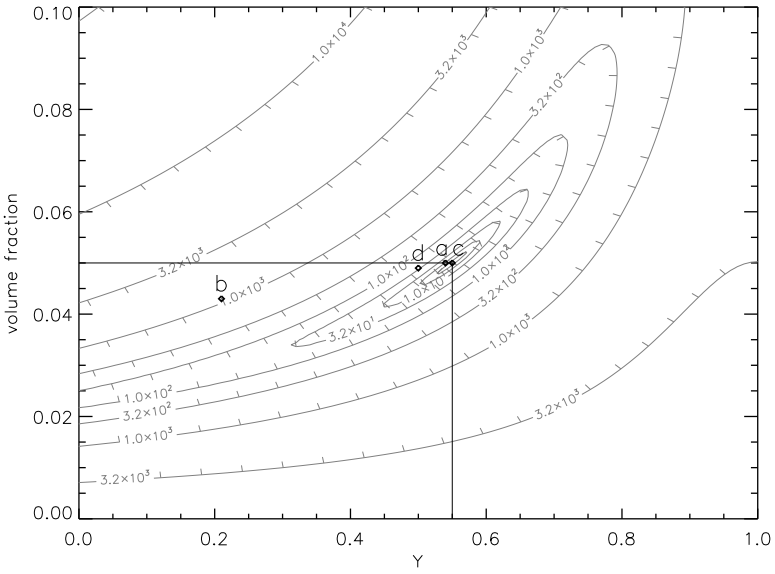

Figure 4.15: *Contour plot of root mean square errors (MSE) as displayed in Fig. 4.11 for the logarithmic scale. The MSE is minimal for the parameter set* $\lambda = 0.05$, $Y = 0.55$ *and* $z \to \infty$ *(solid lines). The symbols labeled with a-d denote the minimal MSE with lower* z *parameters. Please see Tab. 4.3 for further detail.*

4.2.2. Phantom Measurements

4.2.2.1. Single Polypropylene (PP) Strings

The single polypropylene (PP) strings used to build the string network phantom were investigated by the single vessel approach to determine their magnetic property. Due to the restricted spatial resolution of the MRI whole body scanner the smallest string diameter investigated was 100 μm. Fig. 4.16 shows a cross-sectional phase image of strings, orientated perpendicular to the main magnetic field $\vec{B}_0$. The field inhomogeneity induced by the string directly influences the phase in the near surrounding. According to Eq. 3.1 the positive (brighter) phase differences which are aligned in $\vec{B}_0$ direction denote a lower magnetic field. This means that the magnetic susceptibility of the strings is lower than of the surroundings. Thus, the polypropylene material of the strings is more diamagnetic than the silicone oil.

The signal of a single voxel containing a single string shows the typical time course (Fig. 4.17) as known from the single vessel phantom. The magnetic susceptibility difference $\Delta\chi$ (Tab. 4.4) between the string's material and the surrounding oil was determined by fitting the numerical simulation (Eq.3.6) to these signal curves. The $\Delta\chi$ value for the $\varnothing = 340\,\mu$m and 100 μm string is nearly the same with $\Delta\chi \approx 1.6$ ppm, whereas the string with $\varnothing = 200\,\mu$m exhibits $\Delta\chi \approx 1.5$ ppm. For such a $\Delta\chi$ value the mono exponential long time scale asymptotic approximation of the capillary network signal is valid for times longer than 3.74 ms at 3 T (Eq. 2.85). This means, that for correcting the T_2 decay of the string network signal, the function given in Eq. 3.2 has to be fitted for times longer than 3.74 ms with respect to the spin echo time.

The $\Delta\chi$ value of the $\varnothing = 40\,\mu$m string, which was not determined by the single vessel

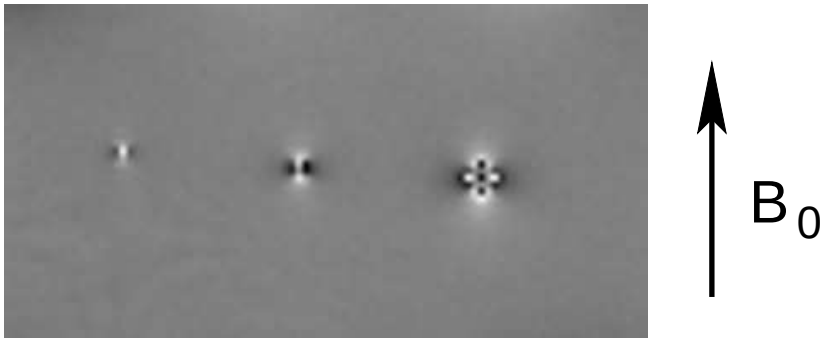

Figure 4.16: *Phase image of single strings (⌀=100, 200, 340 µm, from left to right). As can be seen from the field distortion around the strings, the PP material is more diamagnetic than the silicone oil. Note that phase wraps occur near the strings which are clearly visible at the ⌀=340 µm string.*

method, was assumed to be 1.6 ppm for comparison with the network phantom.

⌀/µm	λ/%	Δχ/ppm
340	36.3	1.58 ± 0.045
200	25.4	1.48 ± 0.050
100	8.9	1.60 ± 0.075
40	n/a	assumed to be 1.6

Table 4.4: *Parameters of single strings immersed in silicone oil. The volume fraction was adjusted by the voxel resolution. The magnetic property (Δχ) was estimated by the previously described single vessel approach.*

4.2.2.2. Capillary Network Phantom

High resolution T_2^*-weighted images of the network phantom showed no inhomogeneities induced by air bubbles trapped inside the string network. However, some inhomogeneities were caused by air trapped within the connection seam of the two hemispheres (Fig. 4.18, black arrows). The distribution of the randomly coiled strings is also well visible. Some regions of the string network seem to be less randomly coiled as visualized in the upper left string compartment in Fig. 4.18 marked with a white arrow.

The results of the measurements of the network phantom are summarized in Tab. 4.5. The signal and MSE contour plots are shown in the Appendix (Sec. A.2.1 and A.2.2). The noise was measured in a homogeneous background ROI according to the Rician noise distribution of MRI data (Gudbjartsson and Patz, 1995). Signal-to-noise ratios of about 170 for the $\varnothing = 340$ and 200 µm string signals, 77 for the $\varnothing = 100$ µm string and 40 for the $\varnothing = 40$ µm string were obtained.

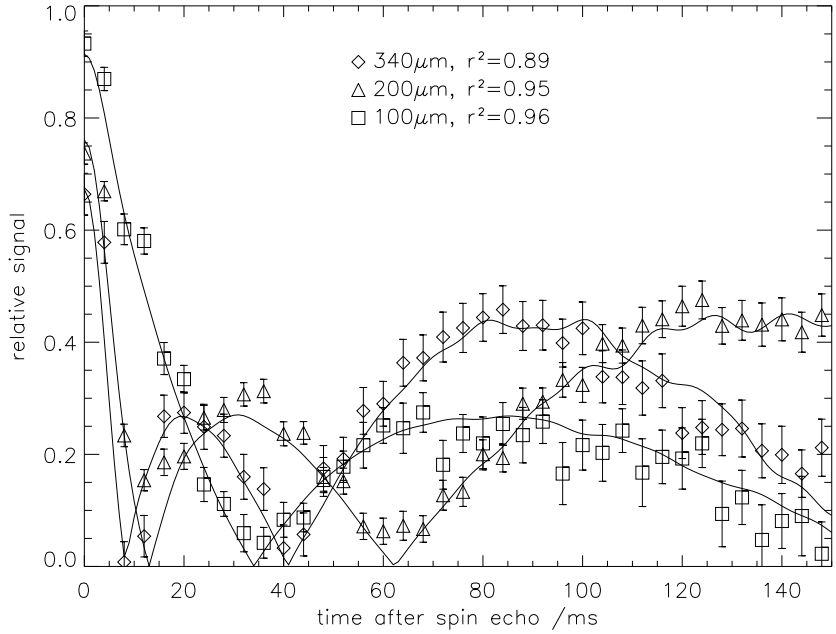

Figure 4.17: *Signal of voxels containing single PP strings oriented perpendicular to $\vec{B}_0$. The signal formation was normalized to a homogenous voxel to eliminate the T_2 signal decay of the surrounding silicone oil.*

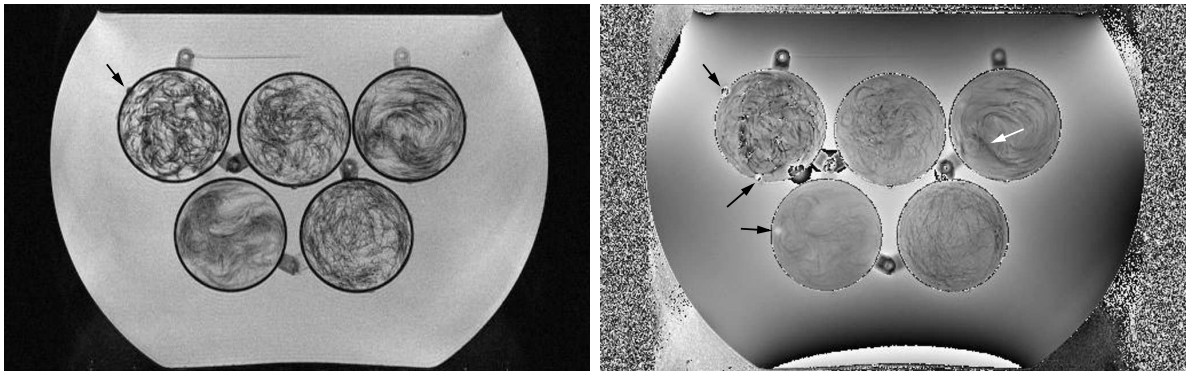

Figure 4.18: *Magnitude and phase image of the cylinder network obtained with the 3D high resolution SWI sequence ($T_E/T_R/\alpha$ = 20 ms/36 ms/15°, FOV = 256×160×64 mm^3, matrix = 512×320×128). The area around residual air bubbles (black arrows) was omitted during ROI definition, whereas regions with insufficiently randomly coiled strings (white arrow) may be located within the ROIs.*

$\varnothing/\mu$m	340	200	200, cut string	100	40
σ / %	0.6	0.6	0.6	1.3	2.5
SNR	167	167	167	77	40
T_2 / ms (GESSE)	383.4 ± 5.8	404.5 ± 3.7	416.4 ± 3.5	431.6 ± 8.5	445.2 ± 4.6
λ / % (free fit)	6.7 + 0.9	5.6 − 0.3	5.1 + 0.2	7.1 + 0.1	6.6 − 2.1
$\Delta\chi$ / ppm (free fit)	1.77 − 0.17	1.43 + 0.07	1.72 − 0.22	1.99 − 0.39	1.16 + 0.44
λ_{fix} / %	7.6 ± 0.14	5.3 ± 0.12	5.3 ± 0.12	7.2 ± 0.10	4.5 ± 0.33
$\Delta\chi$ / ppm (with λ_{fix})	1.58 + 0.02	1.51 − 0.01	1.66 − 0.16	1.96 − 0.36	1.68 − 0.08
$\Delta\chi$ / ppm (λ_{fix}, upper limit)	1.56 + 0.04	1.48 + 0.04	1.63 − 0.13	1.94 − 0.34	1.55 + 0.05
$\Delta\chi$ / ppm (λ_{fix}, lower limit)	1.62 − 0.02	1.56 − 0.06	1.72 − 0.22	2.01 − 0.41	1.80 − 0.20

Table 4.5: *Results of the capillary network phantom. The noise of the measured signal is shown with its standard deviation σ which reseluts in the listed signal to noise ratios. The T_2 times with their variation were obtained by fitting Eq. 3.2 to the signal curve. The freely obtained λ and $\Delta\chi$ values are listed with their deviation to the expected values of the phantom. Fixing the volume fraction λ_{fix} to the values known from phantom construction (Tab. 3.1) yields the $\Delta\chi$ values shown in the last three rows with their deviation to the expected values known from the single string measurements. The signal and root mean square error (MSE) contour plots of all string compartments are shown in the Appendix (Sec. A.2.1 and A.2.2).*

The T_2 times listed in Tab. 4.5 were obtained by fitting Eq. 3.2 to the symmetrically sampled spin echo. Only time points with $|t| \geq 4\,\text{ms}$ were chosen for fitting, because of the mono-exponential signal behavior of the long time scale asymptote. mono-exponential. The T_2 times obtained by the GESSE sequence differ a little from the times obtained by a CPMG sequence which was found to be $T_{2,CPMG} = 422 \pm 15\,\text{ms}$ for all string compartments. However, the measured GESSE signal curves were corrected with the T_2 times of the GESSE measurement found intrinsically. The T_2-corrected curves of all compartments are shown in the Appendix (Sec. A.2.1).

The λ and $\Delta\chi$ values of the different string networks were estimated by the position of the minimal MSEs. For this purpose the MSEs were calculated between the T_2-corrected signal-time curve around the spin echo and the signal simulation of the cylinder network model (Eq. 2.81). The simulation parameters were changed for $\lambda = 0.0$-0.1 in steps of

0.001 and $\Delta\chi = 0.7\text{-}2.2\,\text{ppm}$ in steps of 0.01 ppm. This resulted in MSE contour plots shown in the Appendix (Sec. A.2.2). The minimal MSEs, one for each string diameter, gave the λ and $\Delta\chi$ pairs with the best fitting signal curves. They are listed in Tab. 4.5 and denoted with "free fit".

The obtained volume fractions λ were close to those known from phantom construction (λ_{fix}), except for the $\varnothing = 40\,\mu\text{m}$ string network which was overestimated due to its low $\Delta\chi$ and vice versa. The $\Delta\chi$ values found for the $\varnothing = 200$ and $340\,\mu\text{m}$ strings were comparable to the $\Delta\chi$ known from the single string measurements (Tab. 4.4). However, the $\Delta\chi$ of the $\varnothing = 100\,\mu\text{m}$ string is too high although the volume fraction matches λ_{fix}.

Fixing the volume fraction to λ_{fix} yields $\Delta\chi$ values shown in the last three rows of Tab. 4.5. These $\Delta\chi$ values are even closer to those obtained from the single string measurements. Also, the $\Delta\chi$ of the $\varnothing = 40\,\mu\text{m}$ string network is now close the expected value with 1.6 ppm. However, for the $\varnothing = 100\,\mu\text{m}$ string network $\Delta\chi$ is still overestimated. This suggests that the non-sufficiently randomly oriented strings, which were observed in the high resolution phase image for the $\varnothing = 100\,\mu\text{m}$ string compartment (Fig. 4.18, white arrow), compromise the measured signal. Thus, the signal simulation of a network with randomly oriented cylinders fails to describe the observed signal correctly.

4.2.3. In Vivo Measurement

To further investigate the network signal evolution a healthy volunteer was scanned. The GESSE signal curve is shown in Fig. 4.19 for white and gray matter. The signal-to-noise ratio was about 140 for both, white and gray matter. Each curve was corrected for T_2 decay in a similar manner as described above for the capillary network phantom. The time for which the long scale asymptotic approximation is valid was estimated with an assumed blood oxygenation of $Y = 0.55$ which results in12.2 ms for 3 T (Eq. 2.85). Thus, Eq. 3.2 was fitted to the signal for times longer than $|t| \geq 14\,\text{ms}$. The obtained T_2 times were 75.4 ± 3.8 and $61.8 \pm 1.0\,\text{ms}$ for white and gray matter, respectively. The T_2 of white matter found, was comparable with the literature, where a T_2 of $69 \pm 3\,\text{ms}$ at 3 T was reported by Stanisz et al. (2005). The T_2 time of gray matter, however, is lower as known from the literature ($T_2 = 99 \pm 7$ at 3 T, Stanisz et al. (2005)) and even lower as the white matter T_2 time. This discrepancy may be caused by the careful definition of the gray matter ROI in the presented work, where voxels close to the cerebrospinal fluid were omitted.

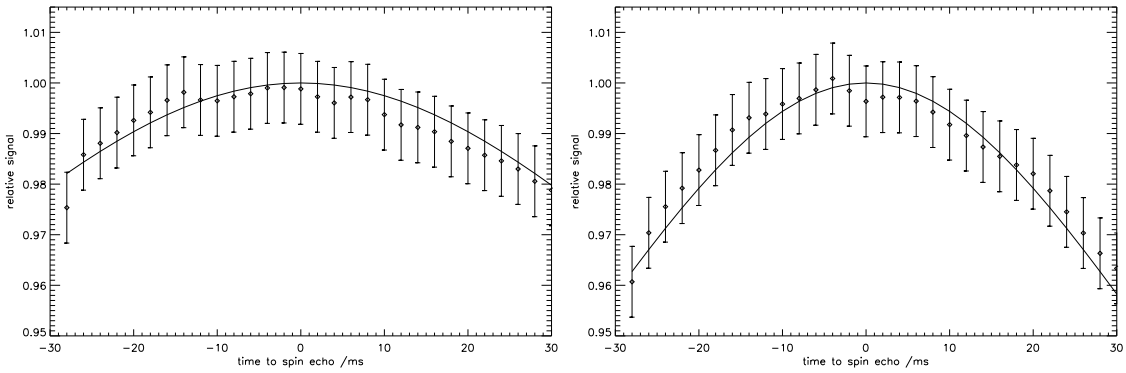

Figure 4.19: *T_2 corrected signal around spin echo obtained in vivo for white (left, $r^2 = 0.91$) and gray (right, $r^2 = 0.98$) matter. The noise was measured to be $\sigma = 0.007$ in a homogenous background ROI which corresponds to a SNR of about 143.*

The contour plots of MSEs, calculated from Eq. 2.81 and the measured signal curve, are shown in Fig. 4.20. The position of the minimal MSE is marked by dashed lines and a cross symbol. The counter plot was calculated for blood volume fractions λ ranging from 0 to 5% and blood oxygenations Y from 50 to 100%. The results of the MSE evaluation is summarized in Tab. 4.6 and shows the obtained T_2 times, λ and Y values for white and gray matter. The values for the blood oxygenation seem to be in agreement with the literature (Schmidt and Thews, 1987; Hagendorff et al., 1994), but the blood volume fraction differs from the expected values of about 1.5% for white and 3.0% for gray matter (Sec. 2.3.6). This mismatch in λ also compromises the simultaneously obtained Y value. Thus, a better verification of the capillary network model *in vivo* can only be achieved if one of the two parameters λ or Y will be determined independently.

	T_2 / ms	λ / %	Y / %
white matter	75.4 ± 3.8	2.1	72
gray matter	61.8 ± 1.0	2.6	66

Table 4.6: *Results of in vivo application of the capillary network signal simulation in white and gray matter. The T_2 times were obtained by fitting Eq. 3.2 to the GESSE signal-time curve. The λ and Y values obtained by the minimum MSE in the contour plots shown in Fig. 4.20. Y was calculated using the individual hematocrit of Hct = 0.41.*

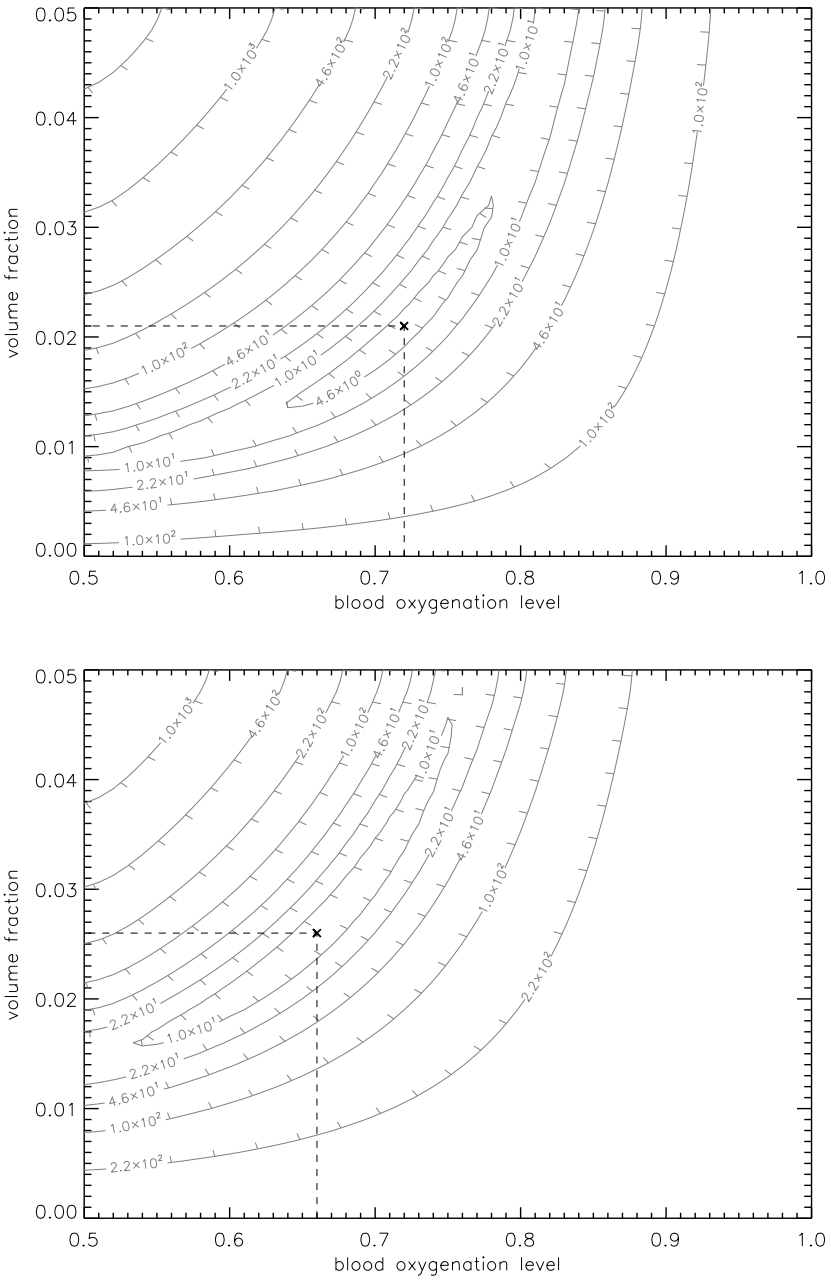

Figure 4.20: *Minimal root mean square errors (MSE) obtained between signal theory and in vivo measurement for white (top) and gray (bottom) matter.*

One man's artifact is another man's contrast.

Roberts and Rowley (2003)

V
Discussion

The MR signal formation of magnetic heterogeneous tissue was investigated in the work presented in this thesis. The signal was acquired using special T_2^*-weighted multi echo gradient echo sequences which are sensitive to susceptibility differences.

The model of a single magnetized cylinder was used for simulating the MR-signal. The shape of a voxel as encountered in real MRI measurements was taken into account for simulation. The simulation's results were verified by systematic phantom measurements for the first time. The *in vivo* application of this method resulted reasonable physiological parameters which were also comparable with literature.

The extension of the single cylinder model to a network of randomly oriented and positioned cylinders was also verified by phantom measurements. However, the ambiguity between the blood volume fraction and oxygenation level causes difficulties in separating these two parameters under *in vivo* conditions. A closer investigation of this ambiguity has to be carried out in future studies which should include invasive oxygen measurements by using microelectrodes in animal experiments.

5.1. Single Capillaries and Veins

5.1.1. Simulation

The results of the numerical simulation of the signal in presence of a single cylinder coincides for the cylindrical voxel only with the analytical solution given by Yablonskiy

and Haacke (1994). Numerical errors which may have been caused by the simulation's discretized grid were negligible because of the large array size chosen (with $2^{10} \times 2^{10}$ points). No errors could be observed in a comparison of the analytical solution with the results of the numerical simulation.

The advantage of the numerical simulation developed within the scope of this thesis is the ability to consider non-cylindrical voxel shapes as well as additional concentric compartments, which can be used to simulate the glass wall of a capillary in phantom measurements. Thus, the simulation proposed in the presented work can be extended easily. Macroscopic field gradients, for instance, could also be taken into account by superimposing the field distribution of the cylinder with a linear gradient. This flexibility of the numerical simulation is important for comparisons with actual MRI measurements in which no cylindrical voxels can be acquired.

A voxel's signal is determined by the sampling point spread function (sPSF) which depends on the k-space sampling scheme of the specific MRI sequence. For example, simple Cartesian sampling of a cubic k-space results in a sinc-shaped sPSF. The shape of the sPSF determines the influence of the field distribution on the sampled signal and, consequently, how the signal evolves over time. This effect was successfully demonstrated in this work. Simulated signals with identical simulation parameters except for the voxel shape showed differences up to 100% at late echo times (Fig. 4.1).

For vessels oriented parallel to $\vec{B}_0$, the voxel geometry does not influence the signal, because the extravascular field inhomogeneity vanishes for $\theta = 0°$. In such cases the computationally less demanding and faster analytical signal solution proposed by Yablonskiy and Haacke (1994) can be used to simulate a voxel's signal (see Sec. 2.3.5.3). This might be applicable for phantom experiments, where the capillary orientation can be adjusted parallel to the main magnetic field precisely. However, for *in vivo* measurements only few vessels, like the *Vv. centrales* are oriented parallel to $\vec{B}_0$. Investigating veins with other orientations by using only the analytical solution will lead to tremendously inaccurate results.

The proposed numerical simulation is also capable to optimize the venous contrast of the susceptibility weighted imaging (SWI) sequence, e.g., for different slice thicknesses, voxel aspect ratios and main magnetic field strengths (Deistung et al., 2007). This will further improve the understanding of signal formation and contrast mechanisms in SWI.

5.1.2. Single Capillary Phantom Measurements

The single capillary phantom was chosen, because it represents the basic model used in many MRI studies to investigate the signal formation of tubular structures. The work of Yablonskiy (1998), An and Lin (2002), Schröder et al. (2006) and He and Yablonskiy

(2007) used the capillary network theory which is based on the model of randomly oriented and positioned cylinders to study the influence of capillary network phantoms or the cerebral blood capillary network *in vivo* on MR signal formation. A main drawback of these studies, however, has always been the missing experimental verification of the fundamental model of a single infinitely long cylinder. This verification was conducted for the first time in the work presented in this thesis.

Good agreement was observed between simulated and measured signal decays for all phantom experiments. The variation between the experimentally adjusted λ and $\Delta\chi$ values and those obtained by fitting the simulation to the measurement was only 12% for λ and 10% for $\Delta\chi$. This variation can be attributed to experimental limitations such as the adjustment of an accurate $\Delta\chi$, the precise angle between the capillary axis and $\vec{B_0}$ and an exact positioning of the imaging plane perpendicular to the cylinder axis. In a few cases the mismatch between the adjusted and the estimated values for λ and $\Delta\chi$ was up 30%. Although these deviations are relatively, they occurred only sporadic and were not correlated to other parameters, such as θ or B_0, which further characterize the experimental setup. Thus, it can be assumed that these relatively strong errors were outliers which may have been caused by improper experimental setup or other non-systematic errors.

Other potential error sources, such as macroscopic field inhomogeneities or improper sub-voxel shifts, were not found to influence the results substantially. Placing the cylinder off-center in x- and y-direction within the voxel resulted only in a drop of the extravascular T_2 decay time which was caused by the additional inhomogeneity resulting from the asymmetric field distribution within the voxel.

The measurements of the single capillary phantom with different background field gradient strengths showed no detectable influence of those inhomogeneities on the voxel signal. The investigated voxels were relatively small, but a reasonable signal loss was visible in voxels enlarged artificially by complex summation over a number of voxels. Macroscopic field inhomogeneities were eliminated at the beginning of each measurement by carefully shimming the region around the voxel of interest. Therefore, any effect of macroscopic inhomogeneities on the voxel signal can be excluded.

5.1.3. In Vivo Measurements

Applying the validated single cylinder signal simulation to the *in vivo* experiments yielded blood oxygenation levels ($\bar{Y}_{MESWI} = 0.55 \pm 0.02$) which were in good agreement with the values obtained for several vessels of the same volunteers by using a different MRI method which is based on high resolution phase information ($\bar{Y}_{PHSWI} = 0.53 \pm 0.03$). Another MRI study of Haacke et al. (1995) used a similar high resolution phase-based method but with two additional echo times. That work reported blood oxygenation levels of $Y = 0.54 \pm 0.03$, based on the analysis of 14 small

cerebral veins in five healthy volunteers, which is in excellent agreement with the results obtained in the work presented in this thesis.

All these findings are in agreement with blood oxygenation values determined by PET using ^{15}O labeled oxygen. Ito et al. (2004) reported an OEF of 0.44 ± 0.06 in 70 healthy volunteers, which corresponds to a blood oxygenation of $Y \approx 0.56$. These values were validated independently in animal experiments in which oxygenation partial pressures in normal rat brains were determined by using microelectrodes with a mean values of $Y = 0.6 \pm 0.07$ (Hagendorff et al., 1994).

The correct susceptibility difference between completely oxygenated and deoxygenated blood $\Delta\chi_{do}$ has to be known to calculate the blood oxygenation level Y (Eq. 2.69). The value measured by Weisskoff and Kiihne (1992) has been widely used in the MRI literature and it was applied here in order to compare the results directly with the MRI study of Haacke et al. (1995) who also used $\Delta\chi_{do}$ as given by Weisskoff and Kiihne (1992). By applying, for example the $\Delta\chi_{do}$ found by Spees et al. (2001), the mean oxygenation $\bar{Y}_{MESWI} = 0.55$ would rise to 0.70. Since the work presented herein does not allow a determination of $\Delta\chi_{do}$, it is not possible to comment on the true value of blood's susceptibility. Spees et al. (2001) pointed out the discrepancy between their own measurements and the results of Weisskoff and Kiihne (1992). However, they gave no explanation of possible reasons for this discrepancy. Thus, for correct comparison with other MRI studies the methods for calculating the blood oxygenation and the values of the constants used have to be considered.

The presented method is also able to detect and quantify changes in Y induced by vasodilation or vasoconstriction caused by carbogen or caffeine, respectively. The simulated signal fitted the *in vivo* data very well and the Y values altered in the expected manner. The blood oxygenation level increased during carbogen breathing and decreased after caffeine ingestion.

Effects of macroscopic field inhomogeneities can be neglected for the *in vivo* measurements, since the investigated vessels were located in regions not much affected by strong macroscopic field inhomogeneities, as those would appear near the nasal cavity or petrous portion of the temporal bone. The spatial resolution in our study was also relatively high for field inhomogeneities with low spatial frequencies compared to the narrow field inhomogeneity produced by a small vein and have a negligible effect in small voxels. Furthermore, as in the case of the phantom measurements, a considerable effort was under taken into obtaining a good shim near the investigated vessels for all *in vivo* measurements. The shim was adjusted to a small region around the investigated vessel, which was larger than the voxel size but smaller than the subject's head. This ensured good reduction of background field inhomogeneities.

5.2. Capillary Network

5.2.1. Simulations

Signal-time curves of the capillary network were calculated for different λ and Y values according to Eq. 2.81. The initial signal magnitude of the curves scales with the volume fraction λ. The signal decay depends on the blood oxygenation level Y but also on λ. The decay is less pronounced for low λ and high Y and more pronounced for high λ and low Y values (Fig. 4.10). As can also be seen in Fig. 4.10 some signal curves nearly coincide for different λ and Y pairs. In a further simulation is was shown that parameter pairs with low values (e.g. $\lambda = 0.025$ and $Y = 0.25$) describe nearly the same signal curve as pairs with high values (e.g. $\lambda = 0.075$ and $Y = 0.75$). The root mean square errors (MSE) between signal curves calculated with such correlated parameter pairs are very close to zero. Thus, the case of MSE = 0, where λ and Y as well as their resulting signal curve exactly matches the previously defined parameters (e.g. $\lambda = 0.05$ and $Y = 0.55$), could be visualized only on a logarithmic scale (Fig. 4.11).

This finding leads to the assumption that a fitting routine, which simultaneously optimizes the λ and Y parameters, will not find the true parameter set. The routine will only obtain arbitrary values within the subset of correlated λ-Y pairs. He and Yablonskiy (2007), who employed a similar MRI technique and additionally fitted the transverse relaxation time and an additional signal compartment of the cerebrospinal fluid, mentioned that a good initial estimate of all free parameters is essential for the fitting routine. Furthermore, if the measured signal curve is compromised by noise, as simulated for different noise levels in this work, the minimal MSE does not necessarily reflect the true λ-Y pair.

The effects caused by mutual avoiding cylinders, as assumed in the simulation of the network's signal, showed a negligible influence for the parameter $z = 1$ which describes a network formed by randomly positioned and oriented, non-overlapping cylinders. Since such a network was generated by the network phantom constructed for the work presented in this thesis the influence of the effects of mutual avoiding cylinders on the signal could not be further investigated by using this phantom.

For a z value of 2λ, which is a good approximation of a network formed by blood capillaries in brain tissue, the signal showed a distinct deviation for echo times later than 30 ms. This deviation causes an extreme underestimation of the blood oxygenation level. If only time points below 30 ms are taken into account, the blood oxygenation will be underestimated by less than 10%. These findings were used for the first *in vivo* measurements of a healthy human brain by acquiring the signal only for echo times up to 30 ms. As a result the effects of mutual avoiding cylinders could be neglected in the simulation of the *in vivo* measurement.

A further verification of the effect of mutual avoiding cylinders was beyond the scope of the work presented herein. Such a verification has to be addressed to future studies, for which more sophisticated phantoms that are able to mimic mutually avoiding cylinders with z-values smaller than one have to be constructed.

5.2.2. Capillary Network Phantom Measurements

First, the single cylinder method was applied to determine the magnetic susceptibility difference between the single polypropylene (PP) strings and the silicone oil. The thinest string with $\varnothing = 40\,\mu$m was excluded, because of the limited gradient strength and, thus, limited spatial resolution of the whole body MR system. For the $\varnothing = 340$ and $100\,\mu$m strings, $\Delta\chi$ values of about 1.6 ppm were obtained, for the string with $\varnothing = 200\,\mu$m a $\Delta\chi$ of 1.5 ppm. These different $\Delta\chi$ values might be caused by different bulk materials of which the strings were produced. Despite the fact that all these strings were made from polypropylene (PP) slight differences in the material's density or concentration of different additives, such as the strings' color may influence the magnetic property of the bulk material.

The signal arising from the capillary network showed a weak oscillation around the simulated signal-time curve. This oscillation is caused by the slightly different resonance frequency of protons in the CH_3-group at the end of the -Si-O- backbone of the silicone oil compared to protons in the other CH_3-groups. The protons in the end groups are in a different molecular surrounding. This changes the local magnetic field which causes, in consequence, a different resonance frequency (chemical shift). As can be seen in the signal plots of Sec. A.2.1 the oscillation occurs several times along the evolution of the sampled signal, however the fit corrects for these oscillations. Thus, the effect of this signal oscillation was neglected for the investigations of the capillary network phantom.

The noise of the signal curves for the strings with $\varnothing = 340$ and $200\,\mu$m was very low due to the large voxels. Higher spatial resolution, i.e. smaller voxels, as it was necessary for the thinner strings, resulted in increased noise. Thus, the highest noise level was observed for the $\varnothing = 40\,\mu$m string and had a relative standard deviation of $\sigma = 0.025$. Noise of this magnitude can cause errors of up to 10% for both, λ and Y, parameters as it was demonstrated in the simulations of noisy signals (see Tab. 4.2). Furthermore, some discontinuities in the signal-time curve, particularly visible for the $\varnothing = 340$ and $100\,\mu$m strings, caused by the interleaved signal acquisition might induce additional errors in the estimation of the λ and Y parameters.

The λ and $\Delta\chi$ values obtained for the $\varnothing = 340$ and $200\,\mu$m strings were close to the expected values known from the construction of the phantom (λ) and single string measurements ($\Delta\chi$). The λ value of the $\varnothing = 40\,\mu$m string was a little higher than expected and thus its $\Delta\chi$ value was a slightly lower, because of the correlation between these two parameters. The λ of the $\varnothing = 100\,\mu$m string was as expected, but the $\Delta\chi$

was much higher compared to the single string experiment. This mismatch can not be attributed to different pairs of λ and $\Delta\chi$ having similar signal shapes. Thus, this overestimated $\Delta\chi$ value has to be ascribed to other effects.

Fixing λ to values known from the amount of material used for the phantom yields a better match of $\Delta\chi$ obtained by the single string measurements. As a result, the parameters of the $\varnothing = 40\,\mu$m string are also in better agreement. Only the high $\Delta\chi$ of the $\varnothing = 100\,\mu$m string persists. This might be caused by the string being less randomly coiled in some regions. This hypothesis was strengthened by the findings in high resolution phase images (Fig. 4.18 white arrow).

The mismatch between the two $\varnothing = 200\,\mu$m strings shows a slightly higher $\Delta\chi$ for the compartment containing a string cut into short pieces. It can be assumed that additional field inhomogeneities were generated by the ends of the pieces which cause additional signal loss. Thus, the model of an infinite cylinder is better imitated by a single, long, randomly coiled string. The coiling technique, however, can influence the results even more. This can be observed in the $\varnothing = 100\,\mu$m string compartment with cylinders insufficiently randomly oriented inside the network.

In summary, the capillary network signal simulation and the phantom measurements are in good agreement. The use of the silicone oil, to exclude any diffusion effects, was the key point for phantom construction. It led to similar results for all string diameters. In contrast, Schröder et al. (2006), who also conducted systematic capillary network phantom experiments, observed a correlation between $\Delta\chi$ and the string diameter. This dependency was caused by diffusion, since data in that study was obtained by using an aqueous solution as network matrix.

The difference between the magnetic susceptibilities of the PP strings and silicone oil was more than three times higher than the susceptibility difference expected in a healthy human brain under normal physiological condition. This high susceptibility difference causes an additional problem: the time interval in which the short term asymptotic behavior can be applied becomes very short. This results in a few sampled time points for this interval due to the limited temporal resolution of the MR sequence. For this short time interval the signal shows an quadratic exponential time dependency for $\Delta\chi$ and a linear exponential time dependency for λ (Eq. 2.83). The long term approximation (Eq. 2.84), however, is not sufficient to separate $\Delta\chi$ and λ, because both parameters are only linear exponential time dependent. If both time intervals of the short and long term asymptotic signal behavior contribute with high confidence, $\Delta\chi$ and λ might be separated. Thus, a network phantom with a lower $\Delta\chi$ value, for instance, 0.5 ppm would result in an even better agreement between signal theory and experiments.

Despite the ambiguity between λ and $\Delta\chi$, the capillary network phantom experiments in combination with the single string measurements sufficiently verified the signal simulation of the cylinder network as is was proposed by Yablonskiy and Haacke (1994).

5.2.3. In Vivo Measurement

The signal's evolution around the spin echo of the initial *in vivo* measurement showed a more pronounced signal loss for gray brain matter, compared to white matter. This behavior implies that there must be a higher blood volume fraction and/or lower blood oxygenation level in gray matter. This assertion was confirmed by estimating the λ and Y parameters using the minimal MSE (Fig. 4.20). However, the obtained blood volume fractions were almost equal for gray and white matter and do not agree with values known from physiology (Sec. 2.3.6), where a venous blood volume fraction of approximately 1.5% and 3% is expected for white and gray matter, respectively. If λ is fixed to these physiologic values, the blood oxygenation level of white matter will slightly drop and it will slightly increase for gray matter. Surprisingly, in this case, both blood oxygenation values would than almost be equal to $Y \approx 0.7$.

Such an uniform blood oxygenation of gray and white matter is in agreement with findings of An and Lin (2002) and He and Yablonskiy (2007) who also investigated the MR signal evolution around a spin echo. In the more recent study of He and Yablonskiy (2007), the authors found Y values of about 0.7 for ROIs drawn in white and gray matter. They also calculated maps of the Y parameter by fitting the simulated signal for each voxel and the resulting maps further confirmed the uniform blood oxygenation level in the brain. However, He and Yablonskiy (2007) found substantially lower venous blood volume fractions of 0.6% for white and 1.5% for gray matter which underestimate the physiological expected venous blood volume by a factor of two. If λ values this low would be assumed for the *in vivo* measurement as conducted in this work, the blood oxygenation level would drop to about 0.5. This obvious discrepancy is caused by the use of different hematocrit and blood susceptibility values for the calculation of Y (Eq. 2.69). He and Yablonskiy (2007) assumed a low Hct of 0.34, which is predominant in small vessels and blood capillaries (Eichling et al., 1975) and a higher $\Delta\chi_{do}$ value of $4\pi \cdot 0.27\,\text{ppm} = 3.39\,\text{ppm}$ as reported by Spees et al. (2001). If the Y value found by He and Yablonskiy (2007) is recalculated using the same values for Hct and $\Delta\chi_{do}$ as in the work presented in this thesis, a blood oxygenation level of about 0.52 is obtained. Also this result is in agreement with the Y value which would be observed using the results of this work for such low volume fractions. In summary, it can be asserted that the *in vivo* measurements conducted for the work presented herein yielded realistic results. However, a better separation of the λ and Y parameters has to be investigated in future studies.

Compared to the *in vivo* measurement of a single venous vessel, a higher blood oxygenation level was found in the *in vivo* measurement of the capillary network. The Y values of both methods were calculated in the same fashion using the Hct of the respective subject, but using the same $\Delta\chi_{do}$ of $4\pi \cdot 0.18 = 2.26\,\text{ppm}$ (Weisskoff and Kiihne, 1992) for all subjects. The discrepancy between the capillary network and the single vein may

be attributed to the fact that the oxygen exchange between blood and tissue is taking place in the capillary network. The oxygenation level in the capillary network is an average over different states of the oxygen extraction ongoing in the network. It is thus higher than in the veins only. Animal experiments, in which the blood oxygenation in a distinct brain region can be determined by microelectrodes and compared to Y values estimated by MR measurements, should be helpful to further verify the observed *in vivo* blood oxygenation levels.

The studies of An and Lin (2002) and He and Yablonskiy (2007) employed a correction for macroscopic field inhomogeneities. These macroscopic inhomogeneities cause additional signal loss and thus an overestimation of λ or an underestimation of Y. However, such an error was not observed for the *in vivo* measurement of this work, because considerable effort was made to minimize the influence of macroscopic field inhomogeneities and, thus, making a correction unnecessary. The investigated region was well shimmed but also chosen to be in a more cranial and occipital region at a distance from field inhomogeneities induced by the frontal sinuses, nasal cavity and petrous portion of the temporal bone. Additionally, the thickness of the imaged slice of 3 mm was relatively thin compared to the 8 and 6 mm slice thicknesses of An and Lin (2002) and He and Yablonskiy (2007), respectively.

The longer T_2 time of white matter compared to gray matter is contrary to values found in literature, where a longer T_2 time is assigned to gray matter, e.g. Stanisz et al. (2005) who reported T_2 times for *in vitro* bovine brain matter at 3 T. However, the same discrepancy was also observed by Gröhn et al. (2005) and Zhou et al. (2001) who investigated irreversible transverse relaxation times in human brain. They attributed this effect to a partial volume of cerebrospinal fluid in gray matter voxels as it occurs in low resolution MR images. The gray matter ROI used for the investigation of the GESSE signal in the work presented in this thesis was defined carefully, omitting voxels with a partial volume of cerebrospinal fluid. Thus, the T_2 time of gray matter obtained in the presented work should be reasonable.

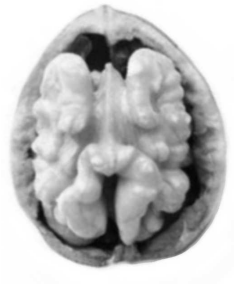

The seat of all human behaviour, of emotions, memory and consciousness, the human brain is the most complex structure known to science, containing hundreds of billions of connected, communicating cells. Scientists know more about the universe than the brain, which really is the final frontier of human knowledge.

The Brain in a Nutshell, Costandi (2007)

VI

Conclusion and Outlook

It was demonstrated in the work presented in this thesis that the blood oxygenation of single venous vessels can be extracted *in vivo* by exploiting their influence on the MR signal decay. For the first time the theoretical model of an infinitely long cylinder was verified by systematic phantom experiments in MRI. The recovery of the signal at late echo times differed depending on the vessel orientation, volume fraction and susceptibility difference in both phantom and *in vivo* measurements. This behavior was confirmed by simulations. The study of Barth et al. (1999) found apparently paradox signal behaviors in high resolution multi echo functional MRI measurements. The authors correctly attributed this finding to single veins within the investigated voxel. The work presented in this thesis demonstrates a method to simulate and quantify this effect. The results for the carbogen and caffeine induced oxygenation changes are also very encouraging for further studies, e.g. quantification of blood oxygenation changes during neuronal activation. Such a study would be helpful for a deeper understanding of the BOLD-response and its relation to the underlying neural activity. The method can already be used for improving the diagnostics of stroke or cerebral tumors as well as for monitoring the therapeutic progress.

For the first time, the signal shape around a spin echo created by a phantom containing a capillary network were verified by additional measurements of a single string. As it was already apparent in the simulations, the interdependency of volume fraction and blood oxygenation hampers the separation of these two parameters. A solution to this limitation has to be addressed to future studies. It was further shown that the effect of mutually avoiding cylinders has no impact on the signal's evolution observed in the

network phantom. However, the signal simulation for a more realistic blood capillary network showed a distinct influence on the signal evolution for late echo times. These findings in simulations with mutually avoiding cylinders were applied to minimize their influence in an initial *in vivo* measurement by sampling the signal only for short echo times.

The initial *in vivo* measurement did not jet allow a separation of λ and Y. However, fixing λ to values known from physiology yielded results comparable to the MRI study of He and Yablonskiy (2007), who encountered the same limitation. A robust and trustworthy separation of these two parameters from the MR signal evolution will be a challenge for future studies. Nevertheless, the theoretical cylinder network model and its application is a promising tool for MR-based *in vivo* quantification of tissue hemodynamics. Future verifications and improvements of the method will give this method a significant advantage over ^{15}O-PET, which, up to now, is the standard method for measurements of brain hemodynamics and metabolism, in studies of hemodynamic responses during neuronal activity and clinical diagnosis of cerebral pathologies.

Bibliography

A. Abragam. *Principles of Nuclear Magnetism*. Oxford Science Publications, 1994.

A. L. Alexander, B. E. Chapman, J. S. Tsuruda, and D. L. Parker. A median filter for 3D FAST spin echo black blood images of cerebral vessels. *Magn Reson Med*, 43 (2):310–313, 2000.

H. An and W. Lin. Cerebral oxygen extraction fraction and cerebral venous blood volume measurements using Magn Reson Imaging: effects of magnetic field variation. *Magn Reson Med*, 47(5):958–966, 2002.

G. Badurek. *Biological and Medical Applications of Nuclear Physics 2*, chapter 6 NMR - Nuclear Magnetic Resonance, pages 73–75. Lecture Notes, Technical University Vienna, 1998.

H. Barrett and K. Myers. *Foundations of Image Science*, chapter Fourier Analysis, page 123. John Wiley & Sons, 2004.

M. Barth, J. R. Reichenbach, R. Venkatesan, E. Moser, and E. M. Haacke. High-resolution, multiple gradient-echo functional MRI at 1.5 T. *Magn Reson Imaging*, 17(3):321–329, 1999.

M. Barth, I. M. Nöbauer-Huhmann, J. R. Reichenbach, V. Mlynárik, A. Schöggl, C. Matula, and S. Trattnig. High-resolution three-dimensional contrast-enhanced blood oxygenation level-dependent magnetic resonance venography of brain tumors at 3 Tesla: first clinical experience and comparison with 1.5 Tesla. *Invest Radiol*, 38(7):409–414, 2003.

P. Basser, M. Mattiello, and D. Le Bihan. *Diffusion and Perfusion Magnetic Resonance Imaging*, chapter Anisotropic Diffusion: MR Diffusion Tensor Imaging, pages 140–149. Raven Press, New York, 1995.

C. R. Becker, L. R. Schad, and W. J. Lorenz. Measurement of diffusion coefficients using a quick echo split NMR imaging technique. *Magn Reson Imaging*, 12(8): 1167–1174, 1994.

M. A. Bernstein, K. F. King, and X. J. Zhou. *Handbook of MRI Pulse Sequences*. Elsevier, 2004.

R. Bhagwandien, R. van Ee, R. Beersma, C. J. Bakker, M. A. Moerland, and J. J. Lagendijk. Numerical analysis of the magnetic field for arbitrary magnetic susceptibility distributions in 2D. *Magn Reson Imaging*, 10(2):299–313, 1992.

F. Bloch. Nuclear Induction. *Phys. Rev.*, 70(7-8):460–474, 1946.

R. Bracewell. *The Fourier Transform and Its Applications*. McGraw-Hill, New York, 1986.

W. G. Bradley. Carmen lecture. Flow phenomena in MR imaging. *AJR Am J Roentgenol*, 150(5):983–994, 1988.

E. Brigham. *The Fast Fourier Transform*. Prentice-Hall, Englewood Cliffs, NJ, 1974.

R. J. S. Brown. Distribution of fields from randomly placed dipoles : Free precession signal decay as result of magnetic grains. *Phys Rev*, 121(5):1379–1383, 1961.

H. F. Bunn and B. G. Forget. *Hemoglobin: Molecular, genetic and clinical aspects*. W.B. Saunders Company, 1986.

P. T. Callaghan. *Principles of Nuclear Magnetic Resonance Microscopy*. Oxford Science Publications, 1995.

O. G. Cameron, J. G. Modell, and M. Hariharan. Caffeine and human cerebral blood flow: a positron emission tomography study. *Life Sci*, 47(13):1141–1146, 1990.

M. Cerdonio, S. Morante, D. Torresani, S. Vitale, A. DeYoung, and R. W. Noble. Reexamination of the evidence for paramagnetism in oxy- and carbonmonoxyhemoglobins. *Proc Natl Acad Sci U S A*, 82(1):102–103, 1985.

M. Costandi. The Brain in a Nutshell. *Neurophilosophy Weblog*, 2007. URL `http://scienceblogs.com/neurophilosophy`. (Retrieved April 26, 2003).

A. Deistung. Entwicklung einer flexiblen Benutzerschnittstelle zur Rekonstruktion von hochaufgelösten MR-Daten in der suszeptibilitätsgewichteten Bildgebung. Master's thesis, Fachhochschule Jena, November 2005.

A. Deistung, H. J. Mentzel, A. Rauscher, S. Witoszynskyj, W. A. Kaiser, and J. R. Reichenbach. Demonstration of paramagnetic and diamagnetic cerebral lesions by using susceptibility weighted phase imaging (SWI). *Z Med Phys*, 16(4):261–267, 2006.

A. Deistung, J. Sedlacik, A. Rauscher, J. Stadler, C. Tempelmann, J. Bernarding, P. Müller, E. Dittrich, and J. R. Reichenbach. Susceptibility Weighted Imaging at 1.5T, 3T and 7T. In *Proc Intl Mag Reson Med*, volume 15, page 2076, 2007.

W. C. Dickinson. The Time Average Magnetic Field at the Nucleus in Nuclear Magnetic Resonance Experiments. *Physical Review*, 81(5):717–731, 1951.

M. D. Does, J. Zhong, and J. C. Gore. In vivo measurement of ADC change due to intravascular susceptibility variation. *Magn Reson Med*, 41(2):236–240, 1999.

H. M. Duvernoy. *The human brain : surface, three-dimensional sectional anatomy with MRI, and blood supply*. Springer, Wien, New York, 2 edition, 1999.

H. M. Duvernoy, S. Delon, and J. L. Vannson. Cortical blood vessels of the human brain. *Brain Res Bull*, 7(5):519–579, 1981.

W. Edelstein, J. Hutchison, G. Johnson, and T. Redpath. Spin warp NMR imaging and applications to human whole-body imaging. *Phys. Med. Biol.*, 25:751–756, 1980.

J. O. Eichling, M. E. Raichle, R. L. Grubb, K. B. Larson, and M. M. Ter-Pogossian. In vivo determination of cerebral blood volume with radioactive oxygen-15 in the monkey. *Circ Res*, 37(6):707–714, 1975.

W. H. Elliott and D. C. Elliott, editors. *Biochemistry and molecular biology*. Oxford Univ. Press, 2005.

F. H. Epstein, J. P. Mugler, 3rd., and J. R. Brookeman. Spoiling of transverse magnetization in gradient-echo (GRE) imaging during the approach to steady state. *Magn.Reson.Med.*, 35(2):237–245, 1996.

R. Ernst and W. Anderson. Application of Fourier Transform Spectroscopy to Magnetic Resonance. *Rev Sci Instrum*, 37:93–102, 1966.

M. Essig, J. R. Reichenbach, L. R. Schad, S. O. Schoenberg, J. Debus, and W. A. Kaiser. High-resolution MR venography of cerebral arteriovenous malformations. *Magn Reson Imaging*, 17(10):1417–1425, 1999.

M. A. Fernández-Seara, A. Techawiboonwong, J. A. Detre, and F. W. Wehrli. MR susceptometry for measuring global brain oxygen extraction. *Magn Reson Med*, 55 (5):967–973, 2006.

M. Ferrari, L. Mottola, and V. Quaresima. Principles, techniques, and limitations of near infrared spectroscopy. *Can J Appl Physiol*, 29(4):463–487, 2004.

A. S. Field, P. J. Laurienti, Y. F. Yen, J. H. Burdette, and D. M. Moody. Dietary caffeine consumption and withdrawal: confounding variables in quantitative cerebral perfusion studies? *Radiology*, 227(1):129–135, 2003.

L. R. Frank, A. P. Crawley, and R. B. Buxton. Elimination of oblique flow artifacts in magnetic resonance imaging. *Magn Reson Med*, 25(2):299–307, 1992.

B. B. Fredholm, K. Bättig, J. Holmén, A. Nehlig, and E. E. Zvartau. Actions of caffeine in the brain with special reference to factors that contribute to its widespread use. *Pharmacol Rev*, 51(1):83–133, 1999.

A. Garroway, P. Grannell, and P. Mansfield. Image formation in NMR by a selective irradiative process. *J. Phys. C: Solid State Phys.*, 7:457–462, 1974.

M. A. Griswold, P. M. Jakob, R. M. Heidemann, M. Nittka, V. Jellus, J. Wang, B. Kiefer, and A. Haase. Generalized autocalibrating partially parallel acquisitions (GRAPPA). *Magn Reson Med*, 47(6):1202–1210, 2002.

H. I. Gröhn, S. Michaeli, M. Garwood, R. A. Kauppinen, and O. H. Gröhn. Quantitative T(1rho) and adiabatic Carr-Purcell T2 magnetic resonance imaging of human occipital lobe at 4 T. *Magn Reson Med*, 54(1):14–19, 2005.

H. Gudbjartsson and S. Patz. The Rician distribution of noisy MRI data. *Magn Reson Med*, 34(6):910–914, 1995.

D. Güllmar, T. Jaap, M. E. Bellemann, J. Haueisen, and J. R. Reichenbach. DTI measurements of isotropic and anisotropic media. In *Biomedizinische Technik*, volume 47 Suppl 1, pages 420–2, 2002.

R. R. Gupta. *Landolt-Börnstein Numerical data and functional relationships in science and technology: new series II*, volume 16, Diamagnetic susceptibility. Springer, 1986.

D. Güllmar, J. Haueisen, and J. Reichenbach. Analysis of b-value calculations in diffusion weighted and diffusion tensor imaging. *Concepts in Magnetic Resonance Part A*, 25A(6):53–66, 2005.

E. M. Haacke. The effects of finite sampling in spin-echo or field-echo magnetic resonance imaging. *Magn Reson Med*, 4(5):407–421, 1987.

E. M. Haacke, S. Lai, D. A. Yablonskiy, and W. Lin. In vivo validation of the BOLD mechanism: A review of signal changes in gradient echo functional MRI in the presence of flow. *Int J Imag Syst Technol*, 6:153–163, 1995.

E. M. Haacke, R. W. Brown, M. R. Thompson, and R. Venkatesan. *Magnetic Resonance Imaging; Physical Principles and Sequence Design*. Wiley, 1999.

E. M. Haacke, C. Hu, T. B. Parrish, and Y. Xu. Whole Brain Stress Test Using Caffeine: Effects on fMagn Reson Imaging and SWI at 3T. In *Proc Intl Mag Reson Med*, volume 11, page 1731, 2003.

E. M. Haacke, Y. Xu, Y. C. Cheng, and J. R. Reichenbach. Susceptibility weighted imaging (SWI). *Magn Reson Med*, 52(3):612–618, 2004.

A. Haase, J. Frahm, D. Matthaei, W. Hänicke, and K.-D. Merboldt. FLASH Imaging. Rapid NMR Imaging Using Low Flip-Angle Pulses. *J Magn Reson*, 67:258–266, 1985.

A. Hagendorff, J. Grote, and Z. K. *Regulation of blood flow and tissue oxygen supply*, chapter An improved open cranial window technique preserving brain tissue oxygen supply conditions, pages 195–216. Fischer, 1994.

E. Hahn. Spin Echoes. *Phys. Rev.*, 80:580 – 594, 1950.

L. Harrison and K. Blackwell. Hypoxia and anemia: factors in decreased sensitivity to radiation therapy and chemotherapy? *Oncologist*, 9 Suppl 5:31–40, 2004.

X. He and D. A. Yablonskiy. Quantitative BOLD: mapping of human cerebral deoxygenated blood volume and oxygen extraction fraction: default state. *Magn Reson Med*, 57(1):115–126, 2007.

M. Hermier and N. Nighoghossian. Contribution of susceptibility-weighted imaging to acute stroke assessment. *Stroke*, 35(8):1989–1994, 2004.

H. Ito, I. Kanno, C. Kato, T. Sasaki, K. Ishii, Y. Ouchi, A. Iida, H. Okazawa, K. Hayashida, N. Tsuyuguchi, K. Ishii, Y. Kuwabara, and M. Senda. Database of normal human cerebral blood flow, cerebral blood volume, cerebral oxygen extraction fraction and cerebral metabolic rate of oxygen measured by positron emission tomography with 15O-labelled carbon dioxide or water, carbon monoxide and oxygen: a multicentre study in Japan. *Eur J Nucl Med Mol Imaging*, 31(5):635–643, 2004.

R. Jennison. *Fourier Transforms and Convolutions for the Experimentalist*. Pergamon Pr, Oxford etc., 1961.

G. Johnson and J. Hutchison. The limitations of NMR recalled-echo imaging techniques. *J Magn Reson*, 63:14–30, 1985.

G. Johnson, J. M. S. Hutchison, T. W. Redpath, and L. M. Eastwood. Improvements in Performance Time for Simultaneous Three-Dimensional NMR Imaging. *J. Magn. Reson.*, 54:374–384, 1983.

J. H. Kaanders, J. Bussink, and A. J. van der Kogel. Clinical studies of hypoxia modification in radiotherapy. *Semin Radiat Oncol*, 14(3):233–240, 2004.

E. Kholmovski and D. Parker. High Resolution Magnetic Resonance Venography at 3 Tesla: Optimized Acquisition, Reconstruction, and Post-Processing. In *Proc Intl Soc Mag Reson Med*, volume 14, page 810, 2006.

P. B. Kingsley, R. J. Ogg, W. E. Reddick, and R. G. Steen. Correction of errors caused by imperfect inversion pulses in MR imaging measurement of T1 relaxation times. *Magn Reson Imaging*, 16(9):1049–1055, 1998.

V. G. Kiselev. Effect of magnetic field gradients induced by microvasculature on NMR measurements of molecular self-diffusion in biological tissues. *J Magn Reson*, 170 (2):228–235, 2004.

V. G. Kiselev and S. Posse. Analytical Theory of Susceptibility Induced NMR Signal Dephasing in a Cerebrovascular Network. *Phys. Rev. Lett.*, 81(25):5696–5699, 1998.

V. G. Kiselev and S. Posse. Analytical model of susceptibility-induced MR signal dephasing: effect of diffusion in a microvascular network. *Magn Reson Med*, 41(3): 499–509, 1999.

R. Klinke. *Lehrbuch Physiologie*. Thieme, 2005.

A. Kondo, R. Safaei, M. Mishima, H. Niedner, X. Lin, and S. B. Howell. Hypoxia-induced enrichment and mutagenesis of cells that have lost DNA mismatch repair. *Cancer Res*, 61(20):7603–7607, 2001.

A. Kumar, D. Welti, and R. Ernst. Imaging of macroscopic objects by NMR Fourier zeugmatography. *Naturwissenschaften*, 62:34, 1975.

K. K. Kwong, J. W. Belliveau, D. A. Chesler, I. E. Goldberg, R. M. Weisskoff, B. P. Poncelet, D. N. Kennedy, B. E. Hoppel, M. S. Cohen, R. Turner, H. M. Cheng, T. J. Brady, and B. R. Rosen. Dynamic Magnetic Resonance Imaging of Human Brain Activity During Primary Sensory Stimulation. *Proc. Natl. Acad. Sci. USA*, 89:5675–5679, 1992.

G. A. Laub and W. A. Kaiser. MR angiography with gradient motion refocusing. *J Comput Assist Tomogr*, 12(3):377–382, 1988.

P. C. Lauterbur. Image formation by induced local interactions: Examples employing nuclear magnetic resonance. *Nature*, 242:190–191, 1973.

D. Le Bihan, E. Breton, D. Lallemand, P. Grenier, E. Cabanis, and M. Laval-Jeantet. MR imaging of intravoxel incoherent motions: application to diffusion and perfusion in neurologic disorders. *Radiology*, 161(2):401–407, 1986.

D. Le Bihan, R. Turner, and N. Patronas. *Diffusion and Perfusion Magnetic Resonance Imaging*, chapter Diffusion MR Imaging in Normal Brain and in Brain Tumors, pages 134–140. Raven Press, New York, 1995.

B. C. Lee, K. D. Vo, D. K. Kido, P. Mukherjee, J. Reichenbach, W. Lin, M. S. Yoon, and M. Haacke. MR high-resolution blood oxygenation level-dependent venography of occult (low-flow) vascular lesions. *AJNR Am J Neuroradiol*, 20(7):1239–1242, 1999.

M. H. Levitt. Demagnetization field effects in two-dimensional solution NMR. *Concepts in Magnetic Resonance*, 8:77–103, 1996.

Z. P. Liang and P. C. Lauterbur. *Principles of Magnetic Resonance Imaging*. IEEE Press, 2000.

S. Ljunggren. A simple graphical representation of Fourier-based imaging methods. *J. Magn. Reson.*, 54:338–343, 1983.

M. J. Lunt, S. Ragab, A. A. Birch, D. Schley, and D. F. Jenkinson. Comparison of caffeine-induced changes in cerebral blood flow and middle cerebral artery blood velocity shows that caffeine reduces middle cerebral artery diameter. *Physiol Meas*, 25(2):467–474, 2004.

J. M. Lupo, S. Banerjee, K. E. Hammond, D. A. Kelley, D. Xu, C. S. M, D. B. Vigneron, S. Majumdar, and S. J. Nelson. Susceptibility-weighted imaging of brain tumor patients at 7T using an autocalibrating parallel technique. In *Proc Intl Mag Reson Med*, volume 15, page 1769, 2007.

D. Lurie, M. Foster, J. Hutchinson, T. Redpath, S. Semple, and H. Seton. *Physical Basis of Magnetic Resonance Imaging*. University of Aberdeen, Jun 2001. Script of the MRI Summer School.

J. Ma and F. W. Wehrli. Method for image-based measurement of the reversible and irreversible contribution to the transverse-relaxation rate. *J Magn Reson B*, 111 (1):61–69, 1996.

Mansfield. Imaging by nuclear magnetic resonance. *J . Phys. E : Sci. Instrum.*, 21: 18–30, 1988.

P. Mansfield. Multi-planar image formation using NMR spin echoes. *J. Phys. C: Solid State Phys.*, 10:55–58, 1977.

P. Mansfield and P. Grannell. NMR 'diffraction' in solids? *J. Phys. C: Solid State Phys.*, 6:422–426, 1973.

P. Mansfield and I. L. Pykett. Biological and Medical Imaging by NMR. *J. Magn. Reson.*, 29:355–373, 1978.

S. Meiboom and D. Gill. Modified Spin-Echo Method for Measuring Nuclear Relaxation Times. *Rev Sci Instrum*, 29(8):688–691, 1958.

J. R. Meno, T. S. Nguyen, E. M. Jensen, G. Alexander West, L. Groysman, D. K. Kung, A. C. Ngai, G. W. Britz, and H. R. Winn. Effect of caffeine on cerebral blood flow response to somatosensory stimulation. *J Cereb Blood Flow Metab*, 25 (6):775–784, 2005.

H. J. Mentzel, A. Dieckmann, C. Fitzek, U. Brandl, J. R. Reichenbach, and W. A. Kaiser. Early diagnosis of cerebral involvement in Sturge-Weber syndrome using high-resolution BOLD MR venography. *Pediatr Radiol*, 35(1):85–90, 2005.

Y. E. Moskalenko, editor. *Biophysical aspects of cerebral circulation.* Pergamon Press, Oxford, 1980.

A. Nehlig, J. L. Daval, and G. Debry. Caffeine and the central nervous system: mechanisms of action, biochemical, metabolic and psychostimulant effects. *Brain Res Brain Res Rev*, 17(2):139–170, 1992.

G. C. Newman, E. Delucia-Deranja, A. Tudorica, F. E. Hospod, and C. S. Patlak. Cerebral blood volume measurements by T*2-weighted MRI and contrast infusion. *Magn Reson Med*, 50(4):844–855, 2003.

I. M. Noebauer-Huhmann, K. Pinker, M. Barth, V. Mlynarik, A. Ba-Ssalamah, W. F. Saringer, M. Weber, T. Benesch, S. Witoszynskyj, A. Rauscher, J. R. Reichenbach, and S. Trattnig. Contrast-enhanced, high-resolution, susceptibility-weighted magnetic resonance imaging of the brain: dose-dependent optimization at 3 tesla and 1.5 tesla in healthy volunteers. *Invest Radiol*, 41(3):249–255, 2006.

D. C. Noll, D. G. Nishimura, and A. Macovski. Homodyne detection in magnetic resonance imaging. *Medical Imaging, IEEE Transactions on*, 10(2):154–163, 1991.

S. Ogawa, T. M. Lee, A. R. Kay, and D. W. Tank. Brain magnetic resonance imaging with contrast dependent on blood oxygenation. *Proc Natl Acad Sci U S A*, 87(24): 9868–9872, 1990.

E. Ongini and B. B. Fredholm. Pharmacology of adenosine A2A receptors. *Trends Pharmacol Sci*, 17(10):364–372, 1996.

J. A. Osborn. Demagnetizing Factors of the General Ellipsoid. *Phys. Rev.*, 67(11-12): 351–357, 1945.

L. Pauling and C. D. Coryell. The Magnetic Properties and Structure of Hemoglobin, Oxyhemoglobin and Carbonmonoxyhemoglobin. *Proc.Natl.Acad.Sci.U.S.A.*, 22(4): 210–216, 1936.

G. Pawlik, A. Rackl, and R. J. Bing. Quantitative capillary topography and blood flow in the cerebral cortex of cats: an in vivo microscopic study. *Brain Res*, 208 (1):35–58, 1981.

G. S. Pell, R. S. Briellmann, A. B. Waites, D. F. Abbott, D. P. Lewis, and G. D. Jackson. Optimized clinical T2 relaxometry with a standard CPMG sequence. *J Magn Reson Imaging*, 23(2):248–252, 2006.

J. S. Philo, U. Dreyer, and T. M. Schuster. Diamagnetism of human apo-, oxy-, and (carbonmonoxy)hemoglobin. *Biochemistry*, 23(5):865–872, 1984.

Y. Plyavin' and E. Blum. Magnetic parameters of blood cells and high-gradient paramagnetic and diamagnetic phoresis. *Magnetohydrodynamics*, 19(4):3–14, 1983.

W. H. Press, B. Flannery, S. Teukolsky, and W. Vetterling. *Numerical Recipes in C: The Art of Scientific Computing*, chapter 4.4. Cambridge University Press, 1992.

W. S. Price, H. Ide, and Y. Arata. Self-diffusion of supercooled water to 238K using PGSE NMR diffusion measurements. *Journal of Physical.Chemistry.A.*, 103:448–450, 1999.

E. Purcell, H. Torrey, and R. Pound. Resonance absorption by nuclear magnetic moments in a solid. *Phys. Rev.*, 69:37–38, 1946.

A. Rauscher. *Phase Information in Magnetic Resonance Imaging*. PhD thesis, Technische Universität Wien, Fakultät für Physik, 2005.

A. Rauscher, M. Barth, J. R. Reichenbach, R. Stollberger, and E. Moser. Automated unwrapping of MR phase images applied to BOLD MR-venography at 3 Tesla. *J Magn Reson Imaging*, 18(2):175–180, 2003.

A. Rauscher, J. Sedlacik, M. Barth, E. M. Haacke, and J. R. Reichenbach. Nonnvasive assessment of vascular architecture and function during modulated blood oxygenation using susceptibility weighted magnetic resonance imaging. *Magn Reson Med*, 54(1):87–95, 2005a.

A. Rauscher, J. Sedlacik, M. Barth, H. J. Mentzel, and J. R. Reichenbach. Magnetic susceptibility-weighted MR phase imaging of the human brain. *AJNR Am J Neuroradiol*, 26(4):736–742, 2005b.

A. Rauscher, J. Sedlacik, C. Fitzek, B. Walter, A. Hochstetter, R. Kalff, W. A. Kaiser, and J. R. Reichenbach. High resolution susceptibility weighted MR-imaging of brain tumors during the application of a gaseous agent. *Rofo*, 177(8):1065–1069, 2005c.

A. Rauscher, J. Sedlacik, M. Barth, S. Witoszynskyj, and J. R. Reichenbach. Phase Map Based Investigation of Intravoxel Signal Dephasing in Gradient Echo MRI. In *Proc. Intl. Soc. Mag. Reson. Med.*, volume 14, page 2792, 2006.

J. R. Reichenbach and E. M. Haacke. High-resolution BOLD venographic imaging: a window into brain function. *NMR Biomed*, 14(7-8):453–467, 2001.

J. R. Reichenbach, T. Hacklander, T. Harth, M. Hofer, M. Rassek, and U. Modder. 1H T1 and T2 measurements of the MR imaging contrast agents Gd-DTPA and Gd-DTPA BMA at 1.5T. *Eur Radiol.*, 7(2):264–274, 1997a.

J. R. Reichenbach, R. Venkatesan, D. J. Schillinger, D. K. Kido, and E. M. Haacke. Small vessels in the human brain: MR venography with deoxyhemoglobin as an intrinsic contrast agent. *Radiology*, 204(1):272–277, 1997b.

J. R. Reichenbach, R. Venkatesan, D. A. Yablonskiy, M. R. Thompson, S. Lai, and E. M. Haacke. Theory and application of static field inhomogeneity effects in gradient-echo imaging. *J Magn Reson Imaging*, 7:266–279, 1997c.

J. R. Reichenbach, M. Barth, E. M. Haacke, M. Klarhöfer, W. A. Kaiser, and E. Moser. High-resolution MR venography at 3.0 Tesla. *J Comput Assist Tomogr*, 24(6):949–957, 2000.

M. Reiser and W. Semmler. *Magnetresonanztomographie: mit 253 Tabellen*. Springer, 1992.

R. Roberts. *Theory of Signal Detectability:Composite Deferred Decision Theory*. PhD thesis, Department of Electrical Engineering, The University of Michigan, 1965.

T. P. Roberts and H. A. Rowley. Diffusion weighted magnetic resonance imaging in stroke. *Eur J Radiol*, 45(3):185–194, 2003.

L. Rossi-Bernardi, M. Luzzana, M. Samaja, M. Davi, D. DaRiva-Ricci, J. Minoli, B. Seaton, and R. L. Berger. Continuous determination of the oxygen dissociation curve for whole blood. *Clin Chem*, 21(12):1747–1753, 1975.

F. M. M. Santiesteban, S. D. Swanson, D. C. Noll, and D. J. Anderson. Object Orientation Independence of Susceptibility Weighted Imaging by Using a Sigmoid-Type. In *Proc Intl Soc Mag Reson Med*, volume 14, page 2399, 2007.

J. F. Schenck. The role of magnetic susceptibility in magnetic resonance imaging: MRI magnetic compatibility of the first and second kinds. *Med Phys*, 23(6):815–850, 1996.

R. Schmidt and G. Thews, editors. *Physiologie des Menschen*. Springer, 1987.

H. Schröder, A. Bongers, and L. R. Schad. Testing of model assumptions of MR oxygen extraction fraction mapping using a phantom study. *Z Med Phys*, 16(4):275–284, 2006.

H. Schröder. Optimierung und Verifizierung BOLD-sensitiver MR-Bildgebungsmethoden zur Bestimmung der Gewebeoxygenierung. Master's thesis, Fakultät für Physik und Astronomie, Ruprecht-Karls-Universität Heidelberg, 2005.

J. Sedlacik, K.-H. Herrmann, A. Rauscher, and J. R. Reichenbach. Fast Susceptibility Weighted Imaging (SWI) using different k-Space Undersampling Mechanisms. In *Biomedizinische Technik*, volume 50, pages 1190–1191, 2005.

Y. Shen, Z. Kou, C. W. Kreipke, T. Petrov, J. Hu, and E. M. Haacke. In vivo measurement of tissue damage, oxygen saturation changes and blood flow changes after experimental traumatic brain injury in rats using susceptibility weighted imaging. *Magn Reson Imaging*, 25(2):219–227, 2007.

C. P. Slichter. *Principles of Magnetic Resonance*. Springer, 1992.

W. M. Spees, D. A. Yablonskiy, M. C. Oswood, and J. J. Ackerman. Water proton MR properties of human blood at 1.5 Tesla: magnetic susceptibility, T(1), T(2), T*(2), and non-Lorentzian signal behavior. *Magn.Reson.Med.*, 45(4):533–542, 2001.

C. S. Springer. *NMR in Physiology and Biomedicine*, chapter Physicochemical principles influencing magnetopharmaceuticals, pages 75–99. Academic Press, San Diego, 1994.

G. J. Stanisz, E. E. Odrobina, J. Pun, M. Escaravage, S. J. Graham, M. J. Bronskill, and R. M. Henkelman. T1, T2 relaxation and magnetization transfer in tissue at 3T. *Magn Reson Med*, 54(3):507–512, 2005.

L. Stryer, editor. *Biochemie*. Spektrum Akad. Verlag, 1994.

A. L. Sukstanskii and D. A. Yablonskiy. Theory of FID NMR signal dephasing induced by mesoscopic magnetic field inhomogeneities in biological systems. *J Magn Reson*, 151(1):107–117, 2001.

I. L. Tan, R. A. van Schijndel, P. J. Pouwels, M. A. van Walderveen, J. R. Reichenbach, R. A. Manoliu, and F. Barkhof. MR venography of multiple sclerosis. *AJNR Am J Neuroradiol*, 21(6):1039–1042, 2000.

G. Thomas. Raising hemoglobin: an opportunity for increasing survival? *Oncology*, 63 Suppl 2:19–28, 2002.

K. R. Thulborn, J. C. Waterton, P. M. Matthews, and G. K. Radda. Oxygenation dependence of the transverse relaxation time of water protons in whole blood at high field. *Biochim.Biophys.Acta.*, 714(2):265–270, 1982.

K. A. Tong, S. Ashwal, B. A. Holshouser, J. P. Nickerson, C. J. Wall, L. A. Shutter, R. J. Osterdock, E. M. Haacke, and D. Kido. Diffuse axonal injury in children: clinical correlation with hemorrhagic lesions. *Ann Neurol*, 56(1):36–50, 2004.

D. B. Twieg. The k-trajectory formulation of the NMR imaging process with applications in analysis and synthesis of imaging methods. *Med Phys.*, 10:610–621, 1983.

P. Vaupel and A. Mayer. Hypoxia in cancer: significance and impact on clinical outcome. *Cancer Metastasis Rev*, 26(2):225–239, 2007.

M. T. Vlaardingerbroek and J. A. den Boer. *Magnetic Resonance Imaging; Theory and Practice*. Springer, 2003.

R. L. Vold, J. S. Waugh, M. P. Klein, and D. E. Phelps. Measurement of spin relaxation in complex systems. *J Chem Phys*, 48(8):3831–3832, 1968.

N. A. Watson, S. C. Beards, N. Altaf, A. Kassner, and A. Jackson. The effect of hyperoxia on cerebral blood flow: a study in healthy volunteers using magnetic resonance phase-contrast angiography. *Eur J Anaesthesiol*, 17(3):152–159, 2000.

H. J. Weinmann, R. C. Brasch, W. R. Press, and G. E. Wesbey. Characteristics of gadolinium-DTPA complex: a potential NMR contrast agent. *AJR Am J Roentgenol*, 142(3):619–624, 1984.

R. M. Weisskoff and S. Kiihne. MRI susceptometry: image-based measurement of absolute susceptibility of MR contrast agents and human blood. *Magn.Reson.Med.*, 24(2):375–383, 1992.

R. M. Winslow, M. L. Swenberg, R. L. Berger, R. I. Shrager, M. Luzzana, M. Samaja, and L. Rossi-Bernardi. Oxygen equilibrium curve of normal human blood and its evaluation by Adair's equation. *J Biol Chem*, 252(7):2331–2337, 1977.

S. Witoszynskyj, A. Rauscher, J. R. Reichenbach, and M. Barth. ΦUN (Φase UNwrapping) - Validation of a 2D Region-Growing Phase Unwrapping Program. In *Proc Intl Mag Reson Med*, volume 15, page 3436, 2007.

N. D. Wycliffe, J. Choe, B. Holshouser, U. E. Oyoyo, E. M. Haacke, and D. K. Kido. Reliability in detection of hemorrhage in acute stroke by a new three-dimensional gradient recalled echo susceptibility-weighted imaging technique compared to computed tomography: a retrospective study. *J Magn Reson Imaging*, 20(3):372–377, 2004.

W. Xu and I. Cumming. A region-growing algorithm for InSAR phase unwrapping. *Geoscience and Remote Sensing, IEEE Transactions on*, 37(1):124–134, 1999.

D. A. Yablonskiy. Quantitation of intrinsic magnetic susceptibility-related effects in a tissue matrix. Phantom study. *Magn Reson Med*, 39(3):417–428, 1998.

D. A. Yablonskiy and E. M. Haacke. Theory of NMR signal behavior in magnetically inhomogeneous tissues: the static dephasing regime. *Magn Reson Med*, 32(6):749–763, 1994.

T. Yamaguchi, I. Kanno, K. Uemura, F. Shishido, A. Inugami, T. Ogawa, M. Murakami, and K. Suzuki. Reduction in regional cerebral metabolic rate of oxygen during human aging. *Stroke*, 17(6):1220–1228, 1986.

M. Zborowski, G. R. Ostera, L. R. Moore, S. Milliron, J. J. Chalmers, and A. N. Schechter. Red blood cell magnetophoresis. *Biophys J*, 84(4):2638–2645, 2003.

J. Zhou, X. Golay, P. C. van Zijl, M. J. Silvennoinen, R. Kauppinen, J. Pekar, and M. Kraut. Inverse T(2) contrast at 1.5 Tesla between gray matter and white matter in the occipital lobe of normal adult human brain. *Magn Reson Med*, 46 (2):401–406, 2001.

C. H. Ziener, W. R. Bauer, and P. M. Jakob. Frequency distribution and signal formation around a vessel. *MAGMA*, 18(4):225–230, 2005.

List of Tables

List of Figures

A
Appendix

A.1. Single Capillary Phantom

A.1.1. Signal Plots of All Measurements

On the following pages the measured and fitted signals of all single capillary phantom experiments are displyed. The parameter sets are given in the heading of each plot. The dotted lines represent the signal of a homogeneous ROI near the evaluated single voxel. The error bars corresponds to the standard deviations of the signal determined from the homogenous ROI for each echo time.

$B_0 = 1.5\,\mathrm{T}$, $0.2\,\mathrm{mM}_{Gd-DTPA}$, $\theta = 0°$, $\lambda = 0.1$

$\Delta\chi = 0.61\,\mathrm{ppm}$

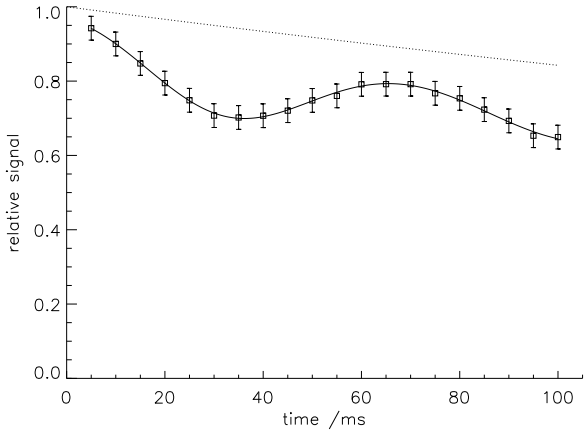

$\Delta\chi = 0.95\,\mathrm{ppm}$

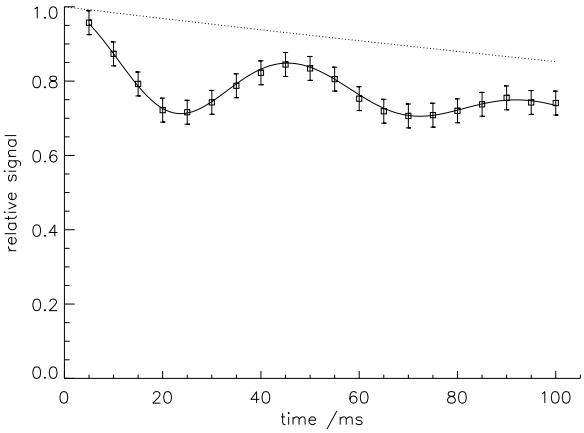

$B_0 = 1.5\,\mathrm{T}$, $0.2\,\mathrm{mM}_{Gd-DTPA}$, $\theta = 0°$, $\lambda = 0.2$

$\Delta\chi = 0.61\,\mathrm{ppm}$

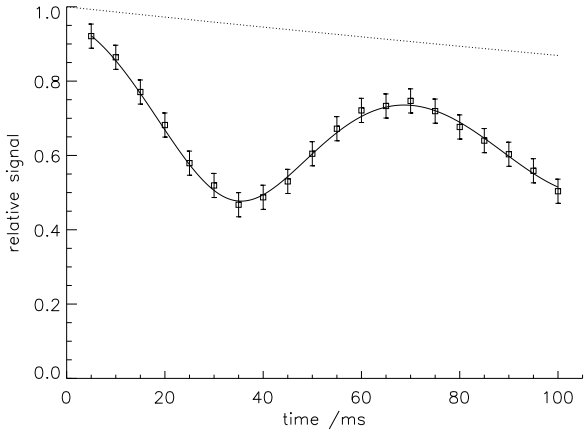

$\Delta\chi = 0.95\,\mathrm{ppm}$

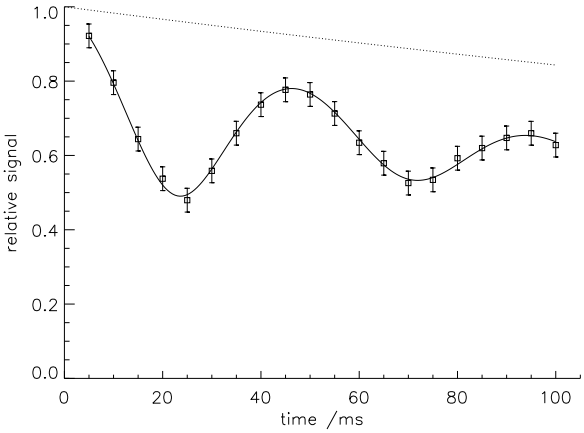

$B_0 = 1.5\,\mathrm{T}$, $0.2\,\mathrm{mM}_{Gd-DTPA}$, $\theta = 0°$, $\lambda = 0.3$

$\Delta\chi = 0.61\,\mathrm{ppm}$

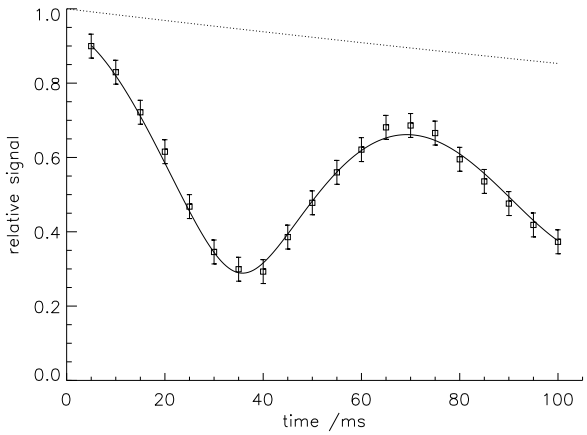

$\Delta\chi = 0.95\,\mathrm{ppm}$

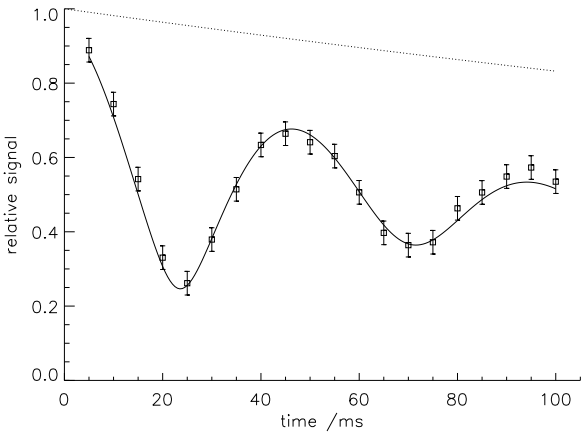

$B_0 = 1.5\,\mathrm{T}$, $0.2\,\mathrm{mM}_{Gd-DTPA}$, $\theta = 55°$, $\lambda = 0.1$

$\Delta\chi = 0.61\,\mathrm{ppm}$

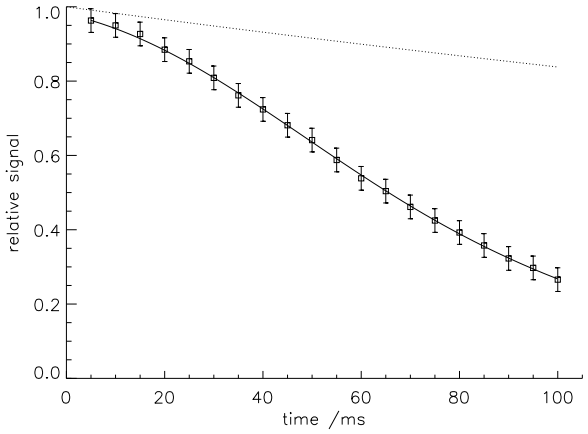

$\Delta\chi = 0.95\,\mathrm{ppm}$

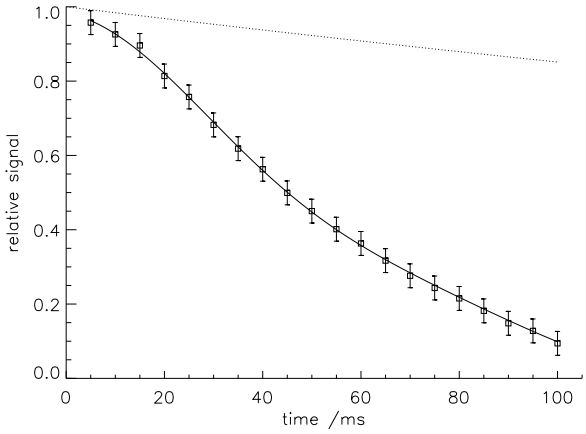

$B_0 = 1.5\,\mathrm{T}$, $0.2\,\mathrm{mM}_{Gd-DTPA}$, $\theta = 55°$, $\lambda = 0.2$

$\Delta\chi = 0.61\,\mathrm{ppm}$

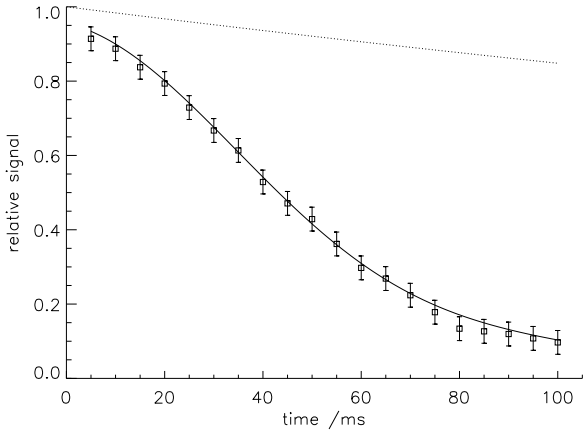

$\Delta\chi = 0.95\,\mathrm{ppm}$

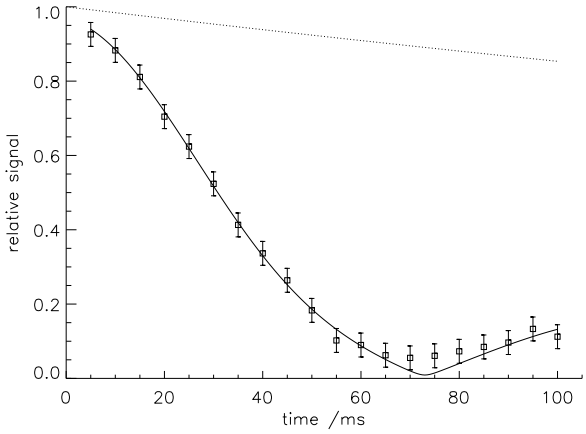

$B_0 = 1.5\,\mathrm{T}$, $0.2\,\mathrm{mM}_{Gd-DTPA}$, $\theta = 55°$, $\lambda = 0.3$

$\Delta\chi = 0.61\,\mathrm{ppm}$

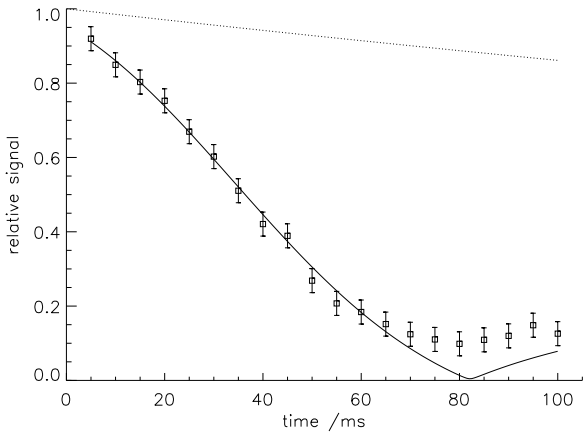

$\Delta\chi = 0.95\,\mathrm{ppm}$

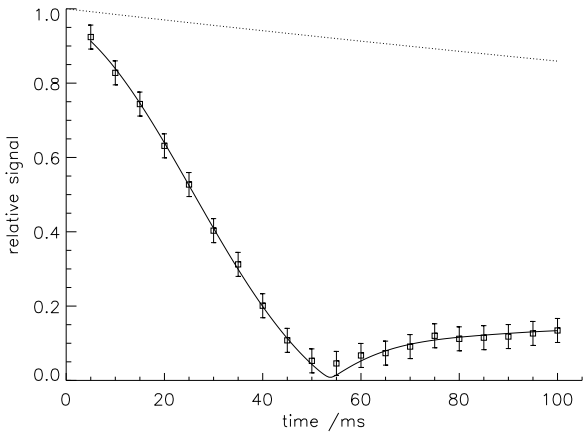

$B_0 = 1.5\,\mathrm{T}$, $0.2\,\mathrm{mM}_{Gd-DTPA}$, $\theta = 90°$, $\lambda = 0.1$

$\Delta\chi = 0.61\,\mathrm{ppm}$

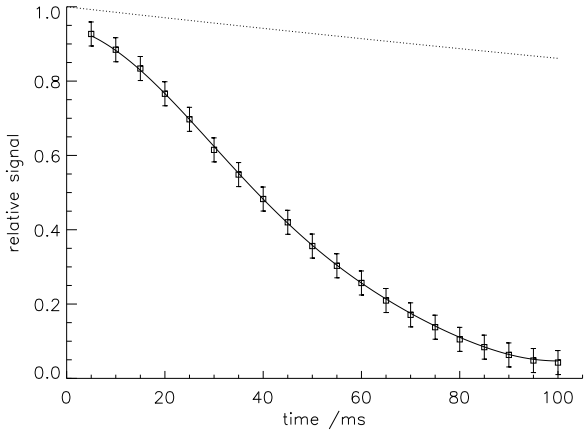

$\Delta\chi = 0.95\,\mathrm{ppm}$

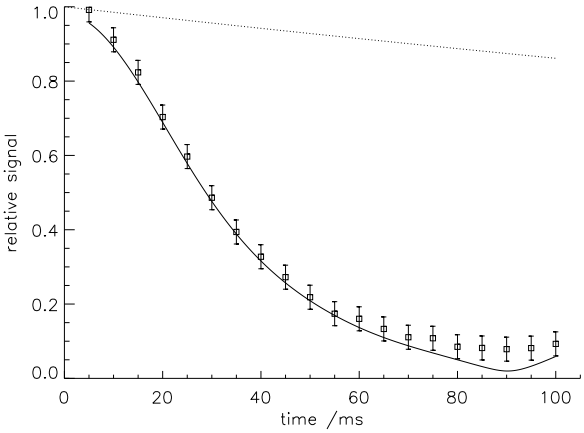

$B_0 = 1.5\,\mathrm{T}$, $0.2\,\mathrm{mM}_{Gd-DTPA}$, $\theta = 90°$, $\lambda = 0.2$

$\Delta\chi = 0.61\,\mathrm{ppm}$

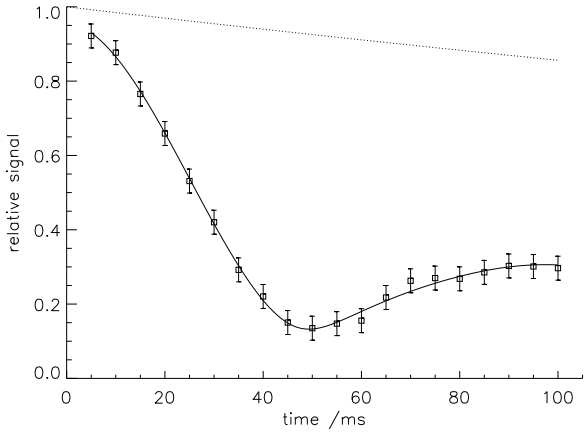

$\Delta\chi = 0.95\,\mathrm{ppm}$

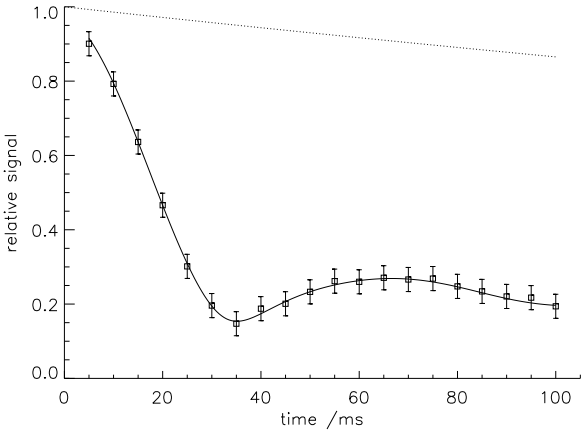

$B_0 = 1.5\,\mathrm{T}$, $0.2\,\mathrm{mM}_{Gd-DTPA}$, $\theta = 90°$, $\lambda = 0.3$

$\Delta\chi = 0.61\,\mathrm{ppm}$

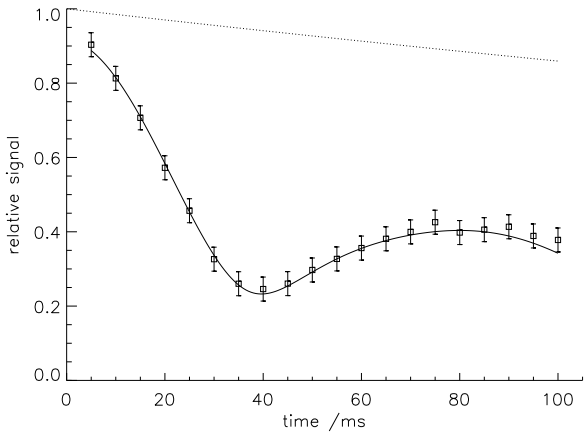

$\Delta\chi = 0.95\,\mathrm{ppm}$

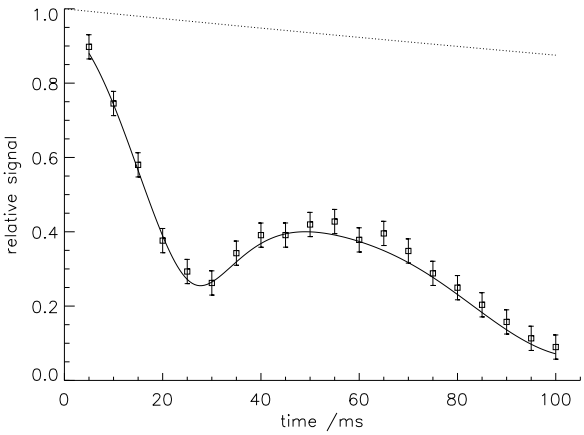

$B_0 = 1.5\,\mathrm{T}$, $1.6\,\mathrm{mM}_{Gd-DTPA}$, $\theta = 0°$, $\lambda = 0.1$

$\Delta\chi = 0.48\,\mathrm{ppm}$

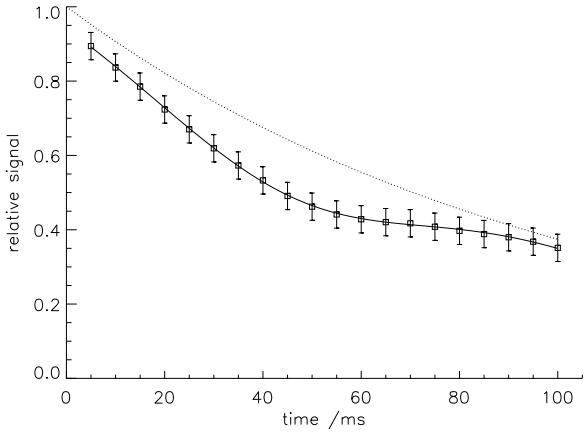

$\Delta\chi = 0.82\,\mathrm{ppm}$

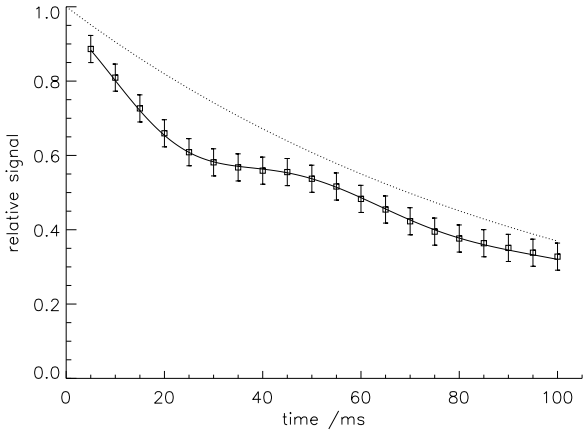

$B_0 = 1.5\,\mathrm{T}$, $1.6\,\mathrm{mM}_{Gd-DTPA}$, $\theta = 0°$, $\lambda = 0.2$

$\Delta\chi = 0.48\,\mathrm{ppm}$

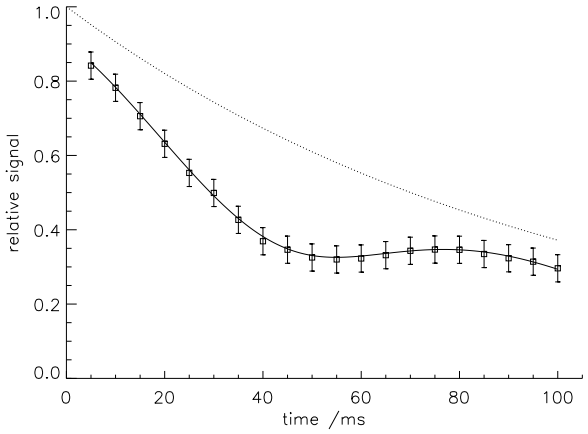

$\Delta\chi = 0.82\,\mathrm{ppm}$

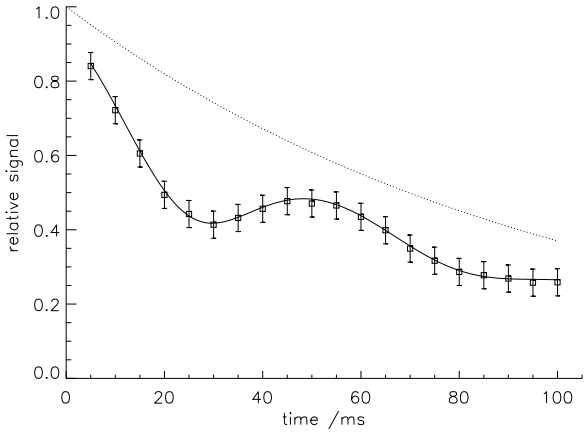

$B_0 = 1.5\,\mathrm{T}$, $1.6\,\mathrm{mM}_{Gd-DTPA}$, $\theta = 0°$, $\lambda = 0.3$

$\Delta\chi = 0.48\,\mathrm{ppm}$

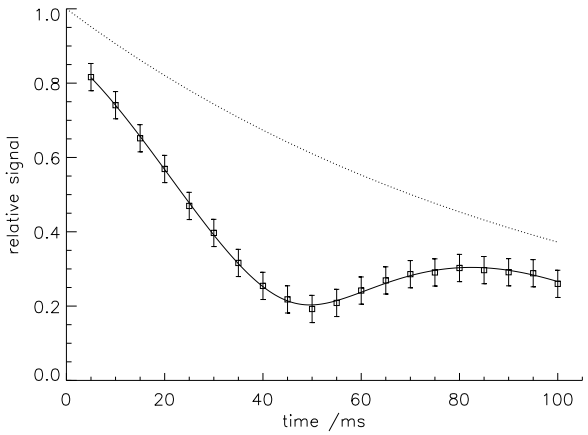

$\Delta\chi = 0.82\,\mathrm{ppm}$

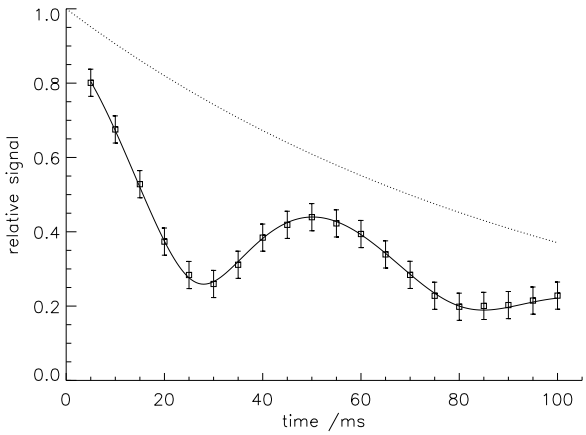

$B_0 = 1.5\,\mathrm{T}$, $1.6\,\mathrm{mM}_{Gd-DTPA}$, $\theta = 55°$, $\lambda = 0.1$

$\Delta\chi = 0.48\,\mathrm{ppm}$

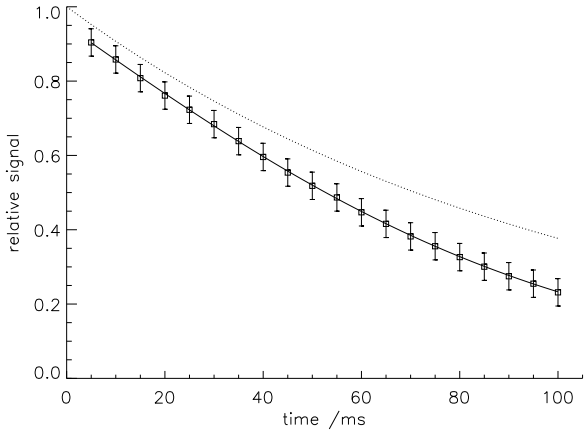

$\Delta\chi = 0.82\,\mathrm{ppm}$

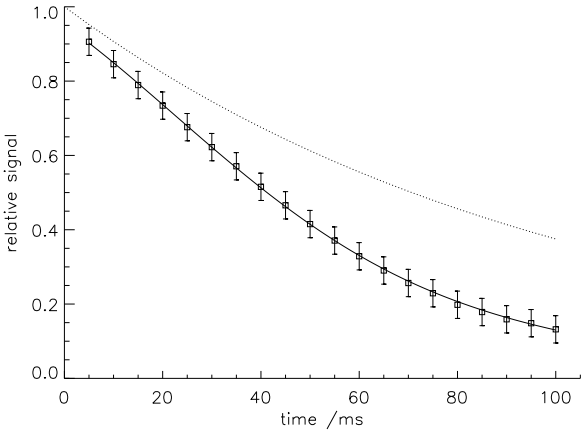

$B_0 = 1.5\,\mathrm{T}$, $1.6\,\mathrm{mM}_{Gd-DTPA}$, $\theta = 55°$, $\lambda = 0.2$

$\Delta\chi = 0.48\,\mathrm{ppm}$

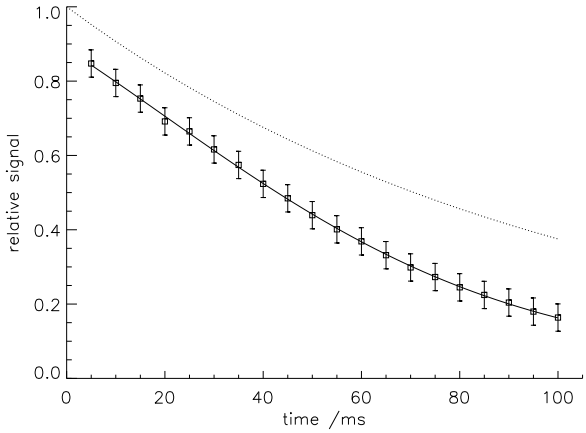

$\Delta\chi = 0.82\,\mathrm{ppm}$

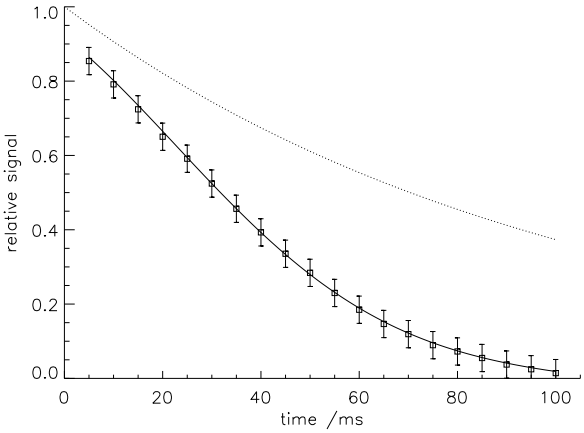

$B_0 = 1.5\,\mathrm{T}$, $1.6\,\mathrm{mM}_{Gd-DTPA}$, $\theta = 55°$, $\lambda = 0.3$

$\Delta\chi = 0.48\,\mathrm{ppm}$

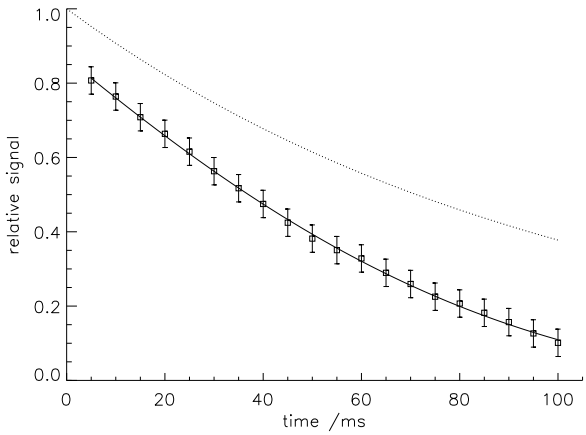

$\Delta\chi = 0.82\,\mathrm{ppm}$

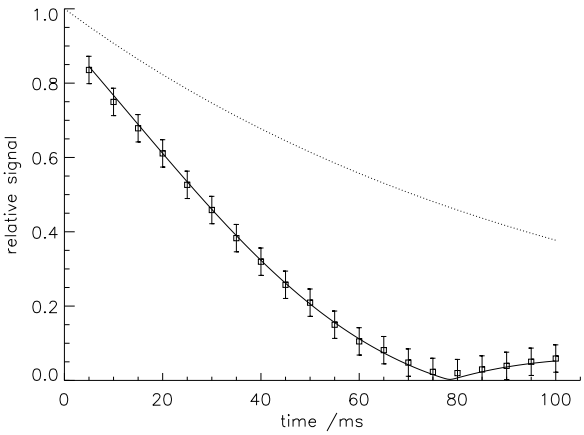

$B_0 = 1.5\,\mathrm{T}$, $1.6\,\mathrm{mM}_{Gd-DTPA}$, $\theta = 90°$, $\lambda = 0.1$

$\Delta\chi = 0.48\,\mathrm{ppm}$

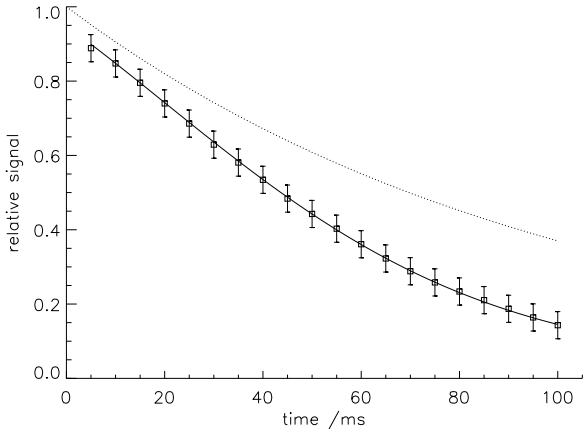

$\Delta\chi = 0.82\,\mathrm{ppm}$

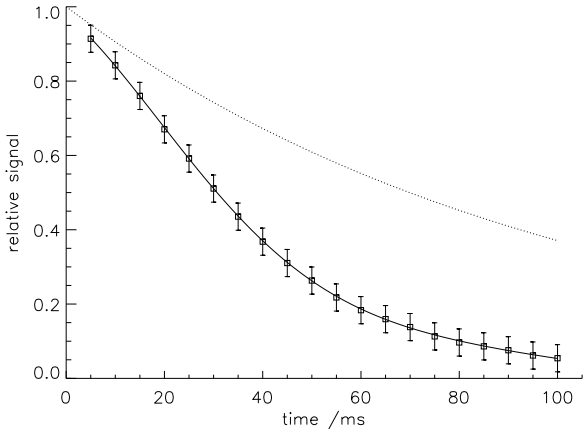

$B_0 = 1.5\,\mathrm{T}$, $1.6\,\mathrm{mM}_{Gd-DTPA}$, $\theta = 90°$, $\lambda = 0.2$

$\Delta\chi = 0.48\,\mathrm{ppm}$

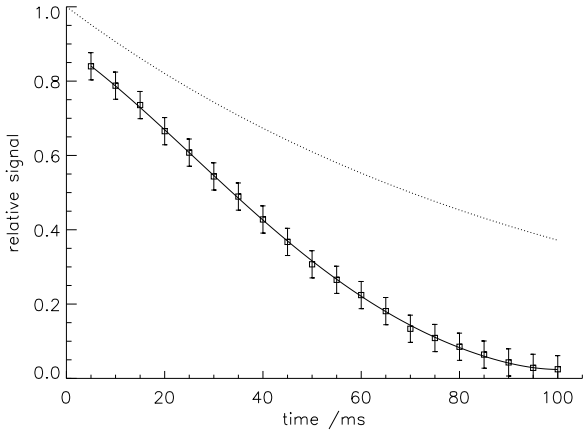

$\Delta\chi = 0.82\,\mathrm{ppm}$

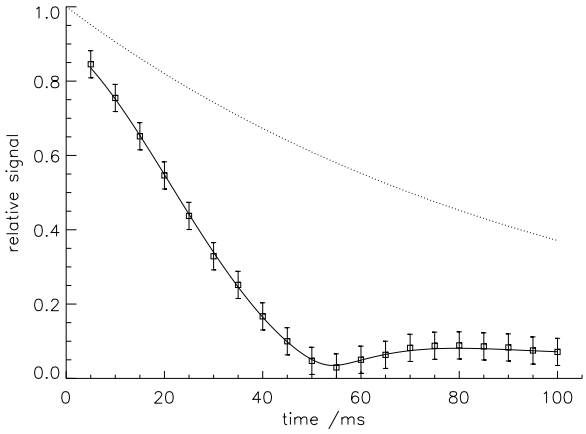

$B_0 = 1.5\,\mathrm{T}$, $1.6\,\mathrm{mM}_{Gd-DTPA}$, $\theta = 90°$, $\lambda = 0.3$

$\Delta\chi = 0.48\,\mathrm{ppm}$

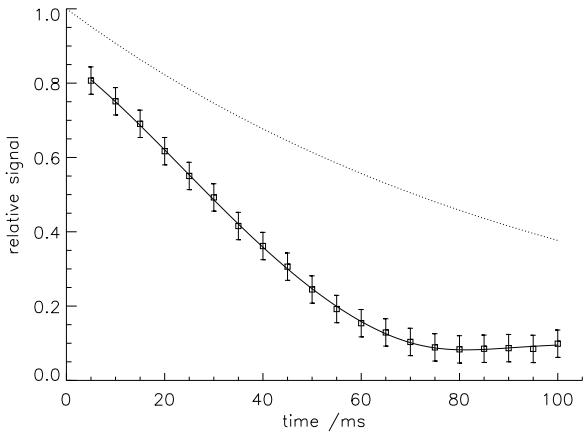

$\Delta\chi = 0.82\,\mathrm{ppm}$

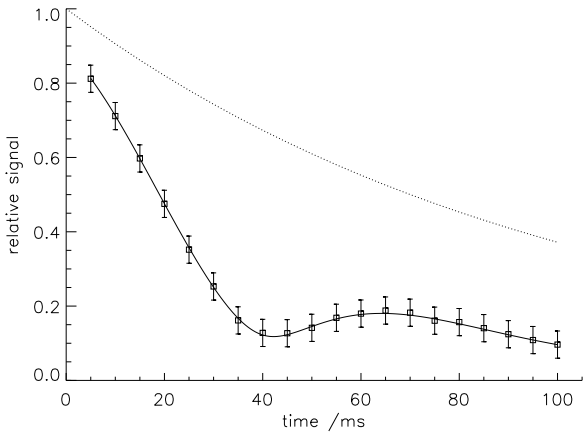

$B_0 = 3.0\,\mathrm{T}$, $0.2\,\mathrm{mM}_{Gd-DTPA}$, $\theta = 0°$, $\lambda = 0.1$

$\Delta\chi = 0.61\,\mathrm{ppm}$

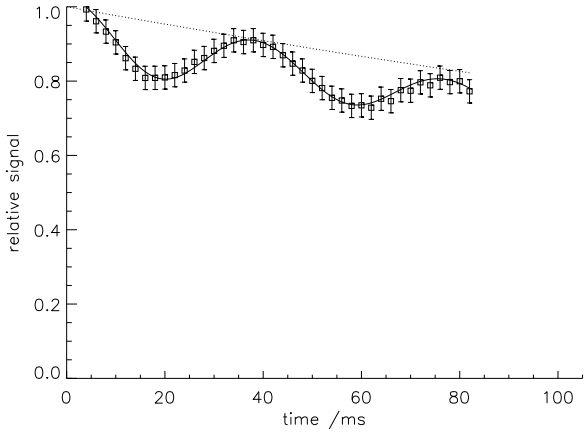

$\Delta\chi = 0.95\,\mathrm{ppm}$

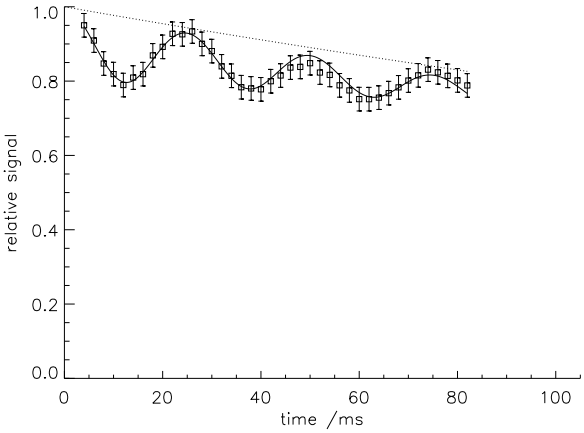

$B_0 = 3.0\,\mathrm{T}$, $0.2\,\mathrm{mM}_{Gd-DTPA}$, $\theta = 0°$, $\lambda = 0.2$

$\Delta\chi = 0.61\,\mathrm{ppm}$

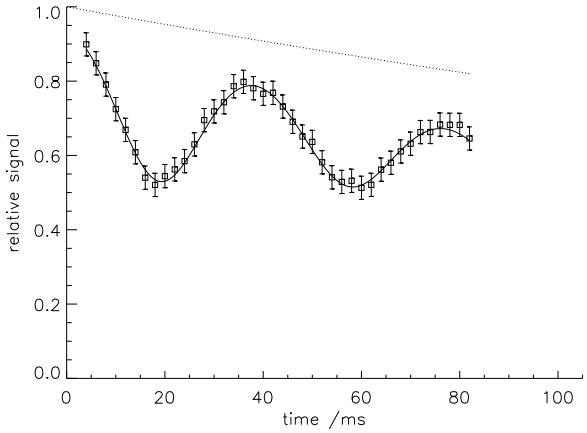

$\Delta\chi = 0.95\,\mathrm{ppm}$

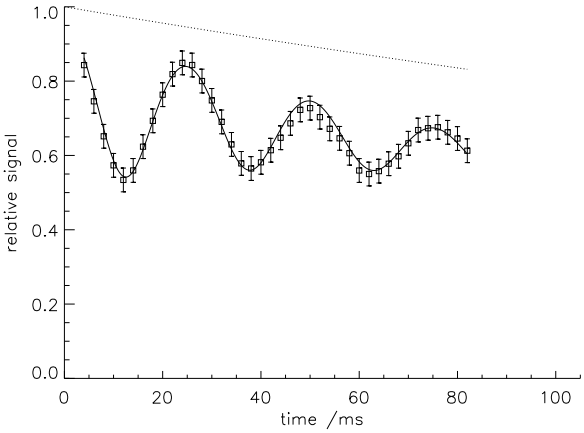

$B_0 = 3.0\,\mathrm{T}$, $0.2\,\mathrm{mM}_{Gd-DTPA}$, $\theta = 0°$, $\lambda = 0.3$

$\Delta\chi = 0.61\,\mathrm{ppm}$

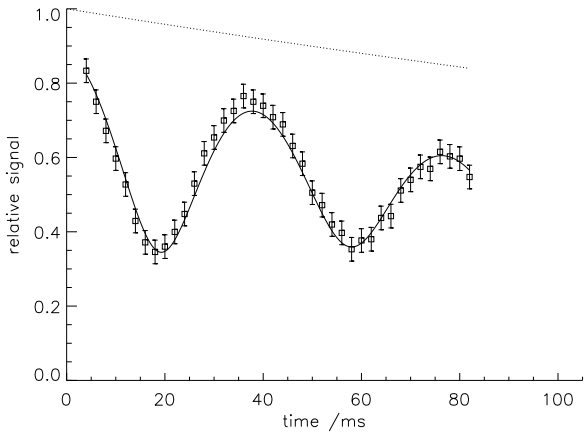

$\Delta\chi = 0.95\,\mathrm{ppm}$

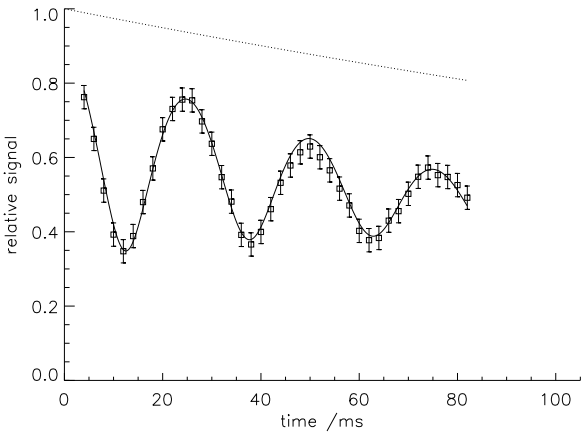

$B_0 = 3.0\,\mathrm{T}$, $0.2\,\mathrm{mM}_{Gd-DTPA}$, $\theta = 55°$, $\lambda = 0.1$

$\Delta\chi = 0.61\,\mathrm{ppm}$

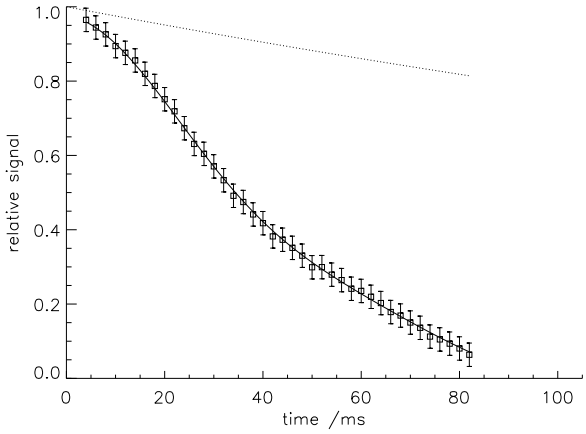

$\Delta\chi = 0.95\,\mathrm{ppm}$

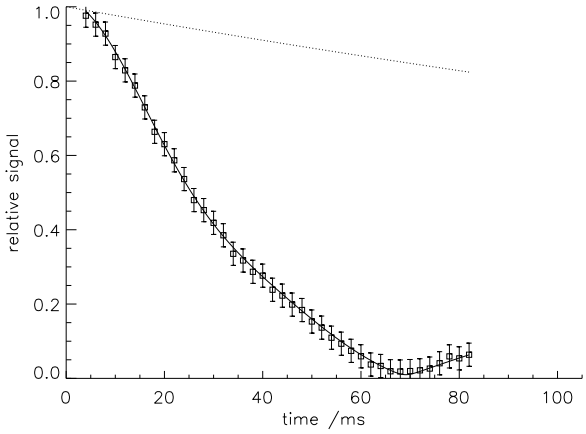

$B_0 = 3.0\,\mathrm{T}$, $0.2\,\mathrm{mM}_{Gd-DTPA}$, $\theta = 55°$, $\lambda = 0.2$

$\Delta\chi = 0.61\,\mathrm{ppm}$

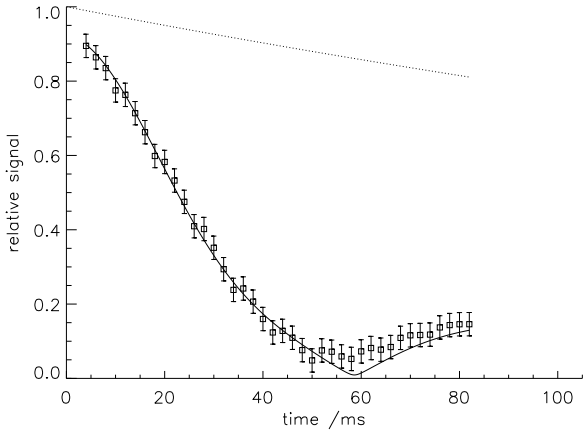

$\Delta\chi = 0.95\,\mathrm{ppm}$

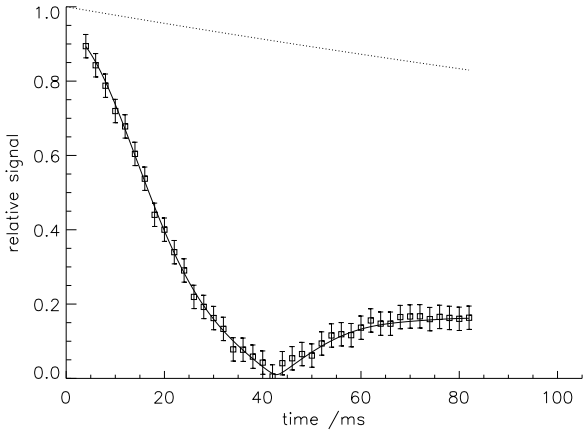

$B_0 = 3.0\,\mathrm{T}$, $0.2\,\mathrm{mM}_{Gd-DTPA}$, $\theta = 55°$, $\lambda = 0.3$

$\Delta\chi = 0.61\,\mathrm{ppm}$

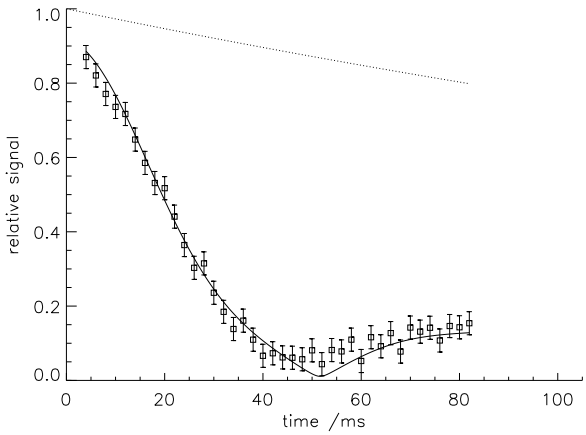

$\Delta\chi = 0.95\,\mathrm{ppm}$

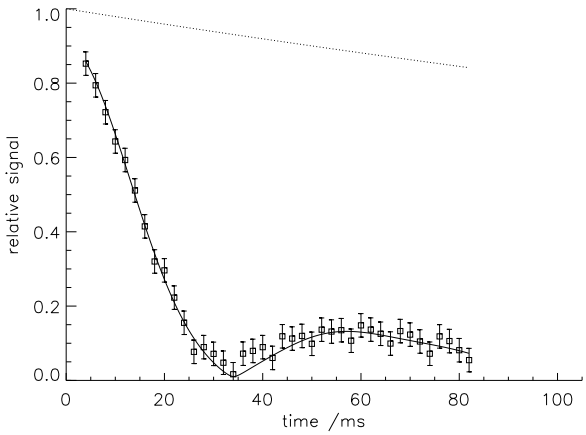

$B_0 = 3.0\,\mathrm{T}$, $0.2\,\mathrm{mM}_{Gd-DTPA}$, $\theta = 90°$, $\lambda = 0.1$

$\Delta\chi = 0.61\,\mathrm{ppm}$

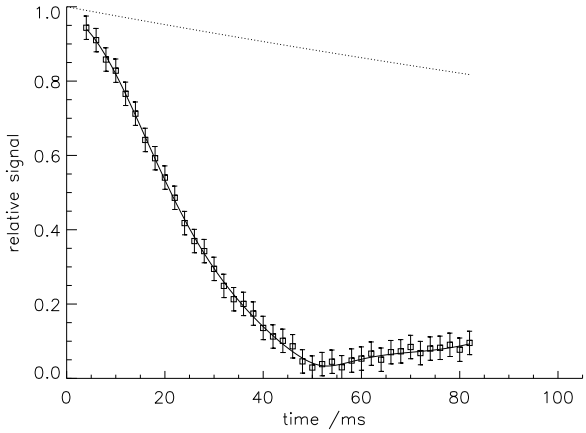

$\Delta\chi = 0.95\,\mathrm{ppm}$

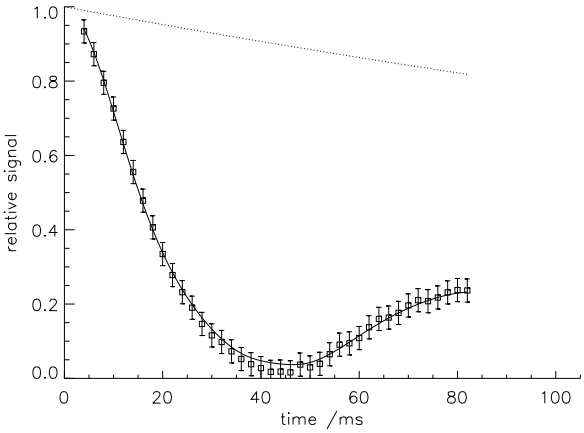

$B_0 = 3.0\,\mathrm{T}$, $0.2\,\mathrm{mM}_{Gd-DTPA}$, $\theta = 90°$, $\lambda = 0.2$

$\Delta\chi = 0.61\,\mathrm{ppm}$

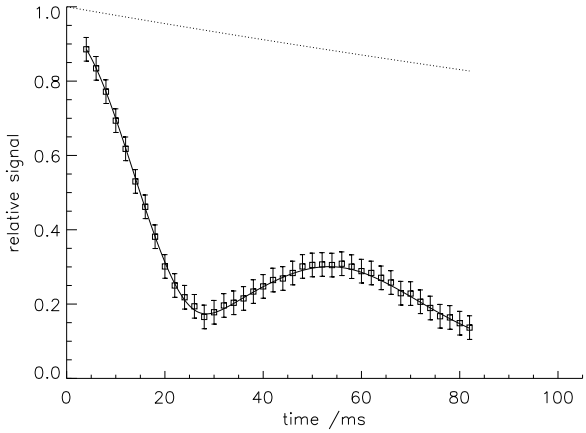

$\Delta\chi = 0.95\,\mathrm{ppm}$

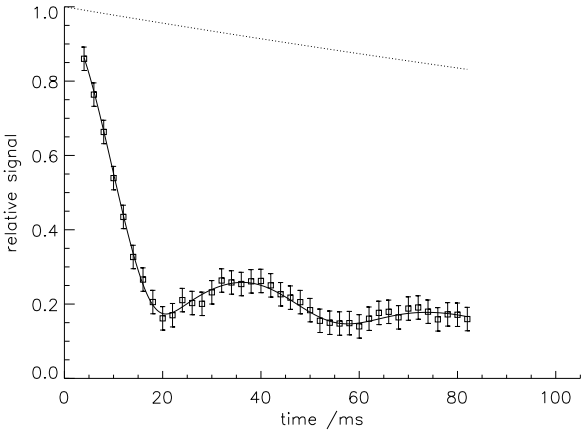

$B_0 = 3.0\,\mathrm{T}$, $0.2\,\mathrm{mM}_{Gd-DTPA}$, $\theta = 90°$, $\lambda = 0.3$

$\Delta\chi = 0.61\,\mathrm{ppm}$

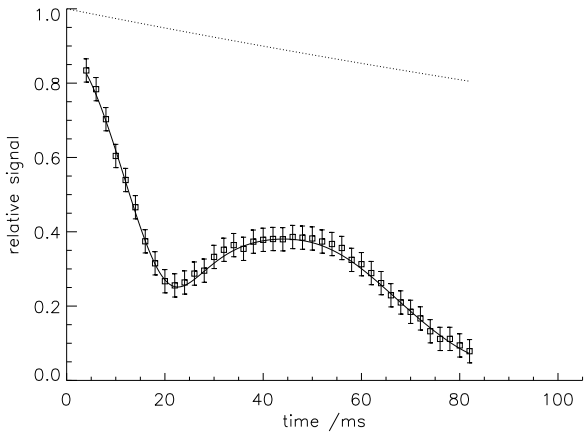

$\Delta\chi = 0.95\,\mathrm{ppm}$

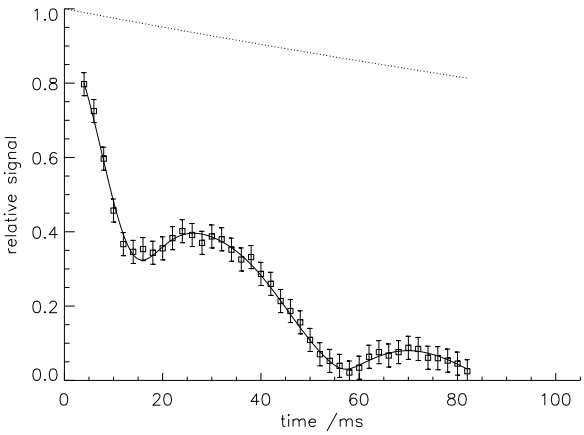

A.1.2. Fit Parameters of All Measurements

			r^2 values		
			1.5 T	1.5 T	3.0 T
θ	λ	$\Delta\chi$	0.2 $\mathrm{mM}_{\mathrm{Gd-DTPA}}$	1.6 $\mathrm{mM}_{\mathrm{Gd-DTPA}}$	0.2 $\mathrm{mM}_{\mathrm{Gd-DTPA}}$
0°	0.1	low	0.9961	0.9997	0.9810
		high	0.9945	0.9992	0.9355
	0.2	low	0.9949	0.9992	0.9851
		high	0.9943	0.9991	0.9776
	0.3	low	0.9922	0.9992	0.9718
		high	0.9832	0.9987	0.9841
55°	0.1	low	0.9996	0.9998	0.9995
		high	0.9996	0.9997	0.9995
	0.2	low	0.9986	0.9995	0.9950
		high	0.9970	0.9997	0.9983
	0.3	low	0.9874	0.9992	0.9800
		high	0.9987	0.9996	0.9955
90°	0.1	low	0.9999	0.9998	0.9993
		high	0.9977	0.9998	0.9984
	0.2	low	0.9979	0.9997	0.9991
		high	0.9991	0.9995	0.9964
	0.3	low	0.9955	0.9996	0.9978
		high	0.9951	0.9996	0.9964
			mean $r^2 = 0.994$		

Table A.1: *Fitted r^2 values of all phantom measurements. The low/high $\Delta\chi$ value means 0.61/0.95 ppm for the measurements with an extracapillary Gd-DTPA concentration of 0.2 mM and 0.48/0.82 ppm for 1.6 mM extracapillary Gd-DTPA.*

			λ values ± relative difference		
			1.5 T	1.5 T	3.0 T
θ	λ	$\Delta\chi$	0.2 mM $_{\mathrm{Gd-DTPA}}$	1.6 mM $_{\mathrm{Gd-DTPA}}$	0.2 mM $_{\mathrm{Gd-DTPA}}$
0°	0.1	low	0.099 + 1.4%	0.095 + 4.9%	0.073 + 26.8%
		high	0.101 − 0.6%	0.102 − 2.2%	0.084 + 16.1%
	0.2	low	0.205 − 2.5%	0.188 + 5.9%	0.193 + 3.6%
		high	0.203 − 1.3%	0.200 − 0.1%	0.187 + 6.7%
	0.3	low	0.310 − 3.4%	0.322 − 7.2%	0.255 + 14.8%
		high	0.359 − 19.7%	0.322 − 7.2%	0.294 + 2.0%
55°	0.1	low	0.123 − 23.3%	0.120 − 20.4%	0.118 − 18.3%
		high	0.101 − 1.0%	0.120 − 19.8%	0.120 − 20.3%
	0.2	low	0.273 − 36.4%	0.197 + 1.5%	0.190 + 4.8%
		high	0.222 − 10.8%	0.203 − 1.3%	0.204 − 1.9%
	0.3	low	0.257 + 14.3%	0.349 − 16.2%	0.208 + 30.8%
		high	0.351 − 17.1%	0.307 − 2.4%	0.265 + 11.6%
90°	0.1	low	0.091 + 8.7%	0.115 − 15.3%	0.100 − 0.0%
		high	0.094 + 5.6%	0.097 + 3.3%	0.101 − 0.5%
	0.2	low	0.208 − 3.8%	0.187 + 6.5%	0.199 + 0.6%
		high	0.212 − 5.8%	0.198 + 1.2%	0.195 + 2.4%
	0.3	low	0.249 + 17.0%	0.264 + 11.9%	0.272 + 9.2%
		high	0.297 + 1.1%	0.302 − 0.8%	0.297 + 0.9%
mean and standard deviation of relative difference = -0.8 ± 12.4 %					

Table A.2: *Fitted λ values of all phantom measurements and their relative difference to the experimentally adjusted values. The low/high $\Delta\chi$ value means 0.61/0.95 ppm for the measurements with an extracapillary Gd-DTPA concentration of 0.2 mM and 0.48/0.82 ppm for 1.6 mM extracapillary Gd-DTPA.*

			$\Delta\chi$ values ± relative difference		
			1.5 T	1.5 T	3.0 T
θ	λ	$\Delta\chi$	0.2 mM $_{\mathrm{Gd-DTPA}}$	1.6 mM $_{\mathrm{Gd-DTPA}}$	0.2 mM $_{\mathrm{Gd-DTPA}}$
0°	0.1	low	0.672 − 10.2%	0.482 − 0.5%	0.616 − 1.0%
		high	0.988 − 4.0%	0.843 − 2.8%	0.952 − 0.2%
	0.2	low	0.657 − 7.7%	0.498 − 3.8%	0.617 − 1.1%
		high	0.982 − 3.4%	0.837 − 2.1%	0.948 + 0.2%
	0.3	low	0.652 − 6.8%	0.491 − 2.3%	0.617 − 1.2%
		high	0.982 − 3.4%	0.849 − 3.6%	0.949 + 0.1%
55°	0.1	low	0.435 + 28.6%	0.429 + 10.5%	0.510 + 16.4%
		high	0.973 − 2.4%	0.772 + 5.8%	0.833 + 12.3%
	0.2	low	0.596 + 2.2%	0.514 − 7.0%	0.649 − 6.5%
		high	0.983 − 3.5%	0.835 − 1.8%	0.933 + 1.8%
	0.3	low	0.578 + 5.2%	0.346 + 27.9%	0.764 − 25.2%
		high	0.896 + 5.7%	0.732 + 10.7%	0.999 − 5.2%
90°	0.1	low	0.557 + 8.7%	0.399 + 16.9%	0.535 + 12.3%
		high	0.968 − 1.9%	0.762 + 7.1%	0.874 + 7.9%
	0.2	low	0.593 + 2.8%	0.415 + 13.6%	0.521 + 14.6%
		high	0.905 + 4.7%	0.755 + 8.0%	0.808 + 14.9%
	0.3	low	0.664 − 8.9%	0.418 + 12.8%	0.536 + 12.1%
		high	0.937 + 1.3%	0.745 + 9.1%	0.826 + 13.1%
mean and standard deviation of relative difference = -3.2 ± 9.6 %					

Table A.3: *Fitted $\Delta\chi$ values of all phantom measurements and their relative difference to the experimentally adjusted values. The low/high $\Delta\chi$ value means 0.61/0.95 ppm for the measurements with an extracapillary Gd-DTPA concentration of 0.2 mM and 0.48/0.82 ppm for 1.6 mM extracapillary Gd-DTPA.*

A.2. Capillary Network Phantom

A.2.1. Signal Plots of All String Compartments

On the following pages the T_2-corrected signal time curve around the spin echo is shown for all string compartments. The corresponding string diameter is given in the top left corner of each plot. The solid lines represent the simulated signal for the best fitting parameters as shown in Tab. 4.5 for the free fit and the fit with fixed λ. Both lines nearly coincide and both fitted the measurement curve with $r^2 > 0.999$. The error (σ) was determined by a homogeneous background ROI according to the Rician noise distribution of MRI data (Gudbjartsson and Patz, 1995) and is indicated by dots below and above each measurement point.

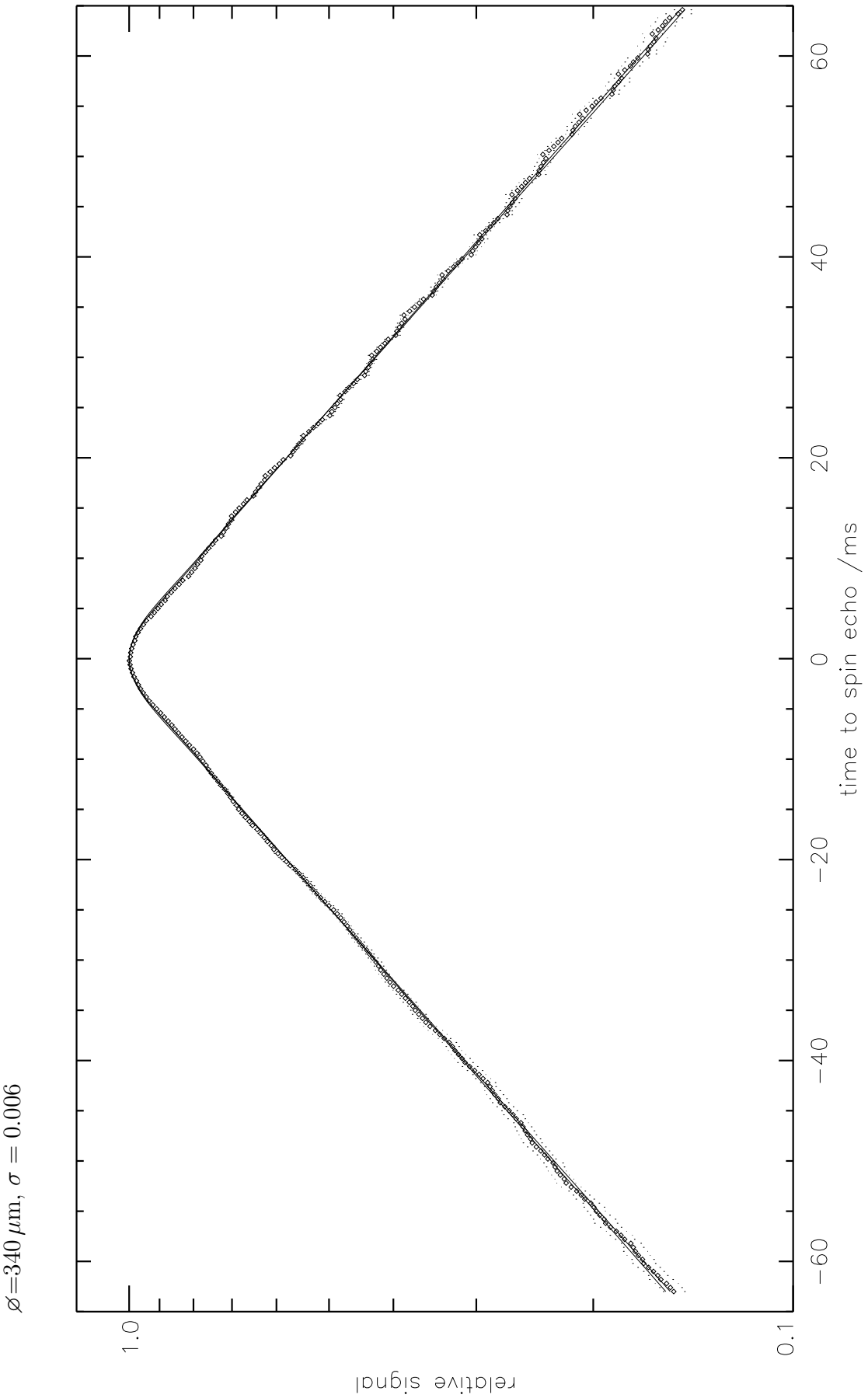
⌀=340 μm, σ = 0.006
relative signal
1.0
0.1
−60
−40
−20
0
20
40
60
time to spin echo /ms

$\varnothing$=200 μm, $\sigma = 0.006$

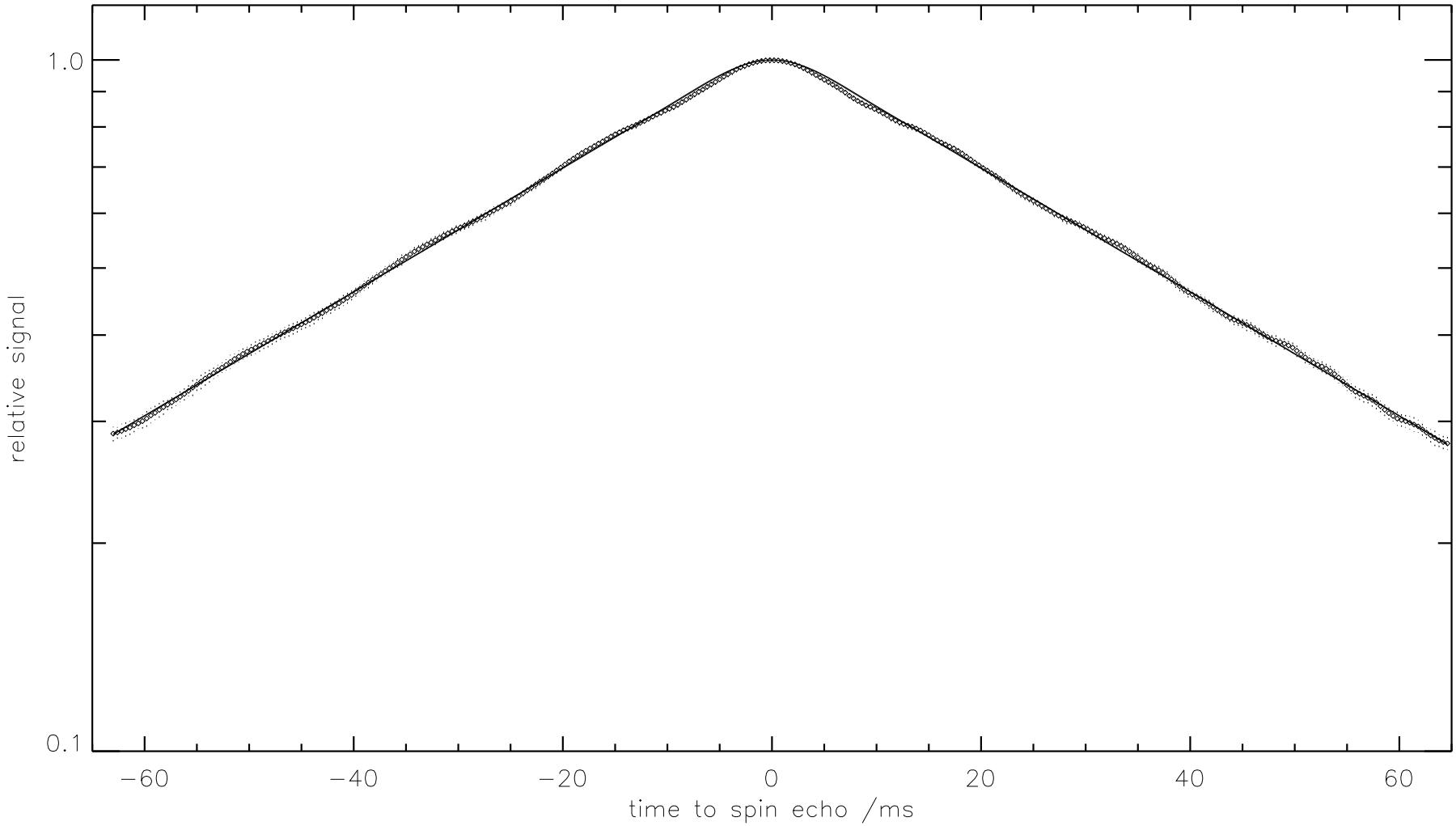

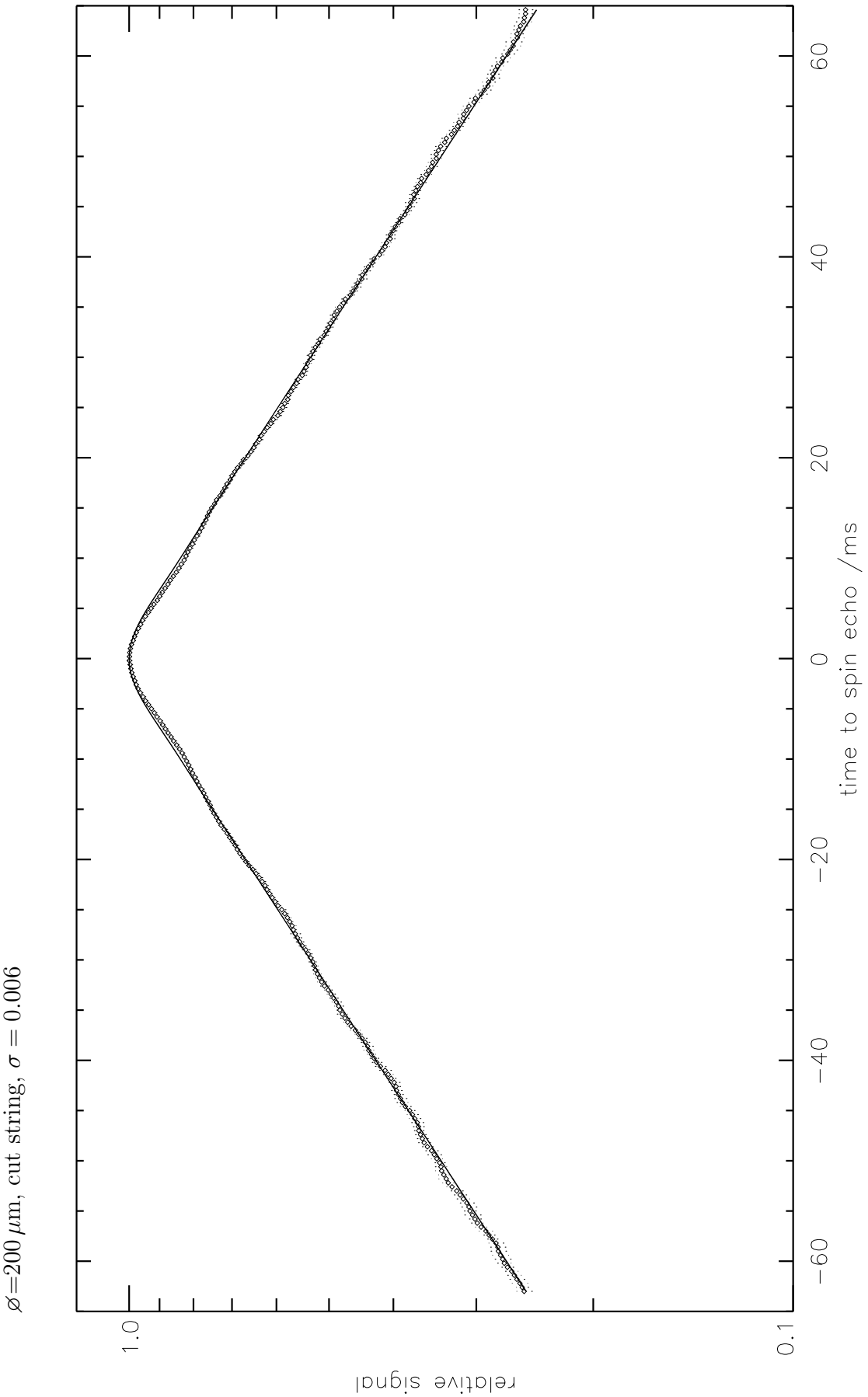
⌀=200 μm, cut string, σ = 0.006
relative signal
1.0
0.1
−60
−40
−20
0
20
40
60
time to spin echo /ms

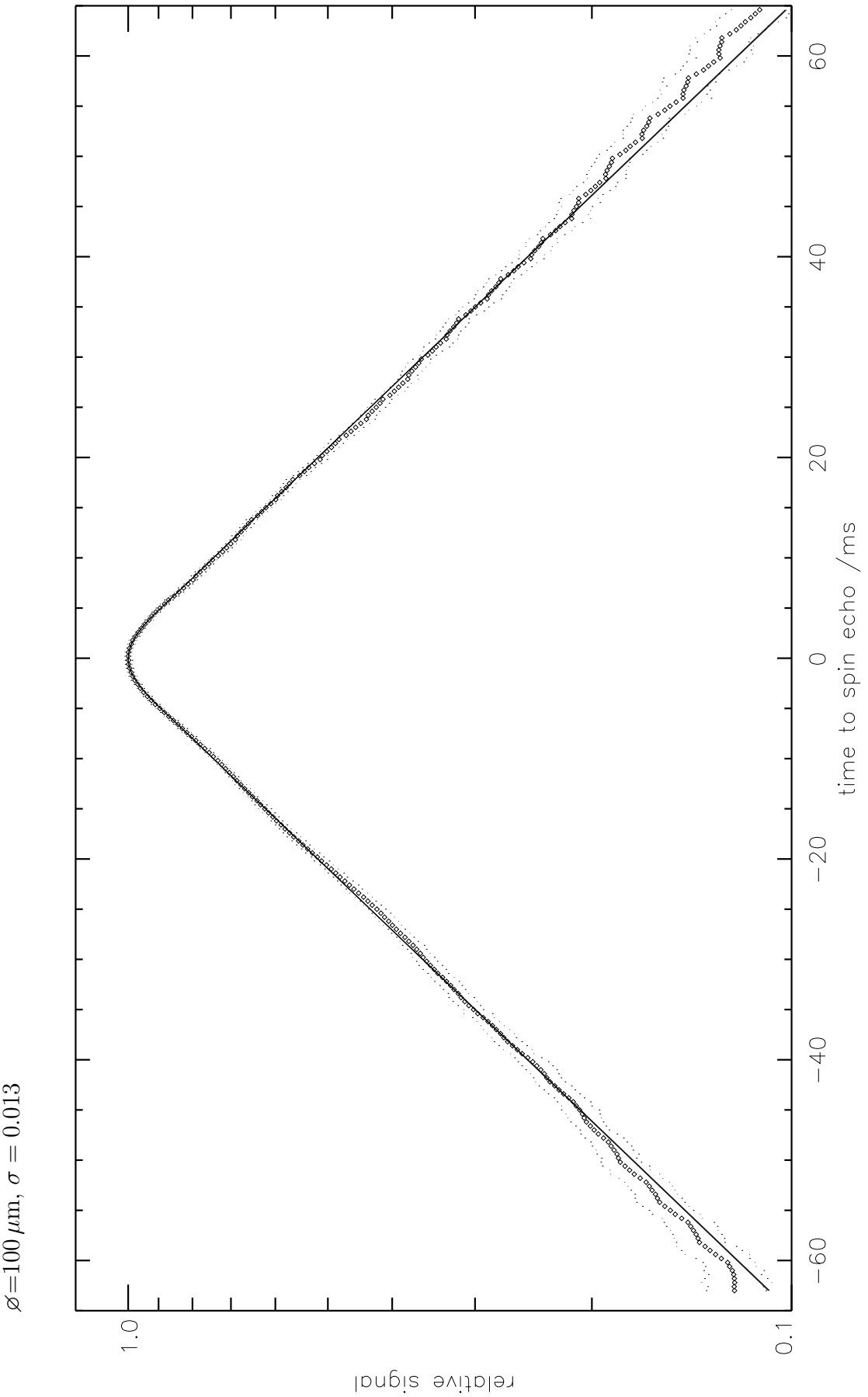
ø=100 μm, σ = 0.013
relative signal
1.0
0.1
−60
−40
−20
0
20
40
60
time to spin echo /ms

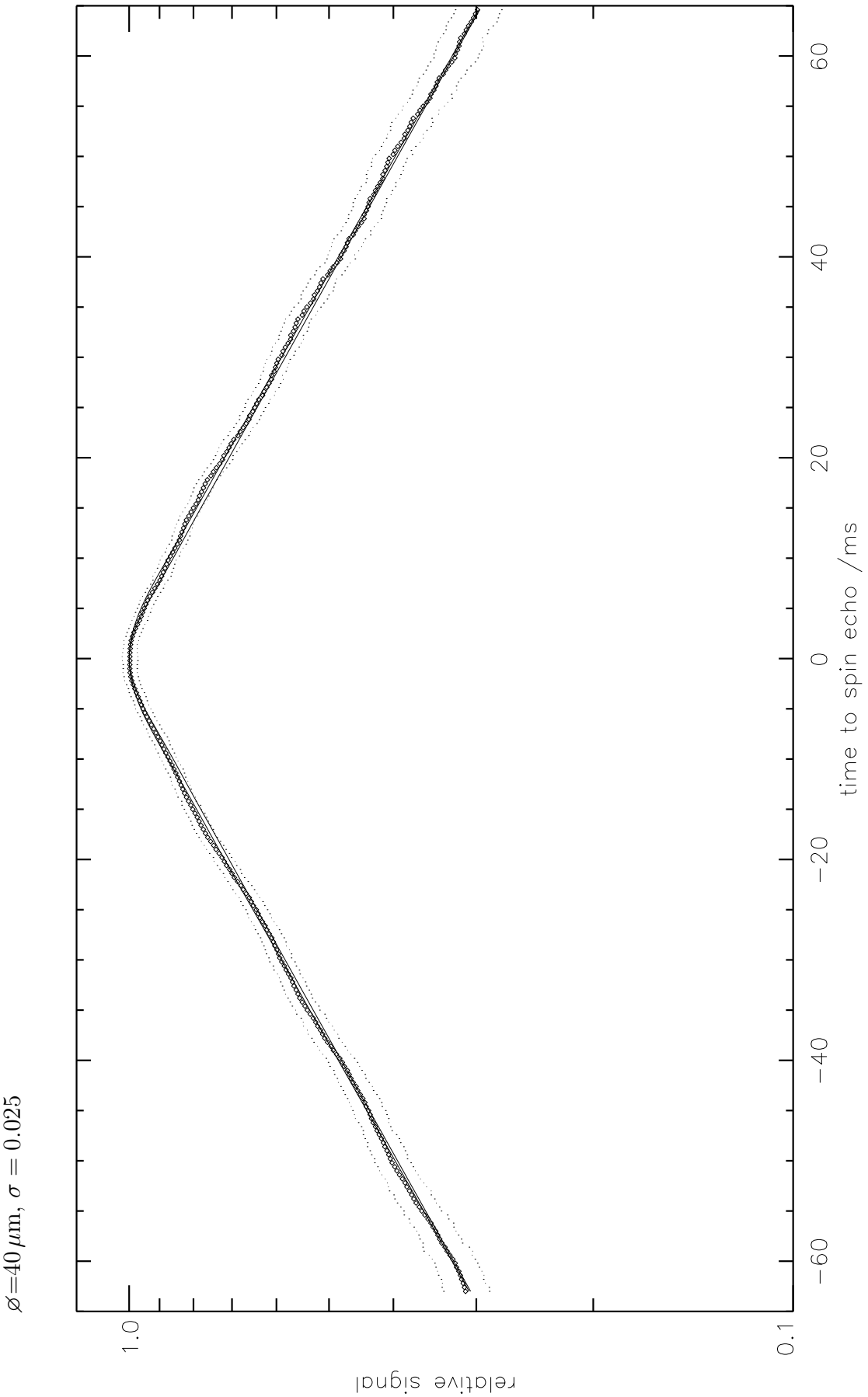
⌀=40 μm, σ = 0.025
relative signal
1.0
0.1
−60
−40
−20
0
20
40
60
time to spin echo /ms

A.2.2. Contour Plots of Root Mean Square Errors (MSE) of All Strings Compartments

On the following pages the MSE contour plot is shown for each string compartment. The corresponding string diameters are given in the top left corner of each page.

The upper diagram shows the MSE for freely changing $\Delta\chi$ from 0.7 to 2.2 ppm and λ from 0.0 to 0.1. The minimal MSE is marked by dotted lines and a cross symbol. The straight solid lines denote the λ_{fix} values known from phantom construction (Tab. 3.1). The dashed lines mark the standard deviation of λ_{fix}.

The bottom diagram illustrates the MSE along the path of λ_{fix} (solid line) and its variation (dashed lines). The dotted lines mark the minimal MSE for these paths. The MSE was normalized to the maximum value of the λ_{fix} path.

All parameters which were resulted from these diagrams are summarized in the Results section (Tab. 4.5).

$\varnothing$=340 μm

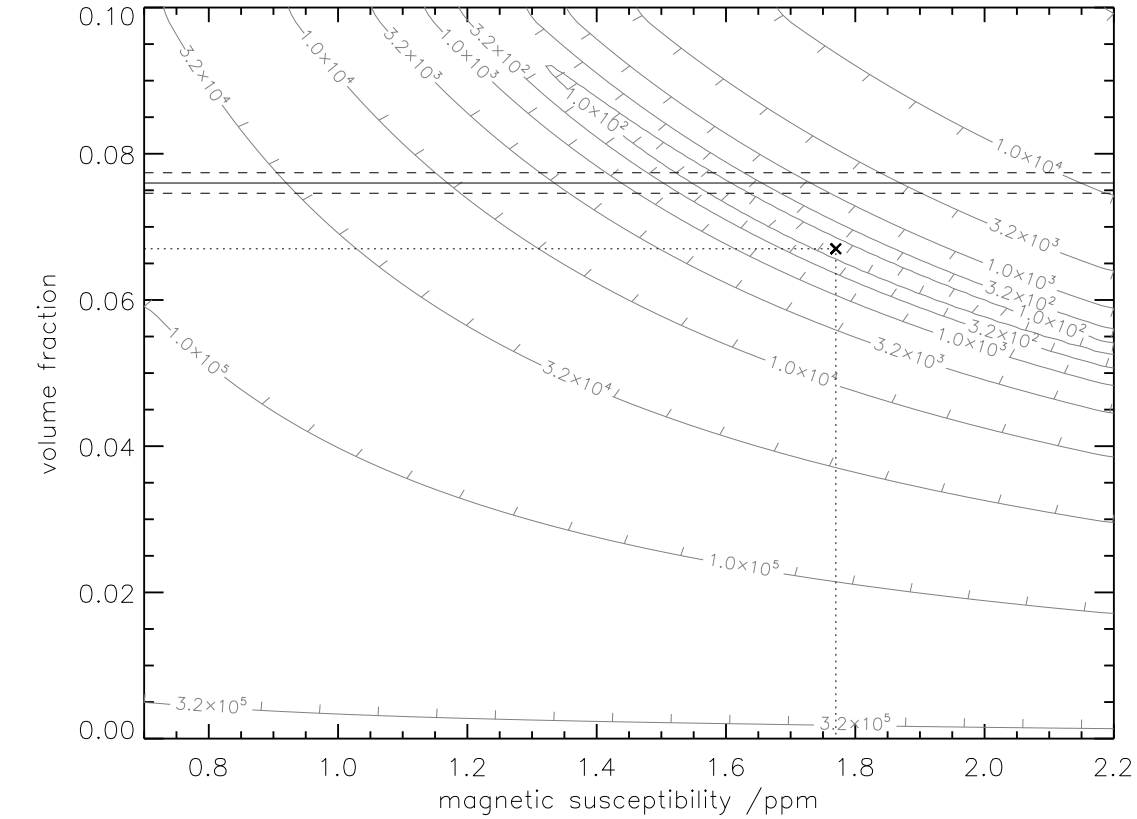

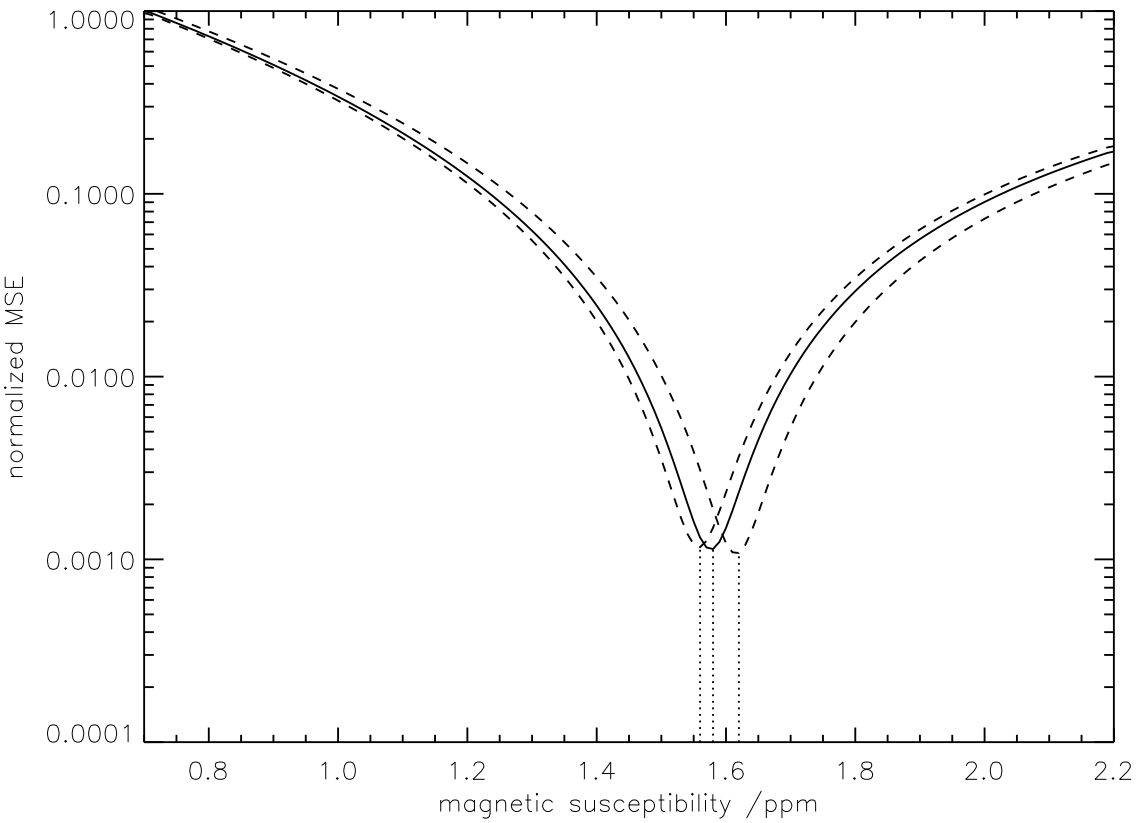

$\varnothing$=200 μm

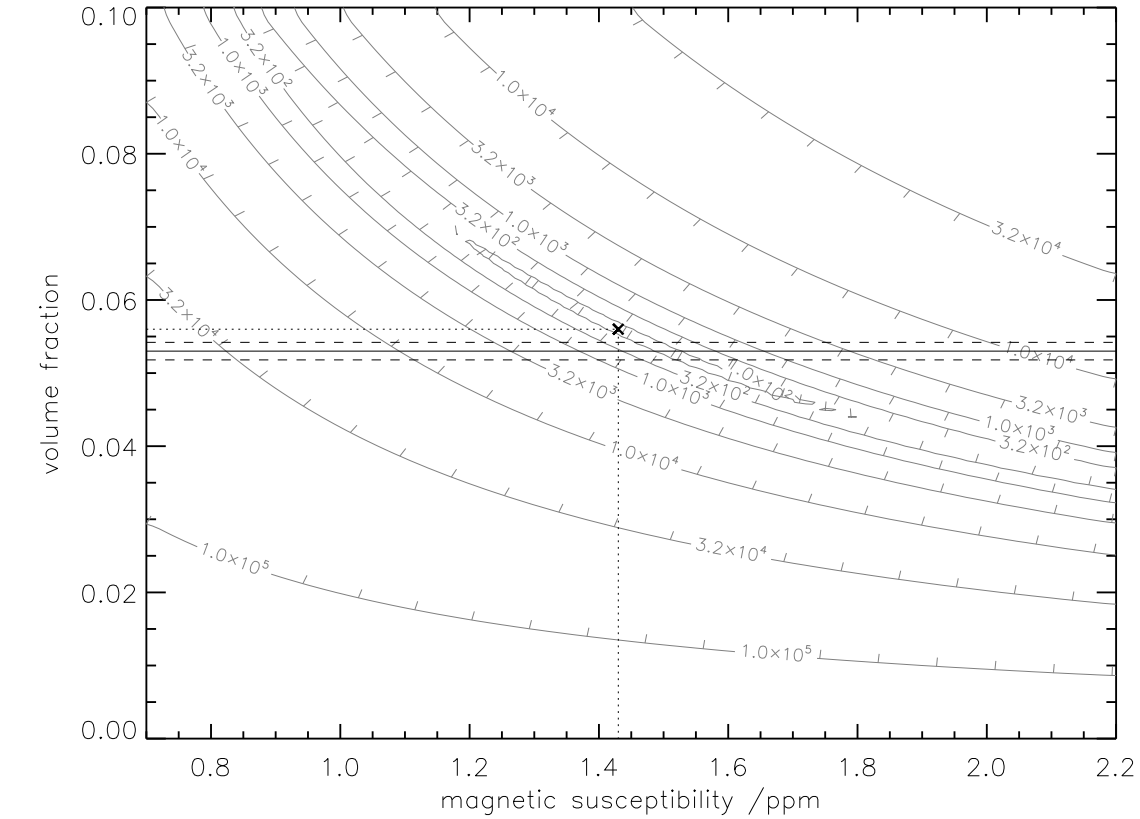

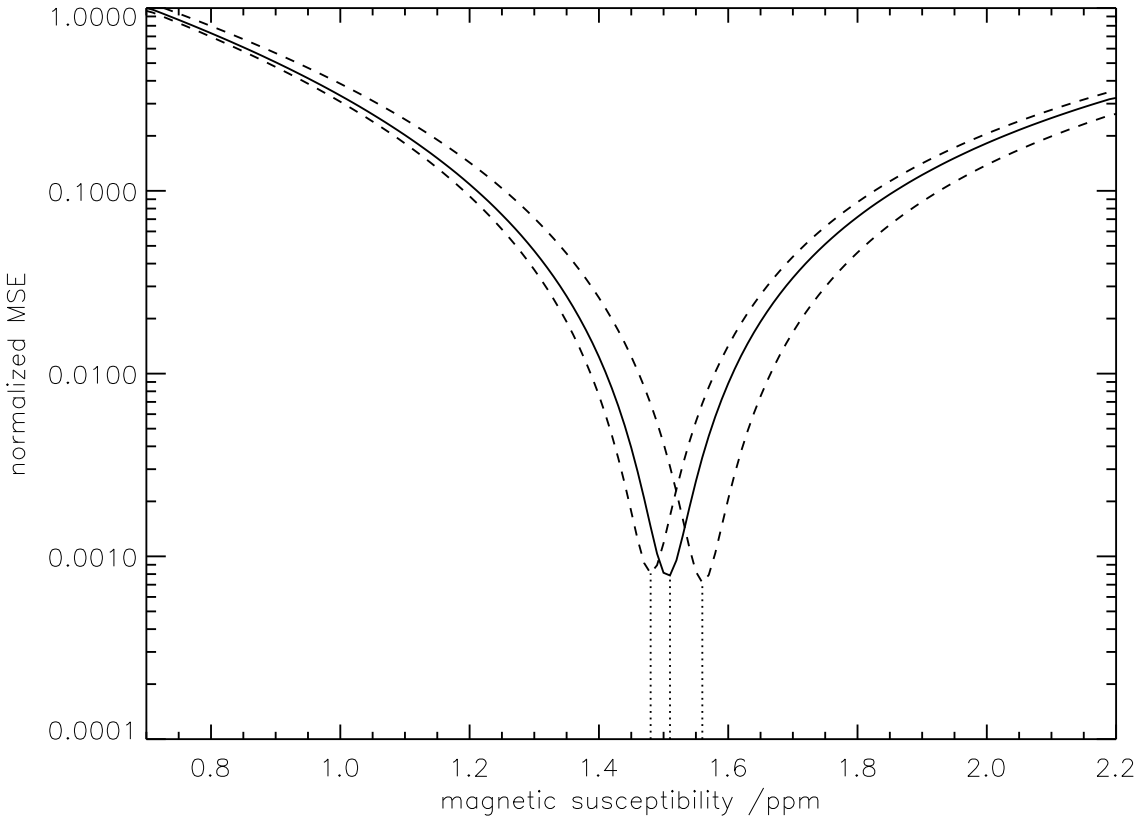

$\varnothing$=200 μm, cut string

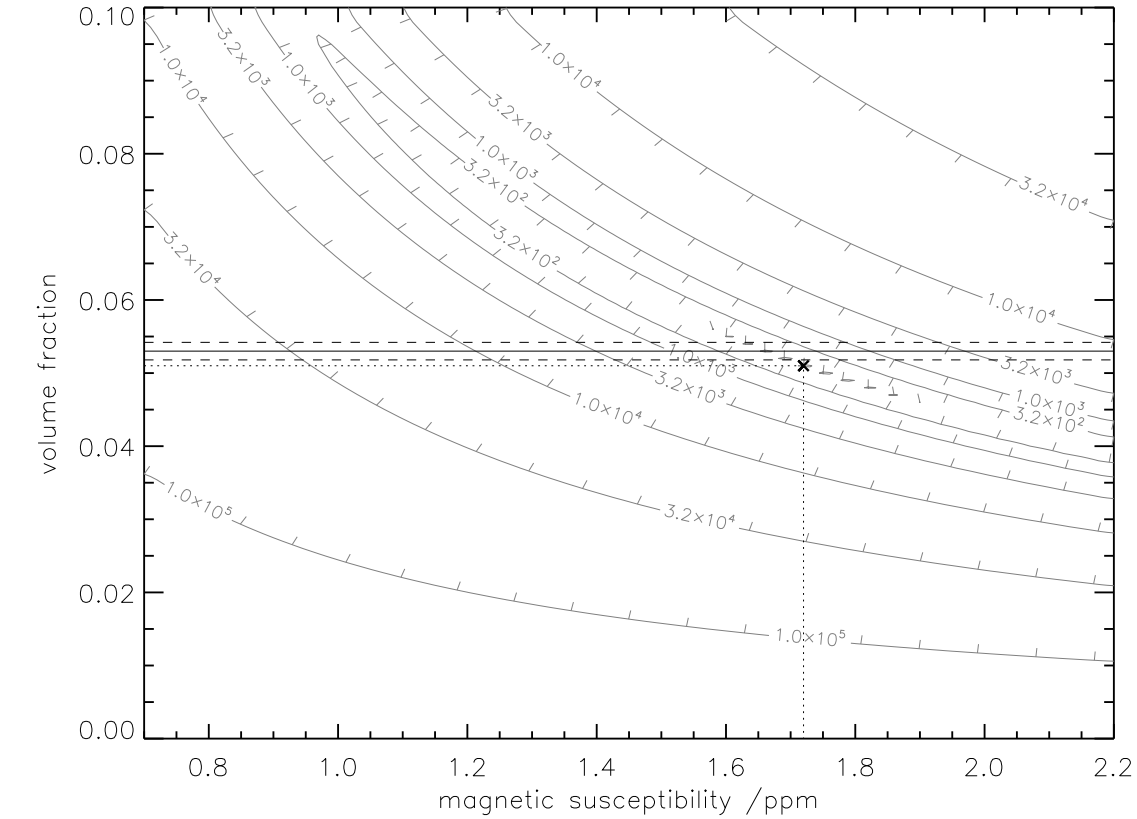

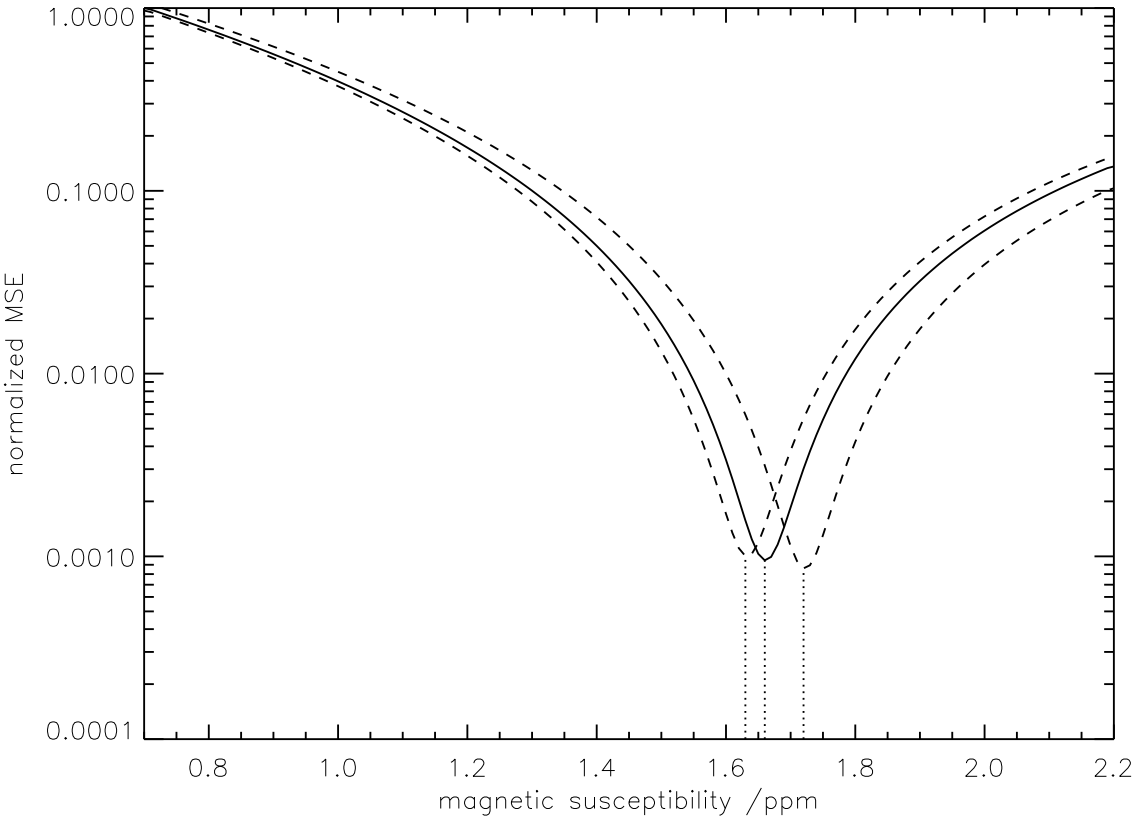

$\varnothing$=100 μm

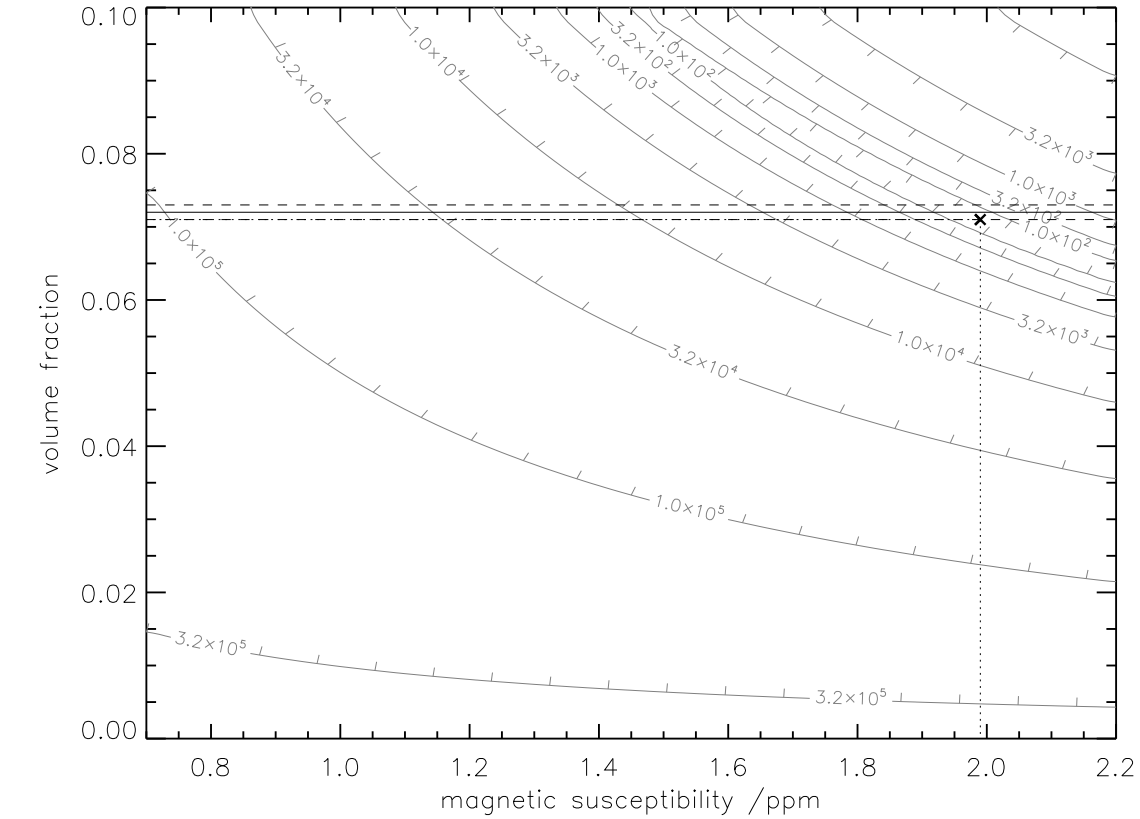

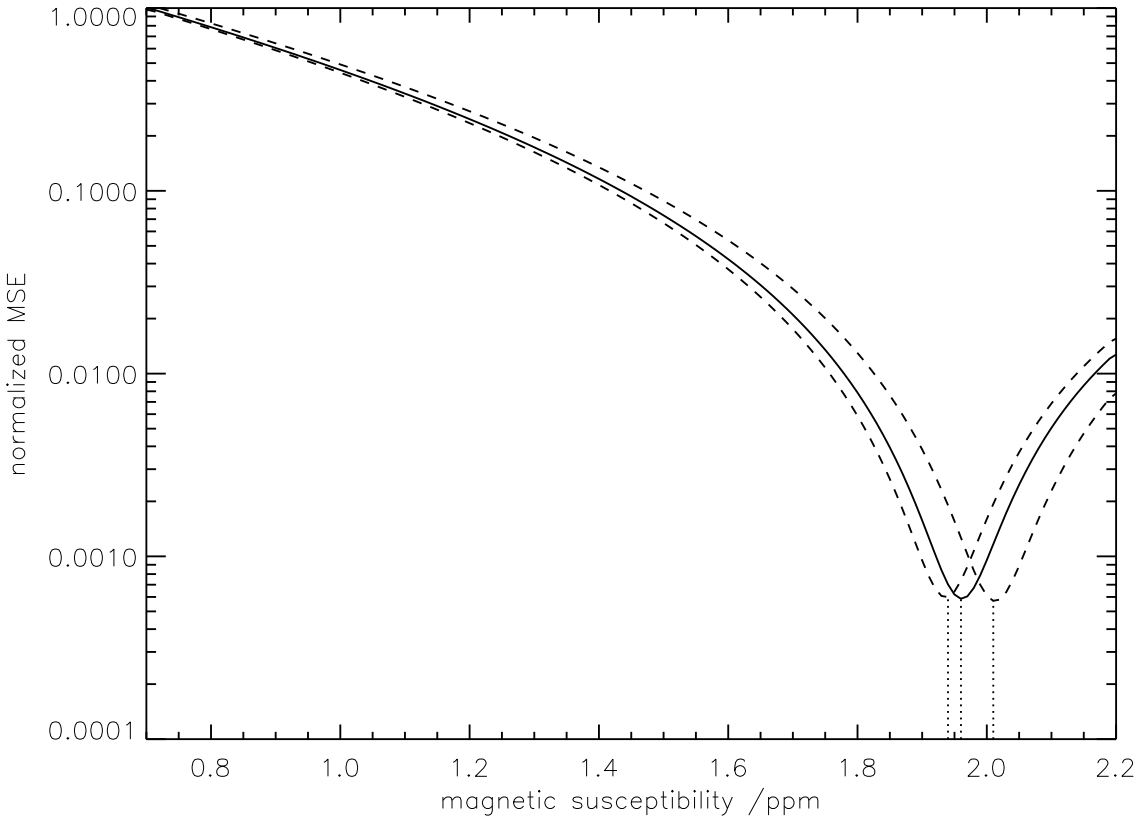

$\varnothing$=40 μm

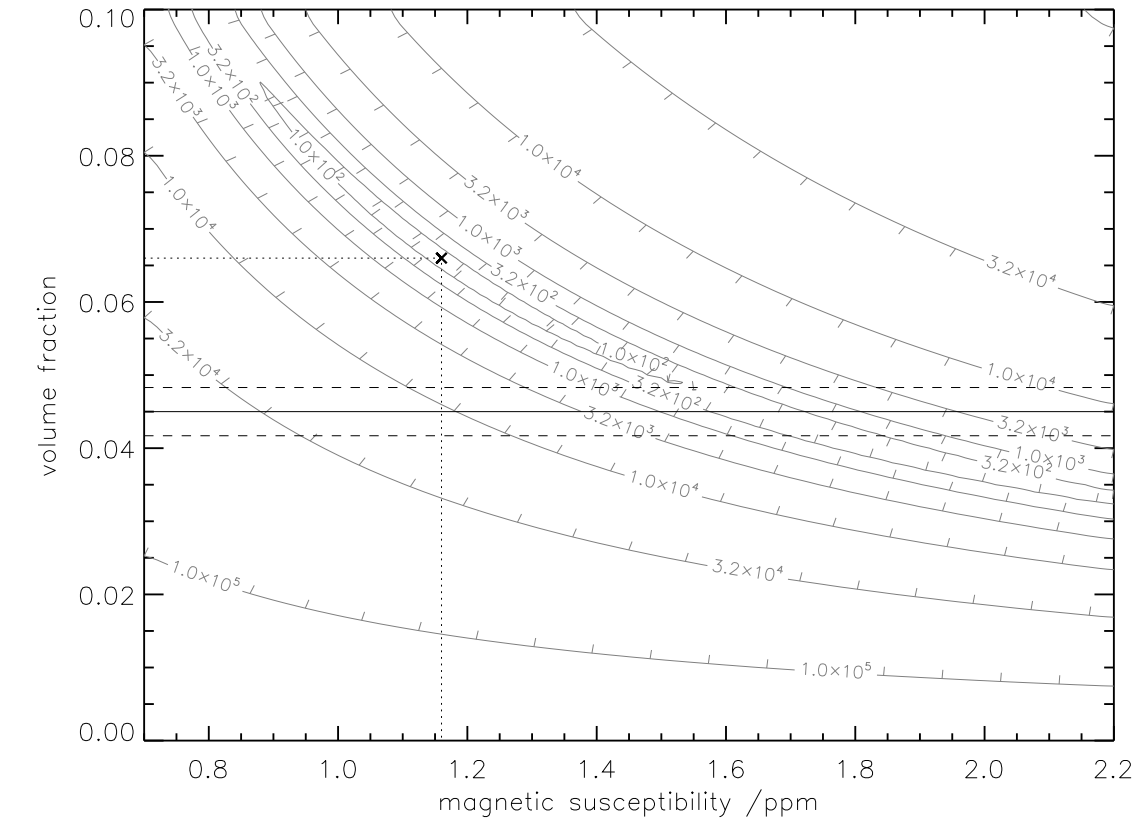

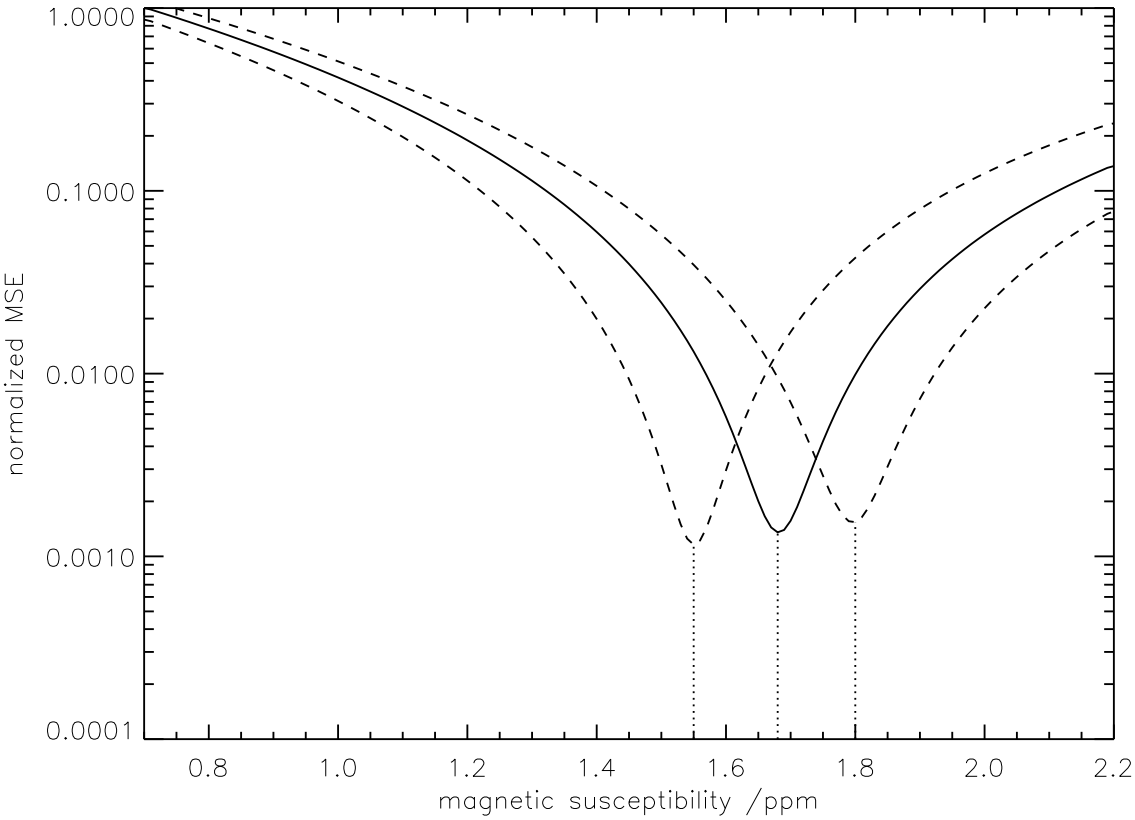

A.3. Selbstständigkeitserklärung

Ich versichere, dass ich die vorliegende Arbeit ohne unzulässige Hilfe Dritter und ohne Benutzung anderer als der angegebenen Hilfsmittel angefertigt habe. Die aus anderen Quellen direkt oder indirekt übernommenen Daten und Konzepte sind unter Angabe der Quelle gekennzeichnet.

An der inhaltlich-materiellen Erstellung der vorliegenden Arbeit waren keine weiteren Personen beteiligt. Insbesondere habe ich hierfür nicht die entgeltliche Hilfe von Vermittlungs- bzw. Beratungsdiensten (Promotionsberater oder anderer Personen) in Anspruch genommen. Niemand hat von mir unmittelbar oder mittelbar geldwerte Leistungen für Arbeiten erhalten, die im Zusammenhang mit dem Inhalte der vorgelegten Dissertation stehen.

Die Arbeit wurde bisher weder im In- noch im Ausland in gleicher oder ähnlicher Form einer Prüfungsbehörde vorgelegt.

Ich bin darauf hingewiesen worden, dass die Unrichtigkeit der vorstehenden Erklärung als Täuschungsversuch angesehen wird und den erfolglosen Abbruch des Promotionsverfahrens zu Folge hat.

(Ort, Datum) (Unterschrift)

Ilmenau, den

Danksagung

Das Gelingen dieser Arbeit und der Abschluss meiner Promotion wäre ohne die Unterstützung einer Vielzahl von Personen nicht möglich gewesen. Ich bedanke mich sehr bei allen die mir dabei behilflich waren.

Allen voran sei meinem Doktorvater an der Technischen Universität Ilmenau Prof. Dr. Philipp Maaß für sein Interesse an diesem Thema, die Vertretung gegenüber der Fakultät und vor allem für sein Vertrauen in meine Arbeit gedankt.

Prof. Dr. Jürgen R. Reichenbach möchte ich besonders danken. Er gab mir die Möglichkeit auf dem spannenden Gebiet der MR-Physik und MR-Bildgebung wissenschaftlich tätig zu werden und lies mir jederzeit seine uneingeschränkte Unterstützung zuteil werden.

Weiterhin bedanke ich mich bei allen, auch ehemaligen, Mitarbeitern der Arbeitsgruppe Medizinische Physik für die gute Zusammenarbeit und dass sie mir immer mit Rat und Tat zur Seite standen. Folgende Kollegen seien hier besonders hervorgehoben: Dr. Alexander Rauscher und Dipl. Ing. Andreas Deistung für die tolle Zusammenarbeit, Dr. Karl-Heinz Herrmann gebührt spezieller Dank für seine ausgiebigen Tipps zu LaTeXund Dipl. Ing. Daniel Güllmar verdient sich ohne Übertreibung den Titel “Bester Mitarbeiter aller Zeiten”, denn ohne sein Organisationstalent und sein unermüdlichen Einsatz zur Aufrechterhaltung einer funktionierenden Computerinfrastruktur wäre die Arbeitsfähigkeit der Arbeitsgruppe sehr eingeschränkt.

Dem klinischen Personal von Radiologen und Medizinisch-technischen Radiologieassistenten am Institut sei auch für ihr gute Zusammenarbeit gedankt. Besonders danke ich Frau Dr. Ulrike Löbel für ihre Unterstützung und ihrer Bereitschaft mir auch noch so einfache medizinische Fragen zu beantworten.

Ich danke sehr herzlich meinen Eltern und Geschwistern für ihr Vertrauen und ihre Unterstützung.

A.4. Curriculum Vitae

Name	Jan Sedlacik
Date of birth	2. January 1978
Place of birth	Zeulenroda
Marital status	single
Citizenship	German

Education

6/2003 - 12/2007	PhD research: *"New Advances in Susceptibility Weighted MRI to Determine Physiological Parameters"*, Medical Physics Group, Friedrich Schiller University Jena, Germany
8/2001 - 12/2002	diploma thesis: *"Aufbau einer Messanordnung für die mikrofluidische online-Erfassung von Doppelstrang-DNA für die Mikrodurchfluss-PCR in Chipthermocyclern"*, Institute of Physical High-Technology, Jena, Germany
8/1997 - 5/2003	graduate engineer in applied physics (Dipl.Ing.), Technical University Ilmenau, Germany
7/1996	high school graduation, Friedrich Schiller Gymnasium, Zeulenroda, Germany.

Experience

4/2001 - 8/2001	internship, Fukui National College of Technology, Material Science, Sabae, Fukui, Japan
4/2001 - 8/2001	assistant in Scientific English, Fukui University, Fukui, Japan
8/1999 - 9/2000	student research assistant in Physical Chemistry, Technical University Ilmenau, Germany
7/2000 - 6/2002	member of the students council, Technical University Ilmenau, Germany

Awards

9/2004	"Siemens-Award for Young Scientists in Medical Physics" for the work *"In vitro und in vivo suszepibilitäts-gewichtete Bildgebung (SWI)"*, conferred on the occasion of the 35. DGMP annual meeting, Leipzig, Germany, 22.-25.September 2004
9/2007	"Philips-Award in Medical Physics", for the work *"Obtaining Blood Oxygenation Levels from MR Signal Behaviour in the Presence of Single Venous Vessels"*, conferred on the occasion of the Dreiländertagung, "Medizinphysik 2007", Bern, Swiss, 25. -28. September 2007

MEMBERSHIPS

since 12/2003	International Society for Magnetic Resonance in Medicine (ISMRM)
since 4/2004	German Chapter of the ISMRM (DS-ISMRM)
since 8/2004	Deutsche Gesellschaft für Biomedizinische Technik (DGBMT)

A.5. Publications

A.5.1. Papers

J. Sedlacik, K. Helm, A. Rauscher, J. Stadler, H-J. Mentzel, W.A. Kaiser, J.R. Reichenbach: *"Investigations on the Effect of Caffeine on Cerebral Venous Vessel Contrast by Using Susceptibility-Weighted Imaging (SWI) at 1.5T, 3T and 7T"*, NeuroImage, accepted, Nov 2007

A. Deistung, A. Rauscher, **J. Sedlacik**, S. Witoszynskyj, J.R. Reichenbach: *"GUIBOLD: A Graphical User Interface for Image Reconstruction and Data Analysis in Susceptibility Weighted Magnetic Resonance Imaging"*, RadioGraphics, accepted, Aug 2007

J. Sedlacik, A. Rauscher, J.R. Reichenbach: *"Obtaining Blood Oxygenation Levels from MR Signal Behaviour in the Presence of Single Venous Vessels"*, Magn Reson Med 58(5):1035-44, 2007

A. Rauscher, **J. Sedlacik**, A. Deistung, J.R. Reichenbach: *"Susceptibility Weighted Imaging: Theory and Applictions"*, Z Med Phys, 16(4):240-50, 2006

H-J. Mentzel, D. Karadag, D. Güllmar, U. Löbel, J.R. Reichenbach, **J. Sedlacik**, J. Seidel, U. Brandl: *"Unidentified bright objects in neurofibromatosis type 1: Results of diffusion tensor imaging in children and adolescents"*, Journal of Pediatric Neurology, 4(1):27-31, 2006

A. Rauscher, **J. Sedlacik**, C. Fitzek, B. Walter, A. Hochstetterr, R. Kalff, W.A. Kaiser, J.R. Reichenbach:*"High Resolution Susceptibility Weighted MR-Imaging of Brain Tumors during the Application of an Exogeneous Gaseous Agent"*, Rofo 177(8):1065-1069, 2005.

A. Rauscher, **J. Sedlacik**, M. Barth, E.M. Haacke, J.R. Reichenbach *"Non-invasive Assessment of Vascular Architecture and Function During Modulated Blood Oxygenation Using Susceptibility Weighted MRI (SWI)"*, Magn Reson Med 54(1):87-95, 2005.

A. Rauscher, **J. Sedlacik**, M. Barth, H.-J. Mentzel, J.R. Reichenbach *"Magnetic susceptibility sensitive MR-phase imaging of the human brain"*, AJNR Am J Neuroradiol 26(4):736-742, 2005.

D.R. Fischer, J.R. Reichenbach, A. Rauscher, **J. Sedlacik**, and W.A. Kaiser *"Application of an exogenous hyperoxic contrast agent in MR mammography: initial results"*, Eur Radiol, 15(4):829-832, 2005.

M. Toyoda, **J. Sedlacik**, M. Inagaki *"Intercalation of formic acid into carbon fibers and their exfoliation"*, Synthetic Metals 130(1):39-43, 2002.

A.5.2. Conference Abstracts (as first author)

J. Sedlacik, A. Rauscher, S. Witoszynskyj, P. Müller, E. Dittrich, W. A. Kaiser, and J. R. Reichenbach *"Verification of Susceptibility Difference and Volume Fraction for the Calculation of Oxygenation Extraction Fraction using Measurements of a Single Capillary and Network Phantom"*, In Proc of ISMRM, vol. 15, p. 2080 (2007).

J. Sedlacik, A. Rauscher, W. A. Kaiser, and J. R. Reichenbach. *"Bestimmung des Blutoxygenierungsgrades anhand von MR-Signalzerfällen einzelner venöser Gefäße"*, In RöFo, vol. 179, Suppl. 1, p.S292 (2007).

J. Sedlacik, A. Rauscher, and J. R. Reichenbach. *"Berechnung der Sauerstoffsättigung anhand des MR Signalverhaltens einzelner venöser Blutgefäße"*, In 9. Jahrestagung der Deutschen Sektion ISMRM e.V., ISSN 1863-6365, pp. 49-50 (2006).

J. Sedlacik, A. Rauscher, J.R. Reichenbach. *"Investigations on the Non-Mono Exponential Signal Decay in Presence of a Single Vessel; Simulations, Phantom and in vivo Measurements"*, In Proc of ISMRM, vol. 14, p. 1531 (2006).

J. Sedlacik, A. Rauscher, C. Fitzek, B. Walter, A. Hochstetter, R. Kalff, W.A. Kaiser, J.R. Reichenbach. *"High-resolution susceptibility weighted MR imaging in patients with brain tumors during the application of exogeneous gaseous agents"*, In European Radiology, vol. 16, p. 158 (2006).

J. Sedlacik, A. Rauscher, Y. Xu, E. M. Haacke, and J. R. Reichenbach. *"Signal Behaviour of Capillary Phantoms and In Vivo Measurements using Multi-Echo Susceptibility Weighted Imaging (SWI)"*, In Biomedizinische Technik, vol. 50, pp. 1166-1167 (2005).

J. Sedlacik, A. Rauscher, and J.R. Reichenbach. *"Fast Susceptibility Weighted Imaging (SWI) using different k-Space Undersampling Mechanisms"*, In Biomedizinische Technik, vol. 50, pp. 1190-1191 (2005).

J. Sedlacik, A. Rauscher, Y. Xu, E. M. Haacke, and J. R. Reichenbach. *"Application of 3D Multi-Echo Susceptibility Weighted Imaging (SWI) for In Vivo Determination of Cerebral Oxygen Extraction Fraction (OEF)"*, In Biomedizinische Technik, vol. 50, pp. 235-236, (2005).

J. Sedlacik, A. Rauscher, and J. R. Reichenbach. *"Verstärkung des Venenkontrastes bei der Suszeptibilitätsgewichteten Bildgebung (SWI) mittels Koffein."*, In 8. Jahrestagung der Deutschen Sektion ISMRM e.V., ISSN 1863-6365, pp. 55-56 (2005).

J. Sedlacik, K-H. Herrmann, A. Rauscher, and J. R. Reichenbach. *"SWI using Different k-Space Undersampling Mechanisms."*, In Proc of ISMRM, vol. 13, p. 1142 (2005).

J. Sedlacik, A. Rauscher, Y. Xu, E. M. Haacke, and J. R. Reichenbach. *"Gradient Echo Signal Recovery at Late TE due to Partial Volume Effects."*, In Proc of ISMRM, vol. 13, p. 1559 (2005).

J. Sedlacik, A. Rauscher, A. Deistung, W. A. Kaiser, and J. R. Reichenbach. *"Caffeine-induced contrast enhancement in volunteers by using susceptibility-weighted imaging (SWI)."*, In European Radiology, vol. 15, p. 241, (2005).

J. Sedlacik, A. Rauscher, and J. R. Reichenbach. *"In vitro und in vivo suszepibilitäts-gewichtete Bildgebung (SWI)."*, In Medizinische Physik, ISBN 3-925218-84-X, pp. 50-51. (2004).

J. Sedlacik, A. Rauscher, P. Maaß, and J. R. Reichenbach. *"Multi Echo Susceptibility Weighed Imaging (SWI) - Phantom and In Vivo Measurements."*, In Biomedizinische Technik, vol. 49, pp. 148-49 (2004).

J. Sedlacik, A. Rauscher, A. Deistung, and J. R. Reichenbach. *"Modulation of Susceptibility-Weighted Contrast in Volunteers Using Caffeine."*, In Klinische Neurophysiologie, vol. 35, p. 197 (2004).

J. Sedlacik, A. Rauscher, C. Labadie, W. A. Kaiser, and J. R. Reichenbach. *"High-resolution BOLD-venography of the human brain during carbogen breathing."*, In European Radiology, vol. 14, p. 298 (2004).

A.5.3. Conference Abstracts (as co-author)

A Rauscher, A Deistung, S Witoszynskyj, D Enrico, **J Sedlacik**, and JR Reichenbach. *"Improved Phase Processing in Susceptibility Weighted Imaging"*, In Proc of ISMRM, vol. 15, p. 3097 (2007).

C Kutschbach, K Helm, **J Sedlacik**, H-J Mentzel, ME Bellemann, WA Kaiser, and JR Reichenbach. *"Effects of several carbogen concentrations on signal changes in susceptibilitiy weighted imaging (SWI)"*, In Proc of ISMRM, vol. 15, p. 3096 (2007).

A Deistung, **J Sedlacik**, A Rauscher, J Stadler, C Tempelmann, J Bernarding, WA Kaiser, P Müller, E Dittrich, JR Reichenbach. *"Susceptibility Weighted Imaging at 15T, 3T and 7T"*, In Proc of ISMRM, vol. 15, p. 2076 (2007).

K Helm, C Kutschbach, **J Sedlacik**, H-J Mentzel, WA Kaiser, and JR Reichenbach. *"MR-Untersuchungen zum Einfluss von Koffein auf die zerebrale Physiologie mit Hilfe der suszeptibilitätsgewichteten Bildgebung (SWI)"*, In RöFo, vol. 179 Suppl. 1, p. S229 (2007).

C Kutschbach, K Helm, **J Sedlacik**, H-J Mentzel, WA Kaiser, and JR Reichenbach. *"MR-Untersuchungen zum Einfluss verschiedener Karbogenkonzentrationen auf die zerebrale Physiologie mit Hilfe der suszeptibilitätsgewichteten Bildgebung (SWI)"*, In RöFo, vol. 179 Suppl. 1, p. S214 (2007).

K Helm, C Kutschbach, **J Sedlacik**, H-J Mentzel, WA Kaiser, JR Reichenbach. *"Caffeine-Induced Changes in Cerebral Physiology Investigated by SWI (Susceptibility-Weighted-Imaging)"*, In European Radiology, vol. 17 Suppl. 1, p. 156 (2007).

K Helm, C Kutschbach, **J Sedlacik**, JR Reichenbach. *"Caffeine-Induced Changes In Cerebral Physiology Investigated by SWI"*, In 9. Jahrestagung der Deutschen Sektion ISMRM e.V., ISSN 1863-6365, pp. 45-46 (2006).

C Kutschbach, K Helm, **J Sedlacik**, JR Reichenbach. *"Effects of Several Carbogen Compositions on Signal Changes in Susceptibility Weighted Imaging (SWI)"*, In 9. Jahrestagung der Deutschen Sektion ISMRM e.V., ISSN 1863-6365, pp. 43-44 (2006).

A Rauscher, **J Sedlacik**, M Barth, S Witoszynskyj, JR Reichenbach. *"Phase map based investigation of intravoxel signal dephasing in gradient echo MRI"*, In Proc of ISMRM, vol. 14, p. 2792 (2006).

H-J Mentzel, A Rauscher, **J Sedlacik**, U Zimmermann, WA Kaiser, JR Reichenbach. *"Enhanced detection of abnormalities in pediatric neuroradiology using high-resolution susceptibility weighted imaging"*, In Pediatr Radiol, vol. 36 Suppl. 1, p. S67 (2006).

A Deistung, A Rauscher, **J Sedlacik**, S Witoszynskyj, JR Reichenbach. *"Optimized image processing in susceptibility weighted MR-imaging (SWI)"*, In European Radiology, vol. 16 Suppl. 1, p. 314 (2006).

A Rauscher, M Barth, S Witoszynskyj, **J Sedlacik**, JR Reichenbach. *"Phase map based simulation of signal dephasing in gradient echo MR imaging"*, In European Radiology, vol. 16 Suppl. 1, p. 286 (2006).

A Rauscher, S Witoszynskyj, **J Sedlacik**, M Barth, JR Reichenbach. *"Untersuchung von Spin-Dephasierung mit hochaufgelösten Fieldmaps "*, In 8. Jahrestagung der Deutschen Sektion ISMRM e.V., ISSN 1863-6365, pp. 16-17 (2005).

A Rauscher, S Witoszynskyj, **J Sedlacik**, M Barth, JR Reichenbach. *"Phaseninformation in der MR-Tomographie"*, In 8. Jahrestagung der Deutschen Sektion ISMRM e.V., ISSN 1863-6365, pp. 67-68 (2005).

H-J Mentzel, A Rauscher, **J Sedlacik**, C Fitzek, U Brandl, JR Reichenbach, WA Kaiser. *"High-Resolution BOLD-MR-angiography as a new diagnostic tool for children"*, In Pediatr Radiol, vol. 35 Suppl. 2, p. S150 (2005).

A Rauscher, S Witoszynskyj, **J Sedlacik**, M Barth, JR Reichenbach. *"Simulation of intravoxel signal dephasing in gradient echo imaging based on high resolution phase maps"*, In Biomedizinische Technik, vol. 50, p. 1186 (2005).

A Deistung, A Rauscher, **J Sedlacik**, S Witoszynskyj, and JR Reichenbach. *"Optimization of Data Processing in Susceptibility-Weighted Imaging"*, In Biomedizinische Technik, vol. 50, p. 1168 (2005).

A Rauscher, **J Sedlacik**, M Barth, S Witoszynskyj, JR Reichenbach. *"An in vivo visualization of the BOLD effect by susceptibility weighted phase imaging"*, In NeuroImage, vol. 26 Suppl. 1, p. 44 (2005).

U Löbel, D Güllmar, H-J Mentzel, **J Sedlacik**, JR Reichenbach, P Stoeter, WA Kaiser. *"Diffusion tensor imaging gesunder Neugeborener, Kinder und Jugendlicher"*, In RöFo, vol. 177 Suppl. 1, p. S201 (2005).

H-J Mentzel, A Rauscher, **J Sedlacik**, C Fitzek, U Brandl, JR Reichenbach, WA Kaiser. *"Hochauflösende suszeptibilitätsgewichtete Bildgebung als diagnostische Möglichkeit in der pädiatischen Neuroradiologie"*, In RöFo, vol. 177 Suppl. 1, p. S324 (2005).

A Deistung, A Rauscher, **J Sedlacik**, S Witoszynskyj, WA Kaiser, JR Reichenbach. *"Entwicklung einer flexiblen grafischen Benutzerschnittstelle zur Rekonstruktion und Darstellung suszebtibilitätsgewichteter MR-Daten"*, In RöFo, vol. 177 Suppl. 1, p. S315 (2005).

A Rauscher, **J Sedlacik**, C Fitzek, B Walter, A Hochstetter, R Kalff, WA Kaiser, JR Reichenbach. *"Hochaufgelöste suszeptibilitätsgewichtete MR-Bildgebung bei Hirntumoren unter Modulation der Blutoxygenierung"*, In RöFo, vol. 177 Suppl. 1, p. S330 (2005).

H-J Mentzel, A Rauscher, **J Sedlacik**, C Fitzek, JR Reichenbach, WA Kaiser. *"Enhanced Detection of Abnormalities in Pediatric Neuroradiology Using High-Resolution Susceptibility Weighted Imaging"*, In Proc of ISMRM, vol. 13, p. 1146 (2005).

A Rauscher, **J Sedlacik**, C Fitzek, B Walter, A Hochstetter, R Kalff, WA Kaiser, JR Reichenbach, *"Investigation of tumor activity and anatomy by SWI during the inhalation of carbogen and air"*, In Proc of ISMRM, vol. 13, p. 2083 (2005)

A Deistung, A Rauscher, **J Sedlacik**, S Witoszynskyj, M Barth, WA Kaiser, JR Reichenbach. *"A graphical user interface for SWI-reconstruction"*, In European Radiology, vol. 15 Suppl 1., p. 155 (2005).

U Löbel, D Güllmar, H-J Mentzel, **J Sedlacik**, JR Reichenbach, WA Kaiser. *"Diffusion tensor imaging of healthy neonates and children up to adolescence"*, In European Radiology, vol. 15 Suppl 1., p. 280 (2005).

A Deistung, A Rauscher, **J Sedlacik**, S Witoszynskyj, M Barth, JR Reichenbach. *"Eine graphische Benutzerschnittstelle Benutzeroberfläche für suszeptibilitätsgewichtete MRT"*, In 7. Jahrestagung der Deutschen Sektion ISMRM e.V., ISSN 1863-6365 (2004).

A Rauscher, **J Sedlacik**, JR Reichenbach. *"Räumlich hochaufgelöste, suszeptibilitätsgewichtete Phasenbildgebung"*, In Medizinische Physik, ISBN 3-925218-84-X, pp. 256-257 (2004).

A Deistung, A Rauscher, **J Sedlacik**, S Witoszynskyj, M Barth, JR Reichenbach. *"Graphische Benutzerschnittstelle zur Rekonstruktion und Darstellung von suszeptibilitätsgewichteten MRT-Daten"*, In Medizinische Physik, ISBN 3-925218-84-X, pp. 192-193 (2004).

A Rauscher, **J Sedlacik**, JR Reichenbach. *"Susceptibility Weighted Imaging (SWI) of the human brain during modulated blood oxygenation"*, In Biomedizinische Technik, vol. 49 Suppl. 2, pp. 152-153 (2004).

A Rauscher, **J Sedlacik**, C Fitzek, A Hochstetter, R Kalff, WA Kaiser, JR Reichenbach. *"Application of Exogeneous Gaseous Agents in Patients with Brain Tumors using High-Resolution Susceptibility-Weighted Imaging"*, In Klinische Neurophysiologie, vol. 35, pp. 185-186 (2004).

A Deistung, A Rauscher, **J Sedlacik**, JR Reichenbach. *"Graphical User Interface for Reconstruction and Visualization of High-Resolution Susceptibility-Weighted MR Data"*, In Klinische Neurophysiologie, vol. 35, pp. 134-135 (2004).

A Rauscher, **J Sedlacik**, M Barth, WA Kaiser, JR Reichenbach. *"Hochaufgelöste T2*-gewichtete MR-Bildgebung unter Verwendung von Modulus- und Phaseninformation"*, In RöFo, vol. 176 Suppl. 1, p. S342 (2004).

A Rauscher, **J Sedlacik**, M Barth, JR Reichenbach. *"Magnetic Resonance Phase Imaging of the Human Brain at Different Degrees of Blood Oxygenation"*, In Proc of ISMRM, vol. 12, p. 1353 (2004).

A Rauscher, **J Sedlacik**, WA Kaiser, JR Reichenbach. *"MR phase imaging of the human brain with high spatial resolution"*, In European Radiology, vol. 14, p. 299 (2004).